UNIVERSITÄT SIEGEN

Miguel Angel Torres Arredondo

Acoustic Emission Testing and Acousto-Ultrasonics for Structural Health Monitoring

Schriftenreihe der Arbeitsgruppe
für Technische Mechanik
im Institut für Mechanik und Regelungs-
technik - Mechatronik

Herausgeber: Claus-Peter Fritzen

Band 7

Impressum

Prof. Dr.-Ing. Claus-Peter Fritzen

Arbeitsgruppe für Technische Mechanik

Institut für Mechanik und Regelungstechnik - Mechatronik

Universität Siegen

57068 Siegen

ISSN 2191-5601

URN urn:nbn:de:hbz:467-7573

Zugl.: Siegen, Univ., Diss., 2013

Acoustic Emission Testing and Acousto-Ultrasonics for Structural Health Monitoring

genehmigte

DISSERTATION

zur Erlangung des Grades eines Doktors

der Ingenieurwissenschaften

vorgelegt von

M.Sc.-Ing. Miguel Angel Torres Arredondo

aus Armenia, Quindío, Kolumbien

eingereicht bei der Naturwissenschaftlich-Technischen Fakultät

der Universität Siegen

Referent: Prof. Dr.-Ing. Claus-Peter Fritzen

Korreferent: Prof. Dr. Jose Rodellar (UPC, Spanien)

Tag der mündlichen Prüfung

26. August 2013

Preface

The following are the products of my work as a doctoral student at the Institute of Mechanics and Control Engineering-Mechatronics of the University of Siegen. I would like to thank all of the people who encouraged and supported me during the execution of this research. Firstly, I would like to thank Prof. Dr.-Ing. Claus Peter Fritzen for introducing me to this very interesting field of research and the opportunity he provided me to work in his group. I would like to thank as well Prof. Dr.-Ing. habil. Otmar Loffeld not only for giving me the opportunity to join the Research School on Multi-Modal Sensor Systems for Environmental Exploration (MOSES) at the Centre for Sensor Systems (ZESS) but also for his continuous and valuable suggestions focused on the improvement of the scientific quality of my work. I would also like to thank Prof. Dr. José Rodellar for taking over the second examiner responsibility as well as Prof. Dr.-Ing. Thomas Carolus for the contributions to the implementation of the doctorate.

I would like to specially express my gratitude to Dr.-Ing. Rolf Schulte and Dr.-Ing. Jochen Moll for their valuable ideas, fruitful discussions and advice for the improvement of my work. Special thanks to Mr. Gerhard Dietrich and Dipl.-Ing. Wolfgang Richter for their support during the majority of the experiments discussed in this thesis. Additional thanks go to my colleagues M.Sc. Cheng Yang, M.Sc. Henning Jung, Dipl.-Ing. Philipp Hilgendorff, M.Sc. Inka Büthe and M.Sc. Rannam Chaaban. Special thanks go to my colleagues and friends M.Sc. Yan Niu, Dipl.-Ing. Erion Zenuni, Dr.-Ing. Saúl Dufoo, M.Sc. Malika Nischal, Mr. Benjamin Coester and Mr. Ricardo Charry for their continuous support and always motivating attitude towards me during the ups and downs of this research. I strongly appreciate the contributions of the different students who worked under my supervision. I would like to specially thank M.Sc. Margarita Maria Ramirez for her valuable contributions to the present work. Moreover, I would also like to say thanks to Dr.-Ing. Teodolito Guillén Girón, Dipl.-Ing. Andrei Grigorescu, Mrs. Lisa Häbel and Mr. Martin Stenke for their support during several experiments which were carried out during the course of this research. I would also like to thank Dipl.-Ing. K. Schubert from Faserinstitut Bremen for providing the viscoelastic plates evaluated in this work and Prof. Dr. Michel Castaings from the Laboratoire de Mecanique Physique in the University of Bordeaux for the fruitful discussions. Furthermore, I would like to thank Professor C. K.

I. Williams from the University of Edinburgh and Dr. M. Álvarez from the University of Manchester for fruitful discussions concerning the concepts and computer programming of Gaussian Processes.

During my research stays in Barcelona and Denmark at the Polytechnique University of Catalunya and at the Risø National Laboratory for Sustainable Energy in the Technical University of Denmark, I would like to specially thank Dr. Diego A. Tibaduiza, Dr. Luis Eduardo Mujica, Mr. Fahit Gharibnezhad, M.Sc. Malcolm McGugan, Dr. K.-K. Borum, Dr. Helmuth L. Toftegaard and Prof. Dr. P. Brøndsted. I would also like to thank Dipl.-Ing. Roger Handschuh for hosting me during all these years in his house for the time of my studies in Siegen.

My greatest debt is to my parents and brother who have provided inspiration, confidence and firm support throughout my life and studies in the city of Siegen.

Siegen, June 2013 Miguel Angel Torres Arredondo

To my family: Miguel Ángel, Lucia, César Augusto

Contents

Nomenclature

Abbreviations

A/D	Analogue-To-Digital Converter
AE	Acoustic Emission
AET	Acoustic Emission Testing
AIC	Akaike Information Criterion
ANFIS	Adaptive Neuro-Fuzzy Inference System
ANN	Artificial Neural Network
ARD	Automatic Relevance Determination
AS	Auto Scaling
CFRP	Carbon Fibre Reinforced Plastic
CLPT	Classical Laminated Plate Theory
CS	Continuous Scaling
DCB	Dual Cantilever Beam
DWT	Discrete Wavelet Transform
FEM	Finite Element Modeling
FFT	Fast Fourier Transform
FRF	Frequency Response Function
FSDT	First-Order Shear Deformation Theory
GA	Genetic Algorithm

GCC	Generalized Cross-Correlation
GFRP	Glass Fibre Reinforced Plastic
GP	Gaussian Process
GS	Group Scaling
h-NLPCA	Hierarchical Non-Linear Principal Component Analysis
HDT	Hit Definition Time
HLT	Hit Lockout Time
MAP	Matching Pursuit Algorithm
MLP	Multilayered Perceptron
MPCA	Multi-Way Principal Component Analysis
NDI	Non-Destructive Inspection
NDT	Non-Destructive Testing
NLPCA	Non-Linear Principal Component Analysis
OBS	Optimal Baseline Selection
OSS	Optimal Signal Stretch
PCA	Principal Component Analysis
PDT	Peak Definition Time
PHAT	Phase Transform
POD	Probability of Detection
PSD	Power Spectral Density
PWVD	Pseudo Wigner-Ville Distribution
PZT	Lead Zirconate Titanate
SHM	Structural Health Monitoring
SNR	Signal-to-Noise Ratio
SOM	Self-Organizing Map

SPWVD	Smoothed-pseudo Wigner-Ville Distribution
STFT	Short-Time Fourier Transform
TFR	Time Frequency Representation
UCC	Unfiltered Cross-Correlation
WVD	Wigner-Ville Distribution

Greek Symbols

α	Group Velocity Angle
β_k	Chirplet Frequency Modulation Rate
η	Viscosity Matrix
$\delta(t)$	Diract Delta Function
γ_{ij}	Engineering Shear Strain Component
κ_j	Shear Correction Factor
ω	Angular Frequency
ω_k	Chirplet Angular Frequency Centre
ρ	Material Density
σ_{ij}	Stress Tensor Component
θ	Angle of Propagation
$\tilde{\omega}$	Material Characterization Frequency
ε_{ij}	Engineering Strain Component
φ	Fibre Orientation Angle

Latin Symbols

$\mathbf{C}$	Stiffness Matrix
$\mathbf{L}_{\mathrm{A}}$	Decoupled Matrix for Antisymmetric Modes
$\mathbf{L}_{\mathrm{S}}$	Decoupled Matrix for Symmetric Modes
$\mathbf{T}_{\mathrm{m}}$	Stress Tensor of a Mode

$\mathbf{u}_{\mathrm{m}}$	Displacement Field Distribution of a Mode
A_i	i^{th} Antisymmetric Mode
SH_i	i^{th} Shear Horizontal Mode
S_i	i^{th} Symmetric Mode
$C_{gr,x}$	Group Velocity Component in x-axis
$C_{gr,y}$	Group Velocity Component in y-axis
C_{gr}	Group Velocity
C_{ij}	Stiffness Matrix Component
C_{ph}	Phase Velocity
E_{ij}	Young Modulus
f	Frequency
f_c	Centre Carrier Frequency
G_{ij}	Shear Modulus
g_k	Chirplet Atom
h	Plate Thickness
$H(\omega)$	Frequency Response Function
$H(t)$	Impulse Response Function
k	Complex Wavenumber
k_{Im}	Wavenumber Imaginary Part
k_{Re}	Wavenumber Real Part
M_{ij}	Moment Resultant
n_c	Number of Cycles
N_{ij}	In-Plane Force Resultant
P_m	Average Power Flow of a Mode
Q_{ij}	Transverse Force Resultant

$s_{act}(t)$	Actuation Signal
s_k	Chirplet Time Extent
t_i^A	Time of Arrival at the i^{th} Sensor
t_k	Chirplet Time Centre
t_{onset}	Stress Wave Onset Time

Mathematical Symbols

$< \bullet, \bullet >$	Inner Product
$\bar{}$	Complex Conjugate
$\mathbf{T}$	Transpose

Abstract

The global trends in the construction of modern structures require the integration of sensors together with data recording and analysis modules so that its integrity can be continuously monitored for safe-life, economic and ecological reasons. This process of measuring and analysing the data from a distributed sensor network all over a structural system in order to quantify its condition is known as structural health monitoring (SHM). The research presented in this thesis is motivated by the need to improve the inspection capabilities and reliability of SHM systems based on ultrasonic guided waves with focus on the acoustic emission and acousto-ultrasonics techniques. The use of a guided wave-based approach is driven by the fact that these waves are able to propagate over relatively long distances, interact sensitively with and/or being related to different types of defect.

The main emphasis of the thesis is concentrated on the development of different methodologies based on signal analysis together with the fundamental understanding of wave propagation for the solution of problems such as damage detection, localisation and identification. The behaviour of guided waves for both techniques is predicted through modelling in order to investigate the characteristics of the modes being propagated throughout the evaluated structures and support signal analysis. The validity of the developed model is extensively investigated by contrasting numerical simulations and experiments.

In this thesis special attention is paid to the development of efficient SHM methodologies. This fact requires robust signal processing techniques for the correct interpretation of the complex ultrasonic waves. Therefore, a variety of existing algorithms for signal processing and pattern recognition are evaluated and integrated into the different proposed methodologies. Additionally, effects such as temperature variability and operational conditions are experimentally studied in order to analyse their influence on the performance of developed methodologies. At the end, the efficiency of these methodologies are experimentally evaluated in diverse isotropic and anisotropic composite structures.

Kurzfassung

Nach den heutigen Standards zur Konstruktion moderner Leichtbaustrukturen ist es zur Strukturüberwachung aufgrund von wirtschaftlichen, ökologischen und Sicherheitsaspekten unerlässlich, Sensoren und Module zur Datenspeicherung und –analyse in diese Strukturen zu integrieren. Den Prozess der Strukturüberwachung anhand der Messung und Analyse von Daten aus einem dezentralen Sensornetzwerk wird als „Structural Health Monitoring (SHM)“ bezeichnet. Die vorliegende Arbeit und die darin vorgestellten Untersuchungen reagieren auf den Bedarf an verbesserter Genauigkeit und höherer Zuverlässigkeit von SHM-Systemen, die auf geführten Ultraschallwellen basieren, wobei der Fokus der Untersuchung auf Schallemissions- und Acousto-Ultraschalltechniken liegt. Da geführte Wellen lange Wege zurückzulegen können und mit hoher Empfindlichkeit und Genauigkeit auf verschiedene Schadenstypen reagieren, eignen sie sich sehr gut für die Überwachung dünnwandiger Strukturen.

Der Schwerpunkt der Arbeit liegt in der Entwicklung verschiedener Methoden zur Signalanalyse zur Lösung von Problemen wie Schadenserkennung, lokalisierung und identifizierung. Dies ist nicht ohne ein grundlegendes Verständnis der Wellenausbreitungsmechanismen möglich, sodass ein Modell entwickelt wird, anhand dessen die Charakteristiken der angeregten Moden sowie die Wellenausbreitung in den zu untersuchenden Strukturen analysiert werden können, um so die Signalanalyse zu unterstützen. Die Validität des entwickelten Modells wird eingehend anhand von verschiedenen numerischen Simulationen und Experimenten untersucht.

Um besonders effiziente Methoden des SHMs zu entwickeln, sind robuste Signalverarbeitungstechniken zur zuverlässigen Interpretation komplexer Ultraschallwellen notwending. Aus diesem Grund erfolgt die Auswertung einer Vielzahl existierender Algorithmen zur Signalverarbeitung und Mustererkennung, die in die hier vorgestellten Methoden integriert werden. Des Weiteren wird experimentell untersucht, welchen Einfluss Effekte wie Temperaturschwankungen und Betriebsbedingungen auf diese Methoden haben. Abschließend wird experimentell die Effizienz der entwickelten Methoden bei der Überwachung diverser isotroper und anisotroper Faserverbundstrukturen nachgewiesen.

1. Introduction

In today's competitive market, manufacturers are required to design and construct safe, ecological and reliable structures. This demand places a heavy burden on designers and manufacturers for the fulfilment of these requirements. In particular, this is the case for the nuclear, petrochemical, aerospace and aeronautic industries in which component reliability is crucial. In order to guarantee that the structures found in such industries perform their function in a safe, reliable and cost effective manner, regular inspection intervals must be defined. There are many existing techniques in use for the assessing of structural condition, each one having its own characteristics and potentials. These techniques are well documented and are covered by a number of publications where they are labelled as non-destructive inspection techniques [Bray and Mcbride 1992]. Common techniques are visual inspections, magnetic particle testing, dye penetrant testing, eddy current inspection, radiography, infrared/thermal testing and standard ultrasonics.

In the case of metallic structures, the inspection intervals can be defined according to fracture mechanics theory based for example on fatigue crack growth rate so that inspections and possible maintenance are accomplished before flaws reach a critical size. However, in case of unforeseen loads, the inspection periodicity can be too long so that structural failure could happen before a new inspection is scheduled. Additionally to this, the current trends in structural design are very actively incorporating the use of advanced composite materials. For aeronautic and aerospace applications, composites materials are, besides aluminium, the most important materials. Due to well-known properties such as high mass specific stiffness and strength, composites use has extensively increased in the design of existing engineering structures, which also increases the analysis complexity of such structures [Chang 2002]. Additionally, one advantage of using composite materials is the possibility to manufacture a material adjusted to the desired application. According to the European Aeronautic Defence and Space (EADS) company, the composites share has reached more than 15% of the structural weight of civil aircraft, and more than 50% of the structural weight of helicopters and fighter aircraft over the last 40 years [Brandt 2004]. Nevertheless, the mechanical properties of composite materials may degrade severely in the presence of damage such as delaminations, matrix cracking, fibre debonding and breakage, coming for example from impact events, which additionally

complicate the definition of inspection intervals since damage evolution and mechanisms cannot be directly correlated to the loading cycles [Schulte 2010]. Moreover, the way in which composite materials fails is highly dependent on the material configuration. Damage in composites can appear anywhere on the structure and crack growth cannot be predicted using traditional techniques [Emery 2007]. As a result, conservative inspection intervals have to be defined to monitor the structure. Many of the previously mentioned damage types can also be introduced to the structure in the course of its lifetime during manufacture, service or maintenance.

As traditional inspection techniques can be very expensive in terms of both man hours and structure down-time, the development of suitable automatic and reliable monitoring methods would be very valuable. This demands techniques which can continuously monitor the given structure and provide suitable early warning before a propagating damage reaches the limits of criticality. Here is the place where structural health monitoring systems enter into play. The next sections will introduce the basics concepts of structural health monitoring systems, together with a brief explanation of the interrogation methods evaluated in this thesis. Additionally, a review of the state of the art of research in the topics covered along this thesis, and a description of the focus and arrangement of the thesis is provided.

1.1. Structural Health Monitoring Concepts and Techniques

Structural health monitoring (SHM) can be defined as the process of implementing a damage identification strategy for a variety of infrastructures [Farrar and Worden 2007]. As it is defined in this reference, the process involves the monitoring of a structure over time using either continuous or periodically spaced measurements, the extraction of damage-sensitive features from the recorded measurements and the statistical analysis of the extracted features in order to determine the current state of system health. The main difference between SHM and NDT techniques is that sensors are permanently installed on the structure providing continuous or on-demand measurements. According to [Rytter 1993], the problem of structural health monitoring can be considered as a four-levels process which are defined in hierarchical order as follows:

1. Detection: It provides a qualitative indication of the presence of damage.
2. Localisation: It provides information about the position of the damage.
3. Assessment: It provides a quantitative indication of the extent of the damage.
4. Prediction: It provides an estimate of the residual life of the structure.

The advantages of using an SHM system are clearly an improved safety, reduction of inspection time, maintenance costs and structural down-time. There exists a number of techniques used for the identification of damage. Every SHM technique is based on the measurement of a given structural property and this is what normally defines the optimal relationship between coverage and sensitivity to a given type of defect. Structural health monitoring systems can be divided into two main groups that allow for global as well as local evaluation [Mengelkamp 2006]. Additionally, inside of these groups, the methodologies contained for SHM can be classified either as active or passive approaches depending on whether they involve the use of actuators or not.

One well-known approach for damage identification based upon changes in dynamic response is a typical method monitoring the changes in the structure on a global basis. The fundamental assumption of vibration-based damage detection is that changes in the physical properties due to damage will cause changes in the measured dynamic response of the structure [Fritzen 2005]. Damage will usually lead to local changes of stiffness and damping causing a shift of the dynamic characteristics like eigen-frequencies, damping coefficients and mode shapes [Fritzen et al. 2003]. Nevertheless, these changes are very small and often embedded in the background noise. Additionally, finite element modelling and modal analysis required for this type of approach often require intensive tuning which could result in significant uncertainties caused by modelling errors [Sohn et al. 2001]. Additionally, in view of the fact that incipient damage is typically a local phenomenon and the local response is mostly captured by higher frequency modes, these techniques present some practical difficulties since it is more complicated to excite the higher frequency response as more energy is required to produce measurable responses at these higher frequencies [Doebling et al. 1998]. For these reasons, approaches based solely on signal analysis are very attractive for the development of an automated health monitoring system [Worden et al. 2011].

On a local level, there exist methods based for example on the electro-mechanical impedance and guided waves. For the electro-mechanical impedance method, changes in impedance indicate changes in the structure, which in turn can indicate that damage has occurred [Liang et al. 1996, Peairs et al. 2004]. Methods based on guided waves are also commonly used either as passive or active sensing techniques. These approaches are very interesting since guided waves can propagate over long distances making it possible to detect flaws over a considerable area. However, more than one propagating mode is usually contained in the recorded ultrasonic signals which are additionally frequency and angular dispersive, i.e. characteristics such a velocities, attenuation and energy concentration vary according to these parameters. These effects make the analysis of guided waves a non-trivial task. Nevertheless, these techniques have emerged as prominent options in order to estimate the presence, location, and in a more sophisticated level estimate the severity and type of damage.

As a result, the previously mentioned advantages and potentials from guided wave-based methods have motivated the selection of the acoustic emission and acousto-ultrasonics techniques for the present thesis. Additionally, both techniques share many similarities since they are based on high frequency ultrasound waves and use a permanently attached sensor network of piezoelectric transducers. Moreover, both techniques have their range of coverage restricted by the structural complexity and environmental conditions [Clarke 2009].

The following subsections will present basic background and concepts for the acoustic emission and acousto-ultrasonics techniques.

1.1.1. The Acoustic Emission Technique

Acoustic emission (AE) is formally defined as the class of phenomena whereby transient elastic waves are generated by the rapid release of energy from localised sources within a material or the transient elastic waves so generated [ASTM 1982]. From this context, acoustic emission events are generated within the material due to a natural mechanism such as deformation or fracture rather than from an ultrasonic transducer as it is the case for active sensing ultrasonic methods. Localized stress redistribution such as that generated due to matrix cracking, delaminations and fibre breakage generate AE waves having a broad frequency content. The elastic waves generated by an AE event within the structure propagate as guided waves as it was shown in [Gorman 1991]. It was shown that generally a combination of the fundamental symmetric and antisymmetric modes of propagation represents a typical AE signal. Once these waves propagate throughout the structure, they may be detected by an ultrasonic transducer on its surface. Finally, the electrically processed signal is then interpreted as the acoustic emission signal.

Acoustic emission is normally termed as a non-destructive testing technique although it has found more success as a health monitoring approach [Holford 2000]. A major problem with an AE system is the discrimination of the AE signals from the background noise produced by other non-damaging events such as mechanical noise, electrical noise, etc. It has been shown for example in the context of in-flight monitoring of critical aircraft components that the detection of true AE events in the presence of various spurious AE sources such as jet engine noise, hydraulic noise, aerodynamic noise and electromagnetic interference presents a great problem for the applicability of the AE technique [Rao 1990]. One possible solution to this problem is normally given by the trade of sensoric range against noise countermeasures which can be accomplished by the selection of the transducers. Resonant transducers are extremely sensitive offering an excellent signal-to-noise ratio but over a limited narrow bandwidth [Grosse and Ohtsu 2008]. Broadband transducers ideally respond to all the frequencies of the stress wave and return a signal which closely replicates the small-scale motion of the surface [McGugan et al. 2006]. Acoustic emission

measurement systems consist traditionally of transducers, amplifiers and signal storage devices. Transducers are typically piezoelectric transforming the surface dynamic motions of the propagated signal and converting it into an electrical response.

Acoustic emission is probably the most developed method for the implementation of an integrated health monitoring system. Early commercial examples of acoustic emission systems can be found in [Carlyle 1989, Odell 1991]. In these studies, commercial systems were used for the monitoring of the entire fuselage of an General Dynamics F-111 Aardvark aircraft and to monitor AE events in the fuselage of a VC10 aircraft during proof pressure testing by the Royal Air Force, respectively.

1.1.2. The Acousto-Ultrasonics Technique

The acousto-ultrasonics (AU) technique was originally developed in the late seventies as a non-destructive tool for the evaluation of the mechanical properties of composite materials [Vary and Bowles 1979]. Since then the AU technique has been used in order to assess and quantify damage in composite materials. This technique works in a frequency range similar to that used in acoustic emission. A review examining this technology and discussing several applications and monitoring scenarios in aeronautic and aerospace structures can be found in [Finlayson et al. 2001, Meyendorf et al. 2012].

Typically in an AU system, an actuator generating guided waves in the structure is excited by a high frequency pulse signal which is normally a modulated sine or cosine toneburst with a limited number of cycles. An active technique such as AU could take advantage of exciting given guided modes in the structure and overcome some of the disadvantages of AE. Additionally, in contrast to AE systems where AE events are non-repeatable, the recorded ultrasonic signals can be averaged so that elimination of incoherent or transient noise can be accomplished, or even the AU system can operate on-demand or continuously. Once the ultrasonic wave is introduced into the structure, the characteristics of the wave after it has propagated through the structure may be related to a discontinuity of the structure. The structural discontinuity could come from the interaction of the guided waves either with damage in the structure or with a structural component or boundary. Therefore, it is required to count with prior information about the structure in its undamaged state in order to be able to distinguish between damage and other structural features such as rivets, ribs, stiffeners, etc [Clarke 2009]. This is accomplished in the form of a baseline/template signal obtained for the healthy state so that it can be used as reference for comparison with the future test cases.

Finally, damage sensitive features are extracted from the recorded signals using specialised signal processing algorithms, and then pattern recognition techniques are used to detect and possibly classify and estimate the severity of damage.

1.2. Literature Review

A wide-ranging amount of research has previously been conducted into the use different SHM methodologies for damage assessment. Nevertheless, for the current interest of this thesis, only relevant literature to guided waves which is of interest for acoustic emission and acousto-ultrasonics under the context of structural health monitoring is reviewed. It is often cited that acoustic emission history started with the work presented in [Kaiser 1950]. In this study, tensile specimens of metallic materials were tested with the purpose of recording AE signals. Since then this technique has widespread and been topic of continuous research. This is probably given by the fact that under the principle of AE, the structure is always monitored while in operation what allows the permanently recording of the structure dynamic processes. This point makes this technique a valuable tool in order to get information regarding the origin and importance of a discontinuity in a structure.

Since the earliest works in this area the efforts have been concentrated mostly in the correlation of AE signals to different types of damage mechanisms specially in the case of composite laminates. For instance, investigations tried to tackle the problem based on amplitude distribution functions [Pollock 1981], pattern recognition techniques for classification based on signal parameters [Murthy et al. 1987, Oliveira and Marques 2006], traditional AE parameter analysis [Komai et al. 1991] and correlation between the frequency content of acoustic emissions and fracture mechanisms [Giordano et al. 1999, Ramirez-Jimenez et al. 2004]. Advanced waveform-based acoustic emission techniques have also been proposed. A discussion of the effects of omitting the effects of wave propagation, such as attenuation, dispersion, and multiple modes of propagation in the damage mechanism identification procedure using traditional parameters is given in [Prosser et al. 1995]. It was concluded that extreme care should be undertaken in order to distinguish the different source mechanisms in composites by conventional amplitude analyses. This is explained by the fact that the signal parameters are influenced by material dispersion, attenuation and the distance that the signal propagates. An evaluation of different clustering algorithms for acoustic emission using traditional AE parameters as features implementing the k-means method, K-Nearest-Neighbour classifier and self-organising neural network was accomplished in [Godin et al. 2004].

Waveform-based clustering and classification of AE transients in composite laminates using principal component analysis has also been proposed, see for example [Johnson 2002]. The aim of this study was to use the AE signals collected during experiments specially tailored to activate matrix cracking and delaminations as the input data for the analysis with principal component analysis instead of the traditional AE parameters used for clustering purposes. Here, only the first two principal components were used as inputs for the clustering algorithm. A similar approach based on principal component analysis and Gaussian statistical methods, Kernel density estimation and neural networks

is presented in [Rippengill et al. 2003]. Another technique for the calculation of the type and orientation of damage based on the radiation pattern of AE sources and the seismic moment has been developed for the analysis of concrete fracture in [Grosse and Ohtsu 2008].

In order to overcome some of the problems described before, it has been proposed to take into account the modal nature of AE waves [Surgeon and Wevers 1999]. It is expected that this type of analysis can lead to more quantitative and accurate results. Studies analysing the different characteristics of the fundamental modes of propagation for acoustic emission testing can be found in [Pullin et al. 2005, Eaton et al. 2006, Lee et al. 2006]. These studies analysed the amplitude ratio of the fundamental modes of propagation for source orientation determination, investigated the wave velocity at varying angles to assist in source location and characterised the AE emanating from fatigue cracks with respect to the modes of propagation in plate-like structures. Recent studies have continued to include advanced signal processing techniques as a matter of feature extraction such as the discrete wavelet transform in order to study damage evolution and fracture events [Bussiba et al. 2008].

Further studies analyse the relation between transient waveforms and the failure sequence in order to provide a deeper insight of the fracture process [Aggelis et al. 2010]. Slow non-linear material dynamics have been studied in samples where damage was gradually induced and quantified using acoustic emission [Bentahar and Guerjouma 2008]. It was shown that the dynamics evolution are clearly related to AE parameters, particularly to the cumulated energy freed during damage creation and propagation. More recent studies have developed methods for quantifying the performance of acoustic emission systems [Scholey et al. 2010a], provide quantitative measurements of damage [Scholey et al. 2010b] and select the optimal combination of features for the identification of AE clusters [Sause et al. 2012].

Regarding localisation of acoustic emissions, many methods have been presented. In [Baxter et al. 2007] a method that does not require knowledge of the sensor location or wave velocities was developed based on the differences in time of arrival information from a number of locations along the structure. A further improvement of this techniques was proposed in [Hensman et al. 2008]. This method aims at learning the relationship between time of flight differences and damage location using data generated by artificially stimulated acoustic emission. Detection and localisation of stress waves generated during impacts events in composite structures using neural-network or genetic algorithms approaches are proposed in [LeClerc et al. 2007, Yan and Zhou 2009]. A more recent technique was developed in [Kundu 2012] in which acoustic source localisation in an anisotropic plate is accomplished without knowing its material properties.

Active techniques based on guided waves have also attracted the attention of many researchers. The study presented in [Worlton 1957] was probably the first to recognise the

advantages of using guided waves. Depending on the material attenuation and geometric beam-spreading effects, guided waves are able to propagate over relatively long distances, interact sensitively with different types of defects like e.g. delaminations [Hayashi and Kawashima 2002], corrosion damage [Yu et al. 2008], holes [Croxford et al. 2010], etc. For example, [Xu et al. 2008] presents a combination of an improved adaptive harmonic wavelet transform and the principal component analysis performed on baseline signals to highlight the critical features of guided wave propagation in the undamaged structure. The detection of damage is facilitated by comparing the features of the different signals collected from the test structure with the features of the baseline signals. Detection of damage has also been accomplished using a method based on the loss of local temporal coherence of signals combined with an optimal baseline selection procedure [Michaels 2008]. Additionally, a delay-and-sum imaging method applied to the residual signals allowed the localisation of damage and provided characterisation information.

Sensor location studies for damage detection with guided waves have been pursued in [Lee and Staszewski 2007b]. The problem is investigated using the local interaction simulation approach for guided wave propagation modelling by means of numerical simulations. An additional method devised for optimal placement of piezoelectric actuators and sensors for detecting damage in plate-like structures is discussed in [Flynn and Todd 2010]. This is accomplished using a detection theory framework where the optimum configuration is defined as the one that minimizes Bayes risk.

An algorithm employing chirplet matching pursuits followed by a mode correlation check was implemented for damage localisation in [Raghavan and Cesnik 2007]. Guided wave sensing using laser vibrometry can be also used for localisation of damages as it is introduced in [Lee and Staszewski 2007a]. An additional method for damage localisation is presented in [Moll et al. 2010] where a generalized formulation of the common ellipse technique is proposed. This method was capable of precisely estimate multiple damages at different positions simultaneously for anisotropic materials. The computational aspects and automation for this kind of damage localisation algorithms are presented by the author in collaborative research in [Moll et al. 2012].

Besides to damage detection, localisation and sensor placement methods based on guided waves, there has been an increasing interest in compensation methodologies for varying environmental and operational conditions. For example, a method based on auto-associative neural network is employed in [Sohn et al. 2002] for data normalization which separates the effect of damage on the extracted features from those caused by the environmental and vibration variations of the system. A study of temperature compensation techniques ability to compensate changes caused by liquid loading or the effects of non uniform temperature is discussed in [Cicero et al. 2009]. An additional method for feature extraction and sensor fusion for ultrasonic SHM able to cope with changes such as temperature and surface wetting is presented in [Lu and Michaels 2009].

In addition to these studies, crack detection using the acousto-ultrasonics technique has been gaining considerable interest recently [Li-Fei et al. 2012, Zhou et al. 2012]. The idea behind is to exploit the non-linear features of acousto-ultrasonic waves to detect damage onset due to their high sensitivity to damage with small dimensions. Other application to the technique is the evaluation of joint integrity in complex structures. For example, the assessment of bonded patch bridge repairs using acoustic emission and acousto-ultrasonics is proposed in [Pullin et al. 2012]. Recently, an overview of structural health monitoring for aircraft, ground transportation vehicles, wind turbines and pipes focused in acousto-ultrasonics and acoustic emission has been presented in [Meyendorf et al. 2012]. Complementary reviews can be found in [Sohn et al. 2004, Brownjohn 2007, Ciang et al. 2008].

1.3. Objectives of the Thesis

The objective of this thesis is to contribute in the enhancement of the effectiveness and reliability of acoustic emission and acousto-ultrasonics techniques by means of ultrasonic guided waves as structural health monitoring applications for metallic and composite structures. As a result, several methodologies are proposed in order to circumvent traditional problems faced with these techniques for the purpose of damage detection, localisation and identification. This task is accomplished with the help of different well-established signal processing and pattern recognition techniques together with the fundamental understanding of wave propagation as an optimal way to pursue the solution of the given problems.

As a result, the following objectives are defined:

1. Development of a mathematical model that captures accurately the wave propagation in isotropic and composite structures together with guided wave modal analysis in order to analyse not only the frequency and directional dispersive characteristics of the modes of propagation, but also to study the influence of environmental and operational conditions on them.
2. Development of a robust data-based methodology for the characterisation of acoustic emissions from the analysis of the recorded stress waves together with its experimental validation from AE events occurring during tensile tests, double cantilever tests and artificially generated AE.
3. Development of a robust data-based methodology for damage detection and identification by means of the acousto-ultrasonics principle together with its experimental validation in structures where damage has been either simulated or introduced.
4. Development of a data-based methodology for impact magnitude estimation and localisation together with its experimental validation.

These four objectives are individually addressed in the subsequent chapters of this thesis.

1.4. Outline of the Thesis

The thesis will follow the sequence of topics described below.

Chapter 2 provides the theoretical background information on the field of guided waves in pipe-like and plate-like structures. The mathematical modelling of these waves is also presented for completeness together with the calculation and discussion of the different dispersive relationships which will help for supporting the understanding of the wave propagation problem. Subsequently, different signal processing and pattern recognition techniques which are integral part of the methodologies developed in the following chapters are introduced. The main goals of the presented signal processing methods are data cleansing, sensor-data fusion, feature extraction and selection of damage-sensitive information from the sensed signals. Pattern recognition is used to identify the different conditions of the extracted and selected features so that an indication of either their innate characteristics or the state of structural health can be accomplished.

Chapter 3 introduces an approximate higher order plate theory for the solution of wave propagation problems in multilayered elastic and viscoelastic materials. This is motivated by the fact that exact solutions from the three-dimensional elasticity theory require very sophisticated and computational expensive procedures for the calculation of the dispersive solutions in complex multilayered and viscoelastic media. With the proposed theory, accurate solutions in the relatively low-frequency range, which is the most used in guided wave applications for structural health monitoring, can be obtained without the incorporation of complex root finding algorithms. The solutions obtained with this model are of great help as a fundamental basis for the implementation of the different methodologies developed in the following chapters. Additionally, the guidelines for a computer implementation of the solutions given by the proposed theory are also discussed in this chapter.

Chapter 4 is exclusively dedicated to the acoustic emission technique. It introduces the concepts of modal acoustic emission for guided wave mode characterisation and localisation with emphasis in the fundamental modes of propagation. Two automatic methodologies are developed for the classification of acoustic emission waveforms. In these methodologies, artificial neural networks and advanced pattern recognition methods are used in conjunction with careful analysis of the dispersive characteristics of the recorded guided waves for the purpose of the identification of the propagation modes and the different type of damage mechanisms which could be developed in composite materials such a matrix cracking, fibre fracture, fibre debonding and delamination.

Chapter 5 introduces a compact methodology in order to demonstrate a potential solution

for the damage detection and identification problems via the construction of data-driven models from baseline measurements using an acousto-ultrasonics system. Criteria for the selection of the optimal excitation signals are explained in detail along with a discussion of affecting factors to the damage detection performance and a possible temperature compensation technique.

Chapter 6 discusses the different approaches for the solution of the problem of impact load identification and introduces an approach based on a Bayesian framework within the context of Gaussian Processes for the purpose of impact magnitude estimation and localisation.

Chapter 7 presents the experimental validation and performance analysis of the model and methodologies proposed in the previous chapters. It is shown that the proposed methodologies performed successfully the health monitoring of a variety of structures.

In Chapter 8, the main outcomes of this thesis are discussed and summarized, and future possible directions of research are suggested.

1.5. Summary of Contributions Made by This Thesis

The main contributions of this thesis to the current state of the art could be divided in four parts. First, the development, implementation and experimental validation of a mathematical model based on an approximate third order plate theory which is applicable for multilayered and multi-oriented elastic and viscoelastic media. Additionally, a computer program implementing not only the previous mentioned model, but also exact solutions for both cylindrical structures and plate-like structures based on exact three-dimensional theory was written and validated. Second, the development and experimental evaluation of different novel approaches devoted for the detection, location and classification of different failure mechanisms by means of pattern recognitions techniques and modal analysis for acoustic emission. Third, the extension, further development and experimental evaluation of a data-driven approach for damage detection and identification for acousto-ultrasonics. Fourth, the development and experimental evaluation of a machine learning methodology for impact magnitude estimation and localisation.

2. Theoretical Background

2.1. Introduction

Elastic waves can propagate in solid, liquid and gaseous media. Nevertheless, the propagation of waves in solids is the major area of interest in structural health monitoring and for this reason only wave propagation in solid media is considered in this work. The aim of this chapter is first to review the equations and solutions of bulk waves propagating in an infinite anisotropic medium before introducing guided waves in hollow cylinders and multilayered plates. This is motivated by the fact that it is only possible to benefit from the advantages of these waves once their complexity has been disclosed.

Studies of bulk waves have been published by many authors [Achenbach 1984, Auld 1990, Rose 1999]. For example, bulk waves properties have been used for material characterisation purposes in [Hosten 1991a;b]. In spite the fact that bulk waves and guided waves are governed by the same wave equations, they are fundamentally different. First, there are an infinite number of modes of propagation related to guided waves. This is in contrast to bulk waves which exhibit a finite number of longitudinal and shear modes. Guided modes are additionally dispersive, i.e. their wave velocity is a function of frequency. Moreover, the mathematical equations of guided waves must satisfy boundary conditions in contrast to bulk wave equations which do not need to satisfy any boundary conditions [Rose 1999].

Guided elastic wave-based methods for evaluating the structural integrity have been developed extensively for several decades as approaches to tackle the problem of damage detection what have led to increased efficiency and sensitivity in comparison to other technologies. In the case of pipe-like structures several approaches based on signal analysis have been proposed [Van Velsor and Rose 2007, Hua and Rose 2010, Buethe et al. 2012]. However, this problem is particularly more difficult to treat in pipe-like systems since at a given frequency many more modes exist in a pipe than in a plate of similar thickness [Alleyne et al. 1996]. Similarly, guided waves have been extensively used for damage detection in metallic and composite materials with other arbitrary geometries [Su et al. 2006]. Normally, these structures are composed of several layers in order to improve their mechanical properties. The multilayered system considered here is a plate system

consisting of an arbitrary number of perfectly flat layers which are stacked together. Each layer consists either of an anisotropic or isotropic material and it is connected rigidly to its upper and lower connecting layer. In the case of plate-like structures, ultrasonic guided waves, i.e. Lamb wave modes, are seen as the superposition of successive reflections of bulk modes inside the plate boundaries. The second aim of this chapter is to introduce different signal processing algorithms for feature extraction and selection, dimension reduction, data-driven modelling and multidimensional data visualization which are going to be extensively used throughout this dissertation. The discrete wavelet transform is used for feature extraction and signal denoising purposes, principal component analysis and hierarchical non-linear principal component analysis are used for dimension reduction, feature selection and data-driven modelling, while self-organizing maps are used for the visualization of high dimensional data. All of these algorithms play a critical role in the algorithms which are going to be developed in the following chapters.

2.2. Wave Propagation in Solid Media

2.2.1. Concepts of Phase and Group Velocity

The phase velocity is the velocity at which the phase of any one frequency component of a wave travels. The phase velocity is defined as $C_{ph} = \frac{\omega}{k}$, where ω is the angular frequency and k denotes the wavenumber. The wavenumber is the spatial frequency of a wave, i.e. the number of waves that exist over a specified distance. Formally, it is the reciprocal of the wavelength. The group velocity C_{gr} is related to the velocity with which the envelope of the wave packet propagates [Rose 1999]. For the case of isotropic media, the group velocity is defined as $C_{gr} = \frac{\partial \omega}{\partial k}$. Figure 2.1 represents the typical example for a superposition of a group of waves of similar frequency where the individual harmonics travel with different phase velocities C_{ph}, but the superimposed packet travels with the group velocity C_{gr}.

In isotropic plates the direction of the group velocity coincides with the direction of the wave vector. However, for composite materials, the direction of group velocity is normally not parallel to the wavenumber vector. It is known that the group velocity vector is perpendicular to the tangent vector of the slowness curve, i.e. the group velocity vector is parallel to the normal direction of the slowness curve [Auld 1990, Wang and Yuan 2007a]. The slowness curve is a plot that represents the inverse of the velocity curve, i.e. the phase velocity curve. Figure 2.2 depicts the geometric relation between wavenumber vector and group velocity vector [Schulte 2010, Moll 2011]. The effect of difference between the directions of the energy flux and the wave vector, i.e. the direction of the phase velocity, has been experimentally observed using a composite long-range variable-length emitting radar (CLoVER) in a unidirectional composite plate in [Salas and Cesnik 2010]. The

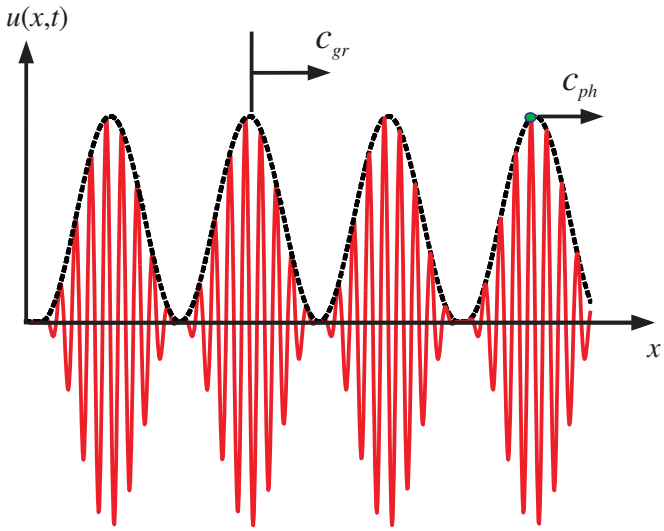

Figure 2.1. *Schematic for phase and group velocity.*

difference between the group velocity angle α and the propagation direction angle θ is known as the skew angle β.

2.2.2. Bulk Waves

Bulk waves exist in infinite homogeneous bodies and propagate indefinitely without being interrupted by boundaries or interfaces. A bulk wave is named pure if its polarization vector is directed either along or normal to the propagation direction. For isotropic materials, only pure modes are possible. One of these waves is known as longitudinal with polarization directed along the propagation direction. The other two are known as shear waves with polarizations directed normal to the propagation direction [Nayfeh 1995]. Figure 2.3 depicts a typical schematic of the three particle displacement vectors and the propagation direction vector.

Wave equations may be developed from the concept of a series of infinitesimally small mass elements, i.e. stresses are transmitted through the media. The properties of these waves

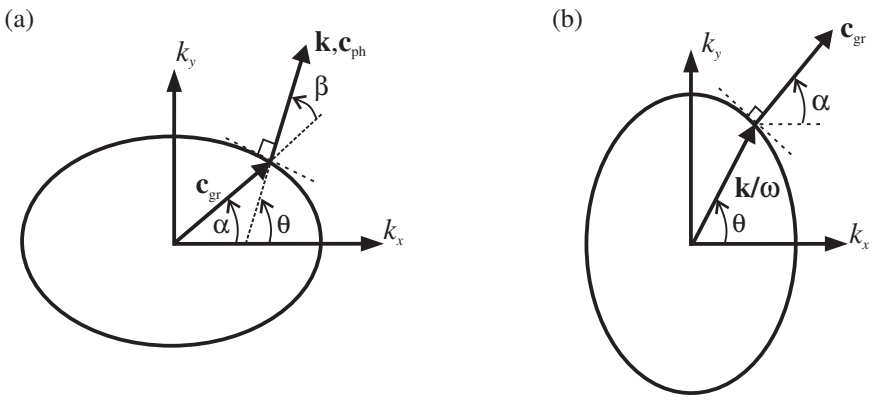

Figure 2.2. *Geometric relation between wavenumber vector and group velocity vector: (a) Wave front curve and (b) Slowness curve.*

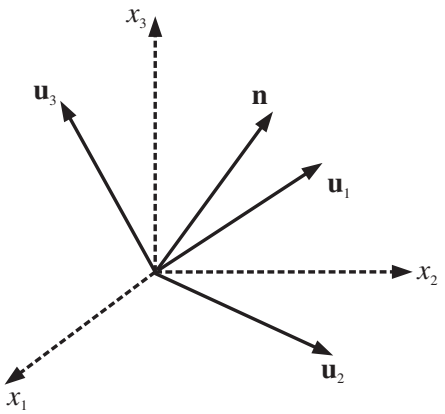

Figure 2.3. *Polarizations of the displacement vector* **u** *and the propagation direction vector* **n**.

are determined by the relationships between the direction of propagation and the properties of the medium. The solutions for bulk waves are the eigenvalues and eigenvectors of the well-known Christoffel equation. In order to develop this equation, and following the Einstein summation convention, one should start with the traditional tensorial definitions of stress-displacement and stress-strain relations as given in Eq.(2.1a) and Eq.(2.1b):

$$\frac{\partial \sigma_{ij}}{\partial x_j} = \rho \frac{\partial^2 u_i}{\partial t^2}, \tag{2.1a}$$

$$\sigma_{ij} = C_{ijlm} \varepsilon_{lm}, \tag{2.1b}$$

where σ_{ij} and ε_{lm}, denote the stress and strain tensors, ρ is the material density, u_i the displacement vector and C_{ijlm} the stiffness tensor [Nayfeh 1995]. Indices i, j, l and m vary over $1,2,3$. The linear strain-displacement relations are defined in accordance to [Hearn 1977] as:

$$\varepsilon_{lm} = \frac{1}{2}\left(\frac{\partial u_m}{\partial x_l} + \frac{\partial u_l}{\partial x_m}\right). \tag{2.2}$$

Substitution of Eq.(2.1b) and Eq.(2.2) into Eq.(2.1a), and taking into consideration the symmetries of C_{ijlm} by interchanging the indices l and m leads to:

$$\rho \frac{\partial^2 u_i}{\partial t^2} = C_{ijlm} \frac{\partial^2 u_m}{\partial x_j \partial x_l}. \tag{2.3}$$

Formal solutions for Eq.(2.3) are sought in the complex plane in the following form:

$$u_i = U_i e^{ik(n_j x_j - C_{ph} t)}, \tag{2.4}$$

where k and n_j denote the bulk wavenumber and the propagation direction with components n_1, n_2 and n_3, and **U** is the displacement amplitude vector defining the polarization. Finally, substitution of Eq.(2.4) into Eq.(2.3) leads to the characteristic equation:

$$\left(\Lambda_{im} - C_{ph}^2 \delta_{im}\right) U_m = 0, \tag{2.5}$$

Table 2.1. *Elastic properties of the unidirectional graphite-epoxy material (units in GPa).*

C_{11}	C_{22}	C_{33}	C_{12}	C_{13}	C_{23}	C_{44}	C_{55}	C_{66}
155.43	16.34	16.34	3.72	3.72	4.96	3.37	7.48	7.48

where $\Lambda_{im} = \lambda_{ijlm} n_j n_m$ and $\lambda_{ijlm} = C_{ijlm}/\rho$. The elements of Λ_{im} are given in Appendix A.1. Since the phase velocity C_{ph} is still unknown in Eq.(2.5), this equation constitutes an eigenvalue problem with its eigenvalues identified as C_{ph}^2. Solutions to Eq.(2.5) can be found by numerical methods [Nayfeh 1995].

A graphite-epoxy material with material properties listed in Table 2.1 is used as an example in order to illustrate the bulk solutions. Without any loss of generality, the solutions are found in the $x_1 - x_3$ plane, being x_2 normal to this plane. The direction x_1 lies along the zero degree direction while x_3 lies along the ninety degree direction. Figure 2.4 shows the solutions for two different directions of propagation. These plots do not depend on the frequency in the case of a purely elastic solid. The fastest longitudinal wave is represented in blue colour while the two shear waves are given in red and green colour. It can be noticed that the velocity for the longitudinal mode is higher in the fibre direction than in $\theta = 30^\circ$. There is also an evident change in the velocities of the two shear waves which can be easily tracked by checking the change in the shape of the slowness curves.

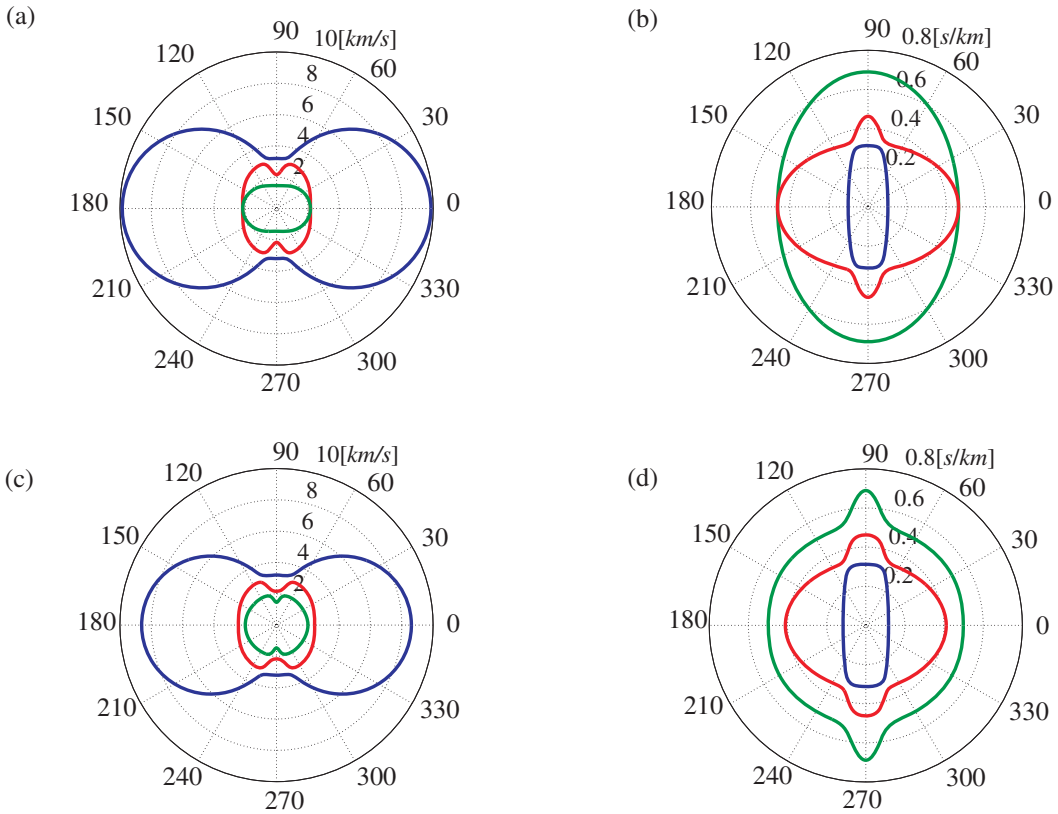

Figure 2.4. *Bulk solutions in a graphite-epoxy material: (a) Velocity curves for $\theta = 0^\circ$, (b) Slowness curves for $\theta = 0^\circ$, (c) Velocity curves for $\theta = 30^\circ$ and (d) Slowness curves for $\theta = 30^\circ$.*

2.2.3. Guided Waves in Hollow Cylinders

Cylindrical wave propagation problems were first studied in the late nineteenth century in [Pochhammer 1876, Chree 1889] which formulated the equations and solutions for wave propagation in semi-infinite elastic cylindrical rods. For longitudinal waves, imposing the boundary condition of zero stress at the outer surface of the rod results in the Pochhammer frequency equation.

In the mid twentieth century more researchers treated the problem concentrated mostly in wave propagation in solid rods for use in delay lines. The dispersion curves for hollow cylinders were first treated in [Gazis 1959a;b]. In that work, the implementation consisted of hollow cylinders for single layer isotropic materials, considering axisymmetric or non-axisymmetric wave propagation. For the purpose of the present work and the type of sensor networks which are going to be implemented in the next chapters, only waves propagating in the axial direction for isotropic materials are considered. Solutions for waves propagating in the circumferential direction can be found in [Liu and Qu 1999], while solutions for composite cylindrical materials can be found in [Yuan and Hsieh 1998]. The equations governing the motions in cylindrical coordinates of a homogeneous, isotropic, linearly elastic medium can be found in any text book of the field of wave propagation in elastic solids [Graff 1975, Achenbach 1984]. For the present case of guided waves in hollow cylinders, and following the Helmholtz decomposition, the three dimensional displacement vector can be written in terms of a scalar φ and a vector potential $\mathbf{H} = \begin{bmatrix} \mathbf{H}_r & \mathbf{H}_\theta & \mathbf{H}_z \end{bmatrix}^{\mathrm{T}}$ as [Achenbach 1984]:

$$u_r = \frac{\partial \varphi}{\partial r} + \frac{1}{r}\frac{\partial \mathbf{H}_z}{\partial \theta} - \frac{\partial \mathbf{H}_\theta}{dz}, \tag{2.6a}$$

$$u_\theta = \frac{1}{r}\frac{\partial \varphi}{\partial \theta} + \frac{\partial \mathbf{H}_r}{dz} - \frac{\partial \mathbf{H}_z}{\partial r}, \tag{2.6b}$$

$$u_z = \frac{\partial \varphi}{\partial z} + \frac{1}{r}\frac{\partial (r\mathbf{H}_\theta)}{\partial r} - \frac{1}{r}\frac{\partial \mathbf{H}_r}{d\theta}, \tag{2.6c}$$

where u_r, u_θ and u_z are the displacement vectors in the directions of r, θ and z. Additionally, the potentials can be expressed as [Achenbach 1984]:

$$\nabla^2 \varphi = \frac{1}{C_L^2}\frac{\partial^2 \varphi}{\partial t^2}, \tag{2.7a}$$

$$\nabla^2 \mathbf{H}_r - \frac{\mathbf{H}_r}{r^2} - \frac{2}{r^2}\frac{\partial \mathbf{H}_\theta}{\partial \theta} = \frac{1}{C_T^2}\frac{\partial^2 \mathbf{H}_r}{\partial t^2}, \tag{2.7b}$$

$$\nabla^2 \mathbf{H}_\theta - \frac{\mathbf{H}_\theta}{r^2} + \frac{2}{r^2}\frac{\partial \mathbf{H}_r}{\partial \theta} = \frac{1}{C_T^2}\frac{\partial^2 \mathbf{H}_\theta}{\partial t^2}, \tag{2.7c}$$

$$\nabla^2 \mathbf{H}_z = \frac{1}{C_L^2}\frac{\partial^2 \mathbf{H}_z}{\partial t^2}, \tag{2.7d}$$

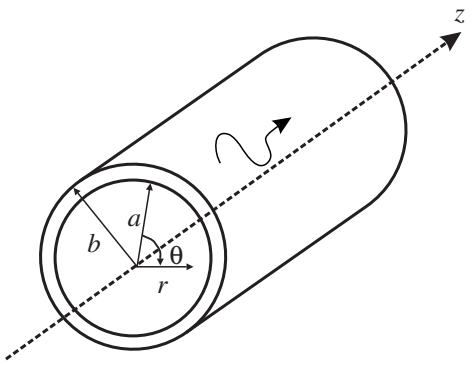

Figure 2.5. *Infinitely long hollow cylinder with inner radius a and outer radius b.*

where C_T and C_L are the transverse and longitudinal wave velocities, and ∇^2 denotes the Laplacian operator. Figure 2.5 depicts a cylindrical structure of circular cross section in which time-harmonic waves propagate in the axial direction, i.e. the z-axis. The displacement potentials can be expressed in terms of sine and cosine notation as follows:

$$\varphi = \Phi(r)\cos(n\theta)\, e^{ik\left(z - C_{ph}t\right)}, \tag{2.8a}$$

$$\mathbf{H}_r = \Psi_r(r)\sin(n\theta)\, e^{ik\left(z - C_{ph}t\right)}, \tag{2.8b}$$

$$\mathbf{H}_\theta = -\Psi_r(r)\cos(n\theta)\, e^{ik\left(z - C_{ph}t\right)}, \tag{2.8c}$$

$$\mathbf{H}_z = \Psi_z(r)\sin(n\theta)\, e^{ik\left(z - C_{ph}t\right)}, \tag{2.8d}$$

where k is the wavenumber. The circumferential order n is an integer that describes the symmetry of the waveform along the z-axis, i.e. the integer number of waves around the circumference.

The following ordinary differential equations, where the dependence on r has been omitted in order to keep the notation simple, are obtained by substitution of Eq.(2.8a) to Eq.(2.8d) into Eq.(2.7a) to Eq.(2.7d):

$$\frac{\partial^2\Phi}{\partial r^2} + \frac{1}{r}\frac{\partial\Phi}{\partial r} + \zeta_1^2\Phi - \frac{n^2}{r^2}\Phi = 0, \tag{2.9a}$$

$$\frac{\partial^2\Psi_r}{\partial r^2} + \frac{1}{r}\frac{\partial\Psi_r}{\partial r} + \zeta_2^2\Psi_r - \frac{(n+1)^2}{r^2}\Psi_r = 0, \tag{2.9b}$$

$$\frac{\partial^2\Psi_z}{\partial r^2} + \frac{1}{r}\frac{\partial\Psi_z}{\partial r} + \zeta_2^2\Psi_z - \frac{n^2}{r^2}\Psi_z = 0, \tag{2.9c}$$

where the expressions ζ_1 and ζ_2 are equal to:

$$\zeta_1 = \sqrt{\left(\frac{\omega}{C_L}\right)^2 - k^2}, \tag{2.10a}$$

$$\zeta_2 = \sqrt{\left(\frac{\omega}{C_T}\right)^2 - k^2}. \tag{2.10b}$$

Eq.(2.9a) to Eq.(2.9c) are Bessel equations and their solutions are Bessel functions of the first (J) and second (Y) kind as follows [Kundu 2003]:

$$\Phi(r) = A_1 J_n(\zeta_1 r) + A_2 Y_n(\zeta_1 r), \tag{2.11a}$$

$$\Psi_r(r) = A_3 J_{n+1}(\zeta_2 r) + A_4 Y_{n+1}(\zeta_2 r), \tag{2.11b}$$

$$\Psi_z(r) = A_5 J_n(\zeta_2 r) + A_6 Y_n(\zeta_2 r). \tag{2.11c}$$

By substituting Eq.(2.8a) to Eq.(2.8d) into Eq.(2.6a) to Eq.(2.6c), making use of the stress-displacement relations (see Appendix A.2) and finally substituting the Bessel solutions from Eq.(2.11a) to Eq.(2.11c), the system of equations can be expressed into the product of a matrix $\mathbf{K}$ and a vector of amplitudes $\mathbf{A}$. Assuming that the surface of the cylinder is free of traction forces, i.e. the boundary conditions at $r = b$ are:

$$\sigma_{rr} = 0, \sigma_{r\theta} = 0, \sigma_{rz} = 0, \tag{2.12}$$

the general system yields to:

$$\mathbf{D} = \mathbf{K}\mathbf{A} = 0, \tag{2.13}$$

where $\mathbf{K}$ is 6×6 matrix, the vector of amplitudes $\mathbf{A} = \begin{bmatrix} A_1 & A_2 & A_3 & A_4 & A_5 & A_6 \end{bmatrix}^{\mathrm{T}}$ and $\mathbf{D} = \begin{bmatrix} u_z & u_r & u_\theta & \sigma_{rr} & \sigma_{rz} & \sigma_{r\theta} \end{bmatrix}^{\mathrm{T}}$. The components of matrix $\mathbf{K}$ are given in Appendix A.3. For nontrivial solutions, the determinant of the matrix $\mathbf{K}$ must equal zero which allows to obtain the desired dispersion relationship between wavenumber, frequency, material properties and the circumferential order. It is known that the solutions of the equations of motion for hollow cylinders lead to three different classes of propagating modes [Rose 1999]. These tube modes are designated as longitudinal, torsional and flexural modes. The modes are labelled $\mathrm{L}(0,m)$, $\mathrm{T}(0,m)$ and $\mathrm{F}(n,m)$, where n is the circumferential order and m the number of the mode [Silk and Baiton 1979]. These waves can travel for long distances and their attenuation rate is much lower than that for bulk waves. Figure 2.6 depicts the mode shapes for the first fundamental modes for a steel pipe with an outer radius of $21mm$ and $2mm$ wall thickness. It can be seen that the torsional mode $\mathrm{T}(0,1)$ has only circumferential displacement while the longitudinal, $\mathrm{L}(0,1)$ has both axial and radial displacements. The modes without axial symmetry, named flexural $\mathrm{F}(n,m)$ with $n > 1$, exhibit all three displacements coupled. For the same structure, dispersion curves calculated using a general-purpose computer program developed by the author in [Torres Arredondo et al. 2011] are depicted in Figure 2.7. As it can be observed from Figure 2.7, the wave propagation phenomenon is very complicated since many modes exist in the pipe. Therefore, this effect makes the interpretation of the signals to be analysed for damage detection

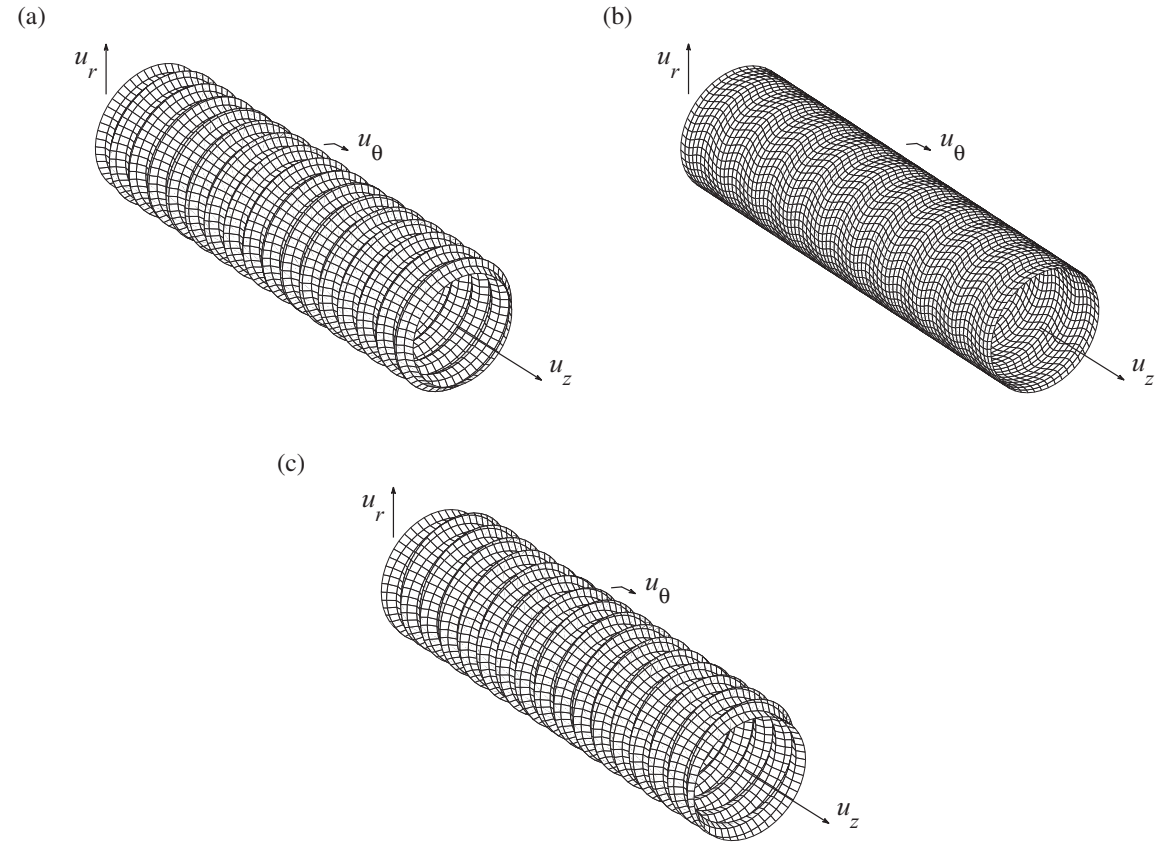

Figure 2.6. *Mode shapes for the first three fundamental modes at $f = 180kHz$: (a) Longitudinal* $\mathrm{L}(0,1)$*, (b) Torsional* $\mathrm{L}(0,1)$ *and (c) Flexural* $\mathrm{L}(0,1)$*.*

very difficult. Just the fundamental modes have been labelled in order to make the figure clearer for the understanding of the dispersive behaviour of the different modes and not crowd the plot with labels. There are 40 modes in the frequency range up to $300kHz$. These are: $\mathrm{L}(0,1)$, $\mathrm{L}(0,2)$, $\mathrm{T}(0,1)$, $\mathrm{F}(n,1)$ for $n \leq 18$, $\mathrm{F}(m,2)$ for $m \leq 12$ and $\mathrm{F}(k,3)$ for $k \leq 7$.

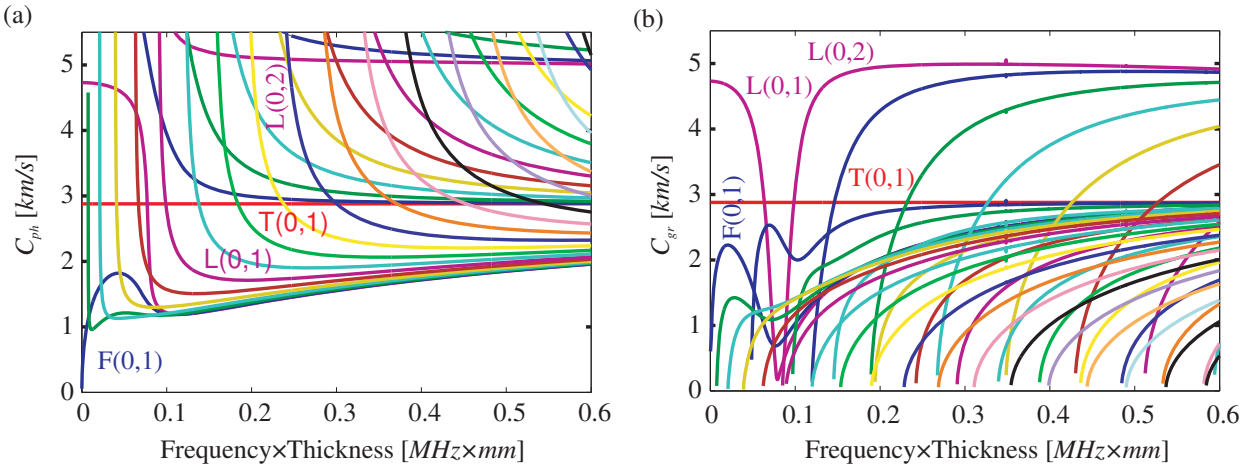

Figure 2.7. *Dispersion curves numerical results in the cylindrical structure: (a) Phase velocity dispersion curves and (b) Group velocity dispersion curves.*

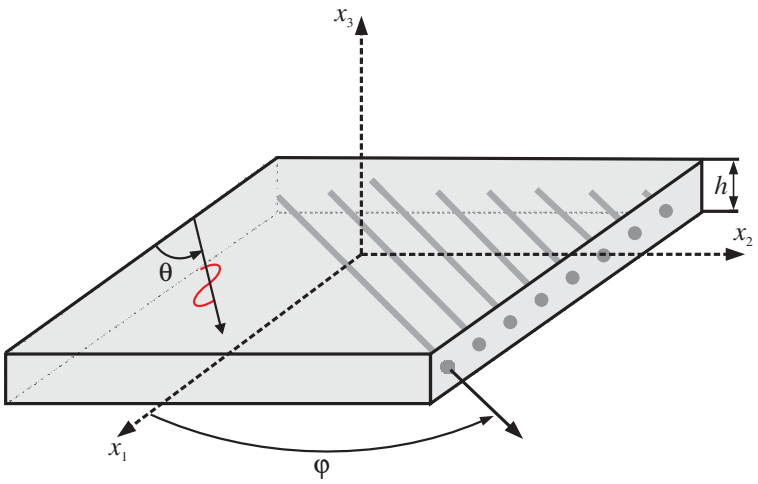

Figure 2.8. *Lamb wave propagation in the global coordinate system.*

2.2.4. Guided Waves in Multilayered Plates

This subsection introduces an extended mathematical model from the formulation introduced in [Nayfeh 1991]. The notation of the original paper is kept, where allowed, for all the procedures presented herein. It is well-known ultrasonic guided waves, i.e. Lamb waves, in plate-like structures result from the superposition of guided longitudinal and transverse shear waves within a layer. There exist two groups of waves, whose particle motion is either symmetric or antisymmetric about the mid-plane of the plate, and each can propagate independently of the other. The common approach for the wave propagation modelling in multilayered materials is to consider a flat, linearly elastic, non-piezoelectric layer of material possessing a monoclinic crystal symmetry subjected to a complex stress system in three dimensions [Moll et al. 2012]. A global Cartesian coordinate system (x_1, x_2, x_3) is assumed with the x_3-axis normal to the mid-plane of the layer with outer surfaces at $x_3 = \pm\frac{h}{2}$, where h denotes the thickness of the layer as depicted in Figure 2.8.

For the sake of clarity, the governing equations of motion in the absence of body forces are repeated here and they are given by:

$$\frac{\partial \sigma_{ij}}{\partial x_j} = \rho \frac{\partial^2 u_i}{\partial t^2}, \tag{2.14}$$

where indices i and j vary over $1,2,3$, ρ denotes the material density, σ_{11},σ_{11}, ... the stress components acting on the faces of the material, and $\mathbf{u}$ the displacement vector in the x_1, x_2 and x_3 global coordinate system, respectively. The usual summation convention over repeated subscripts is assumed. The constitutive relations showing the interdependence of strain and stress are defined in terms of the stiffness matrix $C_{pq}(p,q = 1,2,\ldots,6)$, adopting

the contracted index notation, as given in Eq. (2.15):

$$\begin{bmatrix} \sigma_{11} \\ \sigma_{22} \\ \sigma_{33} \\ \sigma_{23} \\ \sigma_{13} \\ \sigma_{12} \end{bmatrix} = \begin{bmatrix} C_{11} & C_{12} & C_{13} & 0 & 0 & C_{16} \\ C_{12} & C_{22} & C_{23} & 0 & 0 & C_{26} \\ C_{13} & C_{23} & C_{33} & 0 & 0 & C_{36} \\ 0 & 0 & 0 & C_{44} & C_{45} & 0 \\ 0 & 0 & 0 & C_{45} & C_{55} & 0 \\ C_{16} & C_{26} & C_{36} & 0 & 0 & C_{66} \end{bmatrix} \begin{bmatrix} \varepsilon_{11} \\ \varepsilon_{22} \\ \varepsilon_{33} \\ \varepsilon_{23} \\ \varepsilon_{13} \\ \varepsilon_{12} \end{bmatrix}. \tag{2.15}$$

Viscoelastic layers can be simulated by allowing the stiffness matrix to be complex [Szabo and Wu 2000]. If the global coordinate system does not coincide with the material coordinate system, but is rotated by an angle φ around the x_3-axis, a coordinate transformation of the elastic stiffness matrix is required so that the axes of the anisotropic medium coincide with the chosen global coordinate axes [Vasiliev and Morozov 2007]. Formal solutions for the three displacement equations are sought in the complex plane in the following form [Nayfeh 1995]:

$$(u_1, u_2, u_3) = (U_1, U_2, -iU_3) e^{ik(x_1 cos(\theta) + x_2 sin(\theta) + p x_3 - C_{ph} t)}, \tag{2.16}$$

where k is the wavenumber, θ the angle of propagation, p is an unknown parameter, C_{ph} is the phase velocity defined as $C_{ph} = \frac{\omega}{k}$, ω is the angular frequency and $\mathbf{U}$ is the displacement amplitude vector defining the polarization. Combining the equations of motion (2.14) with the strain-stress (2.15) and strain-displacement relations Eq.(2.2), and substituting Eq.(2.16) leads to a quadratic eigenvalue relation in terms of p that can be written as:

$$(\mathbf{A}p^2 + \mathbf{B}p + \mathbf{D})\mathbf{U} = 0, \tag{2.17}$$

where $\mathbf{A}$ and $\mathbf{D}$ are 3×3 symmetric matrices and $\mathbf{B}$ is a 3×3 self-adjoint matrix, whose non-zero elements are given as:

$$A_{11} = C_{55}, A_{12} = C_{45}, A_{22} = C_{44}, A_{33} = C_{33}, \tag{2.18a}$$

$$B_{13} = -i\left[(C_{13} + C_{55})cos(\theta) + (C_{36} + C_{45})sin(\theta)\right], \tag{2.18b}$$

$$B_{23} = -i\left[(C_{36} + C_{45})cos(\theta) + (C_{23} + C_{44})sin(\theta)\right], \tag{2.18c}$$

$$D_{11} = C_{11}cos^2(\theta) + 2C_{16}cos(\theta)sin(\theta) + C_{66}sin^2(\theta) - \rho c_{ph}^2, \tag{2.18d}$$

$$D_{12} = C_{16}cos^2(\theta) + (C_{12} + C_{66})cos(\theta)sin(\theta) + C_{26}sin^2(\theta), \tag{2.18e}$$

$$D_{22} = C_{55}cos^2(\theta) + 2C_{45}cos(\theta)sin(\theta) + C_{44}sin^2(\theta) - \rho c_{ph}^2, \tag{2.18f}$$

$$D_{33} = C_{55}cos^2(\theta) + 2C_{45}cos(\theta)sin(\theta) + C_{44}sin^2(\theta) - \rho c_{ph}^2. \tag{2.18g}$$

Eigenvalue solutions occur in three pairs related to each other by a change of sign, one

or more of which can be imaginary. In a next step, the displacement vector can be normalized without loss of generality by any of the displacement components, e.g. U_{1q}. Using the relations Eq.(2.17) and Eq.(2.18a) to Eq.(2.18g) for each previously calculated p_q $(q = 1,2,\ldots,6)$, one can express the displacement ratios $V_q = \frac{U_{2q}}{U_{1q}}$ and $W_q = \frac{U_{3q}}{U_{1q}}$ as:

$$V_q = \frac{(D_{11} + A_{11}p_q^2)B_{23} - (D_{12} + A_{12}p_q^2)B_{13}}{(D_{22} + A_{22}p_q^2)B_{13} - (D_{12} + A_{12}p_q^2)B_{23}}, \tag{2.19}$$

$$W_q = \frac{p_q\left[(D_{11} + A_{11}p_q^2)B_{23} - (D_{12} + A_{12}p_q^2)B_{13}\right]}{(D_{16} + A_{12}p_q^2)(D_{33} + A_{33}p_q^2) - B_{23}B_{13}p_q^2}. \tag{2.20}$$

Combining the Eq.(2.18a) to Eq.(2.18g) and Eq.(2.19) to Eq.(2.20) with the stress-strain Eq.(2.15) and strain-displacement Eq.(2.2) relations, and using linear superposition of harmonic functions, the formal solutions for the displacements and stresses can be expressed in a matrix form **K** as depicted below:

$$\begin{bmatrix} u_1 \\ u_2 \\ u_3 \\ \sigma_{33} \\ \sigma_{13} \\ \sigma_{23} \end{bmatrix} = \underbrace{\begin{bmatrix} 1 & 1 & 1 & 1 & 1 & 1 \\ V_1 & V_2 & V_3 & V_4 & V_5 & V_6 \\ W_1 & W_2 & W_3 & W_4 & W_5 & W_6 \\ R_{11} & R_{12} & R_{13} & R_{14} & R_{15} & R_{16} \\ R_{21} & R_{22} & R_{23} & R_{24} & R_{25} & R_{26} \\ R_{31} & R_{32} & R_{33} & R_{34} & R_{35} & R_{36} \end{bmatrix}}_{\mathbf{K}} \begin{bmatrix} U_{11} \\ U_{12} \\ U_{13} \\ U_{14} \\ U_{15} \\ U_{16} \end{bmatrix} e^{ik(x_1 cos(\theta) + x_2 cos(\theta) + px_3 - c_{ph}t)}, \tag{2.21}$$

where

$$R_{1q} = C_{13}cos(\theta) + C_{23}sin(\theta)V_q - iC_{33}p_qW_q + C_{36}(sin(\theta) + V_q cos(\theta)), \tag{2.22}$$

$$R_{2q} = C_{44}(p_qV_q + W_q sin(\theta)) + C_{45}(p_q + W_q cos(\theta)), \tag{2.23}$$

$$R_{3q} = C_{45}(p_qV_q + W_q sin(\theta)) + C_{55}(p_q + W_q cos(\theta)). \tag{2.24}$$

At this point, a formal solution of the constitutive equations has been presented. The solution can be used now for the analysis of single and multilayered media since a general expression for the displacement and stress components has been derived. For a required solution, boundary and continuity conditions can be imposed at each interface and free surfaces of the medium. The number and type of conditions depend on the layer and surface type, i.e. solid, liquid or vacuum. At the free surfaces, the stress components (see Eq.(2.21)) are required to vanish. In the case of a single layered system, the boundary conditions are then imposed on the upper and lower surfaces of the same layer. For a multilayered system, under the assumption of perfectly bonded layers, the field components of the layers above and below the interface are specified as equal. There are two popular approaches used in order to solve the wave propagation problem. They are known as

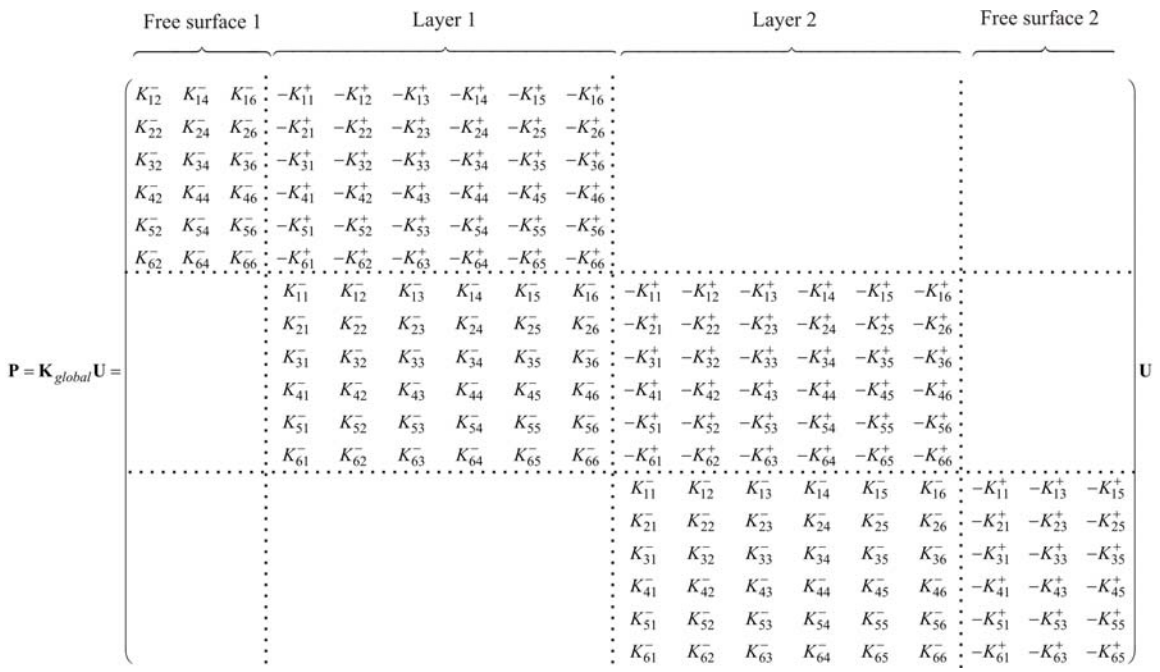

Figure 2.9. *Global matrix structure for a two layer case: The matrix is built of submatrices describing the behaviour of the individual layers. The blank spaces are filled zeros. Signs* $\pm$ *indicate the upper and lower surfaces of the layers.*

the transfer matrix method and the global matrix method. References to the different approaches can be found in [Lowe 1995]. In this work the second approach is recommended since it is more robust and remains numerically stable for any frequency-to-thickness product [Mal 1988]. However, the disadvantage consists in a higher computational demand from the root finding procedure due to the large size of the determinant involved. At the same time, as the complexity of the laminate increases, so does the size of the global matrix.

Figure 2.9 depicts how the global matrix $\mathbf{K}_{global}$ is assembled for a two layer system bounded by a solid interface [Pavlakovic et al. 1997]. Superscripts $\pm$ refer to the top and bottom conditions for each layer at $x_3 = \pm\frac{h}{2}$, $\mathbf{P}$ is the displacement and stress vector, and $\mathbf{U}$ is the displacement amplitude vector. Assembling of the matrix for liquid or vacuum layers requires a modification of the matrix arrangement in order to remove unnecessary boundary conditions and constraints on the displacement fields [Pavlakovic et al. 1997].

Once the global matrix is assembled, the dispersion relations are obtained by setting the determinant of the global matrix depicted in Figure 2.9 to zero. This can be considered as a characteristic function relating the angular frequency, or phase velocity, to wavenumber for given material properties and propagation direction. The characteristic function consists of complex quantities and yields to complex results. In case of symmetric laminates, special conditions on the stresses and displacements at the top and mid-plane of the structure can be imposed in order to separate the symmetric and antisymmetric modes of propagation and reduce the size of the global matrix. This fact plays a critical role in the simplification of the solutions since the characteristic equations decouple in this case,

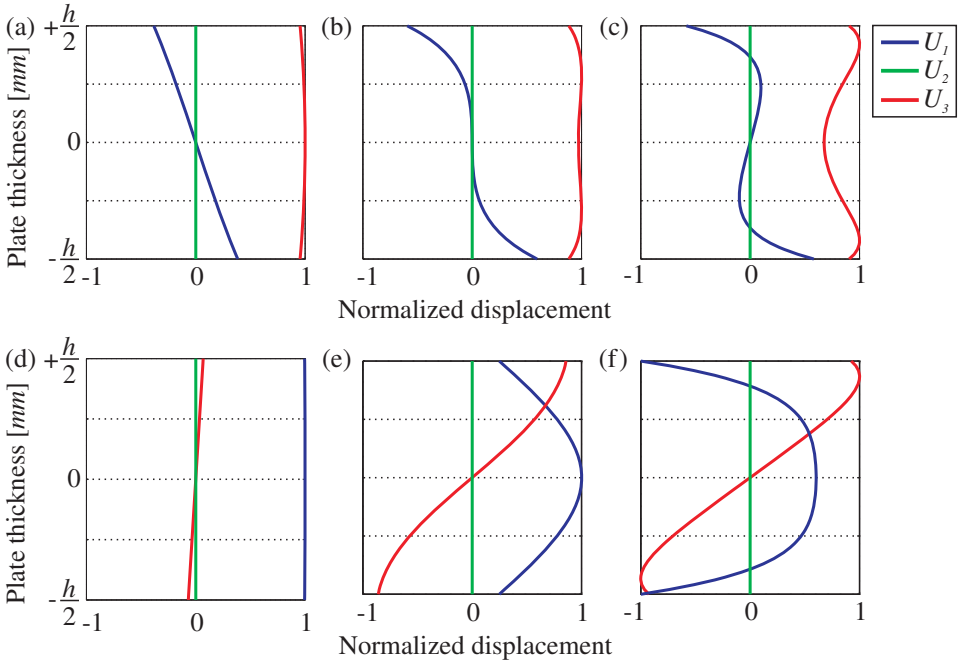

Figure 2.10. *Mode shapes for fundamental modes of propagation: (a)* A_0 *at* $f = 100kHz$*, (b)* A_0 *at* $f = 1MHz$*, (c)* A_0 *at* $f = 2MHz$*, (d)* S_0 *at* $f = 100kHz$*, (e)* S_0 *at* $f = 1MHz$ *and (f)* S_0 *at* $f = 2MHz$*. The direction of travel of the wave is along the* x_1*-axis.*

making the implementation of the tracing procedure easier, more stable and introducing savings in the calculation time. The displacement profiles across the thickness of a $2mm$ thick aluminium lamina for the fundamental A_0 and S_0 modes of propagation are depicted in Figure 2.10 in order to show the mode shape changing behaviour with frequency. As it can be inferred from Figure 2.10, in the low frequency range the A_0 and S_0 are mostly pure flexural and extensional modes, respectively. At higher frequencies, the mode shapes for each mode begin to vary and the dominant motions from the low frequency start to decrease while the non-dominant increase on the outside surfaces where the measurements are normally made.

The dispersion curves for the symmetric and antisymmetric modes of propagation in the $2mm$ thick aluminium lamina are shown in Figure 2.11. From this figure can be observed that the wave propagation phenomenon in a plate is less complicated than that of a pipe when comparing the number of modes present in the frequency spectrum (see the previous section). This is given by the fact that many more modes exist in a pipe than in a plate of similar thickness what makes the analysis of the propagated and recorded signals difficult.

Additionally to Lamb wave modes that exist in flat plates, there also exists a family of time harmonic waves known as shear horizontal (SH) modes whose particle displacement is parallel to the surfaces of the plate [Rose 1999]. This is shown in Figure 2.12 where the direction of propagation is along the x_2 direction and the particle displacement in the x_1 direction. This type of waves cannot be easily generated in isotropic plates with the help of surface mounted piezoelectric actuators. A wedge technique is normally adopted to generate a pure SH wave using ultrasonic probes [Su et al. 2007].

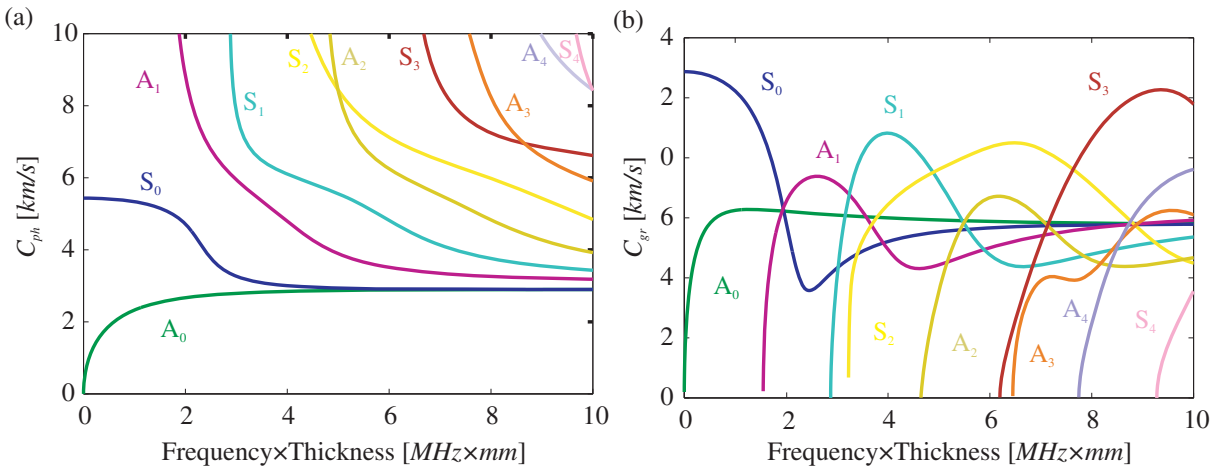

Figure 2.11. *Dispersion curves numerical results in a 2mm thick aluminium lamina for the symmetric and antisymmetric modes: (a) Phase velocity dispersion curves and (b) Group velocity dispersion curves.*

Figure 2.13 depicts the dispersion curves for the shear horizontal modes of propagation in a *2mm* thick aluminium lamina. It can be clearly seen that the SH_0 mode is not dispersive along the frequency spectrum. The modes labelled with even numbers have a symmetric particle displacement distribution across the thickness of the material while the modes labelled with odd numbers have an antisymmetric particle displacement distribution.

2.3. Guided Waves Signal Attenuation

The attenuation of Lamb waves depends on many different factors. According to [Schubert and Herrmann 2011], the four most important aspects are: geometric beam spreading, material damping, dissipation into adjacent media and wave dispersion. Geometric beam spreading is given by the loss of amplitude due to the growing length of a wave front departing into all directions from the source. Material damping describes the amount of

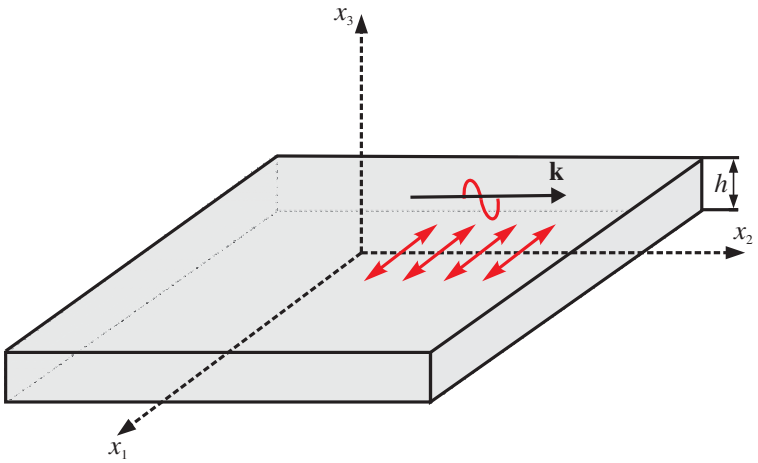

Figure 2.12. *Shear horizontal modes propagation with direction of propagation in the x_2 direction and particle displacement in the x_1 direction.*

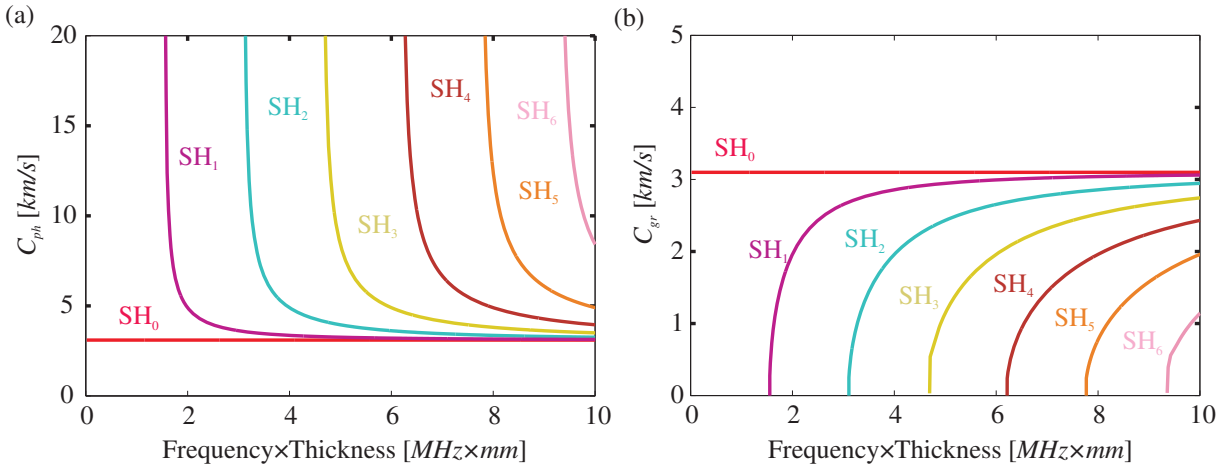

Figure 2.13. *Dispersion curves numerical results in a 2mm thick aluminium lamina for the shear horizontal modes: (a) Phase velocity dispersion curves and (b) Group velocity dispersion curves.*

energy stored in the wave that is dissipated due to non-perfect elastic material behaviour. Effects such as hysteresis and viscoelastic damping cause internal friction and results in energy loss [Hardy 2003]. The dissipation into adjacent media is a consequence of interactions between the structure surfaces and the surrounding media, e.g. in the case of a pressure vessel or a pipe. Wave attenuation due to wave dispersion is a result of the frequency dependence of wave velocities. It is caused since the different frequency components of a broadbanded ultrasonic wave travel at different velocities and the resulting spreading in time causes a loss in amplitude [Holford 2000].

2.4. Ultrasonic Guided Wave Analysis Techniques

2.4.1. Parameter-Based Analysis

In the classic acoustic emission testing and acousto-ultrasonics signal parameters are typically studied. The recorded signals are characterized by different parameters such as arrival time, number of counts, maximum amplitude, signal energy, signal duration, rise time, etc. These parameters are selected from a predefined threshold determined as a function of the background noise. Figure 2.14 shows a typical signal with some of the aforementioned parameters.

The main advantages of the parameter-based signal analysis are the high recording and data storing speed what makes the visualization of the recorded data easier and faster [Grosse and Ohtsu 2008]. The disadvantage by using this kind of analysis is that reducing a complicated signal to only a few parameters presents a great limitation when further analysis are required, for example, for the study of the different wave modes contained in the recorded signals.

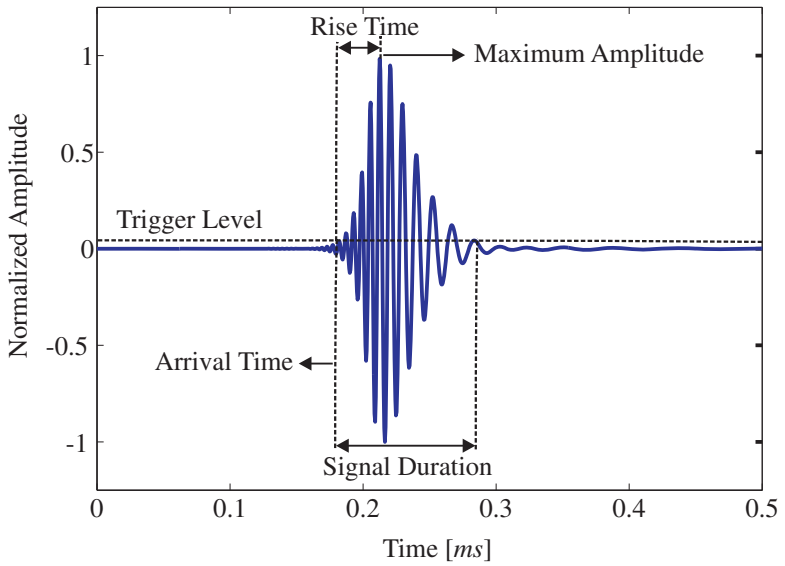

Figure 2.14. *Typical signal parameters.*

2.4.2. Signal-Based Analysis

When a signal-based approach is selected, the whole waveforms recorded by the sensors need to be analysed. One advantage of signal-based analysis is the capability of signal-to-noise discrimination based on waveforms, and additionally, it allows one to use different signal analysis methods using post-processing algorithms in order to extract valuable information regarding the structural state. These algorithms might include filtering techniques to improve the signal-to-noise ratio, feature extraction and selection methods, dimension reduction and classification algorithms [Grosse and Reinhardt 2002, Grosse et al. 2004]. Moreover, in the case of acoustic emission testing, advanced analyses may then be applied, for example, source mechanism calculations. However, these calculations require the complete solution of the Lamb wave three-dimensional problem for determining the elastic disturbance resulting from the failure source, which is not a trivial task [Ohtsu and Ono 1986, Yang et al. 2003].

2.5. Sensors, Actuators and Measurement Chain

The SHM systems which are topic of discussion in this thesis make use of circular piezoelectric transducers for the excitation and measurement of ultrasonic guided waves. A piezoelectric material is one that generates an electric charge when a mechanical stress is applied. This is known as the direct piezoelectric effect. Conversely, a mechanical deformation would be produced in a piezoelectric material when a voltage is applied between the electrodes of the piezoelectric material [Vives 2008]. The piezoelectric transducer works in a passive way as a receiver for ultrasonic guided wave signals which are generated by damaging mechanisms [Seydel and Chang 2001]. Active piezoelectric transducers pro-

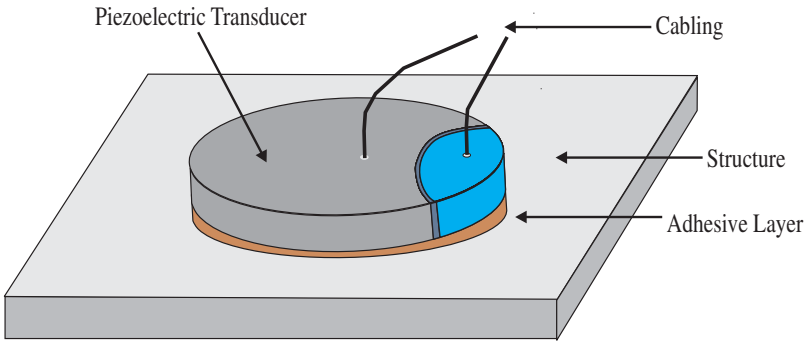

Figure 2.15. *Schematic of a piezoelectric transducer installed in an arbitrary structure.*

duce Lamb waves which are collected by distributed sensors such that distinct subject regions may be observed selectively [Staszewski et al. 2004]. Figure 2.15 depicts a typical schematic of a piezoelectric transducer attached to an arbitrary structure.

The use of circular piezoelectric transducers is motivated by the fact that it has been experimentally proven that an inhomogeneous distribution of the radiation field of the ultrasonic waves is produced due to the corners of the rectangular piezoelectric transducers [Pohl and Mook 2010]. It also has been shown that for rectangular actuators the optimum actuator dimensions depend on the angular location of the piezo-sensor with respect to the piezo-actuator [Raghavan and Cesnik 2005]. This effect has a direct influence on the damage detection procedures [Moll 2011].

Additionally to the transducers, amplifiers and filters are usually employed to magnify the recorded ultrasonic signals and to minimize the amount of electronic noise. Amplifiers with a flat response in the frequency spectrum are preferred for use. Fast data acquisition units must be used to ensure the proper conversion of the ultrasonic signals. An analogue to digital (A/D) converter is usually provided for each channel of the recording unit. Depending on the materials and the structure under monitoring, the selection of sensor location, the optimal frequency of excitation, the techniques employed to eliminate noise and the conditions for system tuning may change [Grosse and Ohtsu 2008].

2.6. Signal Conditioning for Signal Post-processing

Ultrasonic guided wave-based techniques require automatic and intelligent methods in order to separate the recorded signals from noise and accurately localize and characterize the damage and/or source of emission. Digital filters have been extensively used in non-destructive testing for signal conditioning, but they can introduce changes to the signals in the form of precursory signals, phase distortion in case of being ill-defined and amplitude modification [Scherbaum 2001]. This fact presents a great disadvantage since wave theories cannot be properly applied for the analysis of the distorted acoustic emission waveforms and the propagation velocities for reliable source localization and signal characterisation.

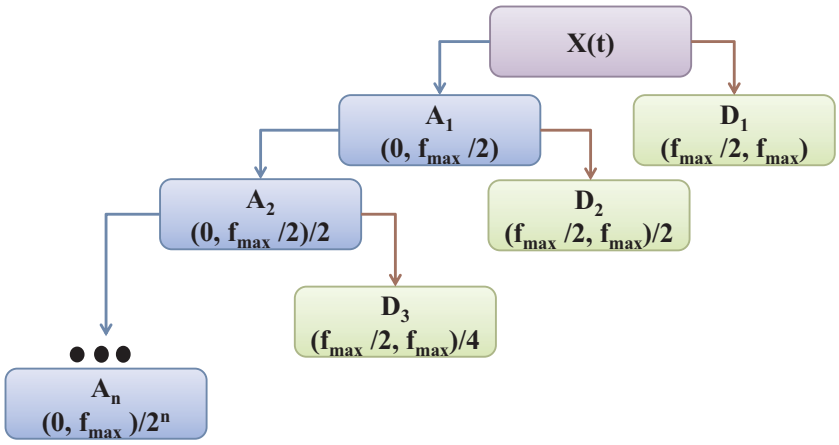

Figure 2.16. *DWT decomposition tree.*

Therefore, the selection of appropriate conditioning techniques plays an important role in the successful analysis of the failure-emitted signals.

2.6.1. Discrete Wavelet Analysis for Signal Denoising and Feature Extraction

In order to fulfil the requirements previously stated, the discrete wavelet transform (DWT) on the basis of a two-channel subband coding scheme is applied to the noisy ultrasonic signals in order to produce the noisy wavelet coefficients to the level in which the signal is properly distinguished. This analysis is performed by means of a fast pyramidal algorithm using a special class of filters called quadrature mirror filters [Mallat 1989]. In this algorithm, the signal is analysed at different frequency bands with different resolutions by decomposing the signal into a coarse approximation and detailed information. This is achieved by successive high-pass and low-pass filtering of the input signal.

One of the most important advantages of DWT is the ability to compute and manipulate data in compressed parameters which are often called features [Uebeyli 2008]. The extracted wavelet coefficients give a compact representation that shows the energy distribution of the structural dynamic responses in time and frequency [Subasi 2007]. Figure 2.16 shows the structure of decomposing the signal and the corresponding frequency bandwidths for the details ($\mathbf{D}_n$) and approximations ($\mathbf{A}_n$).

The approximations represent the high-scale, low-frequency components of the signal. The details are the low-scale, high-frequency components. The frequency f_{max} represents the maximum frequency contained in the recorded signal and n is the decomposition level. The approximation and details coefficients for an input signal $x(i)$ can be calculated as follows:

$$\mathrm{A}_{n,m} = 2^{-\frac{n}{2}} \sum_{i=1}^{j} x(i)\, \Gamma\left(2^{-n} i - m\right), \tag{2.25}$$

$$\mathrm{D}_{n,m} = 2^{-\frac{n}{2}} \sum_{i=1}^{j} x(i)\, \varsigma\left(2^{-n} i - m\right), \tag{2.26}$$

where Γ is called the scaling function, j is the number of discrete points of the input signal, n and m are considered to be the scaling (dilation) index and the translation index, and ς is the wavelet basis function. Each value of n corresponds to a different resolution level of the signal.

The family of Daubechies wavelet basis function 'db8' was carefully chosen for the methodologies presented in this thesis since it proved to be adequate to encode and approximate the ultrasonic waveforms. This is accomplished by means of different trial and error tests by evaluating different mother wavelets and levels of decomposition so that the signals could be properly reconstructed from the calculated wavelet coefficients. The chosen 'db8' wavelet is an orthogonal wavelet with the advantage of avoiding phase shifts and allowing exact reconstruction of the signal what makes this wavelet appropriate for analysing transient signals [Mallat 1997]. The index number refers to the number of coefficients. The number of vanishing moments for each wavelet is equal to half the number of coefficients, so the 'db8' has 4 vanishing moments. A vanishing moment confines the ability of the wavelet to represent polynomial behaviour [Mallat 1997, Kalogiannakis and Hemelrijck 2011].

Special attention was paid to the selection of the optimum decomposition level in order to avoid removing important information that could be related to some of the modes of propagation contained in the signal. The optimum number of level decompositions is determined based on both a minimum-entropy decomposition algorithm and systematic trials [Coifman and Wickerhauser 1992]. The entropy-based methods performs a systematic comparison of the signal and noise using the Shannon information theory [Mallat 1997]. It has been shown that a signal representing pure noise has the largest entropy while a systematic signal has zero entropy [Taha et al. 2006]. The cost function for this optimization problem is defined in Eq.(2.27) as follows:

$$\arg\min_{\mathrm{A_n}} \left(\mathrm{E}\left(\mathrm{A}_{n,m}\right)\right) = -\sum_{i=1}^{m} \mathrm{A}_{\mathrm{n,i}}^{2} \log_{10}\left(\mathrm{A}_{\mathrm{n,i}}^{2}\right), \tag{2.27}$$

where E represents the Shannon entropy. The result of applying the two-channel subband coding algorithm to an AE signal contaminated by high frequency noise is shown in Figure 2.17. It can be observed how the denoising greatly helps to elucidate the appearance of the $\mathrm{S_0}$ mode that was completely hidden behind the signal noise. Furthermore, this denoising technique will be of great help in order to improve the performance of the automatic onset-pickers which will be later used for source localization. It is well-known that the performance of onset-pickers is affected a great deal by the signal-to-noise ratio (SNR) and, therefore, the improvement of the SNR plays an important role in mode detection

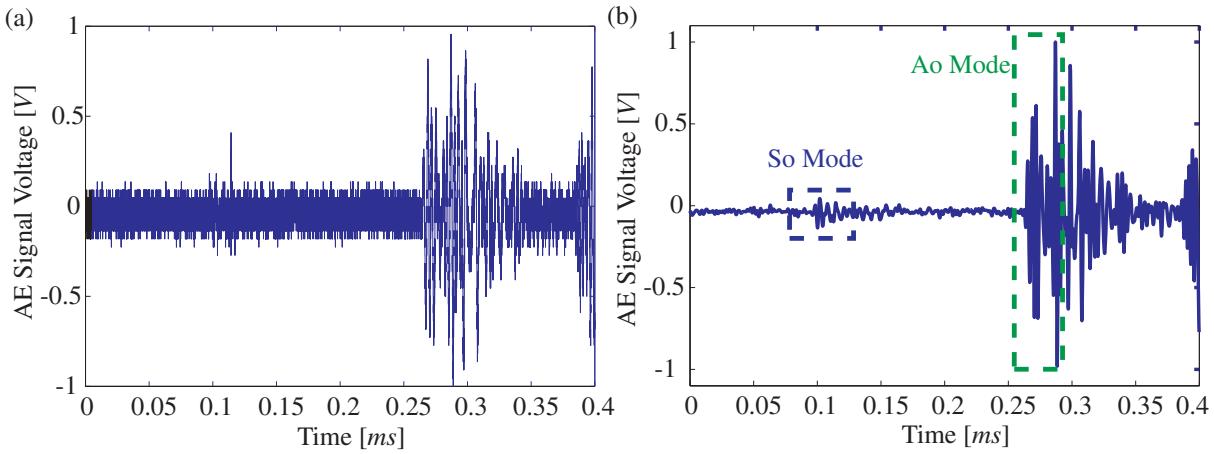

Figure 2.17. *Ultrasonic guided waves analysis: (a) Noisy AE signal and (b) Denoised AE signal.*

and localization [Kurz et al. 2005].

2.7. Dimension Reduction Techniques and Data-Driven Modelling

2.7.1. Principal Component Analysis

Principal Component Analysis (PCA) is a classical method of multivariate statistics and its theory and use are well documented in any textbook from that field [Jollife 2002]. It is a technique which may provide arguments for reducing a complex data set to a lower dimension and reveal some hidden and simplified structure/patterns that often underlie it. Let a matrix $\mathbf{X}$ with dimensions $\mathrm{I} \times (\mathrm{M} \cdot \mathrm{N})$ contain the information from $\mathbf{N}$ sensors, $\mathbf{I}$ experiments and $\mathbf{M}$ samples per experiment and sensor. To apply PCA, first a normalization step of the $\mathbf{X}$ matrix should be considered [Westerhuis et al. 1999]. For the case of the sensor networks used in this study, group scaling (GS) is selected since it allows to analyse the changes between sensors. This process includes the step of mean subtraction where the data need to be centred before installing the new low-dimensional coordinate system. Had the mean of the data not been subtracted, the best fitting hyperplane would pass through the origin and not through the centroid [Miranda et al. 2008]. Using this normalization, each data point is scaled using the mean of all measurements of the sensor at the same time sample and the variance of all measurements of the given sensor according to the following equations:

$$\mu_n = \frac{1}{\mathrm{I} \cdot \mathrm{M}} \sum_{i=1}^{\mathrm{I}} \sum_{m=1}^{\mathrm{M}} x_{inm}, \; \mu_{nm} = \frac{\sum_{i=1}^{\mathrm{I}} x_{inm}}{\mathrm{I}}, \tag{2.28a}$$

$$\sigma_n^2 = \frac{\sum_{i=1}^{\mathrm{I}} \sum_{m=1}^{\mathrm{M}} (x_{inm} - \mu_n)^2}{\mathrm{I} \cdot \mathrm{M}}, \bar{x}_{inm} = \frac{x_{inm} - \mu_{nm}}{\sigma_n}, \tag{2.28b}$$

where x_{inm} is the m^{th} sample of the of the n^{th} sensor in the i^{th} experiment, μ_n is the mean of all measurements of the n^{th} sensor, μ_{nm} is the mean of all the m^{th} samples of the n^{th} sensor, σ_n is the standard deviation of all measurements of the n^{th} sensor, and $\bar{x}_{inm}$ is the scaled sample. The normalized matrix $\mathbf{X}_{norm}$ will be hereafter referred to as $\mathbf{X}$.

Using this normalized matrix, the covariance matrix $\mathbf{C}_\mathrm{x}$ can be calculated as follows:

$$\mathbf{C}_\mathrm{x} = \frac{1}{\mathrm{I}-1}\mathbf{X}^\mathrm{T}\mathbf{X}. \tag{2.29}$$

This is a square symmetric $(\mathrm{M}\cdot\mathrm{N}) \times (\mathrm{M}\cdot\mathrm{N})$ matrix that measures the degree of linear relationship within the data set between all possible pairs of variables, i.e. sensors. The subspaces in PCA are defined by the eigenvectors and eigenvalues of the covariance matrix as follows:

$$\mathbf{C}_\mathrm{x}\mathbf{P} = \mathbf{P}\Lambda, \tag{2.30}$$

where the eigenvectors of $\mathbf{C}_\mathrm{x}$ are the columns of $\mathbf{P}$ and Λ is a diagonal matrix whose diagonal elements are the eigenvalues of $\mathbf{C}_\mathrm{x}$. The off-diagonal terms of Λ are equal to zero. The matrix $\mathbf{P}$ can be considered as a transformation matrix seeking to find a new transformed space with minimal redundancy. The columns of matrix $\mathbf{P}$ are sorted according to the eigenvalues by descending order and they are called principal components of the data. Choosing only a reduced number $r < (\mathrm{M}\cdot\mathrm{N})$ of principal components, the reduced transformation matrix $\hat{\mathbf{P}}$ could be defined for the purposes of dimension reduction and/or data-driven modelling of the investigated process. Geometrically, the transformed data matrix $\mathbf{T}$, i.e. score matrix, represents the projection of the original data over the direction of the principal components $\mathbf{P}$. This matrix is defined as:

$$\mathbf{T} = \mathbf{X}\mathbf{P}. \tag{2.31}$$

One can think of PCA as a method to squeeze as much information, as measured by variance, as possible into the first principal components. In the full dimensional case, using $\mathbf{P}$, the projection is invertible and the original data can be recovered according to $\mathbf{X} = \mathbf{T}\mathbf{P}$. In the reduced case, using $\hat{\mathbf{P}}$ and with the given $\mathbf{T}$, it is not possible to fully recover $\mathbf{X}$, but $\mathbf{T}$ can be projected back onto the original (M·N)-dimensional space and another data matrix can be obtained as follows:

$$\hat{\mathbf{X}} = \mathbf{T}\hat{\mathbf{P}}^\mathrm{T} = \mathbf{X}\hat{\mathbf{P}}\hat{\mathbf{P}}^\mathrm{T}. \tag{2.32}$$

Therefore, the residual data matrix, i.e. the error for not using all the principal compon-

ents, can be defined as the difference between the original data and the data projected back as follows:

$$\begin{aligned} \mathbf{E} &= \mathbf{X} - \hat{\mathbf{X}}. \\ \mathbf{E} &= \mathbf{X}\left(\mathbf{I} - \hat{\mathbf{P}}\hat{\mathbf{P}}^{\mathrm{T}}\right). \end{aligned} \tag{2.33}$$

Defining the optimal number of principal components required for building the PCA models is a very important step for the analysis of the data. It is well known that if fewer principal components are selected than required, a poor model will be obtained and an incomplete representation of the process results. On the other hand, if more principal components are selected than necessary, the model will be over-parameterised and will include noise. In order to define the optimal number of principal components required for building the models, an analysis of the variances retained in the components could be performed. Principal components contributing less than a certain percentage to the total variance of the data set could be discarded as a criterion to select the number of required components.

There are several kinds of indices that can give information about the accuracy of the model and/or the adjustment of each experiment to the model. One very well-known index that is commonly used to this aim is the squared prediction error (SPE) statistic [Qin 2003, Mujica et al. 2010]. This is based on analysing the residual data matrix to represent the variability of the data projection within the residual subspace. The SPE index measures the variability that breaks the normal process correlation, which often indicates an abnormal situation. Denoting $\mathbf{e}_i$ as the i^{th} row of the matrix $\mathbf{E}$, the SPE for each experiment can be defined as follows:

$$\mathrm{SPE}_i = \mathbf{e}_i\mathbf{e}_i^{\mathrm{T}} = \mathbf{x}_i\left(\mathbf{I} - \hat{\mathbf{P}}\hat{\mathbf{P}}^{\mathrm{T}}\right)\mathbf{x}_i^{\mathrm{T}}, \tag{2.34}$$

where $\mathbf{x}_i$ denotes the i^{th} row of the matrix $\mathbf{X}$.

2.7.2. Hierarchical Non-linear Principal Component Analysis

Standard non-linear principal component analysis (NLPCA) is considered as a non-linear generalization of the standard linear principal component analysis (PCA) [Scholz and Vigario 2002]. The algorithm is carrying out a process of non-linear mapping where the underlying dynamics of the normal condition data is learned and the network can indicate departures from this condition [Worden et al. 2003]. It is expected that NLPCA will describe the data with greater accuracy and/or by fewer factors than PCA, provided that there are sufficient data to support the formulation of more complex mapping functions [Kramer 1991].

In contrast to traditional NLPCA, the method presented here reduces the high-dimensional inputs following a hierarchical procedure in order to decompose the data in a PCA re-

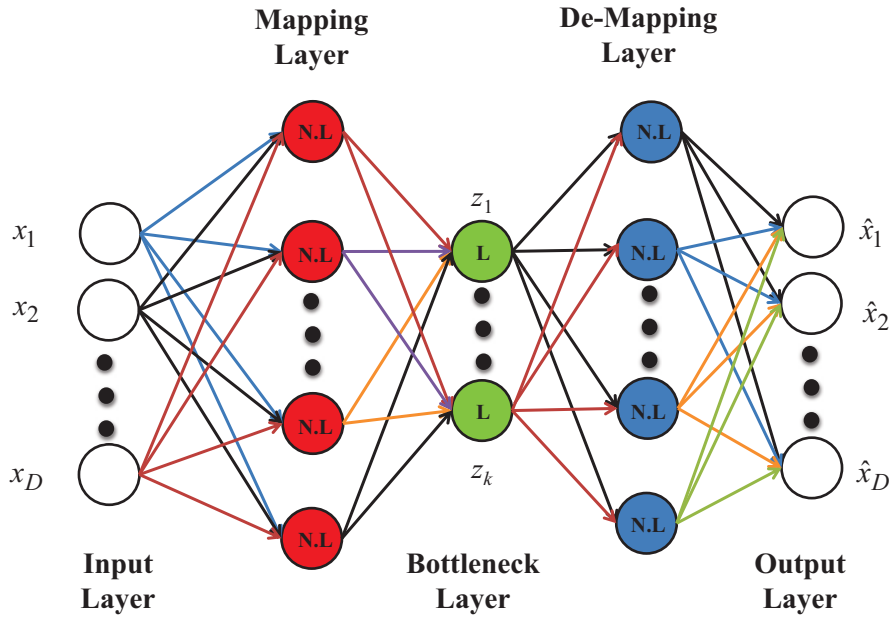

Figure 2.18. *Non-linear autoencoder network.*

lated way [Scholz et al. 2008]. This technique is based on a multilayered perceptron (MLP) architecture with an auto-associative topology as it is depicted in Figure 2.18.

Similarly to the previous section, let a matrix $\mathbf{X}$ with dimensions $\mathbf{I} \times (\mathbf{M} \cdot \mathbf{N})$ contain the information from $\mathbf{N}$ sensors, $\mathbf{I}$ experiments and $\mathbf{M}$ samples per experiment and sensor. As with the traditional NLPCA, this algorithm performs an identity mapping where the output $\hat{\mathbf{x}}_i$ is forced to equal the input $\mathbf{x}_i$ with high accuracy, denoting $\mathbf{x}_i$ the i^{th} row of the matrix $\mathbf{X}$. This is achieved by minimizing the squared reconstruction error defined as:

$$E = \frac{1}{\mathbf{I} \cdot (\mathbf{M} \cdot \mathbf{N})} \sum_{n=1}^{\mathbf{I}} \sum_{j=1}^{\mathbf{M} \cdot \mathbf{N}} \left(x_j^n - \hat{x}_j^n \right)^2 . \tag{2.35}$$

In order to compress the data, there is a bottleneck layer in the middle with fewer units than the input and output layers that forces the data to be projected into a lower dimensional representation. Note that the nodes in the mapping and de-mapping layers must have non-linear transfer functions; non-linear transfer functions are not necessary in the bottleneck layer.

With the purpose of guaranteeing that the calculated non-linear components have the same hierarchical order as the linear components in standard PCA, and in contrast to standard NLPCA, the reconstruction error is controlled by searching a k dimensional subspace of minimal mean square error (MSE) under the constraint that the $(k-1)$ dimensional subspace is also of minimal MSE [Scholz 2002]. This procedure is repeated for any k-dimensional subspace where all subspaces must be of minimal MSE as follows:

$$E_H = E_1 + E_{1,2} + \ldots + E_{1,2,\ldots,k}. \tag{2.36}$$

Therefore, each subspace represents the data in the best way with regard to its dimensionality. In the present work, auto-associative neural networks with different dimensions in the mapping and de-mapping layers are applied to the training data to determine the best network architecture. However, the total number of adjustable parameters is restricted to be less than $\mathbf{I}\cdot\mathbf{M}\cdot\mathbf{N}$. For the whole network, under the assumption that all nodes have biases, the number of adjustable parameters N_{adj} is equal to $(\mathbf{M}\cdot\mathbf{N}+k+1)\times(\mathbf{M1}+\mathbf{M2})+\mathbf{M}\cdot\mathbf{N}+k$, where $\mathbf{M}_1$ and $\mathbf{M}_2$ are the number of nodes in the mapping and de-mapping layers, $\mathbf{M}\cdot\mathbf{N}$ the number of variables and k the number of components to be extracted.

Other approaches to determine the optimal number of nodes can be found in [Kramer 1991]. These approaches involve the use of functions that express the trade-off between fitting accuracy and number of adjustable parameters in explicit terms. Two such functions are the final prediction error (FPE) and Akaike information criterion (AIC):

$$\mathrm{FPE}_{\mathrm{h-NLPCA}} = \frac{E_H}{2}\left(1+\frac{N_{adj}}{N_{tot}}\right)\left(1-\frac{N_{adj}}{N_{tot}}\right)^{-1}, \tag{2.37}$$

$$\mathrm{AIC}_{\mathrm{h-NLPCA}} = \ln\left(\frac{E_H}{2}\right)+\frac{2N_{adj}}{N_{tot}}, \tag{2.38}$$

where $N_{tot}=\mathbf{I}\cdot\mathbf{M}\cdot\mathbf{N}$ is the total number of entries in the matrix $\mathbf{X}$. Minimization of these functions identifies models that are neither over nor under-parametrized. For $N_{adj}\ll N_{tot}$, the AIC and FPE functions are approximately the same, but for larger N_{adj}, FPE will tend to increase faster, indicating a preference for models with fewer adjustable parameters [Kramer 1991]. It has been shown that standard PCA can be accomplished by means of artificial neural networks by eliminating the mapping and de-mapping layers, i.e. the network is composed only of the input, bottleneck and output layers [Worden 2003].

2.8. Visualization Techniques

A Self-Organizing Map (SOM) is a special form of Artificial Neural Network (ANN) which is trained using unsupervised learning allowing to convert the relationships between high-dimensional data into simple geometric relationships of their image points on a low dimensional display [Kohonen 2001]. This type of network has the special property of generating one organized map in the output layer based on the inputs permitting the grouping of the input data with similar characteristics into clusters. To do that, the SOM internally organizes the data based on features and their abstractions from input data. This makes self-organizing maps very useful for imaging low-dimensional views of high-dimensional data. In order to aid the user in understanding the cluster structure, additional visualization techniques such as the U-Matrix [Ultsch 1993], cluster connections

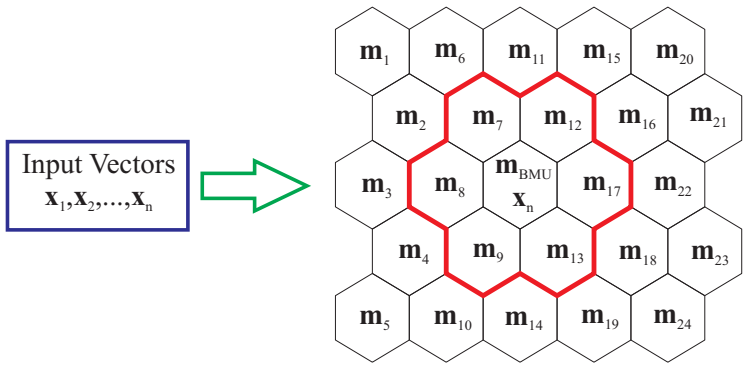

Figure 2.19. *Elements in a self-organizing map.*

[Merkl and Rauber 1997], or local factors [Kaski et al. 1998] have been developed. In particular, these maps have been used in practical speech recognitions, robotics, process control, and telecommunications, among others [Kraemer et al. 2011, Buethe et al. 2012].

A self-organizing map consists of components called nodes or neurons. Associated with each node is a weight vector of the same dimension as the input data vectors and a position in the map space. In general, the SOM works by assigning weights to each relation between the input data and each cluster in the map. The SOM algorithm starts working with a random initialization of these weights. The training is done by comparing the input data set with the weight vectors calculating their Euclidean distance in order to find the best matching unit (BMU). The updating process takes into consideration a neighbourhood set N_c around the cell $\mathbf{m}_{\mathrm{BMU}}$, and by each learning step just the cells within N_c are updated as shown in Figure 2.19.

The updating process is defined as follows:

$$\mathbf{m}_i(t+1) = \begin{cases} \mathbf{m}_i(t) + \alpha(t)\left(\mathbf{x}(t) - \mathbf{m}_i(t)\right) & if\ i \in N_c(t) \\ \mathbf{m}_i(t) & if\ i \notin N_c(t) \end{cases}, \tag{2.39}$$

where t denotes current iteration, $\mathbf{m}_i$ is the current weight vector, $\mathbf{x}$ is the target input vector, and α is a scalar called adaptation gain which is defined between 0 and 1, and it is reduced during each time step. Finally, each incoming dataset can be presented to the map followed by the updating process or all datasets are compared to the map before executing any updating. These methods are known as the sequential and batch algorithms, respectively. After the training phase, different groups will normally form in the map which can be distinguished according to their location on the map. The training algorithm used in this thesis is implemented in a Matlab®-Toolbox created by [Vesanto et al. 2000].

In order to find the optimal map size, a control run is repeated by changing the map size. To accomplish the selection of the optimal map size, two quantitative measures of mapping quality known as the average quantization error (QE) and topographic error

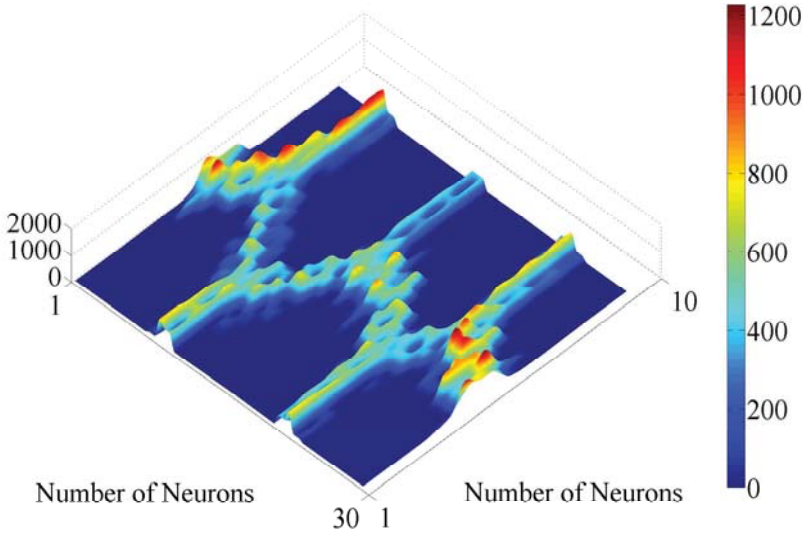

Figure 2.20. *Display of a U-Matrix surface for a seven cluster problem.*

(TE) are analysed. The QE is the average distance between each data vector and the BMU. The TE gives the percentage of the data vectors for which the first two BMUs are not neighbouring units. Lower QE and TE values indicate better mapping quality. The U-Matrix surface, showing the average distance of a cell to its neighbouring cells, can be used to depict the difference between the groups.

The U-Matrix surface will normally contain visible boundaries separating the different groups providing an idea of the extent of their difference and giving a landscape-like visualization of the distance relationships of the input data in the data space. In this manner, once the SOM has been trained, weight vectors of neurons with large U-values are very distant from other vectors in the input data space. Conversely, weight vectors of neurons with small U-values are surrounded by other vectors in the data space. The mountain-like surfaces formed on a U-Matrix define the cluster boundaries. Valleys on a U-Matrix point to cluster centres. Additionally, outliers as well as possible cluster structures can be recognized for high dimensional data spaces.

Figure 2.20 depicts the U-Matrix surface from an ultrasonic guided wave dataset containing seven different clusters. The data come from an active acousto-ultrasonics system where the path between the actuator and sensor has been interfered by placing obstacles on the surface of the structure. As it can be observed from the figure, all seven clusters are well separated by clear boundaries. The projections of the input data points are found in depressions. Using U-Matrix surface method for clustering has the advantage of a non-linear disentanglement of complex cluster structures [Ultsch and Moerchen 2005].

3. Development of a Model for Guided Wave Propagation Analysis

3.1. Introduction

It is well-known that guided ultrasonic waves have many useful properties that can be exploited for the health monitoring of mechanical, civil and engineering structures. However, it is only possible to benefit from their advantages once the complexity of guided wave propagation is disclosed. To set up a structural health monitoring (SHM) or non-destructive (NDT) system for a real-world structure, a deep knowledge of wave propagation phenomena including effects of material damping, beam spreading effects, energy focusing and wave scattering is necessary. Thus, the understanding of dispersion characteristic is of great importance since it plays a critical role in the selection of the optimal inspection frequencies for the improvement of the sensitivity, optimization of sensor networks in terms of sensor placement and number of sensors, and for the modal analysis and localization of the propagating waves. Since the use of composite materials has extensively increased in the design of existing engineering structures, what also increases the analysis complexity of such structures, this poses a necessity for fast modelling tools that can be used for a rapid and reliable analysis.

The modelling of wave propagation in multilayered anisotropic structures has been extensively studied by several researchers and a considerable amount of literature has been published on this topic [Rose 1999, Kundu 2003]. Analysing guided waves in these structures is often categorised into three groups. There are methods based on exact three dimensional elasticity theory, waveguide finite element methods and laminated plate theories of different orders. Exact methods are based on the superposition of bulk waves that include the popular matrix-based methods [Pavlakovic et al. 1997]. Waveguide finite element methods have appeared for modelling the guided wave propagation numerically as an alternative to exact approaches by using a finite element discretization of the cross-section of the waveguide [Bartoli et al. 2006]. A different alternative providing simplicity and low computational cost in comparison to other techniques are laminated plate theories [Whitney and Sun 1973, Reddy 1984]. This approach offers a higher computational efficiency

and simplicity in comparison to traditional exact elasticity methods, while providing an adequate description of the structure global response in the low frequency range which is the most used in guided wave applications for structural health monitoring. As a consequence, several theories such as the classical laminated plate theory (CLPT), the first-order shear deformation theory (FSDT), second and higher-order laminated plate theories have been proposed for the analysis of elastic composite plates [Reddy 2004].

This chapter introduces a higher order plate theory for modelling dispersive solutions in elastic and viscoelastic materials which has been presented in [Torres Arredondo and Fritzen 2011]. First, a third order plate theory that can approximate five symmetric and six antisymmetric Lamb wave modes is described here. The theory expands the displacement fields in terms of the thickness to third degree and reduces the three dimensional continuum problem to a two dimensional problem. The motivation for expanding the displacement field up to the cubic term in the thickness is to provide better kinematics and accurate interlaminar stress distributions. Moreover, the utilization of a two dimensional approach is justified by comparison of dispersion curves to exact three dimensional elasticity theory solutions. This theory can be considered as an extension of the work presented in [Reddy 1984, Wang and Yuan 2007b]. Additionally, with the proposed model, no complicated multi-dimensional root finding algorithms and high computational cost are required in order to find the dispersive solutions as with the model presented in the previous section based on the global matrix method. Second, the two classical models of viscoelastic attenuation are implemented and discussed in detail. At the end, the effect of energy flux concentration of wave modes which is sometimes more concentrated in some directions than in others is analysed. The guidelines for the computer implementation of the solutions given by the proposed theory are also discussed.

3.2. Model Development

3.2.1. Displacement Fields

The laminated plate theory is developed by assuming the form of the displacement fields or stress fields as a linear combination of unknown functions and the thickness coordinate z . Consider a plate of constant thickness h composed of anisotropic layers bonded together. The origin of a Cartesian coordinate system is located within the central plane $x-y$ with the z-axis being normal to this plane. The model assumes either a linear elastic or viscoelastic, non-piezoelectric material for each layer subjected to a complex stress system in three dimensions. The material is considered to have a monoclinic symmetry. Figure 3.1 depicts the definition of stress resultants (N, M, Q) in the three dimensional system for a given propagation direction θ and fibre orientation φ . The quantities N_{xx}, N_{yy} and N_{xy} are named the in-plane force resultants; M_{xx}, M_{yy} and M_{xy} denote the moment resultants;

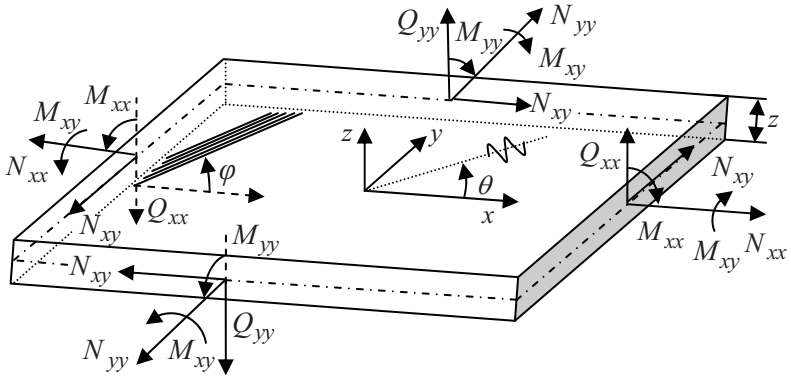

Figure 3.1. *Complex stress system in three dimensions.*

Q_{xx} and Q_{yy} are called the transverse force resultants. The proposed displacement fields are given in Eq.(3.1) by:

$$\begin{aligned} u(x,y,z,t) &= u_0(x,y,t) + \psi_x(x,y,t)\,z + \xi_x(x,y,t)\,z^2 + \phi_x(x,y,t)\,z^3, \\ v(x,y,z,t) &= v_0(x,y,t) + \psi_y(x,y,t)\,z + \xi_y(x,y,t)\,z^2 + \phi_y(x,y,t)\,z^3, \\ w(x,y,z,t) &= w_0(x,y,t) + \psi_z(x,y,t)\,z + \xi_z(x,y,t)\,z^2, \end{aligned} \tag{3.1}$$

where u, v, and w are the displacement components in x, y and z directions, ψ_x and ψ_y represent rotations having the same meaning as in the first order shear deformation theory [Mindlin 1951]. The additional terms expand the displacement field and are functions to be determined. For the following developments, the traditional notation used in [Nayfeh 1995,Reddy 2004] is kept, where allowed, for all the procedures presented herein.

3.2.2. Plate Constitutive Relations

The constitutive relations for a monoclinic material showing the interdependence of strain and stress are defined in terms of the stiffness matrix $\mathbf{C}$ with elements $C_{ij}\,(i,\,j=1,2,\ldots,6)$ as given in Eq.(3.2):

$$\begin{bmatrix} \sigma_{xx} \\ \sigma_{yy} \\ \sigma_{zz} \\ \sigma_{xy} \end{bmatrix} = \begin{bmatrix} C_{11} & C_{12} & C_{13} & C_{16} \\ C_{12} & C_{22} & C_{23} & C_{26} \\ C_{13} & C_{23} & C_{33} & C_{36} \\ C_{16} & C_{26} & C_{36} & C_{66} \end{bmatrix} \begin{bmatrix} \varepsilon_{xx} \\ \varepsilon_{yy} \\ \varepsilon_{zz} \\ \gamma_{xy} \end{bmatrix}, \tag{3.2}$$

$$\begin{bmatrix} \sigma_{yz} \\ \sigma_{xz} \end{bmatrix} = \begin{bmatrix} C_{44} & C_{45} \\ C_{45} & C_{55} \end{bmatrix} \begin{bmatrix} \gamma_{yz} \\ \gamma_{xz} \end{bmatrix}.$$

If the global coordinate system does not coincide with the material coordinate system, but is rotated by an angle φ around the z-axis (see Figure 3.1), a coordinate transformation of the elastic stiffness matrix is required so that the axes of the anisotropic medium

coincide with those of the chosen global coordinate axes [Vasiliev and Morozov 2007]. The transformation matrix $\mathbf{Y}(\varphi)$ in Eq.(3.4) can be used to obtain the elements of the stiffness constants C_{ij} in the global coordinate system from the known elements of the stiffness constants $\bar{C}_{ij}$ in the principal material coordinate system as follows:

$$\mathbf{C} = \mathbf{Y}(-\varphi)\,\bar{\mathbf{C}}\mathbf{Y}^{\mathbf{T}}(-\varphi). \tag{3.3}$$

The transformation matrix $\mathbf{Y}(\varphi)$ is given in Eq.(3.4) by [Altenbach et al. 2004]:

$$\mathbf{Y}(\varphi) = \begin{bmatrix} \cos^2\varphi & \sin^2\varphi & 0 & 0 & 0 & 2\cos\varphi\sin\varphi \\ \sin^2\varphi & \cos^2\varphi & 0 & 0 & 0 & -2\cos\varphi\sin\varphi \\ 0 & 0 & 1 & 0 & 0 & 0 \\ 0 & 0 & 0 & \cos\varphi & -\sin\varphi & 0 \\ 0 & 0 & 0 & \cos\varphi & \sin\varphi & 0 \\ -\cos\varphi\sin\varphi & \cos\varphi\sin\varphi & 0 & 0 & 0 & \cos^2\varphi - \sin^2\varphi \end{bmatrix}. \tag{3.4}$$

The required strain-displacement relations have already been given in Eq.(2.2). However, plate theories require the calculation of correction factors in order to match frequencies from the approximate plate theory to frequencies obtained from the exact theory [Reddy 2004]. For the general case of a laminate, this procedure can become burdensome as the value of the correction factors depends on the number, stacking sequence and properties of the constitutive plies [Whitney and Sun 1973]. For the plate theory presented here, the strain-displacement relations with introduction of the respective shear correction factors $\kappa_j\,(j = 1,2,\ldots,8)$ are described by:

$$\begin{aligned}
\varepsilon_{xx} &= \frac{\partial u}{\partial x} = \frac{\partial u_0}{\partial x} + z\frac{\partial \psi_x}{\partial x} + z^2\frac{\partial \xi_x}{\partial x} + z^3\frac{\partial \phi_x}{\partial x}, \\
\varepsilon_{yy} &= \frac{\partial v}{\partial y} = \frac{\partial v_0}{\partial y} + z\frac{\partial \psi_y}{\partial y} + z^2\frac{\partial \xi_y}{\partial y} + z^3\frac{\partial \phi_y}{\partial y}, \\
\varepsilon_{zz} &= \frac{\partial w}{\partial z} = \kappa_1\psi_z + 2\kappa_2 z\xi_z, \\
\gamma_{xy} &= \frac{\partial u}{\partial y} + \frac{\partial v}{\partial x} = \frac{\partial u_0}{\partial y} + \frac{\partial v_0}{\partial x} + z\left(\frac{\partial \psi_x}{\partial y} + \frac{\partial \psi_y}{\partial x}\right) + z^2\left(\frac{\partial \xi_x}{\partial y} + \frac{\partial \xi_y}{\partial x}\right) + z^3\left(\frac{\partial \phi_x}{\partial y} + \frac{\partial \phi_y}{\partial x}\right), \\
\gamma_{yz} &= \frac{\partial v}{\partial z} + \frac{\partial w}{\partial y} = \kappa_3\left(\psi_y + \frac{\partial w_0}{\partial y}\right) + \kappa_4 z\left(\frac{\partial \psi_z}{\partial y} + 2\xi_y\right) + \kappa_5 z^2\left(\frac{\partial \xi_z}{\partial y} + 3\phi_y\right), \\
\gamma_{xz} &= \frac{\partial u}{\partial z} + \frac{\partial w}{\partial x} = \kappa_6\left(\psi_x + \frac{\partial w_0}{\partial x}\right) + \kappa_7 z\left(\frac{\partial \psi_z}{\partial x} + 2\xi_x\right) + \kappa_8 z^2\left(\frac{\partial \xi_z}{\partial x} + 3\phi_x\right),
\end{aligned} \tag{3.5}$$

where the dependence of the functions on x, y and t has been omitted to simplify the notation. The shear correction coefficients were calculated by matching specific cut-off frequencies from the higher order modes obtained with the approximate theory to frequen-

cies computed from the exact elasticity theory what led to the following values: $\kappa_1 = \sqrt{\frac{\pi^2}{12}}$, $\kappa_2 = \kappa_4 = \kappa_7 = \sqrt{\frac{\pi^2}{15}}$, $\kappa_3 = \kappa_6 = \sqrt{\frac{\pi^2}{11}}$ and $\kappa_5 = \kappa_8 = \sqrt{\frac{\pi^2}{17}}$. For the model developed here, the strain energy U of each layer is represented as:

$$U = \frac{1}{2}\int_V (C_{11}\varepsilon_{xx}^2 + 2C_{12}\varepsilon_{xx}\varepsilon_{yy} + 2C_{13}\varepsilon_{xx}\varepsilon_{zz} + 2C_{16}\varepsilon_{xx}\gamma_{xy} + C_{22}\varepsilon_{yy}^2 + 2C_{23}\varepsilon_{yy}\varepsilon_{zz} + 2C_{26}\varepsilon_{yy}\gamma_{xy} + C_{33}\varepsilon_{zz}^2 + 2C_{36}\varepsilon_{zz}\gamma_{xy} + C_{66}\gamma_{xy}^2 + C_{44}\gamma_{yz}^2 + 2C_{45}\gamma_{yz}\gamma_{xz} + C_{55}\gamma_{xz}^2)dV, \tag{3.6}$$

where the V in the integral of the above expression means that the strain energy is obtained by integrating over the entire volume of the body [Vasiliev and Morozov 2007]. Additionally, the relations between stress components and strain energy are given in Eq.(3.7):

$$\sigma_{xx} = \frac{\partial U}{\partial \varepsilon_x}, \sigma_{yy} = \frac{\partial U}{\partial \varepsilon_y}, \sigma_{zz} = \frac{\partial U}{\partial \varepsilon_z}, \qquad \sigma_{xy} = \frac{\partial U}{\partial \gamma_{xy}}, \sigma_{yz} = \frac{\partial U}{\partial \gamma_{yz}}, \sigma_{xz} = \frac{\partial U}{\partial \gamma_{xz}}. \tag{3.7}$$

Finally, stress and moment resultants, each per unit length, are defined in Eq.(3.8) to Eq.(3.10) as:

$$N_{\alpha\beta} = \int_{-h/2}^{h/2} \sigma_{\alpha\beta} dz, N_{zz} = \int_{-h/2}^{h/2} \sigma_{zz} dz, Q_{\alpha\beta} = \int_{-h/2}^{h/2} \sigma_{\alpha\beta} dz, \tag{3.8}$$

$$M_{\alpha\beta} = \int_{-h/2}^{h/2} z\sigma_{\alpha\beta} dz, M_{zz} = \int_{-h/2}^{h/2} z\sigma_{zz} dz, P_{\alpha z} = \int_{-h/2}^{h/2} z\sigma_{\alpha z} dz, \tag{3.9}$$

$$R_{\alpha\beta} = \int_{-h/2}^{h/2} z^2\sigma_{\alpha\beta} dz, T_{\alpha z} = \int_{-h/2}^{h/2} z^2\sigma_{\alpha z} dz, S_{\alpha\beta} = \int_{-h/2}^{h/2} z^3\sigma_{\alpha\beta} dz, \tag{3.10}$$

where α and β take the symbols x and y, respectively. The plate constitutive equations may be derived from the strain energy density in Eq.(3.6), the linear elastic stress-strain relations in Eq.(3.2), the strain-displacement relations in Eq.(3.5) and the stress and moment relations given in Eq.(3.8) to Eq.(3.10).

3.2.3. Equations of Motion

The equations of motion of the third-order theory are derived using the dynamic version of the principle of virtual displacements which is given in Eq.(3.11) by:

$$\int_{t_1}^{t_2} (\delta U + \delta V - \delta K)\, dt = 0, \tag{3.11}$$

where δU is the virtual strain energy, δV the virtual work done by applied forces, δK the

virtual kinetic energy and the symbol δ the variational operator. Noting that the virtual strains can be written in terms of the generalized displacements, i.e. mixing Eq.(3.1) and Eq.(3.5), integrating by parts to relieve the virtual generalized displacements and using the fundamental lemma of calculus of variations, the equations of motion can be obtained [Reddy 2002].

The set of equations of motion in absence of surface loads is given by:

$$\begin{aligned}
\frac{\partial N_{xx}}{\partial x}+\frac{\partial N_{xy}}{\partial y} &= I_0\frac{\partial^2 u_0}{\partial t^2}+I_1\frac{\partial^2 \psi_x}{\partial t^2}+I_2\frac{\partial^2 \xi_x}{\partial t^2}+I_3\frac{\partial^2 \phi_x}{\partial t^2},\\
\frac{\partial N_{xy}}{\partial x}+\frac{\partial N_{yy}}{\partial y} &= I_0\frac{\partial^2 v_0}{\partial t^2}+I_1\frac{\partial^2 \psi_y}{\partial t^2}+I_2\frac{\partial^2 \xi_y}{\partial t^2}+I_3\frac{\partial^2 \phi_y}{\partial t^2},\\
\frac{\partial Q_{xx}}{\partial x}+\frac{\partial Q_{yy}}{\partial y} &= I_0\frac{\partial^2 w_0}{\partial t^2}+I_1\frac{\partial^2 \psi_z}{\partial t^2}+I_2\frac{\partial^2 \xi_z}{\partial t^2},\\
\frac{\partial M_{xx}}{\partial x}+\frac{\partial M_{xy}}{\partial y}-Q_{xx} &= I_1\frac{\partial^2 u_0}{\partial t^2}+I_2\frac{\partial^2 \psi_x}{\partial t^2}+I_3\frac{\partial^2 \xi_x}{\partial t^2}+I_4\frac{\partial^2 \phi_x}{\partial t^2},\\
\frac{\partial M_{xy}}{\partial x}+\frac{\partial M_{yy}}{\partial y}-Q_{yy} &= I_1\frac{\partial^2 v_0}{\partial t^2}+I_2\frac{\partial^2 \psi_y}{\partial t^2}+I_3\frac{\partial^2 \xi_y}{\partial t^2}+I_4\frac{\partial^2 \phi_y}{\partial t^2},\\
\frac{\partial P_{xy}}{\partial x}+\frac{\partial P_{yy}}{\partial y}-N_{zz} &= I_1\frac{\partial^2 w_0}{\partial t^2}+I_2\frac{\partial^2 \psi_z}{\partial t^2}+I_3\frac{\partial^2 \phi_z}{\partial t^2},\\
\frac{\partial R_{xx}}{\partial x}+\frac{\partial R_{xy}}{\partial y}-2P_{xx} &= I_2\frac{\partial^2 u_0}{\partial t^2}+I_3\frac{\partial^2 \psi_x}{\partial t^2}+I_4\frac{\partial^2 \xi_x}{\partial t^2}+I_5\frac{\partial^2 \phi_x}{\partial t^2},\\
\frac{\partial R_{xy}}{\partial x}+\frac{\partial R_{yy}}{\partial y}-2P_{yy} &= I_2\frac{\partial^2 v_0}{\partial t^2}+I_3\frac{\partial^2 \psi_y}{\partial t^2}+I_4\frac{\partial^2 \xi_y}{\partial t^2}+I_5\frac{\partial^2 \phi_y}{\partial t^2},\\
\frac{\partial T_{xx}}{\partial x}+\frac{\partial T_{yy}}{\partial y}-2M_{zz} &= I_2\frac{\partial^2 w_0}{\partial t^2}+I_3\frac{\partial^2 \psi_z}{\partial t^2}+I_4\frac{\partial^2 \xi_z}{\partial t^2},\\
\frac{\partial S_{xx}}{\partial x}+\frac{\partial S_{xy}}{\partial y}-3R_{xx} &= I_3\frac{\partial^2 u_0}{\partial t^2}+I_4\frac{\partial^2 \psi_x}{\partial t^2}+I_5\frac{\partial^2 \xi_x}{\partial t^2}+I_6\frac{\partial^2 \phi_x}{\partial t^2},\\
\frac{\partial S_{xy}}{\partial x}+\frac{\partial S_{yy}}{\partial y}-3R_{yy} &= I_3\frac{\partial^2 v_0}{\partial t^2}+I_4\frac{\partial^2 \psi_y}{\partial t^2}+I_5\frac{\partial^2 \xi_y}{\partial t^2}+I_6\frac{\partial^2 \phi_y}{\partial t^2},
\end{aligned} \tag{3.12}$$

where $I_j=\int_{-h/2}^{h/2}\rho z^j dz$ for $j=0,1,...,6$ and ρ is the density of the layer.

3.2.4. Common Form of Solutions

Formal solutions for the functions proposed in Eq.(3.1) can be found now in alternative forms. In the present thesis, these solutions are sought in the complex plane in the following form:

$$\Upsilon=\mathbf{G}e^{ik\left(x\cos(\theta)+y\sin(\theta)-C_{ph}t\right)}, \tag{3.13}$$

where k is the wavenumber, θ the angle of propagation, C_{ph} is the phase velocity defined as $C_{ph} = \frac{\omega}{k}$ and ω is the angular frequency. Υ is equal to the vector of functions (see Eq.(3.1)) defined by:

$$\Upsilon = \left[\begin{array}{cccccccccc} u_0 & v_0 & w_0 & \psi_x & \psi_y & \psi_z & \xi_x & \xi_y & \xi_z & \phi_x \quad \phi_y \end{array} \right]^{\mathrm{T}}, \tag{3.14}$$

where the dependence of the functions on x, y and t has been omitted to simplify the notation. $\mathbf{G}$ is the amplitude vector of the functions previously described and it is given by:

$$\mathbf{G} = \left[\begin{array}{cccccccccc} U_0 & V_0 & W_0 & \Psi_x & \Psi_y & \Psi_z & \Xi_x & \Xi_y & \Xi_z & \Phi_x \quad \Phi_y \end{array} \right]^{\mathrm{T}}. \tag{3.15}$$

Substitution of the constitutive relations calculated in Section 3.2.2 into Eq.(3.12), and further substitution of Eq.(3.13), in the absence of surface loads, yields to the following homogeneous equation of motion in the form:

$$\mathbf{LG} = 0, \tag{3.16}$$

where $\mathbf{L}$ is a matrix of size 11×11 containing the different terms resulting from the equations of motion. For the case of symmetric laminates, which is normal for engineering structures, the system of equations can be decoupled into two independent system of equations for the symmetric and antisymmetric modes of propagation. For the symmetric modes of propagation, the wave modes are governed by:

$$\mathbf{L_S G_S} = 0, \tag{3.17}$$

where $\mathbf{G_S} = \left[\begin{array}{ccccc} U_0 & V_0 & \Psi_z & \Xi_x & \Xi_y \end{array} \right]^{\mathrm{T}}$, and $\mathbf{L_S}$ is a 5×5 self-adjoint matrix. For the antisymmetric modes of propagation, the wave modes are governed by:

$$\mathbf{L_A G_A} = 0, \tag{3.18}$$

where $\mathbf{G_A} = \left[\begin{array}{cccccc} W_0 & \Psi_x & \Psi_y & \Xi_z & \Phi_x & \Phi_y \end{array} \right]^{\mathrm{T}}$, and $\mathbf{L_A}$ is a 6×6 self-adjoint matrix. In order to obtain solutions for the symmetric and antisymmetric modes of propagation, combinations of frequency and wavenumber where the matrices determinants of $\mathbf{L_S}$ and $\mathbf{L_A}$ go to zero must be found. The complete analytical expressions for the elements of $\mathbf{L_S}$ and $\mathbf{L_A}$ are given in Appendix B.

3.3. Material Viscoelastic Damping Models

The mathematical modelling of viscoelasticity using ideas from elasticity has attracted the attention of a large number of investigators over the past century. In order to account for material damping, the stiffness matrix is represented by a complex matrix $\tilde{\mathbf{C}}$ [Rose 1999].

Table 3.1. *Elastic and viscoelastic properties of the unidirectional carbon-epoxy lamina (units in GPa).*

C_{11}	C_{22}	C_{33}	C_{12}	C_{13}	C_{23}	C_{44}	C_{55}	C_{66}
86.6	13.5	14.0	9.0	6.4	6.8	2.72	4.06	4.7
η_{11}	η_{22}	η_{33}	η_{12}	η_{13}	η_{23}	η_{44}	η_{55}	η_{66}
7.5	0.6	0.28	0.3	0.6	0.25	0.1	0.12	0.28

The real part $\mathbf{C}$ of this complex term relates to the elastic behaviour of the material and defines the stiffness. The imaginary component η relates to the material viscous behaviour and defines the energy dissipative ability of the material. Two models are often used to describe the viscoelastic behaviour. The first model is called the hysteretic model whose complex stiffness matrix is given in Eq.(3.19) by:

$$\tilde{\mathbf{C}} = \mathbf{C} + i\eta. \tag{3.19}$$

The hysteretic model assumes no frequency dependence of the viscoelastic constants. The second model is the Kelvin-Voigt model which assumes a linear dependence of the viscoelastic coefficients. The complex stiffness matrix is expressed as:

$$\tilde{\mathbf{C}} = \mathbf{C} + i\frac{\omega}{\tilde{\omega}}\eta, \tag{3.20}$$

where $\tilde{\omega}$ is the frequency of characterisation. In order to depict the influence on the attenuation predicted by both methods for the fundamental modes of propagation (S_0, A_0 and SH_0) a $3.6mm$ thick unidirectional carbon-epoxy with density $\rho = 1560kg/m^3$ is studied. This example was chosen because it was fully analysed in [Neau 2003, Bartoli et al. 2006, Torres Arredondo et al. 2011]. The characterisation frequency of the material is $2MHz$ and the angle of propagation $\theta = 0°$. The elastic C_{ij} and viscoelastic η_{ij} material constants in the principal directions of material symmetry are given in Table 3.1. Results are depicted in Figure 3.2.

From Figure 3.2 can be clearly seen that the attenuation is a linear function of the frequency in the case of the hysteretic model and a quadratic function of the frequency in the case of the Kelvin–Voigt model. In addition, both models are just coincident in the frequency of characterisation, i.e. around $7.2MHz \times mm$, and away from this point the deviation in the prediction of both models is noteworthy.

3.4. Energy Focusing Effect

Although the problem of wave propagation in multilayered composite materials has been addressed relatively well in the literature, very few studies on the energy focusing effect of Lamb waves exist in the scientific literature [Potel et al. 2005, Chapuis et al. 2011,

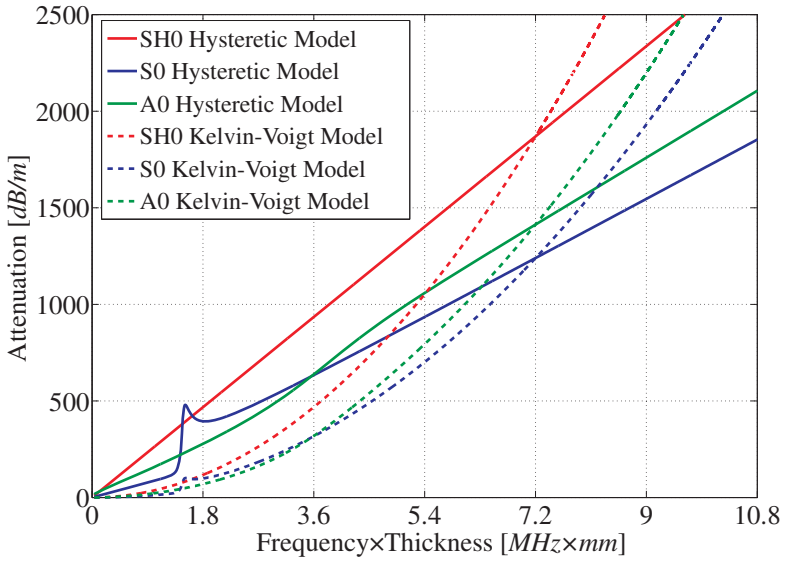

Figure 3.2. *Comparison of attenuation between the Hysteretic and Kelvin-Voigt models.*

Torres Arredondo et al. 2011]. It seems to be related with the fact that this effect is hardly encountered experimentally due to the very low amplitudes of the recorded modes presenting this behaviour. Besides measurements, which are normally done on the structure surface, are more sensible to the out of plane particle motion modes which only show the energy focusing behaviour at fast-attenuative high frequencies. Moreover, the first relevant studies on the topic concentrated their efforts in analysing this effect in bulk waves and surface acoustic waves [Every et al. 1990, Kolomenskii and Maznev 1993, Chen et al. 1994].

It is worthy of notice that the direction θ of the phase velocity and the direction α of the group velocity is not generally the same in anisotropic media. The energy focusing effect can be very strong in some anisotropic materials when the group velocity direction remains the same while the phase velocity direction varies [Maznev et al. 2003]. This uniform distribution of wave vectors, which is not collinear, does not lead to an isotropic distribution of the energy flux [Maris 1971, Wolfe 2005]. Figure 3.3 depicts the deviations of the group velocity vectors from the directions of the corresponding wave vectors. It can be noticed how the energy flux is enhanced in the y-axis direction.

The focusing effect is capable of rendering a superposition of waves into a flux pattern containing caustics. The phenomenon of energy focusing, analogue to the phonon focusing effect in which the energy flux is much more concentrated in some directions, can be analysed by the focusing factor as proposed by [Maznev and Every 1995]. It is given in Eq.(3.21) as:

$$A(\alpha) = \left|\frac{\partial \alpha}{\partial \theta}\right|^{-1} = \left[s^2 + \left(\frac{\partial s}{\partial \theta}\right)^2\right]^{-\frac{1}{2}} |K_s|^{-1}, \tag{3.21}$$

where s is the slowness surface and K_s its curvature. Points of zero curvature correspond

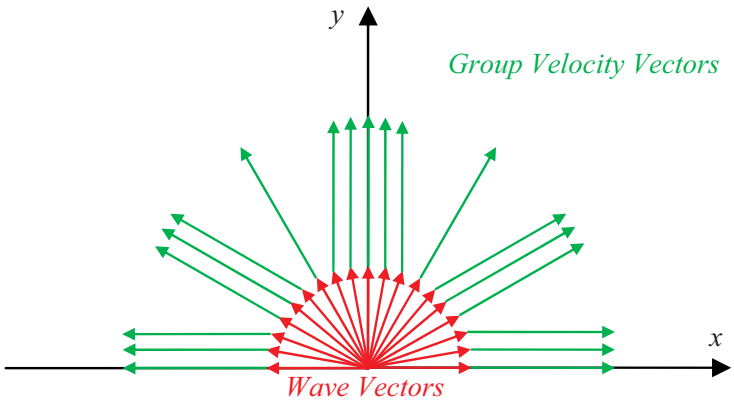

Figure 3.3. *Deviations between group velocity vectors and wave vectors.*

to caustics in the acoustic intensity.

3.5. Software Implementation of the Model

Once the matrix $\mathbf{L}$ is assembled, the dispersion relations are obtained by setting the determinant of this matrix to zero. This can be considered as a characteristic function relating the angular frequency, or phase velocity, to wavenumber for given material properties and direction of propagation. The characteristic function consists of complex quantities and yields to complex results. As previously mentioned, in the case of symmetric laminates, this matrix can be decoupled into two independent matrices $\mathbf{L}_S$ and $\mathbf{L}_A$ which can be used to obtain the dispersive solutions for both the symmetric and antisymmetric modes of propagation. The proposed model has been implemented in a Matlab® computer program called DispWare [Torres Arredondo et al. 2011]. This is a scientific computer program useful for the calculation of dispersion relations in isotropic and anisotropic plate-like and pipe-like structures.

3.5.1. Numerical Strategy for Dispersion Equations Solution

In order to calculate a dispersion curve, it is required to find combinations of frequency and wavenumber where the determinant goes to zero. The flow chart in Figure 3.4 summarizes the main steps from the modelling to the dispersion curves plots. Some aspects of the numerical strategy discussed here were presented by the author in [Moll et al. 2012]. A good technique to start the mode tracing procedure is to find roots by scanning the phase velocity at a fixed frequency or the frequency at a fixed velocity as recommended in [Lowe 1995]. To initialise the search, the minima of the modulus of the determinant of the matrices are calculated since they correspond to existing solutions. These minima are used as the initial guesses of the solution in the root finding algorithm. Each of the calculated roots is then a mode and a point to start the tracing of a dispersion curve.

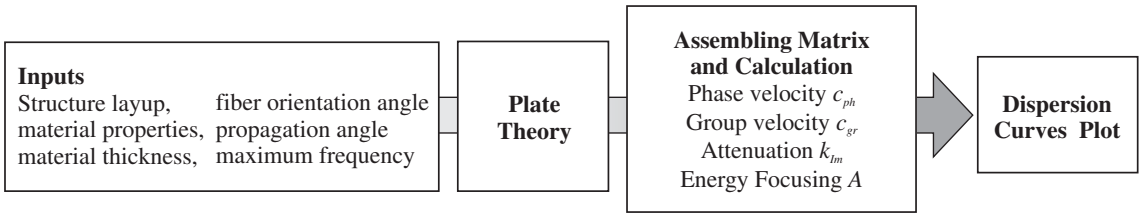

Figure 3.4. *From the modelling to the dispersion curves plot.*

Finally, by selecting a particular true wave mode, cubic extrapolation can be used in order to produce the new seed for the tracing algorithm which improves not only the stability of the result, but also the computational time required to trace a mode.

An algorithm based on the golden section search and parabolic interpolation is used in this thesis for the root finding procedures. The Newton Method is also recommended in case of dealing with real or complex wavenumbers. This has an advantage since the same algorithm can be used for instance for the calculation of dispersion curves in viscoelastic media where modes are not only characterized by their phase and group velocity, but also by the dependence of their attenuation along the frequency axis. In this case, the resulting complex wavenumber $k = k_{Re} + ik_{Im}$ is used to describe the phase velocity of waves travelling through their real part, k_{Re}, and the amplitude decay through their imaginary part, k_{Im}. For a more detailed description for the implementation of the relevant numerical root finding algorithms used here please refer to [Kaw and Kalu 2008].

Particular care has to be taken at the beginning of zones of high dispersion during the tracing procedure. In these zones, it is observed that modes fail to remain in their correct solution and move to a different one. In the same manner, refinements in the search must be accomplished in the vicinity of zones where mode crossing occurs. In order to solve these issues, an extrapolation with intercalated points and reduction in the size of the varying step, whether it is frequency or velocity, is recommended in the tracing phase. It is also recommended to change the method of interpolation in zones of high dispersion, i.e. from cubic to linear, in order to avoid jumping to another solution. Finally, by tracing the right solution of a mode, and once the phase velocity relations have been calculated, the expression of the group velocity as function of the given matrices determinants can be obtained. The group velocity C_{gr} is related to the velocity with which the envelope of a wave packet propagates. It is well known that for anisotropic materials the group velocity differs from the phase front direction and its dispersion characteristics are angular and frequency dependent. As demonstrated in [Auld 1990], in the case of non-absorbing media, the energy velocity is strictly equal to the group velocity. This is a very valuable characteristic that provides important information for signal analysis due to the fact that the received signal contains the energy information. The group velocity components $C_{gr,x}$ and $C_{gr,y}$ in the Cartesian coordinate system can be deducted according to the definition

given in [Auld 1973] as follows:

$$C_{gr} = \sqrt{c_{gr,x}^2 + c_{gr,y}^2},\ \vartheta = tan^{-1}\left(\frac{C_{gr,y}}{C_{gr,x}}\right), \tag{3.22}$$

where

$$C_{gr,x} = \frac{\partial \omega}{\partial k_{Re}} cos(\theta) - \frac{\partial \omega}{\partial \theta}\frac{sin(\theta)}{k_{Re}}, \tag{3.23}$$

$$C_{gr,y} = \frac{\partial \omega}{\partial k_{Re}} sin(\theta) + \frac{\partial \omega}{\partial \theta}\frac{cos(\theta)}{k_{Re}}. \tag{3.24}$$

Equations (3.22), (3.23) and (3.24) can be solved whether for a fixed propagation angle and variable frequency or a variable angle of propagation and fixed frequency. This leads to the calculation of a group velocity dispersion curve or a wavefront curve, respectively. The first derivative term $\frac{\partial \omega}{\partial k}$ can be computed directly by numerical differentiation of the wavenumber curve, and the second derivative $\frac{\partial \omega}{\partial \theta}$ can be approximated by a finite difference scheme. A central difference is recommended since it yields to a more accurate approximation in comparison to other schemes given by the fact that its error is proportional to the square of the spacing. Additionally, special attention has to be taken during the calculation of the group velocity due to the step-size dependency of the routines used for tracing; small errors in the root extraction can be amplified and distort the shapes of the group velocity curves.

4. Modal Acoustic Emission for Source Identification and Localisation

4.1. Introduction

Acoustic emission testing (AET) has been proposed as a structural health monitoring technique due to its ability to locate sources of energy release from within a structure related to undergoing damage processes. The global and local monitoring capabilities of AET make it a valuable tool in order to get information regarding the origin and importance of a discontinuity in a structure for a longer safe life and lower operation costs [Staszewski et al. 2004]. However, much information and analysis regarding the generation and propagation of acoustic emission signals in metals and composites is needed before AE-based techniques can provide useful information for reliable fault monitoring. For this reason, the proper design of automatic fault detection algorithms becomes the backbone in the application of trustworthy quantitative methods for source mechanism characterisation and damage detection.

There is no shortage of techniques in the literature regarding AE [Pao 1978, Pollock 1989, Rios-Soberanis 2011, Paipetis and Aggelis 2012]. It seems to be that the two most important AE topics are related to source localisation and identification. For example, investigations regarding the localisation of synthetic AE sources using a technique based on cross-correlation in thin plates were subject of study in [Ziola and Gorman 1991]. Other studies worked on the basis of wavelet analysis for the localisation of synthetic acoustic emissions on the surface of an isotropic fatigue specimen and thin anisotropic structures [Gaul et al. 2001, Kurokawa et al. 2005]. However, most of these investigations made use of flexural waves and did not extend their procedures to other type of waves. Other notable work in the field is given in [Holford 2000]. More recent investigations have led to the development of algorithms that allow the localisation by learning the relation between arrival times to the sensors and source location such as the work presented in [Baxter et al. 2007] and a later improvement of this technique using Gaussian processes in complex structures [Hensman et al. 2008]. The drawback faced with these methods is that the calculation of the arrival times, needed for the creation of the so-called ΔT maps

or training the Bayesian estimator, is done irrespective of the detected mode leading to potential errors in localisation and do not provide an insight of the present failure modes.

Regarding the topic of AE source characterisation, a big amount of studies has been carried out in order to identify and/or correlate the sources from different failure mechanisms [Anastassopoulos et al. 2002, Ativitavas et al. 2006, Marec et al. 2008, Sause et al. 2012]. Most of these studies are based on the extraction of features representative of the source of damage, i.e. parameters such as amplitudes, frequencies, number of counts, etc. Later on, machine learning algorithms are used in a supervised or unsupervised manner for analysing and correlating the different recorded and processed signals with a damage type. Some other studies have concentrated their efforts in examining the modal content of AE signals as a more intelligent and reliable approach to AE testing [Dunegan 1998, Surgeon and Wevers 1999, Pullin et al. 2005].

The present chapter discusses three different approaches to overcome particular problems faced in source identification and localisation in acoustic emission testing in plate-like isotropic and anisotropic structures on the basis of AE modal analysis [Torres Arredondo and Fritzen 2010; 2012a, Torres Arredondo et al. 2012]. First, the topic of excitability of modes is discussed in order to provide a detailed physical insight into the problem of mode generation. Second, a machine learning algorithm based on a supervised artificial neural network is proposed for classifying AE signals so that mode identification can be accomplished for localisation purposes. Third, an improved version of the previous methodology is presented where the characterisation and classification of modes in acoustic emission is based on dispersion features and energy distribution analysis. Finally, a data fusion technique and acoustic emission clustering methodology is proposed for discrimination of acoustic emission signals.

4.2. Mode Excitability

The propagation of waves in infinite elastic plates has been studied since the frequency equations for the dispersive waves based on the theory of elasticity were established [Lamb 1917, Viktorov 1967]. Theoretical treatments of the excitation of Lamb and other guided waves from point and line source excitation sources can be found in the scientific literature and have been reported based on methods including the generalised ray theory, integral transforms and elastodynamic reciprocity [Ohtsu and Ono 1986, Achenbach and Xu 1999, Velichko and Wilcox 2009]. The latter is of great interest within the context of this thesis as it provides a straightforward way for computing the mode excitability in practice because it can be calculated directly from the mode shapes. For the illustrative case presented here, just the two-dimensional excitability is discussed, i.e. each source in the two-dimensional model is represented by an infinitely long, straight line force applied perpendicular to the plane of the cross section. The excitability is defined as the ratio of particle displacement to excitation force per unit length [Wilcox 2004]. The expression

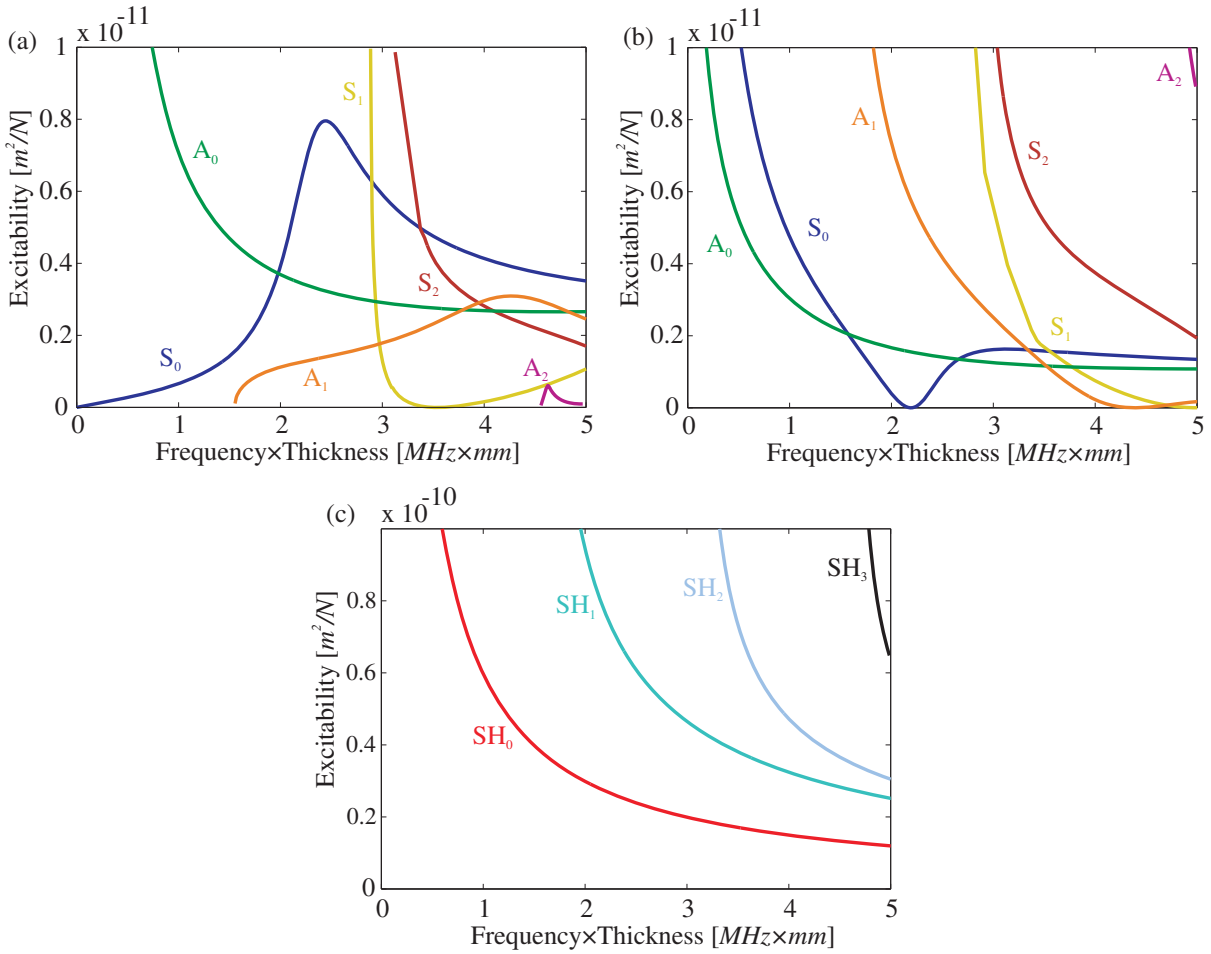

Figure 4.1. *Two-dimensional excitability function curves: (a) Lamb waves generation by an out-of-plane force, (b) Lamb waves generation by an in-plane force and (c) Shear Horizontal waves generation by an in-plane force.*

for the two-dimensional excitability of a propagating mode m is given by:

$$\mathbf{E}_m^{2D} = \frac{\omega}{4P_m}\mathbf{u}_\mathrm{m}\bar{\mathbf{u}}_\mathrm{m}^\mathrm{T}, \tag{4.1}$$

$$P_m = \frac{\omega}{2}\int \mathbf{T}_\mathrm{m}\bar{\mathbf{u}}_\mathrm{m}^\mathrm{T} dz, \tag{4.2}$$

where the over bar denotes complex conjugation, $\mathbf{u}_\mathrm{m} = [u\,v\,w]^\mathrm{T}$ is the displacement field distribution, P_m the average power flow and $\mathbf{T}_\mathrm{m}$ the stress tensor [Auld 1990]. The dependence on x, y, z and t has been omitted to keep the notation simple. In the case of three dimensional excitability functions, the waves are circularly crested and their spatial variation is described by Hankel functions rather than the complex exponential function used in the straight crested two-dimensional case [Wilcox et al. 2006, Velichko and Wilcox 2007; 2009].

The excitability function curves for the three orientations of a line excitation force are shown in Figure 4.1 for the case of a $1mm$ aluminium plate in order to provide an illus-

trative example of the modes that could be generated depending on the orientation of the source. These curves were calculated using the reciprocity method described above with the help of the model described in Chapter 3. For a force at 90° with respect to the plane of the plate, most of the motion is normal to the plate, which normally generates a large fundamental flexural mode, i.e. the A_0 mode in Figure 4.1(a). This has also been experimentally confirmed by exerting pencil lead breaks (Pentel $0.5mm$) on the surface of aluminium plate in order to excite elastic waves as it was presented in [Gorman 1991]. When the force is parallel to the plane of the plate, a large S_0 mode is excited as it can be seen from the excitability values provided in Figure 4.1(b). The excitability of shear horizontal (SH) modes along the frequency axis is also depicted in Figure 4.1(c).

4.3. Time Delay Estimators and Onset Time Detectors

Time delay and onset time estimation of a transient signal is a very important task in acoustic emission testing. The most common approach to compute the time delay between the signals acquired by two sensors is to find the maximum of the cross-correlation between the two acoustic signals. Unfiltered cross-correlation (UCC) is the most commonly used method for time delay estimation. In this technique, the delay estimate is obtained as the time-lag that maximizes the cross-correlation between unfiltered versions of the received signals [Knapp and Carter 1976]. Nevertheless, due to reverberation problems, several techniques have been proposed to improve the cross-correlation in the presence of noise [Aarabi 2003]. It is known that reverberation causes extra peaks in the cross-correlation function as sidelobes what makes difficult the determination of the peak corresponding to the central time-delay.

Assuming two acoustic emission signals $s_1(t)$ and $s_2(t)$ with Fourier transforms $S_1(f)$ and $S_2(f)$, respectively, the generalised cross-correlation (GCC) is given by:

$$\tau = \arg\max_{\beta} \int_{-\infty}^{\infty} \psi(f)\, G_{s_1 s_2}(f)\, e^{i2\pi f\beta} df, \tag{4.3}$$

where $G_{s_1 s_2}(f)$ is the cross power spectral density function and $\psi(f)$ a weighing function. The choice of the weighing function has been studied at length for general sound sources, each with their advantages and disadvantages. There are normally three different choices. First, the unfiltered cross-correlation has a weighing function $\psi(f) = 1$. Second, the GCC phase transform (PHAT) normalises the resulting cross spectral power density of the two acoustic signals to a constant value pre-whitening the cross-correlation function by equalizing the amplitude of the signals across the frequency band and leaving only the phase information. The GCC-PHAT uses a window as given by:

$$\psi(f) = \frac{1}{|\, G_{s_1 s_2}(f)\,|}. \tag{4.4}$$

Finally, the maximum likelihood (ML) or Hannan-Thomson (HT) window is defined by:

$$\psi(f) = \frac{|\,\mathrm{S}_1(f)\,||\,\mathrm{S}_2(f)\,|}{|\,\mathrm{N}_1(f)\,|^2|\,\mathrm{S}_2(f)\,|^2 + |\,\mathrm{N}_2(f)\,|^2|\,\mathrm{S}_1(f)\,|^2}, \tag{4.5}$$

where $\mathrm{N}_1(f)$ and $\mathrm{N}_2(f)$ are the estimated noise spectra for the first and second sensors, respectively. Please keep in mind that the ML window requires knowledge about the spectrum of the sensor-dependent noises.

A further approach for the onset detection of acoustic emissions is based on the so-called Hinkley criterion or energy criterion picker [Reinhardt et al. 2000]. The energy of a digitised acoustic signal $\mathrm{s}_j(j = 1,..,N)$ is given by:

$$E_N = \sum_{j=1}^{N} \mathrm{s}_j^2, \tag{4.6}$$

where N is the number of samples of the signal. The energy function for the onset time detection is given as follows:

$$H(m) = \sum_{j=1}^{m} \left(\mathrm{s}_j^2 - m\frac{E_N}{\varepsilon N} \right), \tag{4.7}$$

where s_j in the signal sample measures at the j^{th} time instant and $m = 1,..,N$. The parameter ε is used to reduce the delaying effect of the global minimum by the modified partial energy of the signal appearing from subtraction of the trend [Kurz et al. 2005]. The minimum of this function indicates the onset point. Values of $20 \leq \varepsilon \leq 200$ are recommended in order to ensure minimal delay. Large values of ε may cause too early onset time calculation which makes it advisable to select it according to the material tested [Reinhardt et al. 2000]. The influence of this parameter in the calculation of the onset times is presented in Figure 4.2. As it can be observed from Figure 4.2, the onset time calculation, depicted by the arrows, is greatly affected by the tuning of this parameter. For a value of $\varepsilon = 20$, the calculated $t_{onset} = 0.0462ms$; for $\varepsilon = 50$, $t_{onset} = 0.044ms$; finally, for $\varepsilon = 100$, $t_{onset} = 0.038ms$.

Another approach is the use of a statistical picker based on the Akaike Information Criterion (AIC). It provides picks with higher accuracy in comparison to traditional threshold methods, cross-correlation methods, and energy based detectors. Additionally, it does not require any parameter to be tuned with the aim that onset time detection can be accomplished. The AIC picker definition for an acoustic signal $\mathrm{s}_j(j = 1,..,N)$ is given by [Maeda 1985, Grosse and Ohtsu 2008]:

$$AIC(t_m) = t_m \log_{10}\left(\mathrm{var}\left(\mathrm{s}_{[1,t_m]}\right)\right) + (t_N - t_m - 1)\log_{10}\left(var\left(\mathrm{s}_{[t_m,t_N]}\right)\right), \tag{4.8}$$

where var denotes the sample variance, s_N is the last sample at time t_N where the onset is

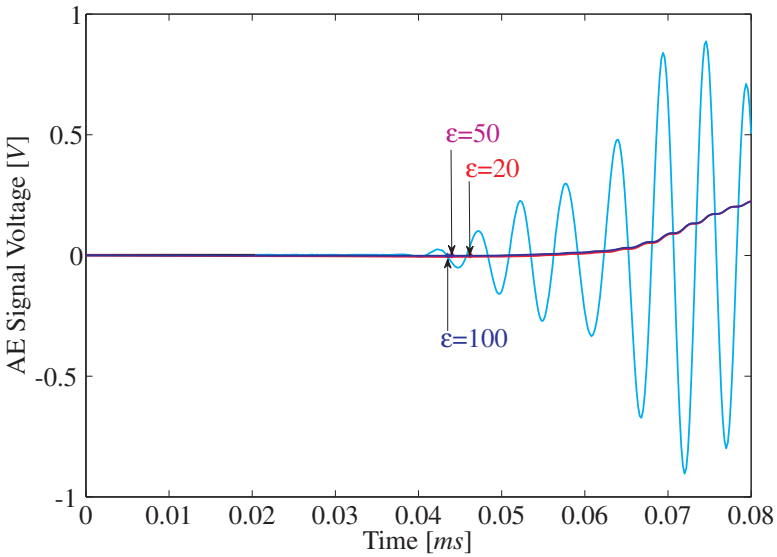

Figure 4.2. *Influence of the parameter ε in the calculation of the onset time.*

contained, and t_m ranges through all the samples of $s_j\,(j = 1,..,N)$. The AIC picker models the noise and signal as two different stationary time series and its minimum indicates the point of separation of the two series, i.e. the onset point. The AIC picker explains the similarity in entropy between the two parts of the signal when t_m coincides with the onset of the signal, i.e. the segment of the signal before t_m is composed of high entropy noise, while the segment after t_m contains the low entropy AE signal depicting marked correlation [Hensman et al. 2008]. The results of applying the AIC picker and the Hinkley picker ($\varepsilon = 100$) to an AE signal are shown in Figure 4.3. From Figure 4.3 can be noticed how the AIC picker performs to some extent better for the onset time estimation than the Hinkley picker. It can be seen how the Hinckley picker generates a systematic delay of the global minimum causing a retarded onset time detection. This could be solved by adjusting the value of ε, but this is something that could be very laborious and will vary from structure to structure.

4.4. Time Frequency Analysis

Time-Frequency analysis techniques provide the capability to analyse AE signals containing multiple propagation modes and characterize Lamb wave dispersion. Since precise knowledge of the velocity dispersion of Lamb wave modes is required in AET, time-frequency representations (TFRs) can offer several advantages not only for the extraction of the velocities of the different modes that could be identified in AE signals but also for the direct identification of these modes. One type of solution for time-frequency representation is given by atomic decompositions. A common example is the short-time Fourier transform (STFT). The STFT uses a windowing technique in which a short time window of the original signal is transformed into the frequency domain. The window is then

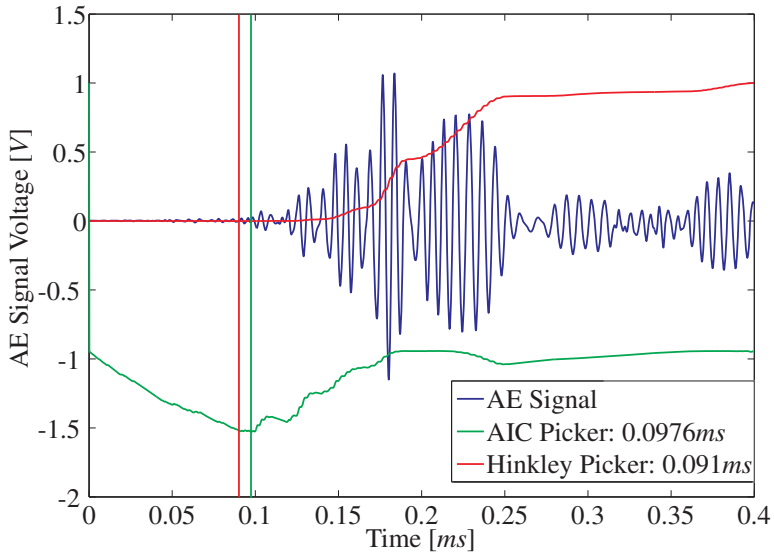

Figure 4.3. *Performance of the AIC and Hinkley pickers in an acoustic emission signal.*

shifted to a new position and the transformation is repeated with a different part of the signal. The shifting window provides the means for breaking up the signal into sections as well as enforcing periodic assumptions. However, the disadvantage of the STFT is that it is not possible to obtain a high resolution in the time domain and in the frequency domain since the chosen time window has a constant size for all frequencies [Auger et al. 1995]. Other possibility is the use of energy distributions where the energy of the signal is distributed over the time and frequency. One time-frequency energy distribution of particular interest is the Wigner-Ville distribution (WVD). The WVD of a signal $\mathrm{s}(t)$ is defined as [Auger et al. 1995, Staszewski and Robertson 2007]:

$$WVD(t,f) = \int_{-\infty}^{\infty} \mathrm{s}\left(t+\frac{\tau}{2}\right)\bar{\mathrm{s}}\left(t-\frac{\tau}{2}\right)e^{-i2\pi f\tau}d\tau, \tag{4.9}$$

where $\bar{\mathrm{s}}$ is the complex conjugate of the signal to be analysed. The drawback with this distribution is that this representation generates cross terms which appear when signals with multi-frequency components are analysed, causing a misconception of the signal frequency content. Some variants of the WVD developed to alleviate the problems of cross terms are the pseudo Wigner-Ville distribution (PWVD) and the smoothed-pseudo Wigner-Ville distribution (SPWVD). These techniques apply a window either in time and/or frequency in order to overcome the problem of the interference terms. Nevertheless, the more it is smoothed in time and/or frequency, the poorer the resolution in time and/or frequency will be obtained [Auger and Flandrin 1995]. However, the effects of cross terms present in the WVD do not have a relevant influence on the performance of the approaches proposed in this chapter as it will be shown later. The resulting three-dimensional data of the distribution can be visualized in a number of ways. It can be displayed as contour plots, 3D surface plots, or as gray-scale or false colour images. The time-frequency representation of an acoustic emission signal together with its time history

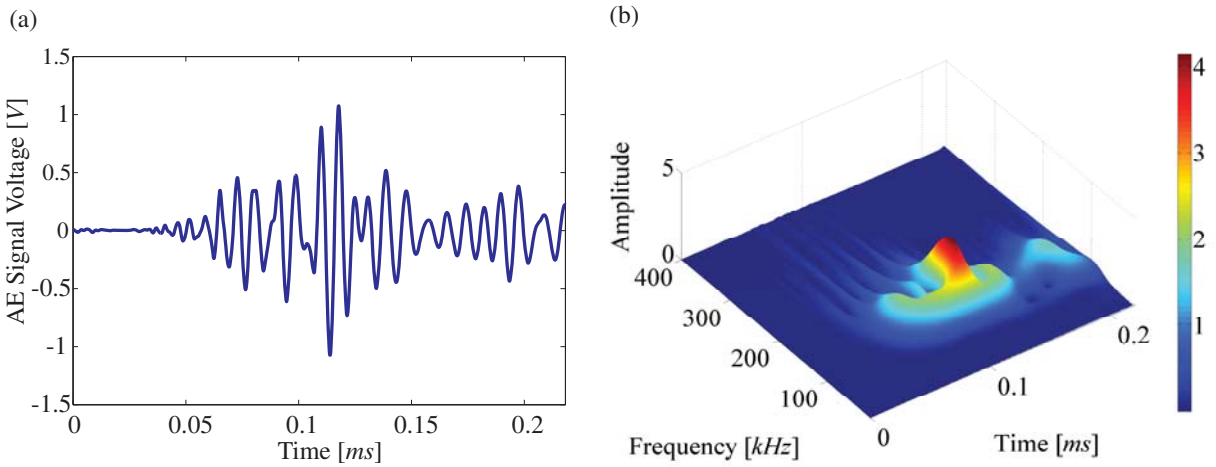

Figure 4.4. *Time-Frequency representation of an AE signal produced by an impact on the surface of an aluminium plate: (a) AE signal and (b) WVD from AE signal.*

can be seen in Figure 4.4 where a normalized 3D surface plot is used. The colour at a given time and frequency point in the image represents the amplitude of the distribution, i.e. the darker the reddish colour, the higher the amplitude. It can be observed how most of the energy is located around $0.12ms$ for a frequency of approximately $f = 200kHz$.

4.5. Mode Identification by Supervised Neural Networks

Literature in neural network applications has shown the advantage of this technique in the solution of problems comprising pattern recognition and classification of signals [Masri et al. 1993, Dai and MacBeth 1997, Mustapha et al. 2007]. Due to the huge amount of data which are recorded in AET, automatic techniques are required to separate the failure-emitted signals from noise and localize the source of emission. In this section, a supervised artificial neural network (ANN) is proposed in order to discriminate modes and eliminate the localisation error produced by the detection of different modes during the application of the onset-time picker in the signals captured by the sensor network. Figure 4.5 displays the proposed automatic procedure for the localisation of acoustic emission signals.

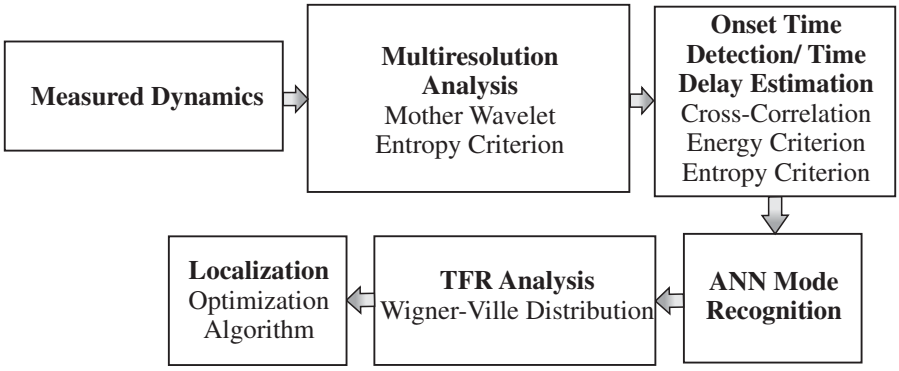

Figure 4.5. *Proposed scheme for AE signals analysis and localisation.*

The neural network proposed in the present methodology is a non-linear multilayer feed-forward back-propagation. A model with two hidden layers is selected since it has been proved to be adequate in most of structural-related problems [Worden et al. 2011]. A hyperbolic tangent sigmoid activation function is established for all the nodes. The training phase uses the 1 of M strategy. With this approach, each pattern class is associated with a unique output, i.e. during the presentation of a pattern to the network during training, it is required to generate a value of 1.0 at the output corresponding to the desired class and 0.0 at all other outputs. Multilayered perceptron (MLP) networks trained with a squared error cost function with the 1 of M strategy estimate the Bayesian posterior probabilities for the classes with which the outputs are associated, i.e. the network actually implements a Bayesian decision rule if each pattern vector is associated with the class with the highest output value [Bishop 1995, Brio and Molina 2002, Bishop 2007].

The training data are composed of segments representing the fundamental symmetric S_0 and antisymmetric A_0 modes as well as noise segments extracted prior to the wave first arrival. The length of the input segment is selected in order to represent typical features of the modes and includes several complete cycles of the wavelets. Before selecting the segments of the signals corresponding to the different modes, these are denoised by means of the DWT. In this case the approximations coefficients are used for the synthesis of the AE signal. A typical denoised AE signal produced by a pencil lead break on the surface of an aluminium plate and an example of the segments selected to form the input vectors to the network are depicted in Figure 4.6.

Once the time difference of arrivals of the signals are calculated, with any of the methods described in Section 4.3, and the modes corresponding to the arrivals have been identified by means of the proposed ANN methodology, time-frequency analyses based on the

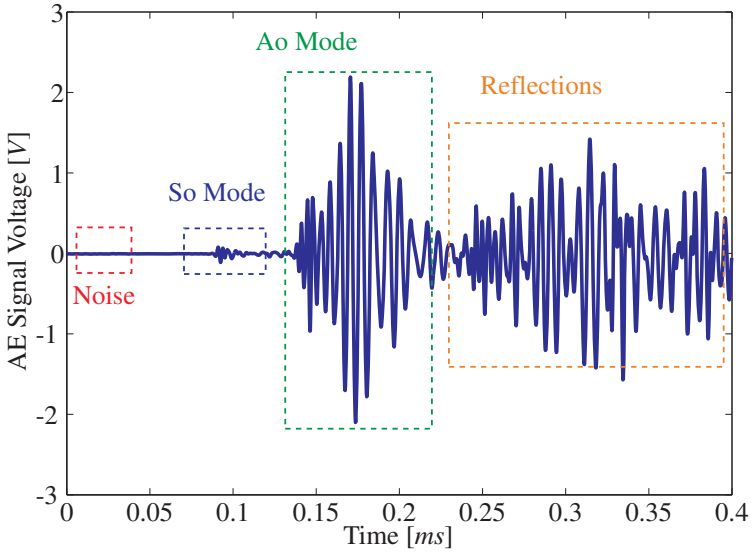

Figure 4.6. *Signal generated from a pencil lead brake on the surface of an aluminium plate containing the fundamental symmetric and antisymmetric modes of propagation together with reflections from the boundaries and noise.*

Wigner-Ville distribution are carried out for the selected segment in order to extract the group velocity of the respective modes from the model described in Chapter 3 and then execute the localisation.

4.6. Mode Identification by Modal Energy Orientation

As it has been mentioned throughout this thesis, in order to make AET a trustworthy technique, reliable source location and damage mechanism characterisation must be accomplished. A novel approach based on a chirplet atomic decomposition, time-frequency energy distribution and dispersion analysis, where the failure-emitted signals are separated from extraneous noise and the detected modes are analysed according to their dispersive behaviour and angular dependence characteristics is presented in this section. Dispersion relations are obtained by the use of the higher order plate theory proposed in Chapter 3, and then used in conjunction with the previous methodologies for mode identification and localisation. A statistical onset-picker (AIC) is used to estimate the wave arrival and dispersion analysis is then conducted on the decomposed signal in conjunction with quadratic time-frequency analysis so that the frequency content is extracted and the energy orientation examined in order to classify the detected modes of propagation in the recorded signals, and then select a common mode to the sensor network.

By recognizing and identifying the dominant modes of propagation in the received AE waveform then it would be possible to discriminate between damage types. For example, the antisymmetric wave modes with dominant out of plane motion will interact most strongly with damages lying parallel to the plane of the wave propagation such as delaminations, skin or core debonding and impact damage. The symmetric wave modes with dominant in-plane motion will be more strongly related with damages lying perpendicular to the plane of wave propagation such as matrix cracking, matrix splitting and core crushing [McGugan et al. 2006]. Thus, by carefully analysing the dispersive characteristics of the signals or by the application of advanced pattern recognition methods the identification of the failure modes with different type of damage mechanism could be accomplished [Paipetis and Aggelis 2012, Sause et al. 2012]. The focus on classification of AE events is based on the dispersive energy attributes of the wave packets constituting the waveform.

4.6.1. Improved Atomic Decomposition

A major difficulty in acoustic emission is the analysis of broad-banded signals and the discrimination of the modes contained in the recorded signals. The matching pursuit algorithm (MAP) is proposed for the atomic decomposition of AE waveforms focused on the ability of the method to classify between modes based on dispersive energy characteristics. The MAP was introduced by [Mallat and Zhang 1993] and has been successfully applied

in SHM by different researchers. It is an iterative algorithm that decomposes a signal into a linear combination of waveforms, so-called atoms, that are selected from a redundant database of atoms, named dictionary, having similar time and frequency characteristics to the original signal, in our case, the AE waveforms. The atom from the dictionary that locally better defines the signal is then selected for reconstruction. The first step of the algorithm is to create a redundant dictionary **D** of atoms g which are well localized in time and frequency, and possess unit energy. The second step is to find the best match from the dictionary (where $< \bullet, \bullet >$ symbolises the inner product) in which the residual $r_0(t)$ equals the sensor signal $\mathrm{s}(t)$ for the first iteration according to:

$$g_i = \arg\max_{g \in \mathbf{D}} |< r_{i-1}, g >| . \tag{4.10}$$

The third step is to compute the residual after subtracting the component along the best atom as shown in Eq. (4.11):

$$r_i = r_{i-1} - < r_{i-1}, g_i > g_i. \tag{4.11}$$

Finally, the second and third steps are repeated until a maximum number of iterations n is met or a predefined energy threshold of the original signal energy is reached. The signal can be finally reconstructed according to Eq.(4.12) as:

$$\mathrm{s} = \sum_{j=0}^{n-1} < r_j, g_j > g_j + r_n. \tag{4.12}$$

The proposed dictionary is composed of chirplet atoms which are well suited for the analysis of dispersive signals with no stationary time-frequency behaviour [Raghavan and Cesnik 2007]. The chirplet atom is defined as follows:

$$g_k(t) = \frac{1}{\pi^{0.25}\sqrt{s_k}} \exp\left(-\frac{1}{2}\frac{(t-t_k)^2}{s_k^2} + i\left(\omega_k (t-t_k) + \frac{\beta_k}{2}(t-t_k)^2 \right) \right), \tag{4.13}$$

where the controlling parameters s_k, t_k, ω_k, and β_k indicate the time extent, time centre, angular frequency centre, and the linear frequency modulation rate, respectively. An example of chirplet atoms with different parameter values is shown in Figure 4.7.

In case of acoustic emission stress waves, the dictionary can be designed with knowledge regarding the spectral characteristics of the expected AE signals. To achieve maximum resolution in time shift, the time translations t_k are selected depending on the sampling interval. The angular frequency ω_k should lie in between the frequency range of the anti-aliasing filters. The parameters s_k and β_k are optimized by finding the optimal values that lead to a better match in the neighbourhood of the initial set of parameters. This strategy significantly improves the resolution of the decomposition without increasing the size of the dictionary. In this context, a small dictionary refers to a coarse discretization

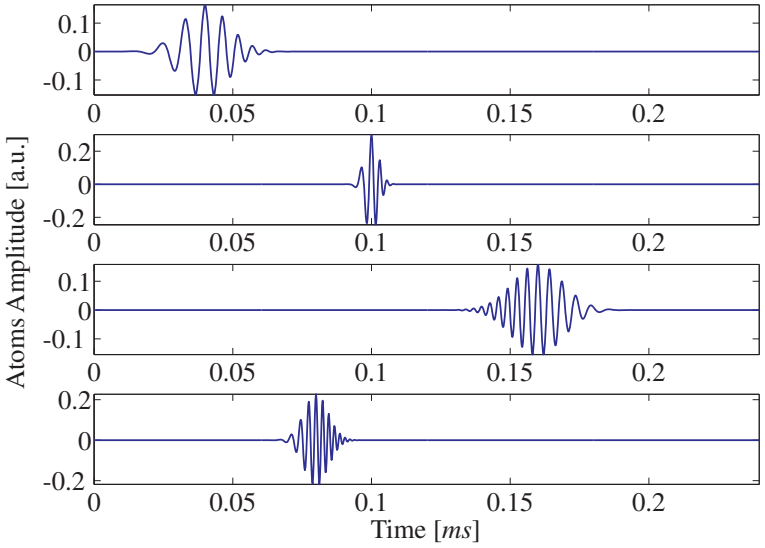

Figure 4.7. *Example of different chirplet signals with different controlling parameters.*

step of the parameters controlling the chirplet atoms contained in it. It is well-known that a smaller discretization interval of the control parameters produces a large number of functions which usually provide a better decomposition in terms of matching the signal. Nevertheless, as the size of the dictionary increases the computational effort also increases. Therefore, the goal of the proposed numerical implementation is to improve the decomposition performance without increasing the size of the dictionary. The dictionary can be further improved by taking into consideration the effects of dispersion in order to count with a dictionary of signals that will reflect the real wave propagation phenomenon. This can be done by means of spectral analysis since once the signal has been characterised, i.e. once the different modes have been calculated with the model proposed in Chapter 3 (wavenumbers, attenuation, excitability, etc.), the propagation and reconstruction of the signal becomes fairly easy. A general diagram depicting the different factors affecting a received time-domain acoustic emission wave once the propagation and attenuation of waves through the structure have taken place is depicted in Figure 4.8.

In essence, the input chirplet atom $g_k(t)$ is transformed to its spectrum $G_k(\omega)$ and the

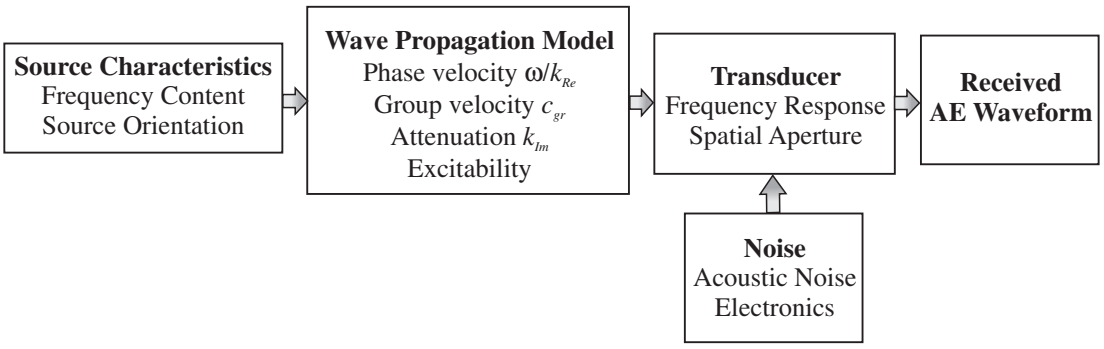

Figure 4.8. *Diagram for complete wave propagation characterisation.*

transformed solution is expressed at each frequency ω_n and some position r in space as follows:

$$u_k(\omega_n) = P(\omega_n) G_k(\omega_n), \tag{4.14}$$

where $P(\omega_n)$ is the analytically known transfer function of the problem. It is good to bear in mind that the loop for PG_k must be evaluated only up to the Nyquist frequency and the remaining part is obtained by imposing that it must be the complex conjugate of the initial part, ensuring that the reconstructed time history is real only [Doyle 1997]. A flow diagram of the complete procedure for waveform reconstruction is presented in Figure 4.9.

For the case discussed here, free wave propagation will be considered, i.e. no effects of boundaries are taken into account for the wave propagation problem. In other words, the propagation of a guided wave through an uninterrupted structure is analysed. Once the amplitude of a mode in a particular direction is known, it is straightforward to simulate its propagation. Taking the previous statements into consideration, the transfer function $P(\omega_n)$ can be defined as follows:

$$P(\omega) = \sum_{All\,modes} E(\omega) \frac{1}{\sqrt{r}} e^{-ik_{Re}(\omega)r} e^{-ik_{Im}(\omega)r}, \tag{4.15}$$

where $E(\omega)$ is the modal excitability at the AE source as explained in Section 4.2, the second term of the equation represents the beam spreading effect, the first exponential describes the propagation of the wave and the second exponential represents the material attenuation both given as exponential decays in signal amplitude with distance.

The dispersion knowledge gained with the proposed plate theory in combination with spectral analysis in the frequency domain and the understanding of the excitability functions can help in the development of a dictionary with optimal acoustic emission signals. However, if the dictionary is built with arbitrary signals with no relation to the physics of underlying signals, then the interpretations gained with the decomposition could lead to incorrect inferences for mode identification.

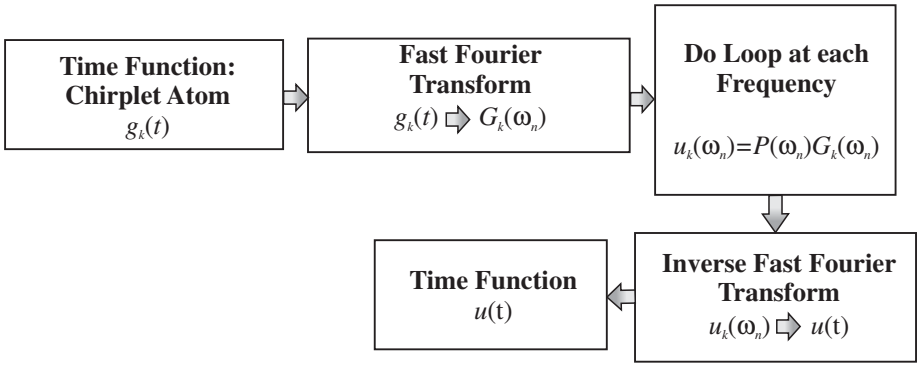

Figure 4.9. *Flow diagram for waveform reconstruction: From input waveform to propagated, attenuated and beam spread signal.*

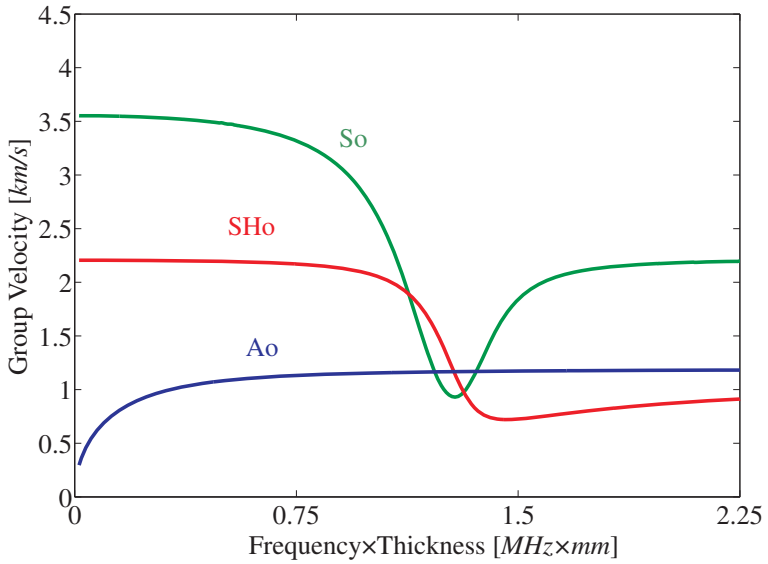

Figure 4.10. *Fundamental modes of propagation: Group velocity dispersion curves.*

4.6.2. Time-Frequency Analysis for Mode Identification

Once the matching pursuit decomposition has been accomplished, an energy distribution can be defined in the time-frequency plane without the interference terms obtained with conventional time-frequency representations (TFRs) [Mallat and Zhang 1993, Raghavan and Cesnik 2007]. As a result, this technique will provide a clearer picture of the energy distribution with well defined clusters of concentrated energy in comparison to traditional smoothed representations. Moreover, since the parameters of every matched atom are known, no special post-processing is required for the analysis. As shown in the previous chapter, the group velocity C_{gr} is related to the velocity with which the envelope of a wave packet propagates and it is equal to the energy velocity [Auld 1990]. Then, by analysing the dispersive characteristics of the recorded modes, it would be possible to identify them. The ability to measure Lamb mode dispersion from time-frequency analysis from acoustic waveforms is of great importance in this context [Prosser et al. 1999, Fucai et al. 2009].

It is known that the low frequency range is the most used in Lamb wave applications for structural health monitoring where just the fundamental S_0 and A_0 modes of propagation are present and the influence of higher order modes of propagation is avoided in order to facilitate the analysis of the recorded signals. Figure 4.10 shows the group velocity dispersion curves for the case of a $1.5mm$ thick GFRP plate with material properties listed in Table 7.1 for the fundamental modes of propagation.

It can be seen that the behaviour of the SH_0 and S_0 modes is different from the A_0 mode in both the low and high frequency zones. In the relatively low frequency range it can be seen that the higher the frequency of the A_0 mode, the faster its group velocity. In an opposite manner for the S_0 mode, the higher its frequency, the slower its group velocity. These energy characteristics of the modes are analysed in order to distinguish the recorded modes in a defined frequency range where their characteristics are noticeable, e.g. in the

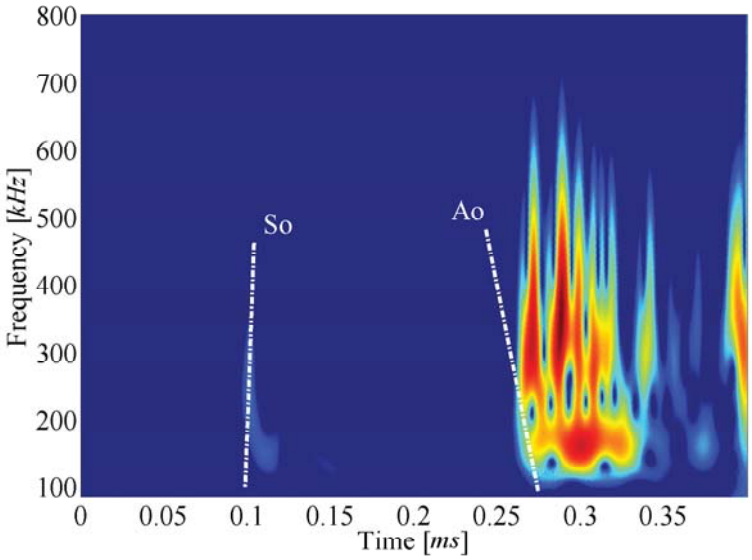

Figure 4.11. *Normalised TFR from Wigner-Ville distribution used in order to depict the energy orientation of the fundamental modes of propagation.*

relatively low frequency range the slopes of the dispersion curves are used to differentiate wave modes. From Figure 4.10 can be inferred that a wave package of the A_0 mode at a relatively higher frequency arrives earlier than one at a lower frequency, whereas the situation for the S_0 wave mode is the opposite of that of the A_0 mode. From these observations made regarding the group velocity distribution, it can be concluded that atoms positive slope in the time-frequency representation are related to the S_0 mode, and conversely, atoms with a negative slope are related to the A_0 mode. This effect of energy orientation is shown in Figure 4.11 for the AE signal depicted in Figure 4.6 where the high intensity of a point in the image represents a high amplitude in time and frequency. Once the onset time of the recorded signals is estimated, the atom with same time arrival characteristics is extracted and analysed for classification according to the interpretation presented above. As it is conventional in AE literature, special attention was not only paid to the A_0 mode since the interest is placed for the analysis of the different fundamental modes of propagation contained in the signals and their correlation with possible damage mechanisms.

4.7. Localisation

Localisation of acoustic emissions is a well investigated topic [Schubert 2004, Grosse and Ohtsu 2008, Kundu 2012] and just the relevant general information for the understanding of the localisation procedures is presented here. It is known that source localisation requires either the knowledge of the direction dependent velocity profile or a dense array of sensors. Suppose that a passive sensor network has $i = 1, \ldots, N$ sensors and that the mode wave arrival times of an acoustic emission event have been calculated by using

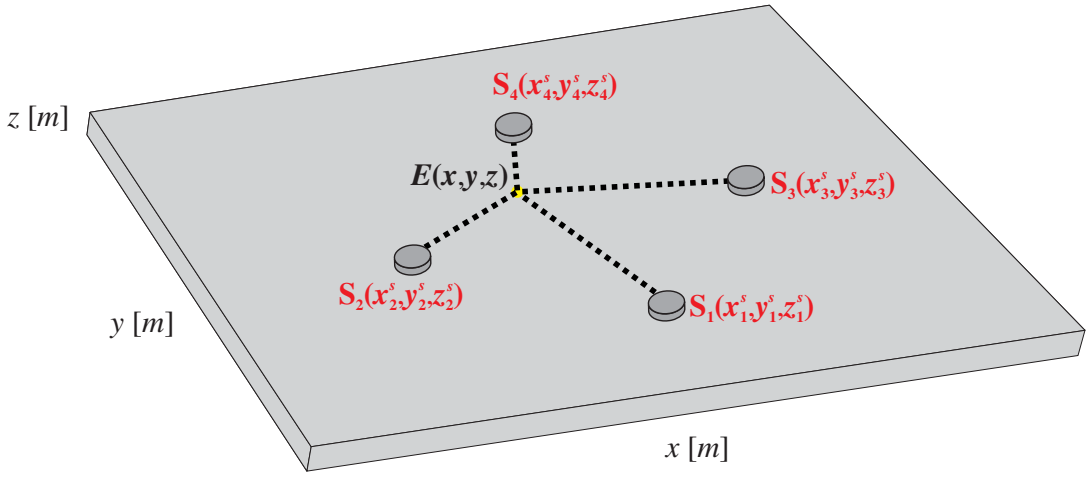

Figure 4.12. *Distributed sensor network for the recording of AE events.*

an appropriate picking algorithm as the ones introduced in Section 4.3. An illustrative example of a typical sensor network for the detection of AE events is depicted in Figure 4.12.

The localisation problem can be expressed in terms of the time of arrival of the waveforms to the different sensors as:

$$t_i^A = t_s + \frac{\sqrt{\left(x_i^s - x\right)^2 + \left(y_i^s - y\right)^2 + \left(z_i^s - z\right)^2}}{C_{gr}(\alpha)}, \tag{4.16}$$

where t_s is the source time, x_i^s, y_i^s and z_i^s are the known positions of the i^{th} sensor, x, y and z are the unknown coordinates of the acoustic event, $C_{gr}(\alpha)$ is the angular dependent group velocity and the assumption of a straight ray model regarding the source-sensor travel path is made.

Nevertheless, the time of the source is not known and Eq.(4.16) can be reformulated in terms of the time difference of arrivals of the mode at the different sensors as an optimization problem for source localisation as follows:

$$\min_{E(x,y,z)} (J) = \sum_{i,j} \triangle T_{ij}^A - \left(t_i^A - t_j^A\right), \tag{4.17}$$

where $\triangle T_{ij}^A$ are the differences in measured arrival times. The directional wave velocity characteristic of the fundamental wave modes can be calculated by the plate theory proposed in Chapter 3. Since Eq.(4.17) represents a non-linear system of equations, a closed analytical solution is not available in general and thus, it has to be solved by an iterative method [Jeong and Jang 2000, Schubert 2004, Price et al. 2005, Grosse and Ohtsu 2008]. Some other localisation approaches are discussed in [Hensman et al. 2008, Moll et al. 2012].

4.8. Acoustic Emission Identification by Unsupervised Neural Networks

In order to identify the type of damage occurring in composite materials, which normally involves fibre failure, transverse failure and delamination, non-destructive testing methods such as ultrasonic C-scans and radiographic techniques are applied [Carlsson and Norrbom 1983, Lundsgaard-Larsen et al. 2009]. Nevertheless, this can be a very time expensive and laborious work. Due to the huge amount of AE events produced and their wide dynamic range carrying considerable information regarding the damage processes and the status of degradation, pattern recognition methods can be used in discriminating the different damage mechanisms hidden in the dynamics of the recorded AE waveforms.

Numerous investigators have considered the use of pattern recognition techniques for the classification of acoustic emission signals generated during material evaluation tests [Oskouei et al. 2009, Loutas and Kostopoulos 2009, Sause et al. 2012]. For example, acoustic emission transients in composite laminate tensile tests are analysed by principal component analysis (PCA) where the input feature vector to the clustering procedure is selected to be the acoustic emission waveform itself collected from a single sensor [Johnson 2002]. Signals features such as amplitude, duration, rise time, counts, counts to peak and energy were used to discriminate the different types of damage occurring in a constrained composite by means of cluster analysis using a unsupervised classifier (Kohonen map) [Godin et al. 2004]. Nevertheless, even when these techniques proved to be successful, first, they did not allow the integration of data from multiple sensors with the objective of providing a more robust and confident analysis, and second, they worked with parameters which are very sensitive and greatly affected by the intrinsic material characteristics.

The purpose of this section is to introduce a robust method able to detect and classify failure processes based on sensor data fusion, feature extraction and selection, and clustering via unsupervised self-organizing maps for the visualization of emerging clusters. It is considered that every failure is a combination of several mechanisms occurring simultaneously, but depending on the specific loading, material, load shape, emitted signal type, the ratio of that failure combination is different. By grouping similar waveforms together, it can be attempted to classify them as mechanisms that are known to be occurring in that particular failure and make a “fingerprint” for a type of failure based on the combination of mechanisms taking place that have been identified from their unique stress wave waveform characteristics. The proposed methodology has been further developed and tested by the author during his research stay at the Risø National Laboratory for Sustainable Energy in the Technical University of Denmark with collaboration of Prof. Povl Broendsted, Dr. Helmuth Langmaack Toftegaard and Mr. Malcolm McGugan.

As a first step, the signals collected from detected AE events are stored and analysed in order to select only failure-related signals and delete spurious signals produced for example

by electronic noise, friction, etc. This can be accomplished by discarding signals with an spectral content outside of the limits of the anti-aliasing filters. This is a reasonable selection criterion since the amplitude spectrum of these spurious signals are totally different to the one of the failure-related signals. The selected signals are then pre-processed by the discrete wavelet transform (DWT) as a feature extraction technique in order to calculate coefficients representing valuable time and frequency information from the recorded stress waveforms. The approximation coefficients are taken since they represent the interesting dynamics of the recorded AE signals. These coefficients can be calculated according to Eq.(2.25). In the context of this section, the detail coefficients will be considered as high-frequency noise, i.e. only the approximations are used for optimal decomposition and further synthesis of the signal. In other words, the wavelet packet transform is not implemented for decomposition purposes. Nevertheless, the DWT generates a large number of coefficients since the input space, i.e. the whole acoustic emission waveform, has a very large dimension. For this reason, feature selection or dimensionality reduction techniques are required for allowing the practical implementation of the methodology [Carreno and Vuskovic 2005].

For the current specific methodology, an auto-associative neural network based on hierarchical non-linear principal component analysis (h-NLPCA) is trained by using the calculated DWT approximation coefficients for dimension reduction purposes. However, before training the network, the data gathered from all the sensors are fused following unfolding procedures (multi-way) as it is done in multivariate statistical procedures for monitoring the progress of batch processes [Nomikos and MacGregor 1994, Mujica et al. 2010]. This is a very common practice in multivariate statistical procedures and in the case of principal component analysis (PCA) it is commonly called as multi-way principal component analysis (MPCA) [Wold et al. 1987]. This method is statistically and algorithmically consistent with PCA and has similar goals and benefits. The relation between hierarchical multi-way NLPCA and h-NLPCA is that the former one is equal to performing standard h-NLPCA on a large two-dimensional matrix created by unfolding a three-way array. This type of unfolding can be considered as a centralised fusion scheme where the feature selection procedure attempts to remove the redundancies between sensors and within each individual sensor [Worden et al. 2003].

It is good to bear in mind that as a preliminary step, standard scaling procedures are performed with the unfolded matrix. For this kind of data sets, unfolded matrix, several studies of scaling have been presented in the literature: continuous scaling (CS), group scaling (GS) and auto-scaling (AS) [Westerhuis et al. 1999]. According to these studies, group scaling is selected here since it considers changes between sensors and does not process them independently. With this type of scaling, each measured i^{th} sample is scaled using the mean of all samples of the respective sensor at the same time instant and the standard deviation of all measurements of the sensor. Once the normalization is applied,

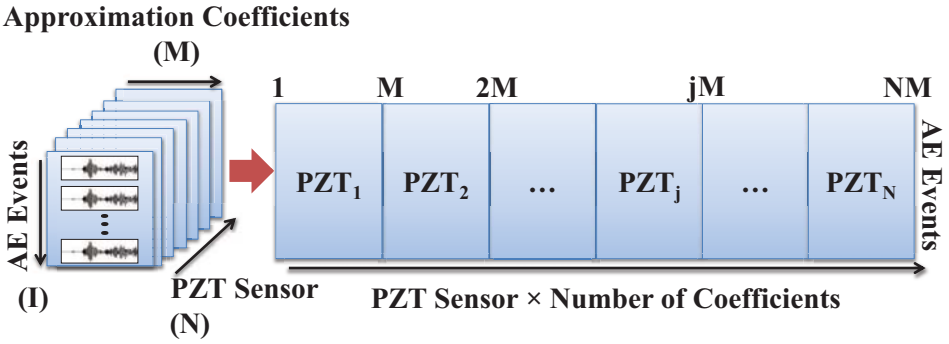

Figure 4.13. *Matrix unfolding procedure for sensor-data fusion.*

the mean trajectories by sensor are removed and all sensors are made to have equal variance.

Figure 4.13 depicts the unfolding approach undertaken before the feature selection procedure. After unfolding and scaling of the matrix, the fused data are presented as inputs and outputs to the neural network for training. Once the training has been accomplished, the calculated scores are presented as input feature vectors to a self-organizing map (SOM) for clusterization allowing to perform the detection and classification tasks. Following standard PCA, the number of non-linear principal components retained is constraint to components contributing more than a certain percentage of the total variance of the data set.

Finally, the U-Matrix surface, showing the average distance of a cell to its neighbouring cells, is then used in order to depict the different formed clusters and allow their analysis so that the clusters can be correlated with different damage mechanisms based on the analysis and time of occurrence of the modes contained in the signals belonging to the different clusters. In this analysis, the separation of the data sets defines the different damage clusters. A diagram of the complete methodology including all the pre-processing and post-processing steps is presented in Figure 4.14.

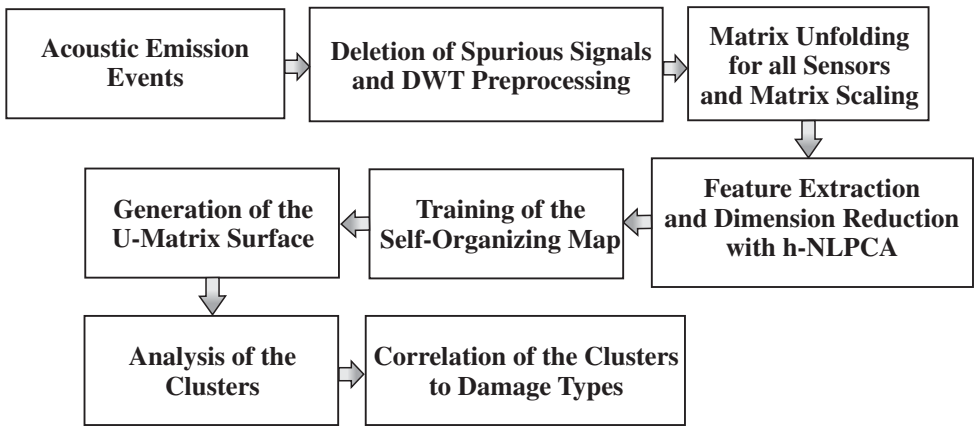

Figure 4.14. *AE signals processing for the proposed methodology.*

It is also intuitive that in some cases the stress waveforms will not trigger all the sensors in the network. In order to solve this problem, sensor subgroups which are activated by given events can be used for the sensor-data fusing approach. Consequently, the results provided by each generated model can be correlated and analysed.

5. Acousto-Ultrasonics for Damage Assessment

5.1. Introduction

Ways for reliable and suitable inspection of structures providing valuable information about the origin and importance of a fault in a structure have been an extensive field of research for long time in the structural health monitoring community. The last years have witnessed a huge increase in efforts for the design of smart structures with the integration of materials, transducers and algorithms which are able to monitor the structural condition in real time and to detect at an early stage any defects that can compromise the structural integrity [Rose 2004].

To date, several useful techniques are available but their applicability depends on factors such as maximum admissible damage size detection, maximum range of inspection, etc. For example, vibration-based techniques have been developed for the global monitoring of structures [Fritzen 2005]. However, in view of the fact that incipient damage is typically a local phenomenon and the local response is mostly captured by higher frequency modes, these techniques present some practical difficulties since it is more complicated to excite the higher frequency response as more energy is required to produce measurable responses at these higher frequencies [Doebling et al. 1998]. On a more local level, conventional non-destructive inspection (NDI) methods based on ultrasonic tests have been successfully applied by well-trained technicians. Nevertheless, due to possible inaccessibility, short range inspection capabilities as well as due to high costs, a vast quantity of critical structures is still monitored with NDI technology only within long intervals. As a result, alternative procedures such as guided ultrasonic wave-based techniques rapidly emerged due to their very well-known properties and were adapted to the concept of SHM [Alleyne and Cawley 1992]. These techniques enable the recording of baseline measurements in order to relate changes in the dynamic responses to structural damage and allow the monitoring of complex structures [Wilcox 1998]. Especially in composite structures, these changes can be very small and the diagnostic methods must be very sensitive to the fault. One possible and interesting technique is the acousto-ultrasonics technique

[Vary 1990]. The monitoring principle, based on an actuator-sensor configuration, is quite similar to the one used in standard guided ultrasonic inspection. The difference resides in that wave modes and propagation paths are not well established since the actuator and sensors are normally not in a line of sight position regarding damage [Staszewski 2005]. Additionally, the acousto-ultrasonics strategy is to collect all the ultrasonic energy that is available as a result of wave interactions within the structure [Vary 1990]. This technique can be considered as a very sophisticated and advanced method where digital signal processing and pattern recognition algorithms play a crucial role. Generally speaking, the damage identification problem can be addressed using model-based approaches where a high-fidelity physical model of the structure is required [Torres Arredondo and Fritzen 2012c] or by data-driven approaches requiring a statistical model representation of the system [Worden and Manson 2007]. For the emphasis presented here, the SHM problem of damage detection will be essentially tackled as one of the statistical pattern recognition [Farrar and Worden 2007]. Within this context, data pre-processing, feature extraction and selection form an important aspect of pattern recognition procedures for reliable health monitoring [Staszewski 2000; 2002].

This chapter is concerned with the development and evaluation of a methodology using multi-way hierarchical non-linear principal component analysis, discrete wavelet transform, squared prediction error measures and self-organizing maps for the detection and identification of damages in mechanical structures [Torres Arredondo et al. 2012; 2013]. The chapter is organised as follows: For completeness, the proposed automatic monitoring strategy is presented first. Second, the selection of an appropriate actuation signal and the effects of its choice with regard to mode excitation, separation of wave packets in time domain and frequency bandwidth are discussed. Third, the several factors affecting the structural dynamic characteristics and the performance of the monitoring system are reviewed. The fourth part presents a methodology for sensor data fusion and a systematic implementation of a damage diagnosis approach where the influence of temperature variations of the system are taken into account.

5.2. Automatic Monitoring Strategy

The standard acousto-ultrasonics transducer configuration is based on transducers installed on the same side of the structure where the testing is carried out by holding the transducers in a fixture and moving them as a unit in order to cover the whole test area. Some other transducer configurations are shown in Figure 5.1. For the case of Figure 5.1 (b) and (d), i.e. for pulse-echo and straight-through transmission modes, these configurations can be used for material characterisation. For the current purpose of interest, the monitoring system should decide autonomously whether the host structure is intact or not. For this reason, the transducers configuration used here required for the realization of such a system needs that the sensors are permanently installed on the host structure.

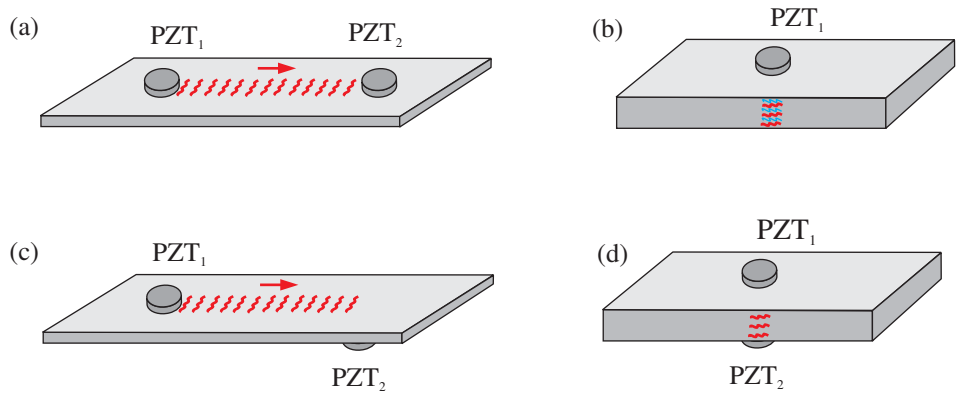

Figure 5.1. *Possible acousto-ultrasonics transducers configuration: (a) Same side, (b) Pulse-echo mode, (c) Opposite side and (d) Straight-through transmission mode.*

The formalism is based on a distributed piezoelectric active sensor network for the excitation and detection of structural dynamic responses where each sensor acts in turn as an actuator during each actuation step. In each actuation step, one piezoelectric transducer is used as an actuator, where a known electrical signal is applied, and the others are used as sensors collecting the wave propagated through the structure at different points.

The acousto-ultrasonics approach presented here is used to collect all the waveform energy that is available, i.e. instead of selecting specific wave packets from the recorded signal, all the multiple reverberations are collected for their subsequent analysis. The schematic for the proposed monitoring strategy is depicted in Figure 5.2. The primary components embrace a computer, several analogue-to-digital converters (A/D) together with a signal generator. Furthermore, several PZT transducers are installed on the surface of the structure to be monitored. The spacing between the transducers and their locations are determined by the transducers characteristics, signal strength and other factors such as structural attenuation. In this manner, given a particular structure and type of actuation signal, the sensor placement and probability of detection (POD) problems of a system can be improved by means of characterising the whole wave propagation problem, e.g. using the model developed in Chapter 3, and applying the concepts of excitability explained in section 4.2. The probability of detection is defined as the probability that an acousto-ultrasonics signal can be detected anywhere in the monitored area or volume of the structure.

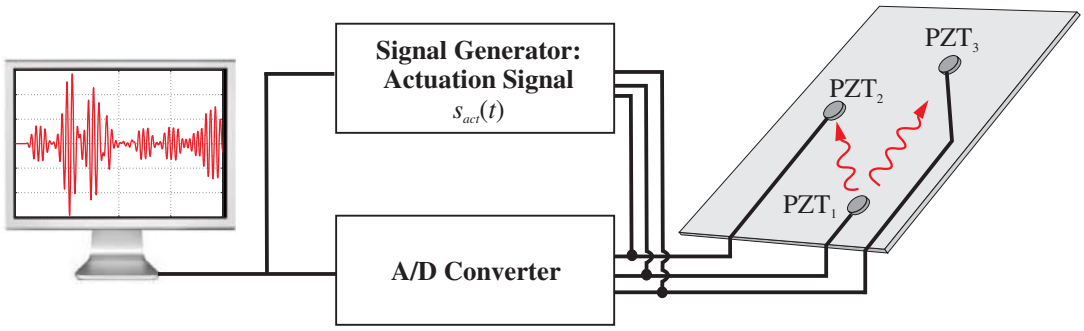

Figure 5.2. *Schematic of the complete system for the acousto-ultrasonics strategy.*

Optimal placement of piezoelectric actuators and sensors for detecting damage in plate structures using a detection theory framework can be found in [Flynn and Todd 2010]. Evolutionary algorithms have also been implemented for actuator-sensor placement in active sensing within the context of pulse-echo actuation scheme [Gao and Rose 2006]. Other approaches based on minimum detection radius are shown in [Das et al. 2009]. Additional relevant literature regarding optimal sensor location methods with focus on combinatorial optimisation, neural network and information theory can be found in [Staszewski and Worden 2001].

5.3. Selection of the Actuation Signal

The selection of the type of actuation signal regarding signal shape and carrier centre frequency is very important in acousto-ultrasonics. In ultrasonic guided wave-based methods, the actuation signals are usually a pulse or toneburst with a limited number of cycles. Pulse excitation is normally used to excite broadband ultrasonic guided waves for the purpose of analysing the effects of dispersion of the different Lamb wave modes along the frequency spectrum. The dispersion effect can be reduced using a signal with a narrow bandwidth, which is one of the reasons that windowed tonebursts rather than pulses are used as actuation signals in applications of Lamb waves. The excitation signal proposed here is a cosine train modified by a Hanning window function and it is defined in Eq.(5.1) by:

$$s_{act}(t) = \underbrace{\frac{1}{2}\left[1-\cos\left(2\pi f_c \frac{t}{n_c}\right)\right]}_{Hanning\,Window} \underbrace{\cos(2\pi f_c t)}_{Cosine\,Train}, \tag{5.1}$$

where f_c is the centre carrier frequency and n_c the number of cycles. An example of three different actuation signals for a carrier centre frequency of $120kHz$ and for different number of cycles is presented in Figure 5.3.

As a first criterion for the selection of the carrier frequency f_c, using wavelengths comparable to the structure thickness guarantees multiple wave reflections that can resolve features within the structure bounding surfaces. Therefore, the selected wavelength has a remarkable effect on the probability of detecting a discontinuity. In the case of standard ultrasonic testing, a general rule of thumb is that a discontinuity must be larger than one-half the wavelength to stand a reasonable chance of being detected [Rose 1999]. The sensitivity to detect small discontinuities generally increases with higher frequency, i.e. shorter wavelengths. Nevertheless, frequency-dependent phenomena such as dispersion effects in signal spreading and the reduction in signal amplitude are undesirable for structural monitoring. For example, in poly-crystalline materials such as rocks, scattering occurs when the wavelength of the stress wave becomes comparable with that of the grain

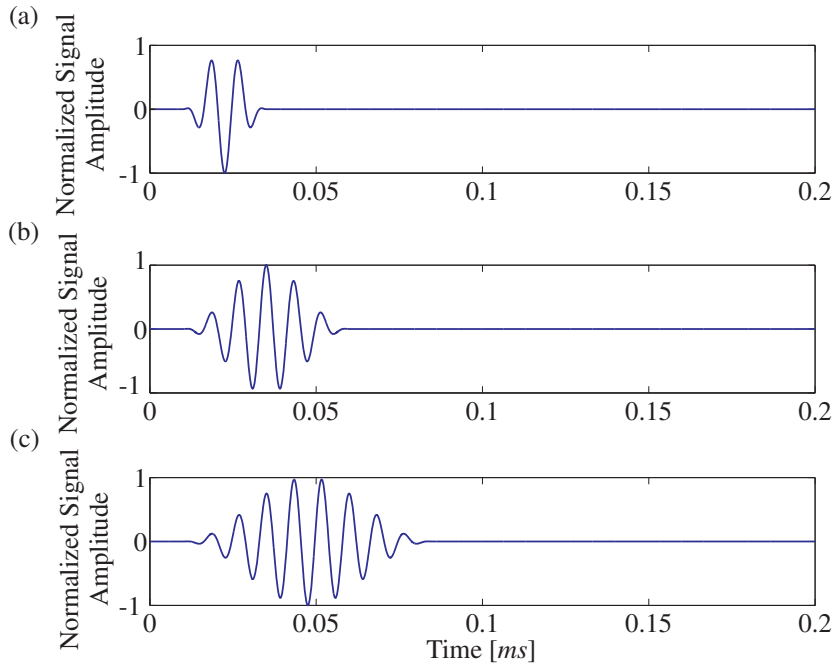

Figure 5.3. *Proposed actuation signal for a carrier frequency* $f_c = 120kHz$*: (a) Three cycles, (b) Six cycles and (c) Nine cycles.*

size. In this case, the incident stress wave sees the grain as an obstacle originating in the generation of secondary waves which spread out in different directions reducing the general directed flow of energy [Hardy 2003]. Moreover, attenuation is generally proportional to the square of sound frequency. For this reason and ideally, before selecting a carrier frequency, the material structure and its thickness, the type of discontinuity, its size and probable location should be considered. Another important parameter is the selection of the number of cycles contained in the actuation signal. This effect is depicted in Figure 5.4 for an excitation signal with different number of cycles and carrier frequency of $120kHz$.

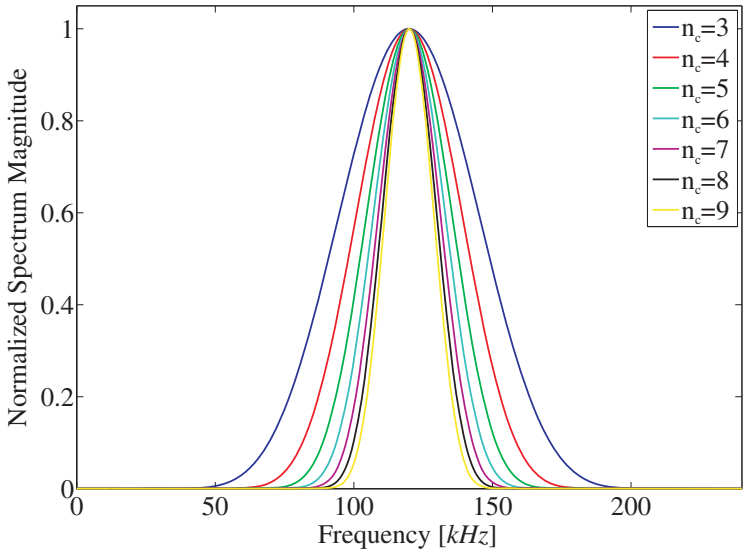

Figure 5.4. *Normalised spectrum of the excitation signal with different number of cycles for a carrier frequency of* $120kHz$.

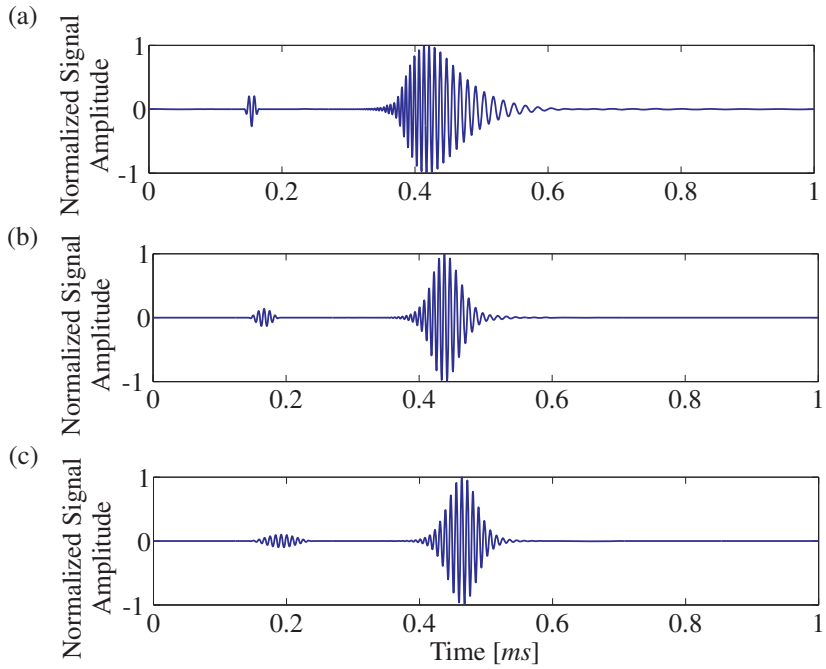

Figure 5.5. *Spreading effects depending on the number of cycles for an actuation signal with carrier frequency of* $120kHz$ *at a propagation distance of* $d = 700mm$*: (a) Three cycles, (b) Six cycles and (c) Nine cycles. The sensor and actuator are treated as point-like.*

If it is desired to get a separation of the different wavepackets in the time domain, then a small number of cycles should be selected. However, at a particular frequency and with a small number of cycles in the excitation toneburst, the bandwidth will be large and the dispersion effects will be significant. As it is shown in Figure 5.4, as the number of cycles is increased, the bandwidth is reduced and, therefore, the dispersion effects become less significant. The effect of broadband excitation of a dispersive ultrasonic guided wave mode is that energy at different frequencies propagates at different velocities. This is exhibited physically as a spreading of the ultrasonic guided wave in space and time as it propagates through the structure. These effects are depicted in Figure 5.5 and Figure 5.6.

The signals shown in Figure 5.5 and Figure 5.6 are simulated by assuming that an actuation signal with carrier frequency $f_c = 120kHz$ is applied at one arbitrary point of a infinite $2mm$ thick aluminium plate and the propagated signal is measured at some known distance from the actuation point. This simulation is accomplished by characterizing the wave propagation in the plate, with the help of the model developed in Chapter 3, and by the application of the spectral analysis procedures described in section 4.6.1. Two wave packets can be clearly identified in both Figures. The wave packet with smaller amplitude and faster group velocity corresponds to the S_0 mode. The wave packet with higher amplitude and lower group velocity corresponds to the A_0. It can be also seen that the S_0 mode exhibits lower dispersive behaviour in comparison to that of the A_0 mode. From Figure 5.5 can be seen how the spatial dispersion effects affects the free propagation of waves over a fixed distance of $d = 700mm$. It is shown how the signal is spread as it propagates along the plate, where the change in the shape of the propagated signal is a

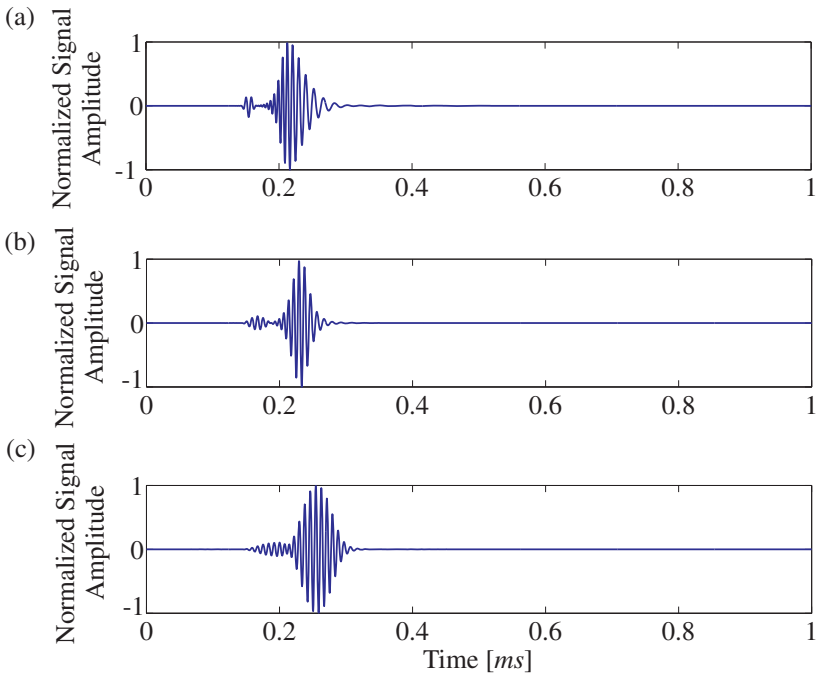

Figure 5.6. *Spreading effects depending on the number of cycles for an actuation signal with carrier frequency of* $120kHz$ *at a propagation distance of* $d = 300mm$*: (a) Three cycles, (b) Six cycles and (c) Nine cycles. The sensor and actuator are treated as point-like.*

function of the degree of dispersion of the different excited modes. In can be also seen that as the number of cycles is increased, the spatial dispersion is reduced as expected. Correspondingly, Figure 5.6 depicts how spreading of the signal occurs in time even when the propagation distance is small. The increasing of the number of cycles has a similar effect like the one depicted in the previous example. It is also evident that the dispersion of the A_0 mode becomes less strong with a smaller propagation path through the structure. Moreover, by decreasing the propagation distance, one can notice that it would be more difficult to identify the propagated modes since they will appear much closer to each other in the time histories.

In addition, it is very important to analyse the mode shape changing behaviour of the different modes which could be excited along the frequency spectrum. This is a crucial point since these characteristics are relevant not only for the detection of the modes being propagated through the structure but also for the control of the wave penetration power and its distribution across the thickness of the structure. As it has been pointed out several times throughout this thesis, the S_0 and the A_0 at low frequencies are the most frequently used modes in Lamb wave applications for structural health monitoring since they are more convenient for effective signal interpretation and damage identification where the influence of high order wave modes with complex mode shapes is avoided. Nevertheless, for illustrative purposes, the characteristics of the first two higher order modes S_1 and the A_1 are also discussed. The displacement profiles across the thickness of the $2mm$ thick aluminium plate are shown in Figure 5.7 for the fundamental S_0 mode of propagation in order to show the mode shape changing behaviour with frequency. As it can be inferred

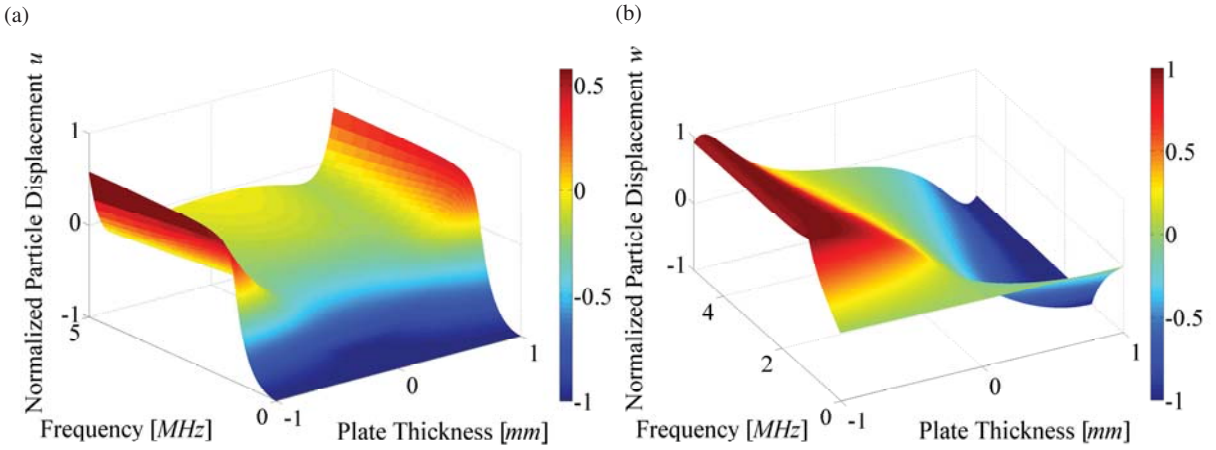

Figure 5.7. *Displacement variations along the plate thickness in a 2mm thick aluminium plate for the* S_0 *mode of Lamb wave propagation up to a frequency of 5MHz:(a) Normalised displacement* u *and (b) Normalised displacement* w*.*

from Figure 5.7 (a) and (b), in the low frequency range, S_0 is mostly an extensional mode where the in-plane displacements are almost constant along the thickness of the structure. At higher frequencies, the mode shapes for the S_0 mode begin to vary and the dominant in-plane motion along the plate thickness from the low frequency starts to decrease while the non-dominant out-of-plane motion increases on the outside surfaces where the measurements are normally made. For this reason, the S_0 mode cannot be considered just as an in-plane vibration mode. For the case of the A_0 mode, although such mode has high dispersion, it should be noted that the particle displacement is highly concentrated close to the surfaces of the plate in the low frequency range. It can be seen how the proportion of out-of-plane to in-plane displacement dramatically changes as one moves along the frequency. Here again, the A_0 mode cannot be considered just as a pure out-of-plane vibration mode.

Figure 5.9 shows the solutions for different values of frequency for the modes S_1 and the

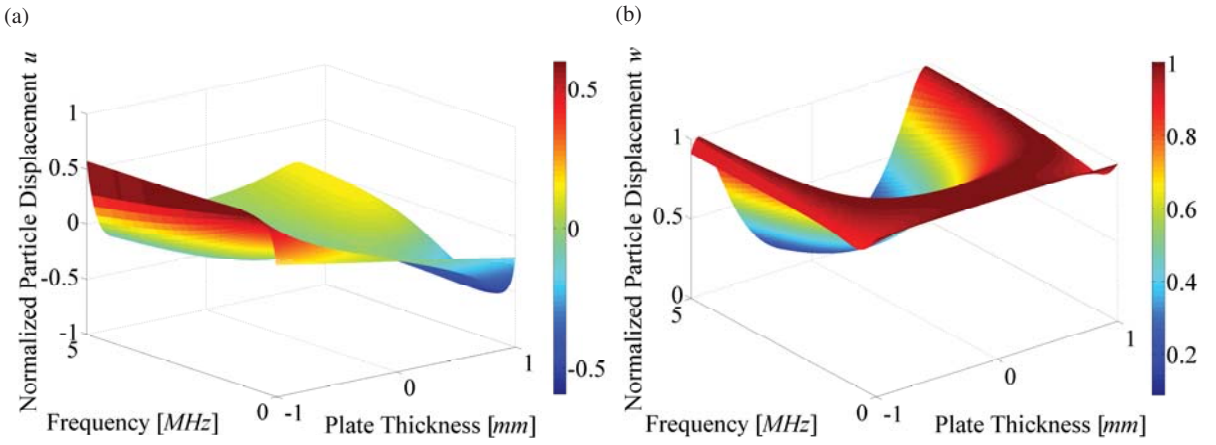

Figure 5.8. *Displacement variations along the plate thickness in a 2mm thick aluminium plate for the* A_0 *mode of Lamb wave propagation up to a frequency of 5MHz:(a) Normalised displacement* u *and (b) Normalised displacement* w*.*

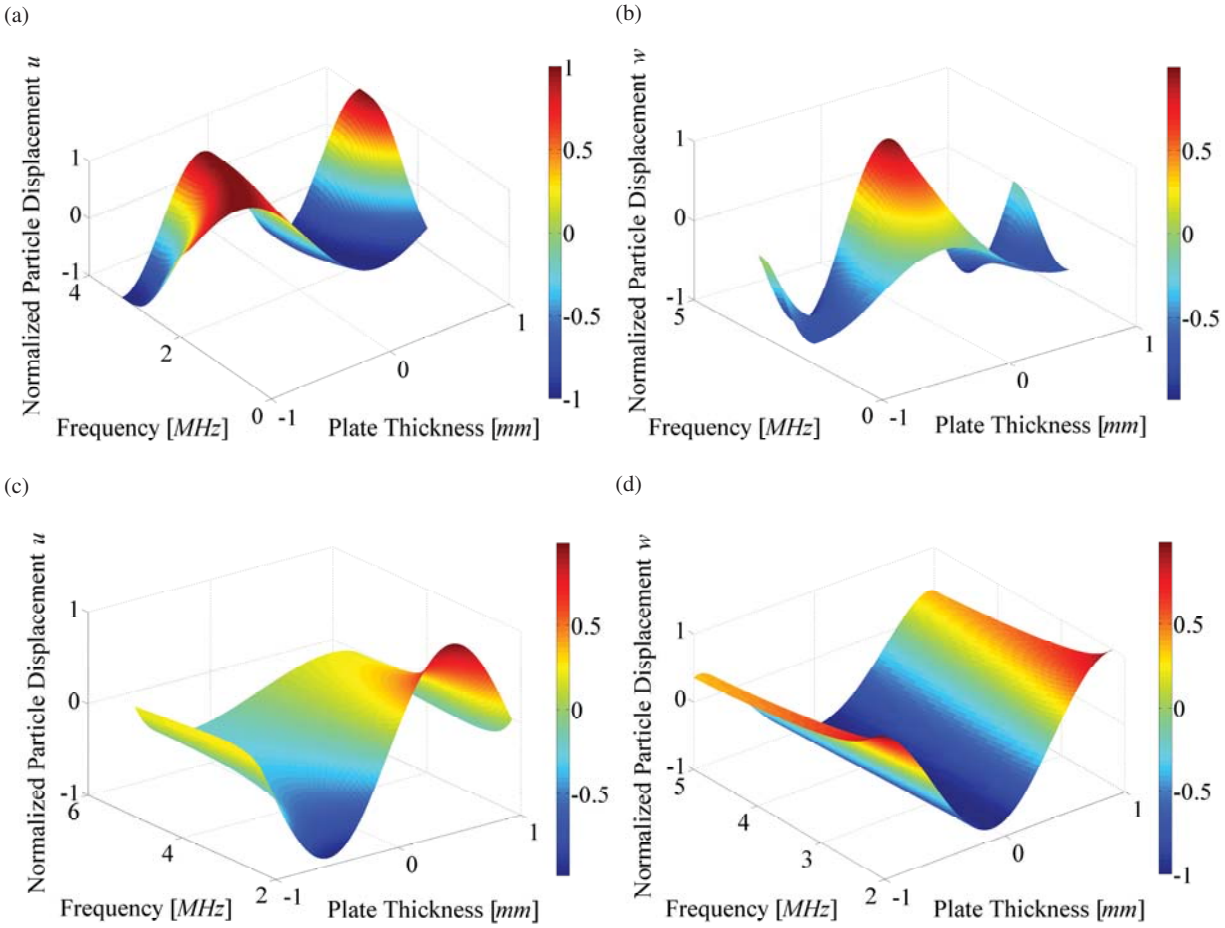

Figure 5.9. *Displacement variations along the plate thickness in a* 2*mm thick aluminium plate for Lamb wave propagation: (a) Normalised displacement* **u** *for* S_1 *mode, (b) Normalised displacement* **w** *for* S_1 *mode, (c) Normalised displacement* **u** *for* A_1 *mode and (d) Normalised displacement* **w** *for* A_1 *mode.*

A_1. For small values of frequency, it can be seen that the in-plane displacement of the S_1 mode reaches a maximum value while its out-of-plane displacement is close to zero. In the case of the A_1 mode, the in-plane particle displacement reaches maximum values at the outer surfaces at frequencies just right after the cut-off frequency. It can be also observed how the out-of-plane displacements are highly concentrated at the centre of the plate. As it can be inferred from these analyses, it can be seen that the knowledge of modal displacement distribution across the thickness of the structure plays a critical role for damage detection. An excellent study of mode selection and wave structure to detect small damages can be found in [Ditri et al. 1992].

5.4. Temperature Effects

Damage detection is based on the assumption that damage in the structure will cause changes in the measured ultrasonic signals. For in-service structures, variations in the structural dynamic responses can be also a result of time-varying environmental and

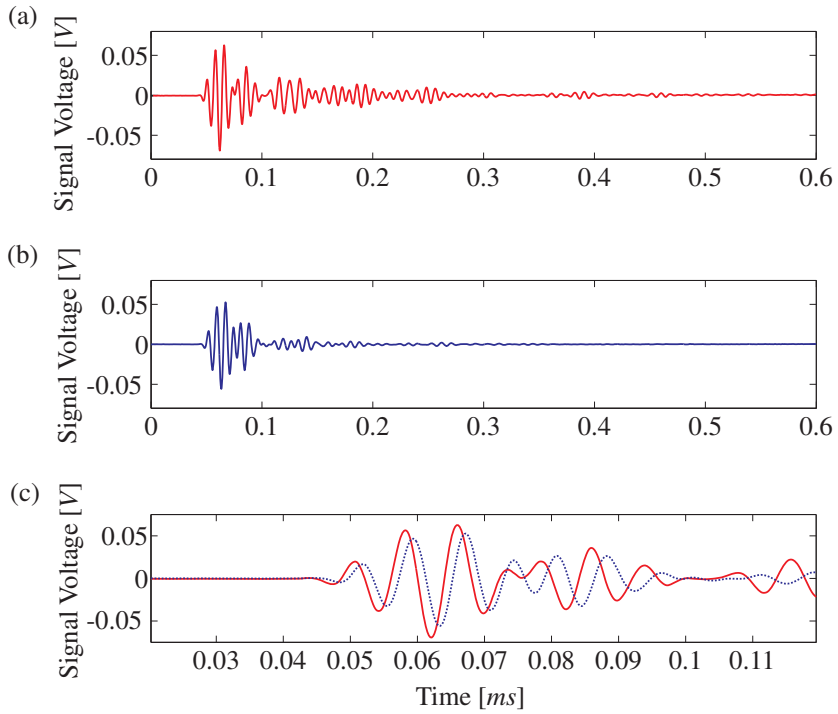

Figure 5.10. *Temperature dependence of ultrasonic signals for a* $2mm$ *thick aluminium plate: (a) AU signal from the specimen at* $20°C$*, (b) AU signal from the specimen at* $60°C$ *and (c) Time window centred around* $0.7ms$ *where the solid signal corresponds to* $20°C$ *and the dotted signal to* $60°C$*. The distance between actuator and sensor is* $120mm$*.*

operational conditions and not only of damage processes [Sohn 2007, Torres Arredondo and Fritzen 2012c]. For this reason, these variations, which are not related to existing or evolving damage in the structure, can negatively affect the performance of the monitoring system. It is well-known that the effects of temperature variability on the measured ultrasonic dynamic responses of structures is the stretch or compression of the ultrasonic signal. Temperature variations also modify the shape of the time histories since the shape of the actuation signal can be distorted. Figure 5.10 depicts the effects of time shift and shape modification for a $10V$ Hanning windowed cosine train excitation signal with 5 cycles in a $2mm$ thick aluminium plate where PZT transducers were used either as actuators and sensors. It can be observed from Figure 5.10(c) that the acousto-ultrasonics signal at 60°C is shifted to the right compared to the one at 20°C. Additionally, it can be seen how the amplitude of the right-shifted signal is reduced as well as its shape is modified as a result of the temperature effects on the material.

Additionally, temperature variations may change the material properties of a structure. Several studies regarding the effects of temperature variability on the measured dynamic responses of structures have shown the change of material properties due to temperature [Halpin 1969]. Moreover, factors such as material age effect, moisture content and structure operation affect significantly the wave propagation characteristics in the material. For example, it was observed that only $1000h$ of cyclic exposure to both ultra-violet (UV) radiation and condensation resulted in a 29% decrease in the transverse tensile strength

of a carbon fibre-reinforced epoxy material [Kumar et al. 2002]. Other studies have shown tensile strength reduction of about 40% due to moisture and temperature changes [Jia and Kagan 2003, Bank et al. 2003]. It has also been studied the deterioration of composite material properties with time when the composites are subject to freeze-thaw cycles, where a 25% reduction in ultimate strain capacity was found [Wu et al. 2006]. In order to clearly depict these effects, the model proposed in Chapter 3 is used here in order to study the sensitivity of the group velocities to the material properties for the GFRP plate with materials constants given in Table 7.1. Figure 5.11 presents the results for a reduction of 20% for each constant independently at a constant frequency of $60kHz$ for the fundamental modes of propagation. Solid lines represent the results for the original values and the dashed lines the results for the reduced values.

It can be seen that both variations of E_{11} and E_{22} have a strong influence on the velocities for the S_0 mode. These influences are reflected for the SH_0 mode only on its caustics and are practicably not noticeable for the A_0 mode. The shear modulus G_{12} has a slight influence on the velocities of the S_0 mode at $\pm 45^\circ$ (and mirrored angles) direction and almost no influence on the $0^\circ/90^\circ$ direction. The A_0 mode is nearly not affected. However, the effect of changing G_{12} is quite strong for the SH_0 mode. The shear moduli G_{13} and G_{23} have a strong influence on the A_0 mode and almost no influence on the S_0 and SH_0 modes. In order to compensate for these effects that temperature could lead to, several methods have been developed so that the performance of SHM systems is not compromised. The most common used methods are the optimal baseline selection (OBS) and the optimal signal stretch (OSS) [Konstantinidis et al. 2007, Clarke et al. 2009]. The optimal baseline selection method is used in order to select the best matching baseline measurement among the available reference signals of the undamaged structure. The optimal baseline is the reference signal for which the subtraction from the current signal yields the residual with the minimum root mean square (RMS). The optimal signal stretch method is used in order to reduce the residual of the difference between the current signal and the optimal baseline signal [Croxford et al. 2010]. The approach proposed here to solve the problem of temperature effects is to collect a baseline related to these environmental conditions over a large range of these changing conditions so that they can be characterized to reflect the different environmental states.

5.5. Additional Affecting Factors to Damage Detection Performance

It is undesirable for damage detection algorithms to indicate damage just because of a change in the environment or operation. However, it is inevitable in reality that structures will not be subjected to changing environmental and operational conditions. These condi-

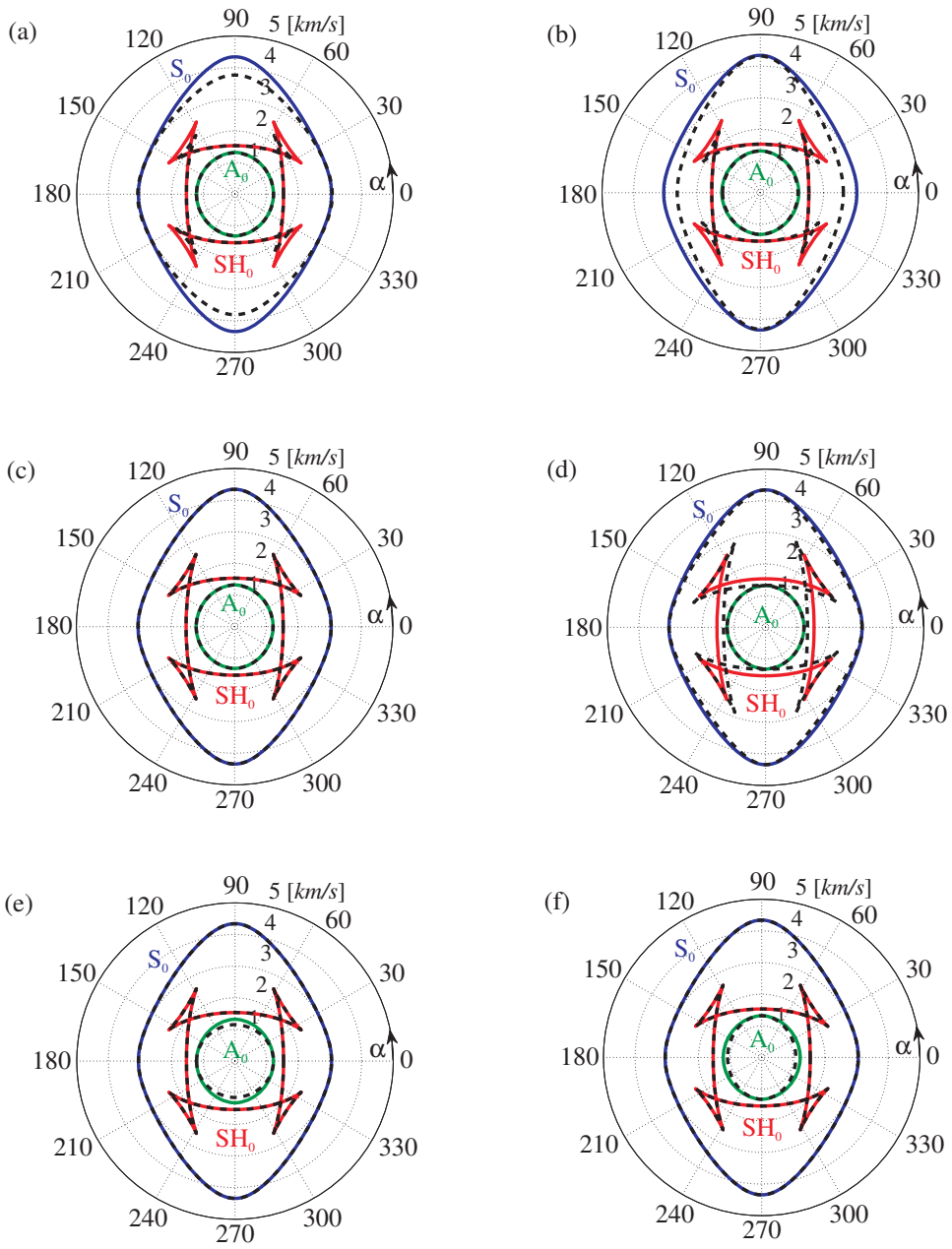

Figure 5.11. *Influence of the material parameters change on the wave curves for a reduction of 20% in: (a) E_{11}, (b) E_{22}, (c) E_{33}, (d) G_{12}, (e) G_{13} and (f) G_{23}.*

tions include changing temperature, moisture, surface wetting, loading conditions, sensor deterioration and sensor damage which affect the propagated ultrasonic signals, and hence the baseline-based models, i.e. changing the waves amplitudes and their time of flight. The effects of surface wetting on ultrasonic wave propagation are depicted in Figure 5.12 for a $2mm$ thick aluminium plate where the excitation voltage signal is a $12Volts$ Hanning windowed toneburst with a carrier frequency of $30kHz$ and 5 cycles. It can be clearly seen from Figure 5.12 how the amplitude of the modes contained in the signal are modified by the presence of water on the surface of the structure. This energy leakage into the fluid causing the attenuation of the ultrasonic signal strongly depends on the ratio of in-plane and out-of-plane displacements on the surfaces of the plate for a particular mode. This

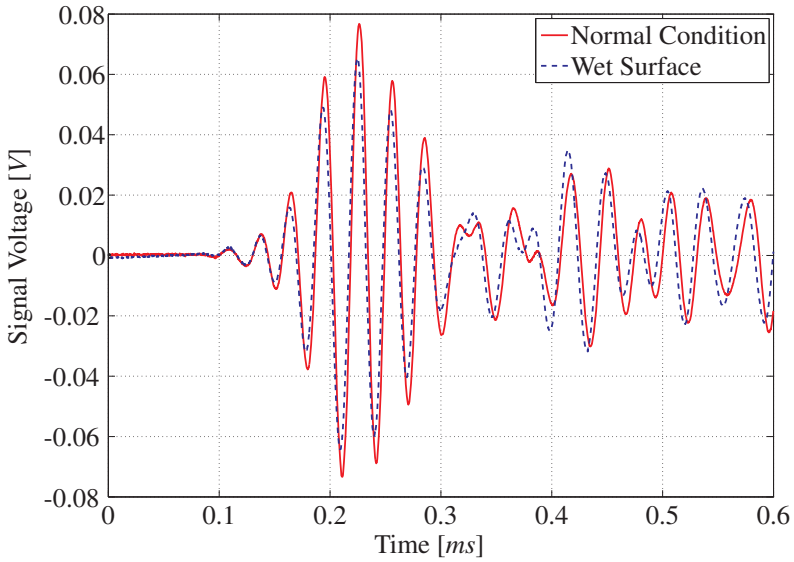

Figure 5.12. *Wet surface effect on ultrasonic signals for a* $2mm$ *thick aluminium plate. The distance between actuator and sensor is* $120mm$.

effect can be reduced by using modes with small out-of-plane particle displacement to minimize the energy leakage into the bounding fluid [Santos et al. 2004].

It is also well-known that transducers may become unavailable due to failure or malfunction. Transducer fracture is the most common type of PZT transducer failure due to its brittle nature. Normally, one would expect that a broken piezoelectric transducer could be easily identified if it does not give any meaningful output when working as a sensor, or if it does not respond to the applied excitation signals when working as an actuator. Nevertheless, if only a small fracture or debonding occurs to the transducer, the transducer will still be able to generate or capture responses which look like of normal monitoring conditions [Park et al. 2006]. Therefore, if the damage detection approach uses the faulty sensor information to predict the structural state, it can potentially lead to a false indication of the structural condition. The structure depicted in Figure 5.13(a) is used in order to show the effects of sensor breakage on the captured ultrasonic signals.

It is a $3mm$ thick aluminium plate with dimensions $200mm \times 200mm$. The structure is provided with five transducers PIC-151 from PI Ceramics which are attached to its surface with equidistant spacing. The piezo-transducers have a diameter of $10mm$ and a thickness of $0.5mm$. The structure is excited by a piezoelectric transducer located in the middle. The excitation voltage signal is again a $12V$ Hanning windowed toneburst with a carrier frequency of $30kHz$ and 5 cycles. The transducers used as sensors are broken with various percentages in order to simulate fracture. Figure 5.13(b) shows that the first wave packets follow a tendency of amplitude reduction as the fracture size is increased. The breakage of the sensor decreases the effective size of the sensors and, therefore, the amount of energy collected from the structure. A similar structure is presented in Figure 5.14(a) which is used to study the sensor debonding effect on the captured ultrasonic

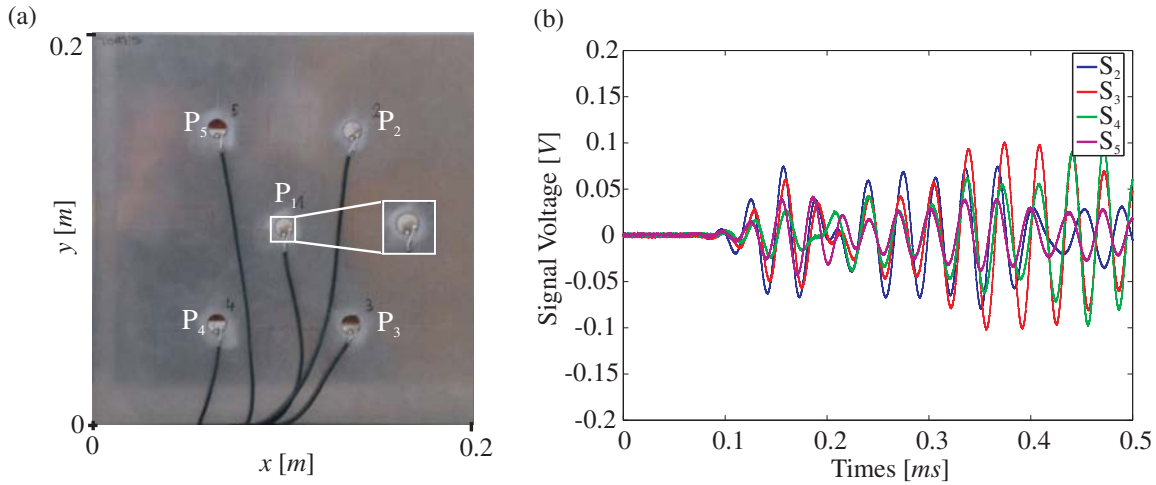

Figure 5.13. *Effect of sensor damage on the recorded ultrasonic signals with various cutting percentages on the piezoelectric transducers. The transducers* P_1 *and* P_2 *are undamaged. Transducers* P_3*,* P_4 *and* P_5 *are broken with percentages of* 50%*,* 25% *and* 75%*, respectively.*

signals. Various debonding percentages are applied to the sensors attached to the structure. The dimensions, material, transducer characteristics and excitation signal are the same of the previous example. This type of transducer failure is of great concern since in contrast to the other failure types, e.g. sensor breakage, it is not easily seen upon visual inspection. Figure 5.14(b) shows again an effect of amplitude reduction as one increases the percentage of debonding of the sensors. This decrease is consistent with the previous analysis regarding the effective are of the sensors bonded to the structure.

It is good to bear in mind that in this work just temperature variations are considered as the main factors affecting the performance of the proposed methodology and which must be taken into account for compensation. Other undesirable factors and sensor validation are not discussed and/or compensated here since they go beyond the scope of this thesis. The problem of identifying and correcting errant sensors has been tackled using different

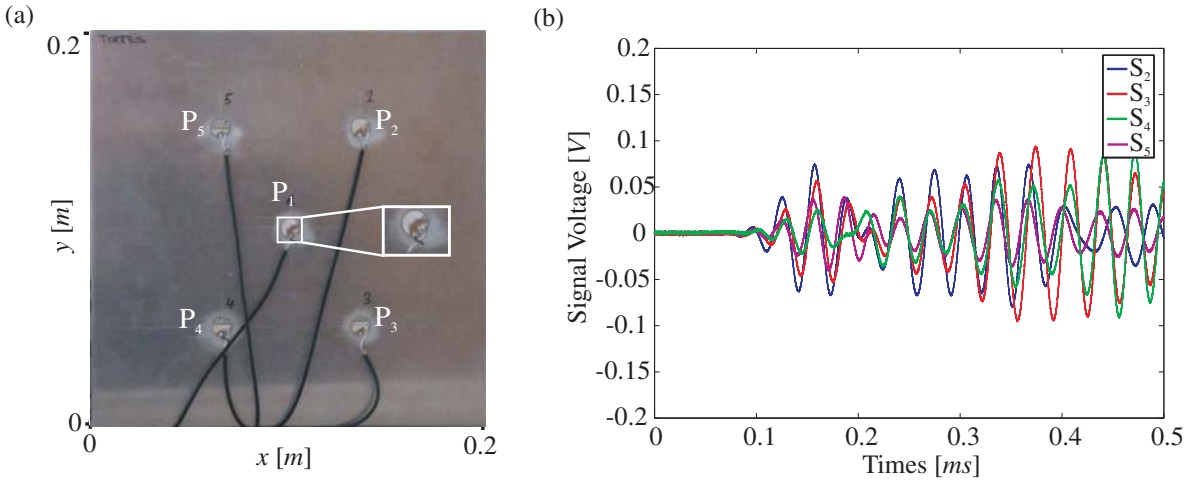

Figure 5.14. *Effect of sensor damage on the recorded ultrasonic signals with various debonding percentages on the piezoelectric transducers. The transducers* P_1 *and* P_2 *are undamaged. Transducers* P_3*,* P_4 *and* P_5 *are debonded with percentages of* 25%*,* 35% *and* 65%*, respectively.*

approaches such a auto-associative neural networks, principal component analysis, auto-regressive models, correlation indexes [Worden 2003, Kerschen et al. 2005, Abdelghani and Friswell 2007]. For further literature regarding sensor validation please see [Xu et al. 2008, Overly et al. 2009].

5.6. Damage Detection Approach

5.6.1. Feature Extraction

Firstly, wave propagation mechanisms in complex structures are very complicated due to multiple reflections and mode conversions at structural boundaries such as ribs or stiffeners. For this reason, appropriate features must be extracted from the raw measured data that allows the separation of the different datasets into meaningful classes. The SHM problem of damage detection can be essentially tackled as one of the statistical pattern recognition [Farrar and Worden 2007]. Within this context, data pre-processing forms an important aspect of pattern recognition procedures for reliable health monitoring [Staszewski 2000].

Until the present time, there exist many dimension reduction and feature extraction techniques, each using different criteria in order to decide which information should be discarded. For instance, Principal Component Analysis (PCA) has been extensively applied to measured structural dynamic response signals with the purpose of dimensionality reduction studies [Manson et al. 2001, Mujica et al. 2008], to distinguish between changes due to environmental and structural damage [Manson 2002, Yan et al. 2005], for sensor validation [Kerschen et al. 2005], among others. Wavelet applications have also been extensively studied for damage detection by several researchers and a considerable amount of literature has been published on this topic [Kishimoto et al. 1995, Taha et al. 2006, Staszewski and Robertson 2007]. Wavelet Packets and Principal Component Analysis were used for the purpose of improving myoelectric signal classification in [Englehart et al. 1999]. An enhanced sensor fault detection, diagnosis and estimation strategy was developed for centrifugal chillers combining Wavelet analysis and Principal Component Analysis in [Xu et al. 2008]. Discrete wavelet transform (DWT) in combination with hierarchical non-linear component analysis was used in order to create the feature vectors from structural dynamic responses for the training of a Gaussian process for the purpose of impact identification and for acoustic emission denoising [Torres Arredondo et al. 2011]. To illustrate the application of the discrete wavelet transform for feature extraction, a series of experiments are carried out in this subsection in order to generate different signals at different levels from the approximation and detail coefficients which could then be investigated using the proposed methodologies. The objective of this investigation is to examine the suitability of coefficients from the different levels of decomposition as robust

features for the detection and classification of damages. The full decomposition of each signal by the wavelet transform is carried out and all the components up to the ninth level are calculated and analysed in order to find the dominant energy levels. As previously mentioned, for the case under study, the family of Daubechies wavelets 'db8' is selected with the index number referring to the number of coefficients.

Figure 5.15 and 5.16 show the signal reconstruction from different wavelet level decompositions of a structural dynamic response signal from a complex structure from the levels number one to nine. Each signal at each level represents a specific frequency range, and the frequency range increases with increasing the wavelet levels. It can be seen from Figure 5.15 that the highest level of decomposition corresponds to the denoising of the original analysed signal. Nevertheless, as one increases the number of level decompositions, the amount of coefficients is reduced. This is a great advantage since less coefficients are required in order to represent the relevant information contained in the recorded dynamic responses. Regarding the different signal reconstructions from the details decompositions shown in 5.16, it can be observed that identifiable waveforms emerge as the level number of decomposition is increased. For this example, approximation level nine was found to be the more appropriate level for signal reconstruction from the approximation coefficients according to the entropy criterion presented in the chapter of theoretical background in the present work. The main idea is to build data-driven models with the DWT coefficients, i.e. the approximation and detail coefficients, calculated from the captured structural dynamic responses allowing the extraction of useful time-frequency information of the regarded signals, and analyse their individual contribution for the performance of the damage detection and classification methodology.

5.6.2. Data-Driven Modelling

It is expected that the extracted feature patterns represent different conditions of the analysed structure. The objective of pattern recognition in damage detection is then to distinguish between dissimilar patterns representing possible damage conditions. As previously discussed, the monitoring system is based on a distributed array of permanently attached piezoelectric transducers where pairs of transducers are used in pitch–catch configuration. The dynamic responses collected from each actuation step are stored and then pre-processed by the discrete wavelet transform (DWT), as a feature extraction technique, in order to calculate the approximation and detail coefficients representing valuable time and frequency information from these responses. This is a very important step since in real applications, where the number of sensors is normally large, the selection of a reduced number of robust features must be highly considered since the application of the damage detection and identification methods can become impractical. This is a common problem in pattern recognition where the design of a good classifier becomes more difficult as the

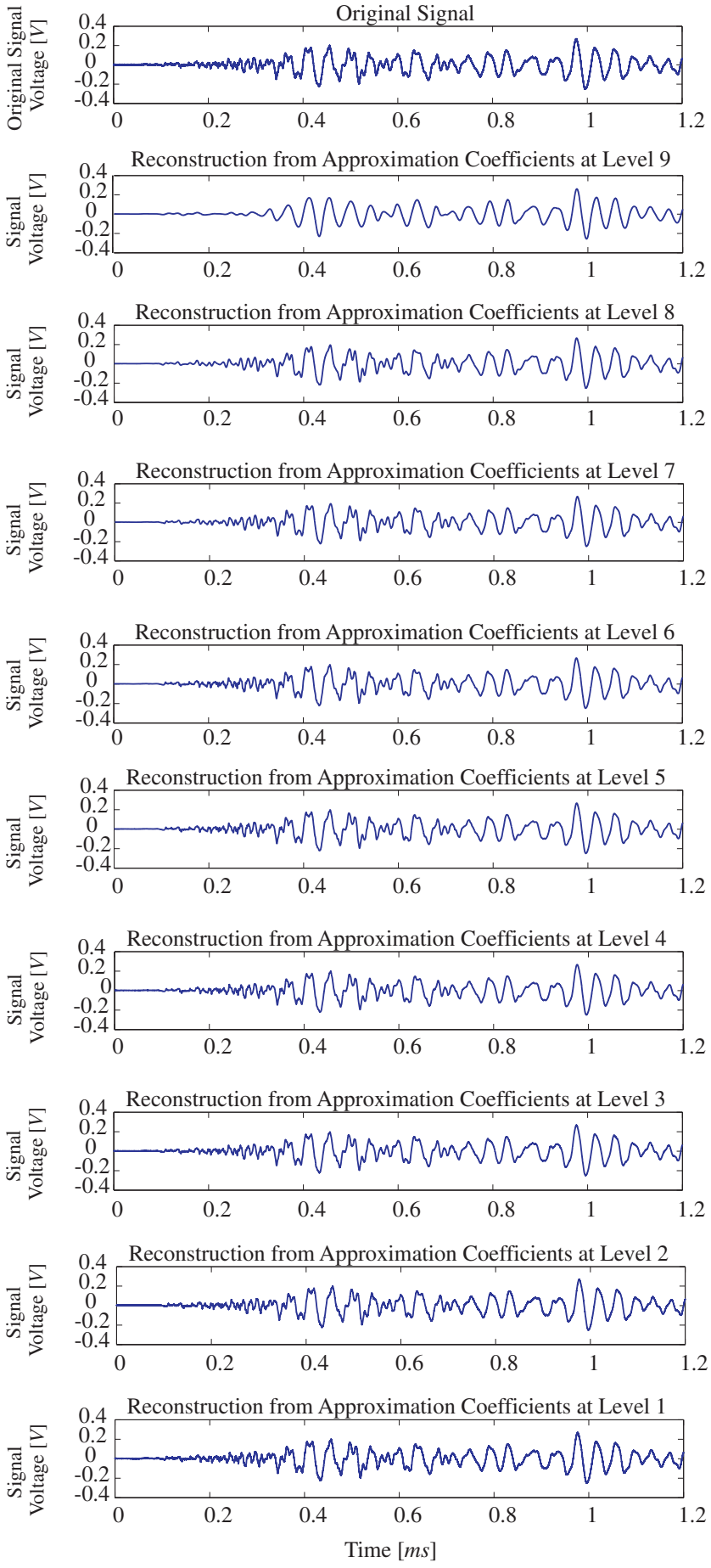

Figure 5.15. *Wavelet decomposition and signal synthesis from approximation coefficients.*

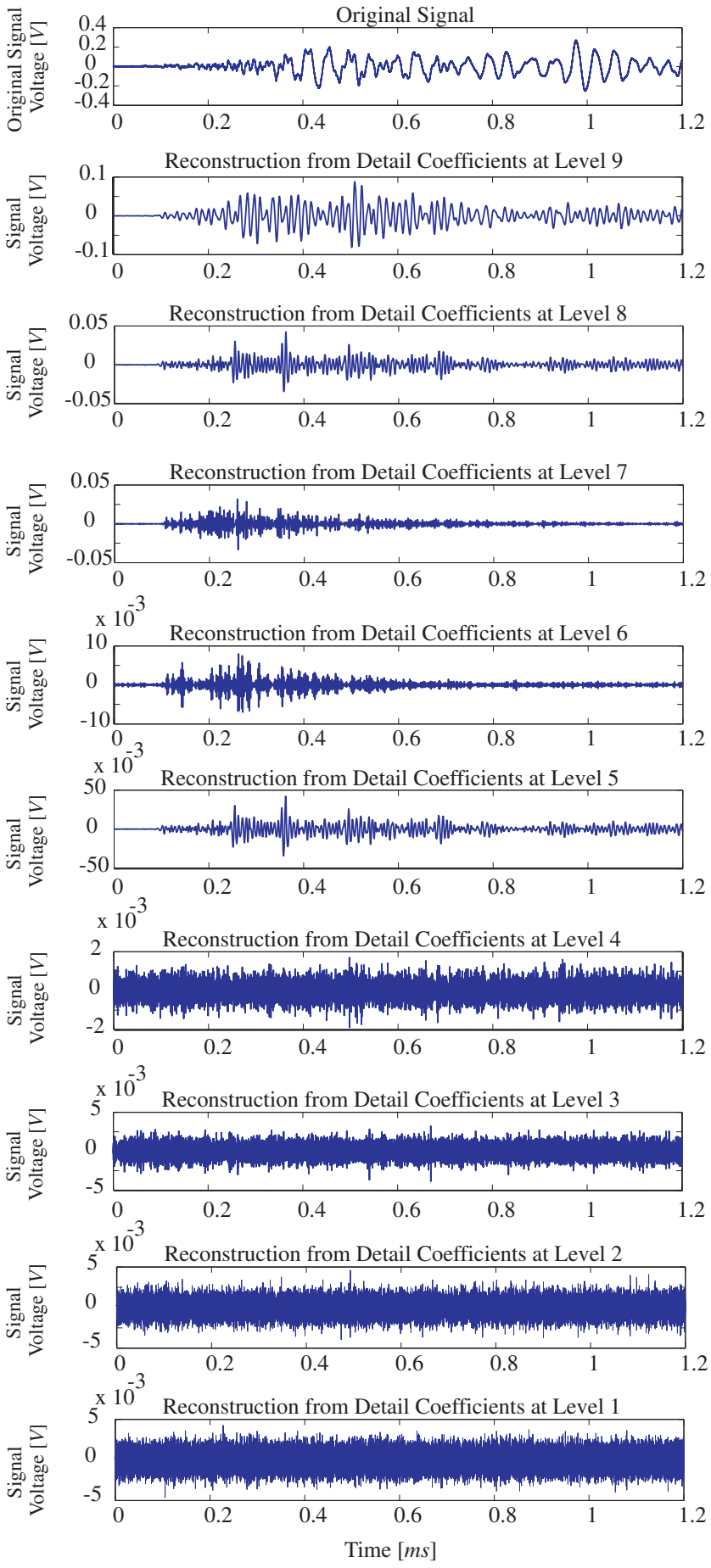

Figure 5.16. *Wavelet decomposition and signal synthesis from detail coefficients.*

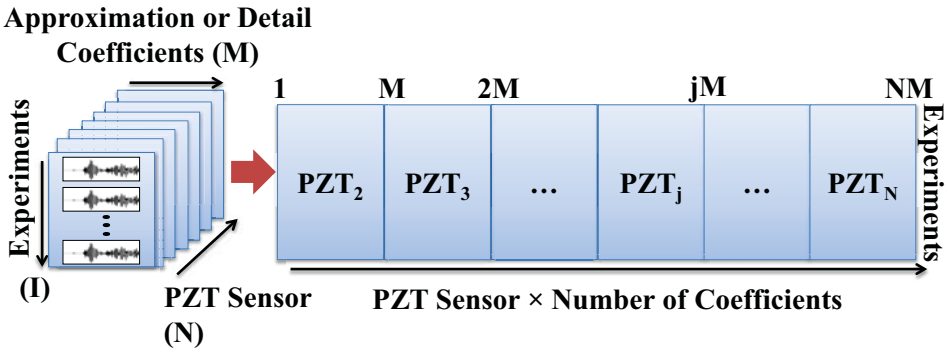

Figure 5.17. *Matrix unfolding procedure in the experiment direction for sensor-data fusion when* PZT_1 *is used as actuator.*

dimensionality of the feature space increases. This problem is known as the curse of dimensionality [Bishop 2007]. Consequently, the approach to be developed should ensure the decrement in the computational cost, but maintaining or increasing reliability and robustness in the treatment of data for analysing the state of the structure.

For the current proposed methodology, auto-associative neural networks based on a hierarchical approach will be trained independently using the calculated DWT approximation and detail coefficients extracted from the healthy system in order to build the data-driven models (template). Additionally, for comparison purposes, data-driven modelling by means of principal component analysis is also performed. Before training the network or generating the PCA model, the coefficients gathered in each actuation step are fused following unfolding procedures. This is done by unfolding in the experiment direction in which correlations between experiments and between sensors are analysed and the differences between experiments are emphasized [Mujica et al. 2009]. This unfolding procedure is depicted in Figure 5.17 in the case of using as actuator the first PZT transducer of a sensor network with $i = 1,\ldots,\mathrm{N}$ PZT transducers. This procedure is then repeated for all actuation steps and for all environmental conditions over a temperature range of these changing conditions.

Finally, standard scaling procedures are performed with the unfolded matrices where group scaling is selected. As it was mentioned in the previous chapter, this type of normalization removes the mean trajectories by sensor and all sensors are made to have equal variance. In the case of h-NLPCA, the fused data are presented as inputs and outputs to the different networks for training, i.e. each actuation step will be modelled with an independent network. Moreover, a percentage of the data from the baseline measurement are kept for the validation of the developed models. Ultimately, when new structural responses are available from each actuation step, e.g. from an undamaged or damaged structural state, the DWT coefficients are extracted from these responses and then projected into the respective models to obtain the model scores and squared prediction measures. In order to define the optimal number of principal components

required for building the models, an analysis of the variances retained in the components by the use of standard PCA can be performed. It is expected that the non-linear modelling technique will describe the data with greater accuracy and/or by fewer components than PCA [Kramer 1991].

5.6.3. Standard Outlier Analysis for Damage Detection

The outlier analysis allows to identify observations that appear inconsistent with the rest of the data. Therefore, it is possible to identify data being generated by an alternate mechanism rather than that of the baseline data, i.e. the damaged states [Worden et al. 2000]. The discrepancy of the outlier is a quantitative measure of the extent of this inconsistency [Barnett and Lewis 1994]. In the present work, the discrepancy measure or also so-called novelty index is taken as the squared prediction error (SPE). The novelty index NI corresponding to a pattern vector $\mathbf{x}$ is given by the squared difference between the pattern $\mathbf{x}$ and the result of presenting it to the network $\hat{\mathbf{x}}$. This index is defined in Eq.(5.2) as follows:

$$NI(\mathbf{x}) = \| \mathbf{x} - \hat{\mathbf{x}} \|^2 . \tag{5.2}$$

The SPE index measures the variability that breaks the normal process correlation, which often indicates an abnormal situation [Qin 2003]. If the new data are characteristic of the healthy structural state, then these data are reproduced accurately at the output of the network and the SPE will be very close to zero. Otherwise, a non-zero value will indicate an abnormality which could be related to a damage condition. Nevertheless, a threshold on the index must be defined in order to provide a statistical analysis. The threshold is estimated from the baseline data when the structure is known to be undamaged. This value is adjusted to $\mu + \varsigma\sigma$, where μ is the mean value and σ is the standard deviation value of the novelty index over the baseline. The factor ς controls the degree of confidence. The confidence level is defined to be 99.99% in this work, i.e. a value of $\varsigma = 3.891$.

It is good to bear in mind that there is a supposition here that the statistics of the novelty index are Gaussian or near-Gaussian distributions [Worden et al. 2003]. One possible disadvantage of using the outlier analysis is that, even when unfolding procedures are taken and the sensor data are fused, the information from each the actuation step, i.e. models, must be analysed independently. This type of analysis can be considered as a pattern-level fusion architecture [Staszewski et al. 2004]. Figure 5.18 depicts the fusion strategy where feature extraction occurs after each actuation step independently as well as the outlier analysis. Even when it is not evident in Figure 5.18, please remember that the baseline data-driven models are built here with both the approximation and detail coefficients extracted from the structural dynamic responses by means of PCA and h-NLPCA.

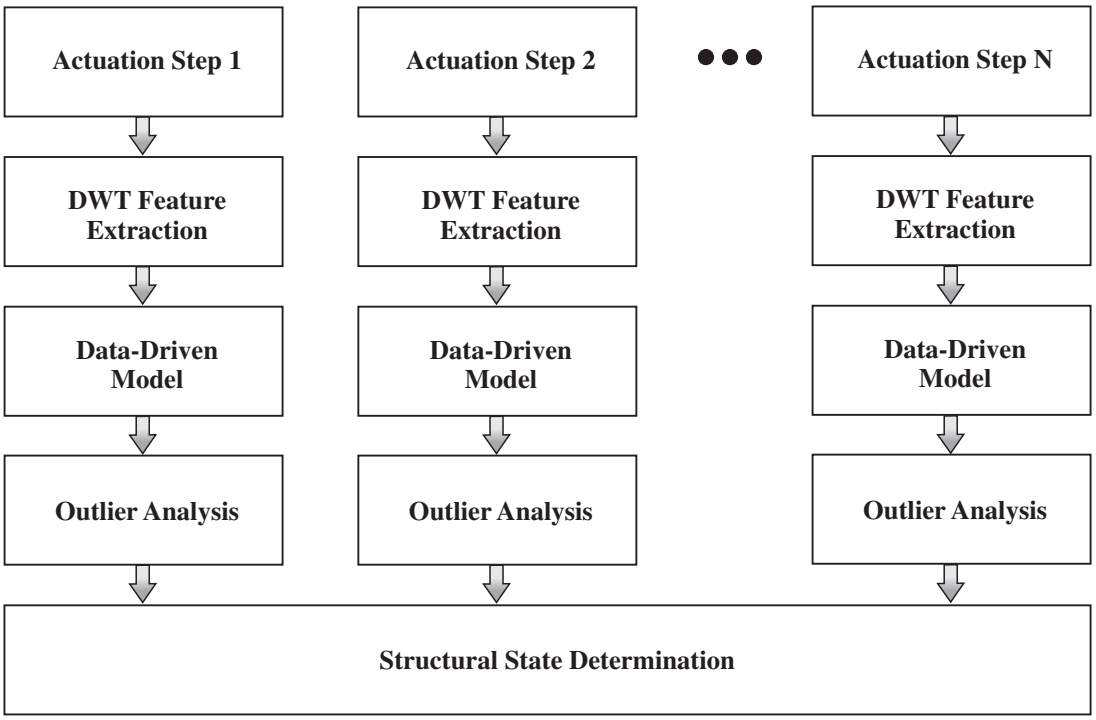

Figure 5.18. *Standard outlier analysis for damage detection.*

5.6.4. Combined Actuation Steps Data Fusion for Damage Detection

Once the data-driven models are generated either with PCA or h-NLPCA, and when new structural responses are available and feature extraction has been accomplished, the scores together with squared prediction error measures are calculated by projecting these data into the models for all actuation steps, and then they are presented as input feature vectors to a self-organizing map for the detection and classification tasks. The idea behind using the SPE measures in conjunction with the projections to the principal components, linear or not, is to provide a robust set of features for the improvement of future inferences regarding the structural condition. This analysis is accomplished by studying the U-Matrix surface so that the different formed clusters can be associated with different damage types and/or damage stages. Figure 5.19 depicts a flow diagram for the proposed methodology taking into consideration all actuation steps for the pattern recognition task. This methodology has been developed with collaboration of Prof. Jose Rodellar, Dr. Luis Mujica and Dr. Diego Tibaduiza from the Polytechnic University of Catalunya, Department of Applied Mathematics III during the research stay from the author in Barcelona and from Dr. Tibaduiza in Siegen.

For the methodology proposed here and the analysis of the U-Matrix surface, the separation of a new data set with respect to the data set from the healthy structure defines the presence of damage. Moreover, the approach can be used for damage identification when the different data sets clusters are identified by well-defined separation boundaries. An advantage of the proposed methodology is the ability to fuse all the information contained

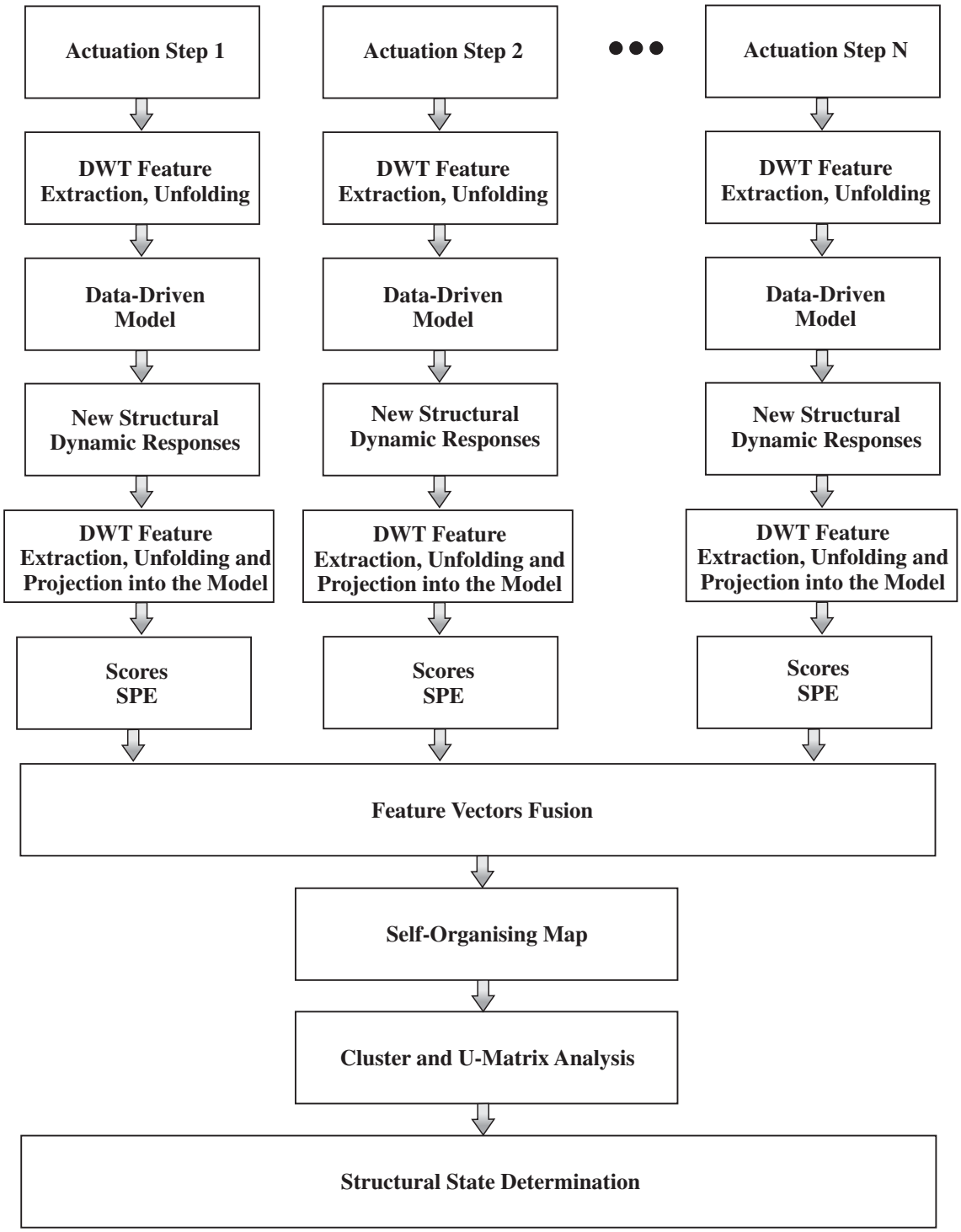

Figure 5.19. *Proposed methodology fusing all the actuation steps for pattern recognition and structural damage determination.*

in the different actuation steps for the analysis rather than just analysing each actuation step one by one as it is done in the traditional outlier analysis. Additionally, the multi-way extension of h-NLPCA can be seen as a very useful fusion strategy for systems involving several sensors since it allows building a model for the whole sensing system instead of one by each actuator-sensor combination.

6. Impact Load Monitoring

6.1. Introduction

The online monitoring of impacts can be considered as a very important structural health monitoring technique required in order to prevent the degradation and breakdown of structures after the incidence of any adverse impact event. In the case of aeronautical and aerospace structures, external impact damage is of great concern for the design of these structures. A very well known example of a catastrophe originated from impact-induced damage is the loss of the Space Shuttle Columbia as a result of impact damage from foam debris during ascent what led to the development of on-board impact detection technologies. In the case of composite laminates, impacts can induce different types of damage such as matrix cracking, fibre/matrix debonding, delamination, indentation and fibre fracture [Coverley and Staszewski 2003]. As a consequence, several studies on the identification of failure mechanisms of composite laminates related to impact loads and post-impact in-plane compressive loadings have been actively pursued [Yokozeki et al. 2010]. Impact monitoring has been extensively studied by several researchers and it has been shown that damage extent can be correlated with the impact magnitude. For this reason, online impact detection systems are essential and require automatic and intelligent techniques providing a probabilistic interpretation of their diagnostics.

For example, an inverse method based on a system-identification technique for identifying impact events on a complex structure with built-in sensors was proposed in [Park et al. 2009]. The method made use of transfer functions in the system-identification technique making possible the identification of the location and force time history of an impact event on a structure. A genetic algorithm (GA)-based approach for impact load identification which could identify the impact location and reconstruct the impact force history simultaneously was proposed in [Yan and Zhou 2009]. The impact load was represented by a set of parameters transforming the impact load identification problem to a parameter identification problem. Some other relevant investigations have made use of artificial neural networks based on the standard multilayered perceptron (MLP) architecture trained with the back-propagation learning rule and/or fuzzy clustering for feature selection and adaptive neuro fuzzy inference system (ANFIS) for impact locating and magnitude estimation

[Jones et al. 1997, Worden and Staszewski 2000, Shan and King 2003]. An alternative way of reaching similar results to the previous methods is to use a Gaussian process (GP). Very few applications of Gaussian processes exist in the structural health monitoring scientific literature: for example the use of single target Gaussian processes in complex structures for locating stress waves using thermoelastic expansion by means of a high power laser was proposed in [Hensman et al. 2008].

This chapter deals with the passive monitoring of stress waves induced by impacts and studies an automatic approach for impact magnitude estimation and localisation in structures based on Bayesian analysis with single target Gaussian processes [Torres Arredondo et al. 2011, Torres Arredondo and Fritzen 2012b]. A combination of time-frequency analysis for feature extraction, auto-associative neural networks for dimension reduction and Gaussian processes for system modelling is developed to automate the impact identification problem. The problem is treated as one of pattern recognition. The layout of this chapter is as follows. First, the different load scenarios and the monitoring approaches are presented. Second, the proposed algorithms for feature extraction and dimension reduction are discussed within the context of the proposed methodology for the purpose of constructing the feature vectors which are going to be presented to the machine learning algorithm. Third, an introduction to the ideas of Gaussian Processes in the context of regression and classification is presented for the purpose of impact magnitude estimation and localisation.

6.2. Load Types and Load Monitoring Approaches

The first step in order to be able to tackle the problem of load monitoring is to identify the different types of external loads to which the structure is subjected. They are divided into two categories [Klinkov 2011]:

1. Concentrated loads such as impact loads and time continuous loads (short or long time excitation).
2. Distributed loads (spatially distributed).

The impact loads are characterized by a short time duration and spatial concentration. The time continuous loads have a longer time duration and they can be classified into deterministic or stochastic. Distributed loads are more complex loads since they are spatially distributed and can exhibit different behaviours, i.e. impact-like or continuous type. For the current interest of this chapter, the first type of concentrated loads, i.e. impact loads, will be studied.

The approach for impact magnitude estimation can be distinguished as a inverse identification problem. This problem is normally divided into two approaches where one is either interested in calculating the system inputs given the system responses, boundary condi-

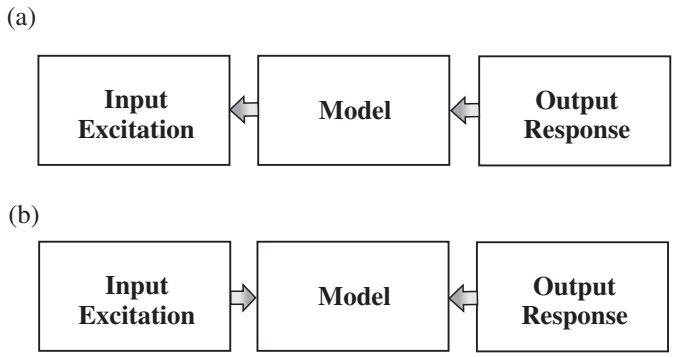

Figure 6.1. *Diagram for impact identification inverse problem: (a) System input estimation and (b) System model estimation.*

tions and the system model, or in finding the system model based on inputs, responses and boundary conditions. This type of problems are shown in Figure 6.1.

The impact force is ideally represented by a Dirac delta function as given in Eq.(6.1) by:

$$\delta(t) = \begin{cases} +\infty, & t = 0 \\ 0, & t \neq 0 \end{cases}, \tag{6.1}$$

where the function integral over the entire real line equals to one. However, since in reality one cannot have a load with infinite amplitude, it is more convenient to express the impact force $p(x,y,t)$ as a short time duration function acting at some location of the structure in a two-dimensional space as follows:

$$p(x_{imp}, y_{imp}, t) = F_0 \delta(x - x_{imp}(t)) \delta(y - y_{imp}(t)) \begin{cases} 1, & 0 < t < \varepsilon \\ 0, & elsewhere \end{cases}, \tag{6.2}$$

where F_0 is the impact force magnitude, $x_{imp}(t)$ and $y_{imp}(t)$ are the locations of the impact force, and ε is the time duration of the impact. A diagram of the impact force for a two-dimensional space and its function are presented in Figure 6.2.

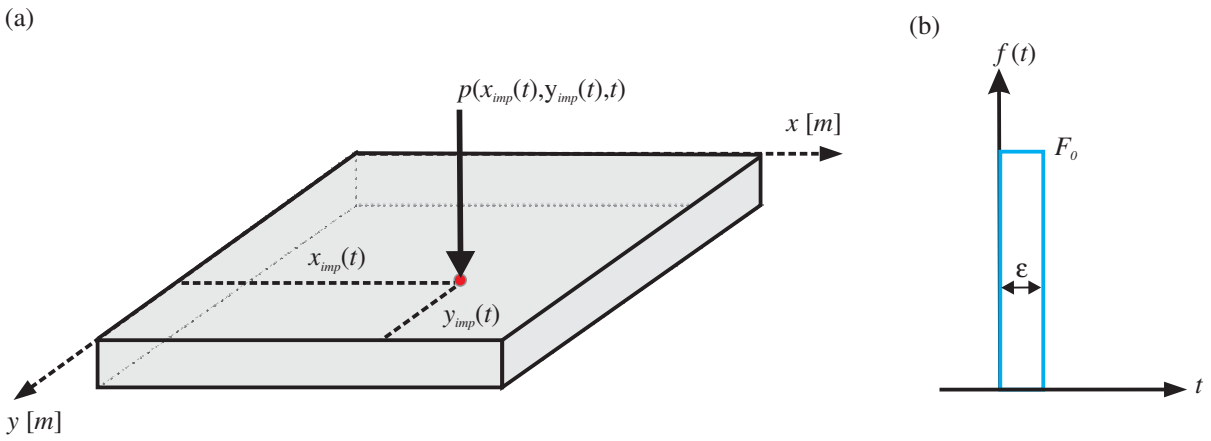

Figure 6.2. *Impact event: (a) Impact force on the surface of a plate and (b) Impact function.*

6.2.1. Structural-Based Model and Stochastic Model Techniques

Model-based techniques are developed from the understanding of the structural properties and dynamics of the system. Therefore, the accuracy of the estimated impact force highly depends on the accuracy of the dynamic model what makes the model development the most critical point in the inverse problem chain. The model identification is normally accomplished by the estimation of the model parameters requiring measurements of the inputs and outputs of the system [Uhl 2007]. Inside this type of modelling one can find methods based on frequency domain and time domain. For the time domain approach, the problem of load identification can be expressed as a special case of the Volterra integral equation as follows:

$$y(t) = \int_0^t H(t-\tau)\, p(\tau)\, \mathrm{d}\tau, \tag{6.3}$$

where $y(t)$ represents the system responses, $H(t)$ is the continuous impulse response kernel and $p(t)$ is the excitation force. In case of working in the frequency domain, one requires to know the frequency response function (FRF) $H(\omega)$ of the structure and the spectrum $Y(\omega)$ of the measured responses so that the force spectrum can be calculated and transformed back to the time domain by means of the inverse Fourier transformation. This can be expressed mathematically as:

$$p(t) = \mathscr{F}^{-1}\left(H^{-1}(\omega)\, Y(\omega)\right), \tag{6.4}$$

where $\mathscr{F}^{-1}(x)$ symbolizes the inverse Fourier transform of the function x. In addition, stochastic methods are based on finding statistical relations between the inputs and outputs of the system as well as their measurements. The most typical statistical model for load identification is the regression model [Trujillo and Busby 1997].

6.2.2. Machine Learning Techniques

In particular, for structures of high complexity with complicated geometrical profiles and material non-uniformity, it is a very difficult task to achieve a reliable inverse model. For this purpose, machine learning algorithms can be adopted. The idea of machine learning is to learn the relationships between some input vector of variables $\mathbf{x}$ with dimension D and an output variable y. The output can also correspond to a vector. Let us suppose that the true relationship is given by $y = f(\mathbf{x})$ but the function f is not known beforehand, so the learning problem is to estimate this function using the training data. Several methods can be used for this purpose such as artificial neural networks, kernel methods, sparse kernel methods, evolutionary algorithms, etc [Bishop 2007]. For the learning process, it is required to conduct measurements of the inputs and outputs of the system which is desired to be modelled. In order to construct an appropriate mapping between inputs and

outputs, it is necessary to establish a set of training data for which this association has already been made. As machine learning algorithms can require large training data sets, the collection of training data can be an expensive process. In the case of very high value structures, the expense of collecting the training data is compensated by the advantage of getting an advance warning alarm of possible damage as it was shown in [Hensman et al. 2008]. Furthermore, numerical simulations of the system behaviour can be carried out in order to help in the process of collecting training data [Yang et al. 2011].

6.3. Feature Vectors Construction

The construction of the features vectors used for the training of the selected machine learning algorithm plays a critical role in the accuracy of the inferences that the developed model will produce. These numerical features should be able to accurately represent the process one is willing to model. In this context, two different feature vectors will be used here for either the impact magnitude estimation and the impact localisation. For the feature vectors belonging to the impact magnitude model, as a first feature extraction step, the discrete wavelet transform (DWT) on the basis of the two-channel subband coding scheme is applied to the different recorded stress waveforms from the sensor network in order to extract coefficients from a level in which the signals could be properly reconstructed with the minimum loss of information [Mallat 1989]. The approximations coefficients are taken here since they represent the interesting dynamics of the recorded stress waveforms and the detail coefficients will be considered as high-frequency noise. As a following step, once the optimal decomposition has been executed and the approximation coefficients are calculated, these are further reduced by means of h-NLPCA in order to decompose the data in a PCA related way [Scholz et al. 2008]. Nevertheless, before training the neural network, the coefficients gathered from each impact experiment are fused following traditional unfolding procedures by unfolding the three-dimensional array in the experiment direction as it is depicted in Figure 6.3. This process is similar to the one depicted in the previous chapters.

As it has been done similarly in the previous chapters, standard scaling procedures are performed with the unfolded matrix where group scaling is selected. Standard PCA is used in order to define the number of non-linear principal components used in the h-NLPCA algorithm. Principal components contributing less than a certain percentage of the total variance of the data set are discarded for the task proposed here. Additional to the extracted components, the feature vectors also include the area under the curve of the power spectral density (PSD) from each sensor belonging to the sensor network. Since the input force spectrum exerted in the structure is a combination of the stiffness of the hammer tip and the stiffness of the structure, one would expect to build a more robust feature vector by incorporating this information from each sensor. An example of typical

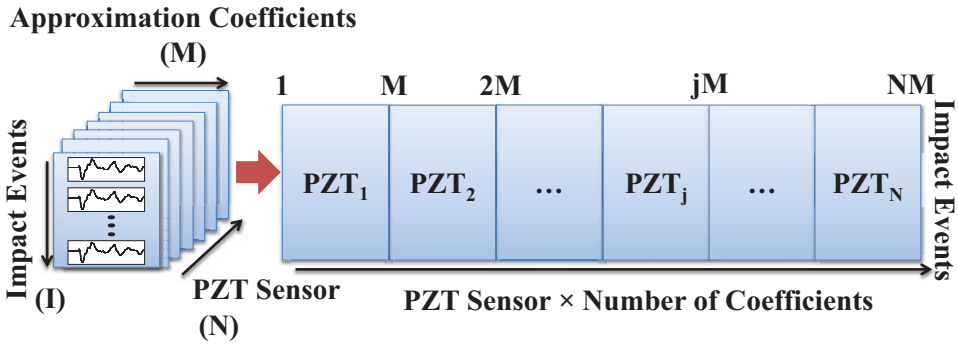

Figure 6.3. *Matrix unfolding procedure for the sensor-data fusion and dimension reduction preprocessing.*

signals recorded during an impact event is presented in Figure 6.4.

For the impact localisation model, the inputs of the feature vectors are defined to be the differences in time of flight between the sensors and the frequency content of the first arrival in every sensor of the network. The first quantities can be calculated by using any of the algorithms proposed in section 4.3. The second quantities are calculated by means of the atomic decomposition of the recorded stress waves as it is presented in section 4.6.1 and further frequency analysis of the extracted atoms for each sensor of the network.

6.4. System Modelling with Gaussian Processes

For the case of impact monitoring, the detection of possible damages generated by an impact event requires time consuming non-destructive testing during which the structure has to be out of service. If one would know if an impact event occurred and its approximate position, then ground inspections could be performed more efficiently. Moreover, in the case of composite materials for example, it has been shown that the delamination area is related to the maximum impact force and impact energy for low-velocity impacts [Zhou 1998]. Having said this, the focus of this section is on a machine learning algorithm where the function of stochastic processing and its application to define a distribution over functions is presented for the purpose of impact magnitude estimation and localisation. The idea is to model the given impact phenomenon from features extracted from observations of the stress waves generated by the impact events.

One modelling approach based on a Bayesian treatment of the problem in order to find the underlying data generative mechanism is Gaussian process (GP) modelling. A Gaussian process model is equivalent to a Bayesian treatment of a certain class of multilayered perceptron networks in the limit of infinitely large networks as it is presented in [Neal 1995]. A Gaussian process is defined as a collection of random variables, any finite number of which have a joint Gaussian distribution [Rasmussen 1996]. It can be defined as a distribution over functions where inference takes place directly in the space of functions

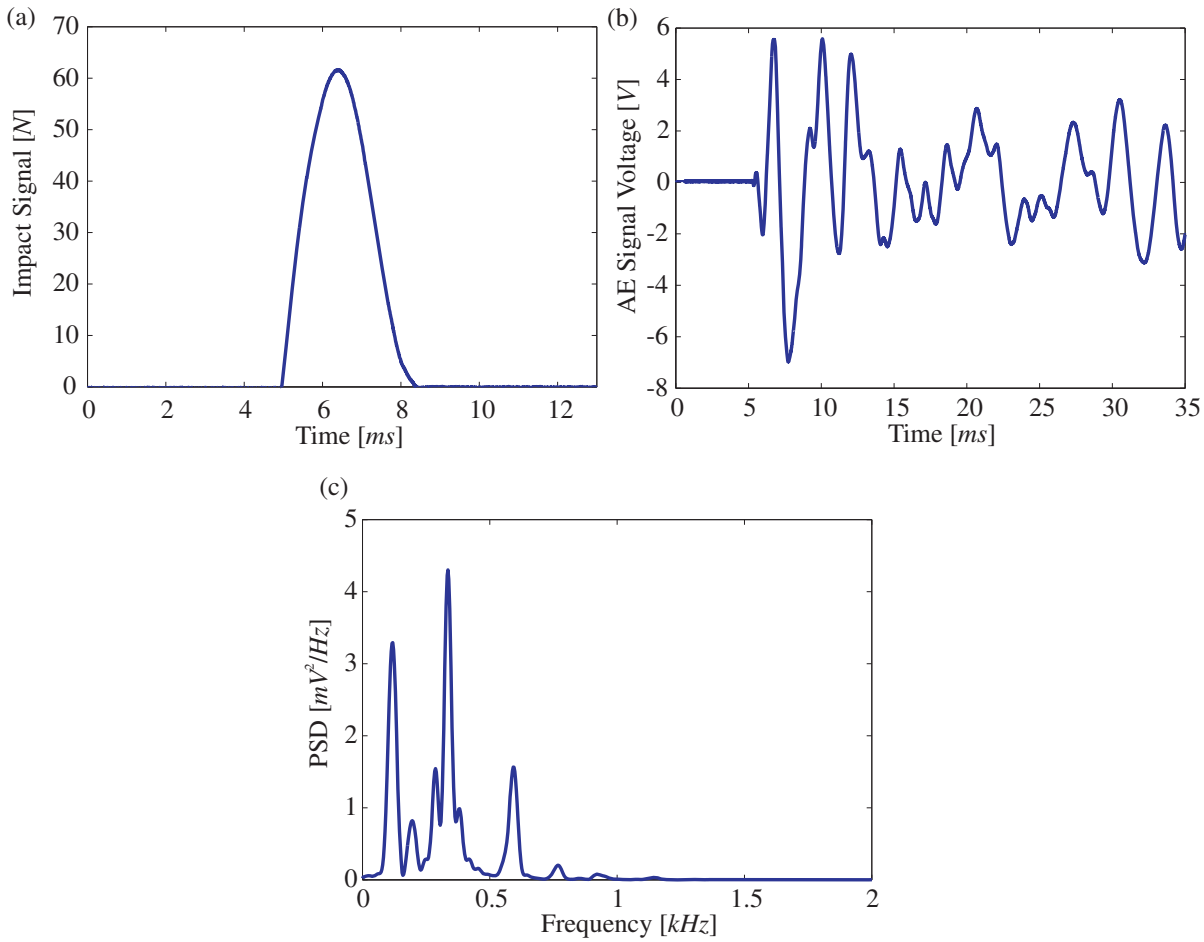

Figure 6.4. *Typical signals from an impact event: (a) Impact signal collected by an impact hammer, (b) Stress wave captured by a PZT transducer and (c) Power spectral density of the recorded stress wave.*

[Rasmussen 2004]. It is completely specified by its mean function and covariance function. This can be seen as a generalization of the Gaussian distribution whose mean and covariance is a vector and matrix, respectively. The Gaussian distribution is defined over vectors, whereas the Gaussian process is defined over functions [Alvarez and Lawrence 2009]. Assuming a Gaussian process model, and given the observed data and a new input, making a prediction corresponds to calculating the Gaussian predictive distribution of the related output whose mean value can be used as an estimate. In this manner, the predictive variance provides a confidence interval on this estimate allowing to quantify the degree of belief of the model in its prediction.

6.4.1. Regression with Gaussian Processes

Gaussian process regression provides several attractive properties such as ease of obtaining and expressing uncertainty in predictions, the ability to capture a wide variety of behaviour through a simple parametrisation, and a natural Bayesian interpretation [Boyle and Frean 2004]. For this reason, Gaussian processes have been suggested as a replacement for

supervised neural networks in the context of non-linear regression and as an extension to handle classification tasks [MacKay 1997, Gibbs and Mackay 2000]. The probabilistic nature of the GP modelling permits to define the space of admissible functions relating inputs and outputs by simply specifying the mean and covariance functions of the process. Given a data set $\mathbf{D}$ of D-dimensional training input vectors $\mathbf{x}_i$ with corresponding training vector $\mathbf{t}$ composed of training targets t_i related by $t_i = f(\mathbf{x}_i) + \varepsilon$ for $i = 1, ..., N$, where $f(\bullet)$ is a non-linear smooth mapping function and ε is additive Gaussian noise, one should be interested in making predictions of the noise-free output targets $f(\mathbf{x}_{N+1})$ for a new input vector $\mathbf{x}_{N+1}$. The non-linear mapping function $f(\bullet)$ is modelled by a Gaussian process with zero mean and covariance matrix $\mathbf{K}$ so that:

$$p(\mathbf{f} \mid \mathbf{D}) \sim N(0, \mathbf{K}), \tag{6.5}$$

where $\mathbf{K}$ is computed from the covariance function $K_{ij} = k(x_i, \mathrm{x}_j)$. From a modelling point of view, it is desired to define covariances so that points with nearby inputs will give rise to similar predictions. For this purpose, the covariance selected in this case is squared exponential with automatic relevance determination (ARD) distance measure defined by [Rasmussen and Williams 2006]:

$$k(\mathbf{x}_i, \mathbf{x}_j) = \sigma_f^2 \exp\left(-\frac{1}{2}(\mathbf{x}_i - \mathbf{x}_j)^{\mathrm{T}} \mathrm{M} (\mathbf{x}_i - \mathbf{x}_j)\right), \tag{6.6}$$

with $\mathbf{M} = diag(\lambda_1, ..., \lambda_{\mathrm{D}})^{-2}$ and where each λ is a characteristic correlation length scale for each input dimension, and σ_f^2 is the signal variance. These variables which control the distribution of model parameters are normally called hyperparameters. With this approach a separate parameter is incorporated for each input variable. As a result, the optimization of these parameters, for example by means of maximum likelihood, allows to infer the relative importance of different inputs from the data and makes possible to detect input variables that have little effect on the predictive distribution. As it can be seen from Eq.(6.5) and Eq.(6.6), the covariances between two outputs are expressed by the covariance function evaluated at the corresponding inputs. For given values of $\mathbf{x}_i$ and $\mathbf{x}_j$, the matrix of covariances between the corresponding outputs, $f(\mathbf{x}_i)$ and $f(\mathbf{x}_j)$ can be calculated. The impact of the parameters controlling the covariance matrix that affects the process realisations is presented in Figure 6.5 using the covariance function presented in Eq. (6.6) for $\mathbf{x}_i$ and $\mathbf{x}_j$ in the range $[1, 10]$. As it can seen from Figure 6.5, as the distance between inputs increases, the covariances between the points for Figure 6.5(a) decreases less rapidly than that of Figure 6.5(b) because of the higher value of λ. It can be also inferred that the magnitudes of the diagonal terms for both figures are controlled by σ_f^2 .

In order to analyse the influence of these two parameters on the possible process realisations, two different Gaussian processes are built as examples. The first process is built

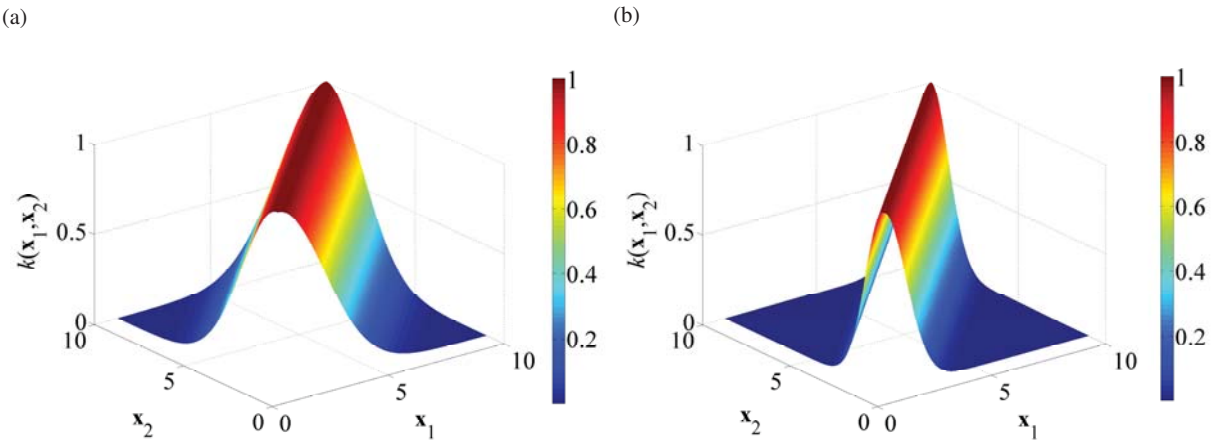

Figure 6.5. *Covariance Matrix for different parameters: (a)* $\sigma_f^2 = 1$ *and* $\lambda = 2$ *and (b)* $\sigma_f^2 = 1$ *and* $\lambda = 1$.

with a correlation length $\lambda = 2$, while the second process is built with a correlation length of $\lambda = 1$. Figure 6.6 depicts the realizations drawn from both models. It can be seen that all the realisations are smooth what is an implicit characteristic of the selected covariance function. The samples from the second Gaussian process vary much more rapidly in the horizontal direction than those of first process. It can be seen how the correlation length λ controls the horizontal variations of the realisations. A small value of λ implies rapid horizontal variations. The signal variance σ_f^2 simply controls the amplitude of the fluctuations around zero.

Additionally, one can analyse the influence of the distance between the inputs on the prediction results. This is illustrated in Figure 6.7 for a simple two-dimensional example.

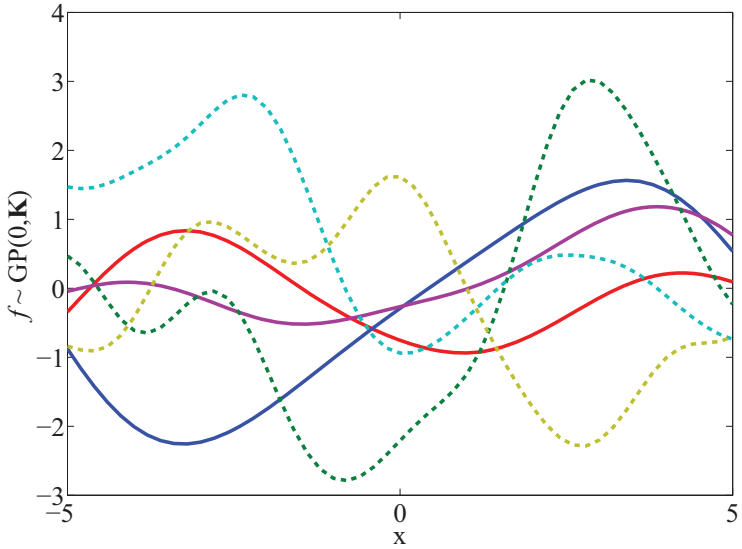

Figure 6.6. *Functions values drawn at random from two different Gaussian processes: Solid lines are sampled from a GP with a correlation length* $\lambda = 2$ *while dashed lines are sampled from a GP with a correlation length of* $\lambda = 1$. *The signal variance* σ_f^2 *is equal to one for both models.*

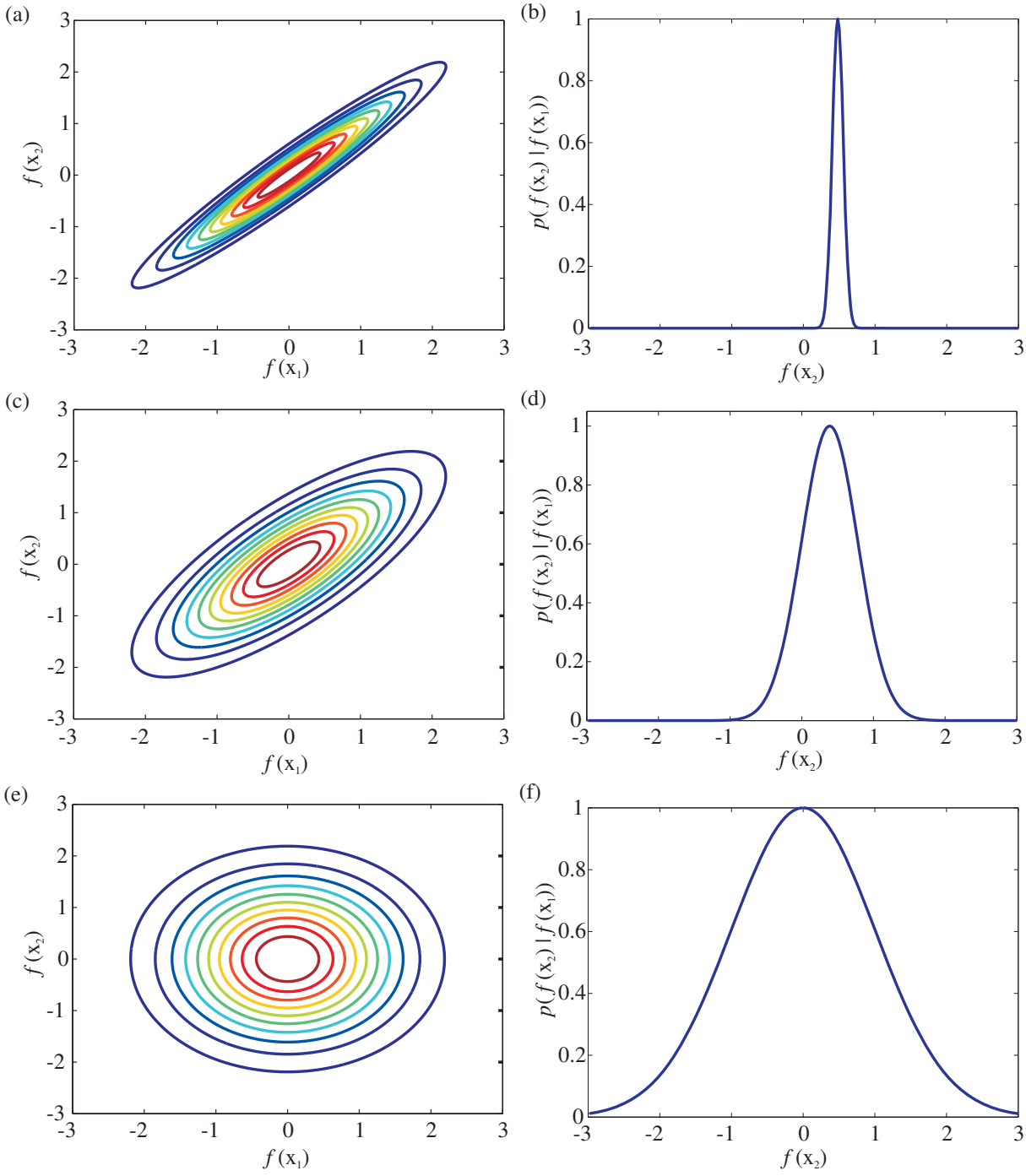

Figure 6.7. *Illustration of jointly distributed variables for differing covariance values given by the distance between the inputs. For the first column* $x_1 = 0.8$ *and* $x_2 = 0.6$*. For the second column* $x_1 = 1.1$ *and* $x_2 = 0.6$*. For the third column* $x_1 = 100$ *and* $x_2 = 0.6$*. All other parameters are defined to be equal to one.*

The column on the left of Figure 6.7 depicts the probability distribution across $f(x_1)$ and $f(x_2)$ for three cases. The first case is when the variables x_1 and x_2 are approximately the same, the second when x_1 and x_2 are closer together, i.e. $k(x_1, x_2) \approx 0.5$, and the third when they are far apart, i.e. $k(x_1, x_2) \approx 0$. The target value for training is set arbitrarily to $f(x_1) = 0.5$. It can be clearly noticed how the uncertainty and the performance on the predictions of the model are deteriorated as the distance between the inputs is increased.

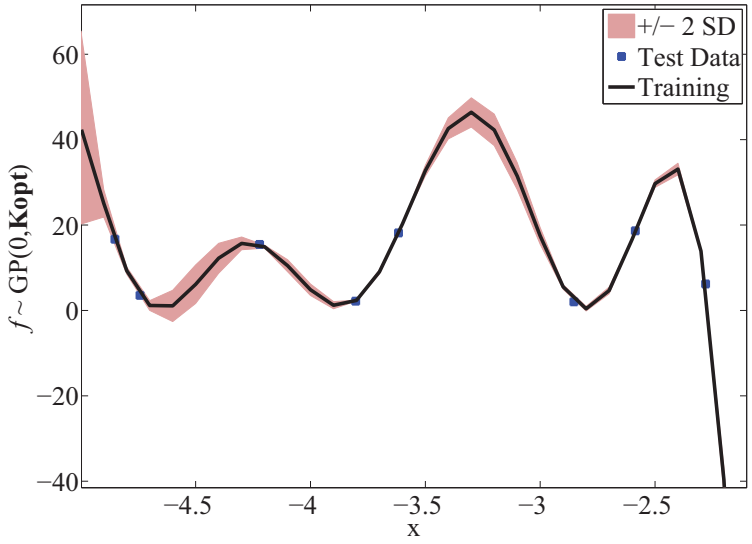

Figure 6.8. *Prior conditioned on noisy observations.*

This posses clearly the necessity, as with any machine learning algorithm, to count with sufficient data to support the formulation of more accurate mapping functions.

With the GP model at hand, the learning task corresponds to tuning the parameters of the covariance function of the process to the data. This can be simply accomplished with a maximum likelihood approach. The unknown hyperparameters Θ in the covariance functions are calculated by maximizing the negative logarithmic marginal likelihood. Because the negative logarithm is a monotonically decreasing function, maximizing the likelihood is equivalent to minimizing the error. This approach is executed by maximization of the following function:

$$\mathscr{L}(\Theta) = -\log(p(\mathbf{t} \mid \mathbf{x})) = \frac{1}{2}\log \mid \mathbf{K} \mid + \frac{1}{2}\mathbf{t}^{\mathrm{T}}\mathbf{K}^{-1}\mathbf{t} + \frac{N}{2}\log(2\pi), \tag{6.7}$$

where $\mid \mathbf{K} \mid$refers to the determinant of $\mathbf{K}$. Given $\mathscr{L}(\Theta)$ and its derivatives with respect to Θ, it is straightforward to feed this information into an optimization package in order to obtain a local maximum of the likelihood. The partial derivatives of the logarithmic likelihood can be expressed analytically in terms of the parameters as given in Eq.(6.8) [Williams and Barber 1998, Girard 2004]:

$$\frac{\partial \mathscr{L}(\Theta)}{\partial \Theta_j} = \frac{1}{2}\mathrm{Tr}\left(\mathbf{K}^{-1}\frac{\partial \mathbf{K}}{\partial \Theta_j}\right) - \frac{1}{2}\mathbf{t}^{\mathrm{T}}\mathbf{K}^{-1}\frac{\partial \mathbf{K}}{\partial \Theta_j}\mathbf{K}^{-1}\mathbf{t}, \tag{6.8}$$

where $\mathbf{Tr}(\bullet)$ denotes the trace of a matrix. The effect of finding the optimal hyperparameters for future realizations of the model based on the training data is depicted in Figure 6.8. This figure shows clearly that the model can follow very well the training data with low values of uncertainty in the zones where no training points are available. The shaded area corresponds to ± 2 standard deviations.

With this model, given a new input, and conditioning on past observations, one can obtain a prediction and the uncertainty attached to it which is given by the mean and variance of the predictive distribution of the future output. This distribution is Gaussian, readily obtained using the definition of conditional probabilities, as a consequence of the Gaussian process assumption.

In the Gaussian Process framework, one can define a joint distribution over the observed training targets at the test location as:

$$p(\mathbf{t}_{N+1}) \sim N\left(0, \begin{bmatrix} \mathbf{K}+\sigma_n^2\mathbf{I} & \mathbf{k} \\ \mathbf{k}^{\mathrm{T}} & k+\sigma_n^2 \end{bmatrix}\right) = N\left(0, \begin{bmatrix} \mathbf{C}_N & \mathbf{k} \\ \mathbf{k}^{\mathrm{T}} & c \end{bmatrix}\right), \tag{6.9}$$

where $\mathbf{t}_{N+1}$ denotes the vector $[t_1,...,t_N,t_{N+1}]^{\mathrm{T}}$, σ_n^2 is the noise variance, $\mathbf{K}$ is a $N \times N$ matrix containing the covariances between pairs of training targets, $\mathbf{k}$ is a $N \times 1$ vector giving the covariances between the test target and the training targets, k is the variance of the training target, and $\mathbf{I}$ the identity matrix. The predictive posterior distribution is obtained by conditioning the previous joint distribution on the observed data $\mathbf{D}$ and the new inputs, i.e. $p(f_{N+1} \mid \mathbf{t}, \mathbf{x}_1, \mathbf{x}_2, ..., \mathbf{x}_{N+1})$.

The Gaussian process formulae for the mean and variance of the predictive distribution with the covariance function in Eq.(6.6) for a new input vector $\mathbf{x}_{N+1}$ is given by [Bishop 2007]:

$$\begin{aligned} \mu(\mathbf{x}_{N+1}) &= \mathbf{k}^{\mathrm{T}}\mathbf{C}_N^{-1}\mathbf{t}, \\ \sigma^2(\mathbf{x}_{N+1}) &= k - \mathbf{k}^{\mathrm{T}}\mathbf{C}_N^{-1}\mathbf{k}. \end{aligned} \tag{6.10}$$

For multiple outputs Gaussian processes a convolution process (CP) can be employed in order to account for non-trivial correlations [Bonilla et al. 2008, Alvarez and Lawrence 2009]. Since the data are used directly for making predictions, the uncertainty of the model predictions depends on the local data density, and the model complexity relates to the amount and the distribution of available data [Williams et al. 1995, Qazaz et al. 1996, Girard 2004].

6.4.2. Classification with Gaussian Processes

Gaussian processes can be adapted to classification problems by transforming the output of the Gaussian process using an appropriate non-linear activation function so that the probabilities lie in the interval $[0,1]$. In the case of a binary classifier, i.e. a two-class problem with a target variable $\pi \in [0,1]$, one can define a Gaussian process over the function $t(\mathbf{x})$ and then transform the function using a logistic sigmoid $\pi(\mathbf{x}) = p(t = 1 \mid \mathbf{x}) = \sigma(f(\mathbf{x}))$, the probability of input $\mathbf{x}$ belonging to class one [Gibbs 1997]. This construction

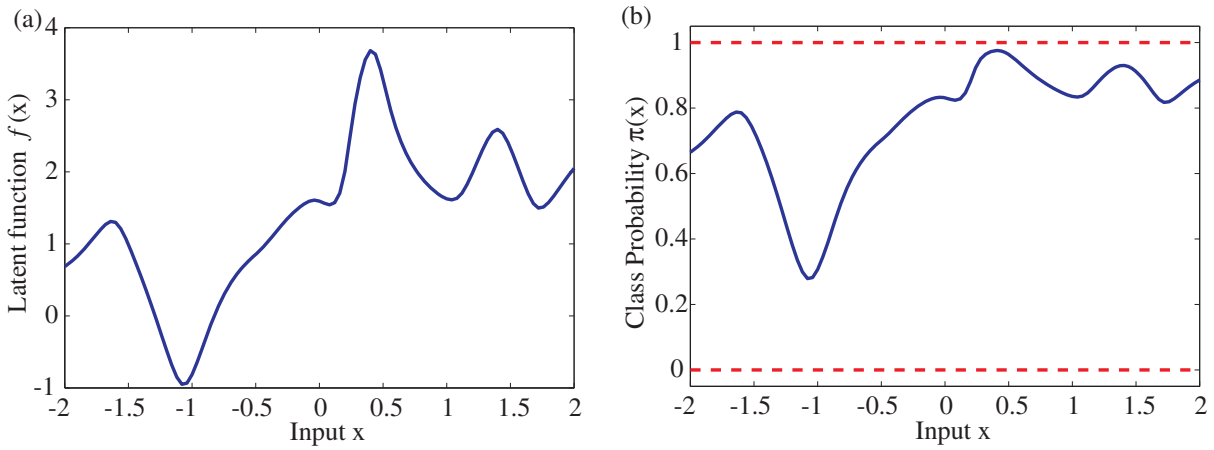

Figure 6.9. *Illustration for a binary classification: (a) A sample latent function* $f(\mathrm{x})$ *drawn from a Gaussian process as a function of* x *and (b) Result of passing this sample function through the logistic sigmoid function.*

is illustrated in Figure 6.9 for a one-dimensional input space. The logistic sigmoid function is defined by:

$$\sigma(f) = \frac{1}{1+\exp(-f)}. \tag{6.11}$$

Please keep in mind that the covariance matrix no longer includes a noise term since it is assumed that all of the training data points are correctly labelled. The objective is again to determine the predictive distribution $p(t_{N+1} \mid \mathbf{t}, \mathbf{x}_1, \mathbf{x}_2, ..., \mathbf{x}_{N+1})$. The predictive distribution is given by [Rasmussen and Williams 2006]:

$$p(t_{N+1} = 1 \mid \mathbf{t}, \mathbf{x}_1, ..., \mathbf{x}_{N+1}) = \int \sigma(f_{N+1})\, p(f_{N+1} \mid \mathbf{t}, \mathbf{x}_1, ..., \mathbf{x}_{N+1})\, \mathrm{d}f_{N+1}. \tag{6.12}$$

However, the integral described in Eq.(6.12) is analytically intractable, and it may be approximated using analytic approximations of integrals or sampling methods [Neal 1995, Gibbs and Mackay 2000]. The value of $p(t_{N+1} = 0 \mid \mathbf{t}, \mathbf{x}_1, ..., \mathbf{x}_{N+1})$ can be found from $1 - p(t_{N+1} = 1 \mid \mathbf{t}, \mathbf{x}_1, ..., \mathbf{x}_{N+1})$. The integration over the parameters Θ, required in order to find the hyperparameters, cannot be done analytically and requires as well of integral approximations or sampling methods.

The extension of the preceding developments to multiple classes is straightforward and the problem can be tackled using a 1 of M class coding scheme together with the softmax function to describe the class probabilities. The probability that an instance labelled by i is in class c is denoted by π_i^c , so that the upper index denotes the example number, and the lower index the class label [Williams and Barber 1998, Rasmussen and Williams 2006]. The functions are represented by f_i^c and specified using a 1 of M coding. The vector of function values at all N training points and for all c classes is given by:

$$\mathbf{f} = \left[f_1^1, ..., f_N^1, f_1^2, ..., f_N^2, ..., f_1^c, ..., f_N^c\right]^{\mathrm{T}}. \tag{6.13}$$

The activations associated with the probabilities are denoted by t_i^c, where the vector $\mathbf{t}$ has the same length as $\mathbf{f}$ which for each $i = 1,...,N$ has an entry of 1 for the class which is the label and 0 for all the other $c-1$ entries.. The softmax function relating the functions and probabilities at a training point i is given in Eq.(6.14) by [Rasmussen and Williams 2006]:

$$p\left(t_i^c \mid \mathbf{f}_i\right) = \pi_c^i = \frac{\exp\left(f_i^c\right)}{\sum_{c'} \exp\left(f_i^{c'}\right)}. \tag{6.14}$$

Additionally, an augmented vector notation is introduced as follows:

$$\mathbf{f}_+ = \left[f_1^1,...,f_N^1,f_{N+1}^1,f_1^2,...,f_N^2,f_{N+1}^2,...,f_1^c,...,f_N^c,f_{N+1}^c\right]^{\mathrm{T}}, \tag{6.15}$$

where, as in the two-class case, f_{N+1}^c denotes the activation corresponding to input $\mathbf{x}_{N+1}$ for class c; this notation is also used to define $\mathbf{t}_+$ and $\boldsymbol{\pi}_+$. As with the two-class case, approximate or sampling methods are required to find $p(\mathbf{f}_+|\mathbf{t})$.

7. Experimental, Numerical and Application Examples

7.1. Introduction

This chapter presents a variety of numerical and experimental examples where the performance of the model and methodologies developed from Chapter 3 to Chapter 6 are evaluated in both isotropic and anisotropic structures. The first part of this chapter presents the experimental validation of the approximate model developed for wave propagation. Numerical and experimental results on the effects of material layup on wave propagation, Lamb wave energy focusing and attenuation, and their importance for the proper development of on-line SHM systems are presented and discussed. Additionally, experimental results on the effects of variable temperature on the wave propagation in composite materials are shown. The second part demonstrates the proposed methodologies for modal acoustic emission analysis based on artificial neural networks, energy distribution analysis and pattern recognition by means of advanced signal processing techniques. The focus on classification of AE events is based on the attributes of the wave packets constituting the captured waveforms so that the present modes can be possibly correlated with different type of damage mechanisms. Additionally, physical knowledge gained from the dispersion characteristics obtained by the use of proposed higher order plate theory is used in order to support the statements made regarding the identification of the present dominant failure modes.

The third part deals with the proposed structural health monitoring methodology presented in Chapter 5 where a damage detection and classification scheme based on an acousto-ultrasonics approach is used and evaluated. This methodology is experimentally evaluated and validated in a range of different complex structures. Moreover, a critical comparison with linear feature extraction methods indicates that the proposed method outperforms in some cases the traditional linear methods for the purpose of damage classification. Finally, the fourth and last section presents a methodology for impact magnitude estimation and localisation based on a Bayesian framework within the context of Gaussian Processes. This is of great importance since online impact detection systems are essential and require

Table 7.1. *Material properties of unidirectional glass fibre reinforced lamina (units in GPa).*

E_{11}	E_{22}	E_{33}	G_{12}	G_{13}	G_{23}	$\nu_{12} = \nu_{13} = \nu_{23}$
30.7	15.2	10	4.0	3.1	2.75	0.3

automatic and intelligent techniques providing a probabilistic interpretation of their diagnostics. At the end, the effectiveness of all the proposed methodologies is demonstrated experimentally and discussed in detail.

7.2. Theoretical Model Validation, Dispersive Characteristics and Further Applications

This section evaluates the higher order plate theory developed in Chapter 3 which is applicable for modelling dispersive solutions in elastic and viscoelastic fibre-reinforced composites so that the investigation of both the frequency and angular dependency of radiation and attenuation of Lamb waves in anisotropic media can be accomplished. Comparisons to exact elasticity theory and experimental data are presented in order to validate the model. Additionally to the analyses of temperature effects on guided waves, an application example for manufacturing control of composite laminates is presented.

7.2.1. Comparison to Elasticity Theory and Experimental Validation

In order to validate the modelling approach, two case studies have been conducted on a unidirectional glass-fibre reinforced plastic (GFRP) plate and a multilayered and multi-oriented carbon fibre reinforced plastic (CFRP) plate. First, a single-layered specimen was selected because of its highly anisotropic character. Figure 7.1(a) shows the structure that has the dimensions $800mm \times 800mm$ and a thickness of approximately $1.5mm$. The density is $1700kg/m^3$. The fibre direction is along the y-axis. Nine piezoelectric transducers are attached to the surface of the structure with equidistant spacing. The piezopatches have a diameter of $10mm$ and a thickness of $0.25mm$. The elastic properties in the principal directions of material symmetry provided by the manufacturer are given in Table 7.1.

In Figures 7.1(b) and (c) the velocities of the different modes of propagation are plotted over the frequency for the $1.5mm$ thick glass fibre reinforced plastic (GFRP) plate for an angle of propagation of $\theta = 30°$. Curves depicted in continuous lines are calculated using exact three dimensional theory and dashed lines using the proposed third order plate theory. It can be clearly seen from these figures that all Lamb waves have cut-off frequencies with the exception of the fundamental modes. For a frequency up to $800kHz$, what corresponds to a frequency-thickness product of $1.2MHz \times mm$, the error in comparison to group velocity of S_0 mode is below 3%. Just as well is the conformity of the out-of-plane mode A_0. Additionally, it can be observed how the S_0 and SH_0 modes

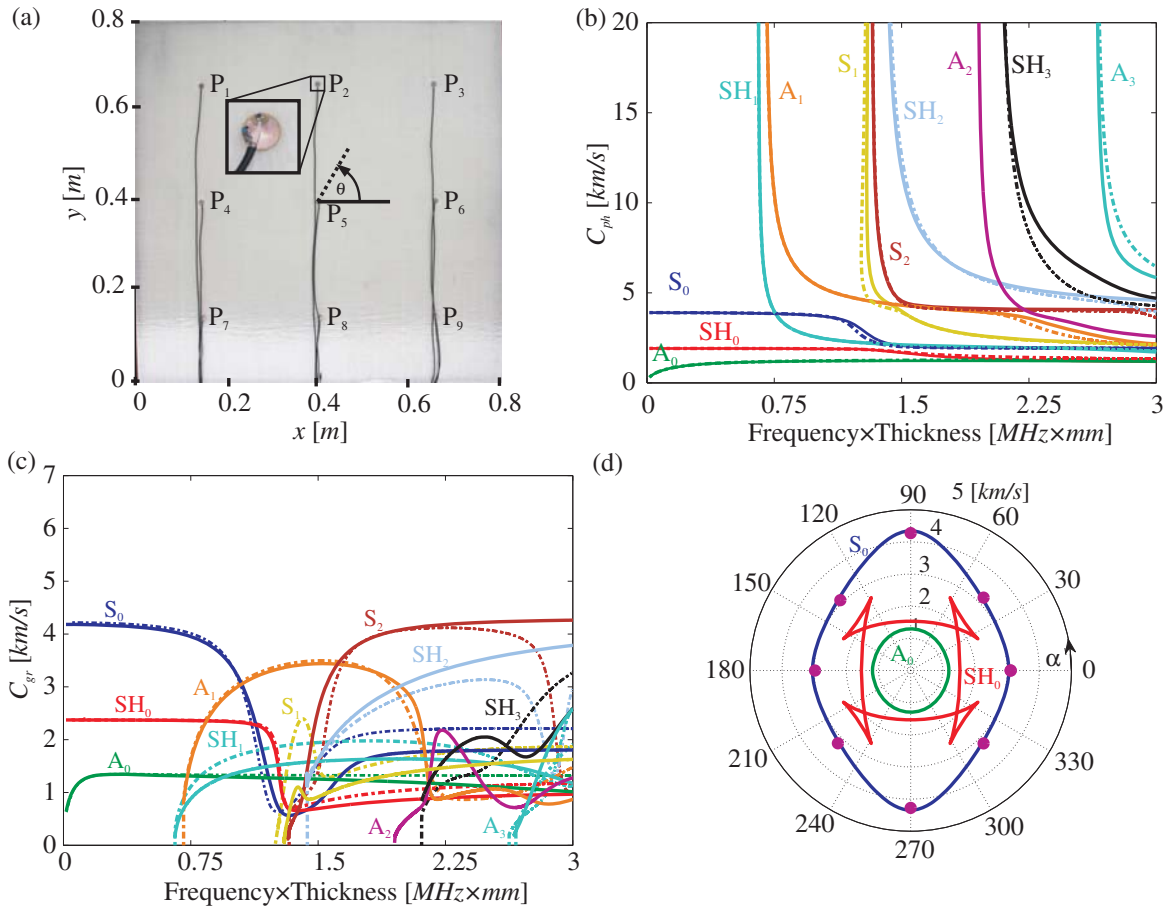

Figure 7.1. *Numerical and experimental validation for a unidirectional glass-fibre reinforced lamina: (a) Experimental setup, (b) Phase velocity dispersion curves, (c) Group velocity dispersion curves and (d) Wave curves plot.*

are little dispersive in the low frequency-thickness range. This is not the case for the A_0 mode.

For the experiments, the input signal to the actuators was generated using the arbitrary signal generation capability of a HandyScope HS3; it is a combined signal generator and oscilloscope instrument manufactured by TiePie Engineering, The Netherlands. The receiver sensors are connected to the input channels of two auxiliary HS4-HandyScopes without a pre-amplifier. The time histories were digitised at a sampling frequency of $50MHz$ and transferred to a portable PC for post-processing. To ensure a good signal to noise ratio each signal was averaged 10 times. Numerical results for the group velocities for the fundamental modes of propagation at a central frequency of $200kHz$ are depicted in Figure 7.1(d). The wave surface for the S_0 mode at $200kHz$ is shown in comparison with some experimental measured values at discrete angular points drawn in magenta circles in order to validate the analytical model with experimental data. The excitation voltage signal is a $12V$ Hanning windowed cosine train signal with 5 cycles. The piezoelectric transducer number five was designated as the actuator. The experimental group velocities were determined in the defined frequency by means of time-delay measurements. It can be seen that the estimated group velocity matches the theoretical curve very well,

Table 7.2. *Material properties of a single carbon fibre reinforced lamina (units in GPa).*

E_{11}	E_{22}	E_{33}	G_{12}	G_{13}	G_{23}	$\nu_{12} = \nu_{13} = \nu_{23}$
155.0	8.5	8.5	4.0	4.0	4.0	0.33

demonstrating the effectiveness of the model.

Second, a carbon fibre reinforced plastic (CFRP) plate made of 16 equal layers is analysed in this section. The stacking sequence is $[0°\,90°\,-45°\,45°\,0°\,90°\,-45°\,45°]_s$ and the total thickness is $4.2mm$. The density of each layer is approximately $1600kg/m^3$. The nominal material parameters of the unidirectional layers provided by the manufacturer are given in Table 7.2. Figure 7.2(a) shows the plate of approximately $500mm \times 500mm$ instrumented with nine piezoelectric transducers. The calculated phase and group velocities at $\theta = 30°$ are depicted in Figures 7.2(b) and (c). It can be noticed that the behaviour of the SH_0 and S_0 modes is different from the A_0 mode in both the low and high frequency zones. In the relatively low frequency range the higher the frequency of the A_0 mode, the faster its group velocity. In an opposite manner for the S_0 mode, the higher its frequency, the slower its group velocity.

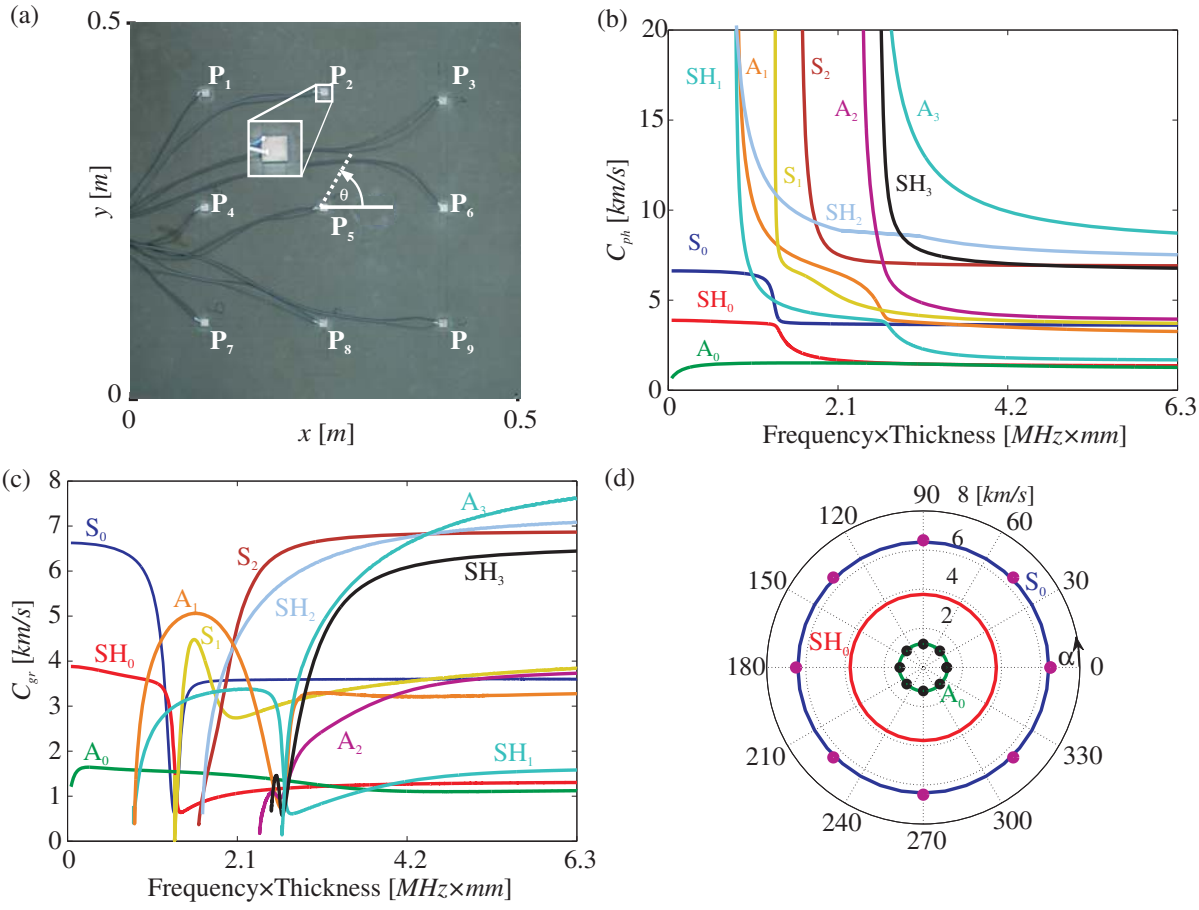

Figure 7.2. *Numerical and experimental validation for a multilayered carbon-fibre reinforced laminate: (a) Experimental setup, (b) Phase velocity dispersion curves, (c) Group velocity dispersion curves and (d) Wave curves plot.*

Table 7.3. *Elastic and viscoelastic properties of the viscoelastic carbon-epoxy lamina (units in GPa).*

C_{11}	C_{22}	C_{33}	C_{12}	C_{13}	C_{23}	C_{44}	C_{55}	C_{66}
132	5.9	12.1	6.9	12.3	5.5	3.32	6.21	6.15
η_{11}	η_{22}	η_{33}	η_{12}	η_{13}	η_{23}	η_{44}	η_{55}	η_{66}
0.4	0.001	0.043	0.001	0.016	0.021	0.009	0.015	0.02

For the experimental evaluation, the excitation voltage signal is a $12V$ Hanning windowed cosine train signal with 3 cycles and a $60kHz$ centre frequency. The piezoelectric transducer number five was designated as the actuator. The calculated group velocities at a frequency of $60kHz$ are depicted in Figure 7.2(d) together with experimental data; magenta circles represent the S_0 mode and black circles the A_0 mode. It is shown again that the proposed method provides accurate estimates of velocity. Moreover, it can be also inferred that the mode wave velocities are not strongly related to the frequency and orientation of propagation. This is given by the fact that the multilayered and multi-oriented composition of the structure mitigates the anisotropic impact of each layer.

7.2.2. Numerical Examples for Attenuation Models Comparison

A viscoelastic orthotropic unidirectional lamina of $1mm$ of thickness is analysed in this subsection. This example was fully studied in references [Deschamps and Hosten 1992, Neau 2003, Bartoli et al. 2006]. The elastic and viscoelastic material properties are given in Table 7.3. The density of each layer is approximately $1500kg/m^3$. The material was characterized at $2.242MHz$ by the use of ultrasonic waves transmitted through a plate-shaped sample immersed in water.

Figure 7.3 presents the results for Lamb wave velocities and attenuation obtained for both the Hysteretic and the Kelvin-Voigt viscoelastic models for the purpose of comparing the two solutions. The phase velocities were calculated at $\theta = 0^\circ$. It can be clearly seen from Figures 7.3(a) and (b) that both models do not affect the phase velocity results in a substantial manner. Here again, it can be observed that the S_0 and SH_0 modes are little dispersive in the low frequency-thickness range while the A_0 mode is very dispersive. Figures 7.3(c) and (b) show that the effect in the prediction of attenuation for both models is appreciable when the working frequency is different from the characterisation frequency as expected. In addition, it can be inferred that the attenuation of the multiple modes are not only dependent on frequency as shown in Section 3.3 but also angle dependent.

7.2.3. Velocity, Attenuation and Energy Focusing Effects

This subsection provides a detailed analysis of velocity, attenuation and energy focusing characteristics in two viscoelastic plate-like structures. The plates have been kindly

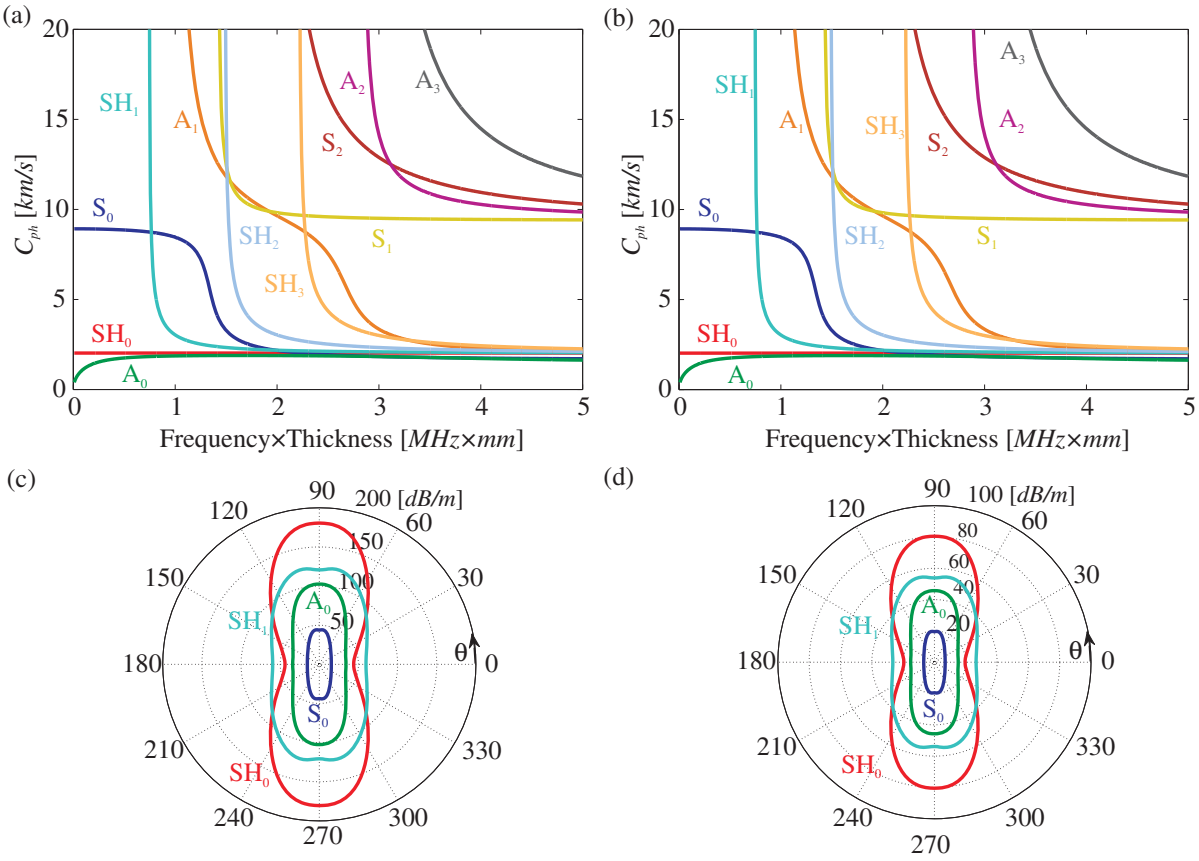

Figure 7.3. *Comparison from Hysteretic and Kelvin-Voigt models: (a) Phase velocity dispersion curves with Hysteretic model, (b) Phase velocity dispersion curves with Kelvin-Voigt model, (c) Attenuation curve with Hysteretic model and (d) Attenuation curve with Kelvin-Voigt model.*

donated by Dipl.-Ing. K. Schubert from Faserinstitut Bremen in Germany. Both materials have been characterised at the Laboratoire de Mecanique Physique in the University of Bordeaux by means of immersion, contact and simulation techniques [Castaings 2007, Calomfirescu 2008]. Numerical simulations are being conducted with both the higher order plate theory proposed in this thesis and the spectral element method (SEM) in time domain. This method combines the accuracy of global pseudo-spectral methods with the flexibility of finite element modelling (FEM) [Patera 1984]. A SEM program developed at the University of Siegen is used here to simulate the displacement fields produced by the fundamental modes of propagation [Schulte 2010, Fritzen et al. 2011]. It is good to bear in mind that the attenuation calculations, which are going to be presented next, are being done by using the Hysteretic material damping model. This model has shown to be more frequently used in composites literature for SHM and NDT applications [Neau 2003, Calomfirescu and Herrmann 2007].

First, a viscoelastic CFRP plate with unidirectional woven fabric reinforcement, a thickness of $5.1mm$, density of $1500kg/m^3$ and a $[0°]_{18}$ layup is analysed. The elastic and viscoelastic material properties are provided in Table 7.4. The structure is excited by a piezoelectric patch located in the middle of the structure using a $12Volts$ Hanning windowed toneburst with a carrier frequency of $95kHz$ with 5 cycles. The piezopatch has a

Table 7.4. *Elastic and viscoelastic properties of the carbon fibre lamina (units in GPa).*

C_{11}	C_{22}	C_{33}	C_{12}	C_{13}	C_{23}	C_{44}	C_{55}	C_{66}
125	13.9	14.5	6.3	5.4	7.1	3.7	5.4	5.4
η_{11}	η_{22}	η_{33}	η_{12}	η_{13}	η_{23}	η_{44}	η_{55}	η_{66}
3.0	0.6	0.6	0.9	0.4	0.23	0.12	0.3	0.5

diameter of $10mm$ and a thickness of $0.25mm$. The plate is meshed with 80×80 spectral shell elements using 36 nodes per element.

Following a similar behaviour as for GFRP case depicted in Section 7.2.1, it can be seen from Figures 7.4(a) and (b) how the fibres act as a guide for the energy in their direction

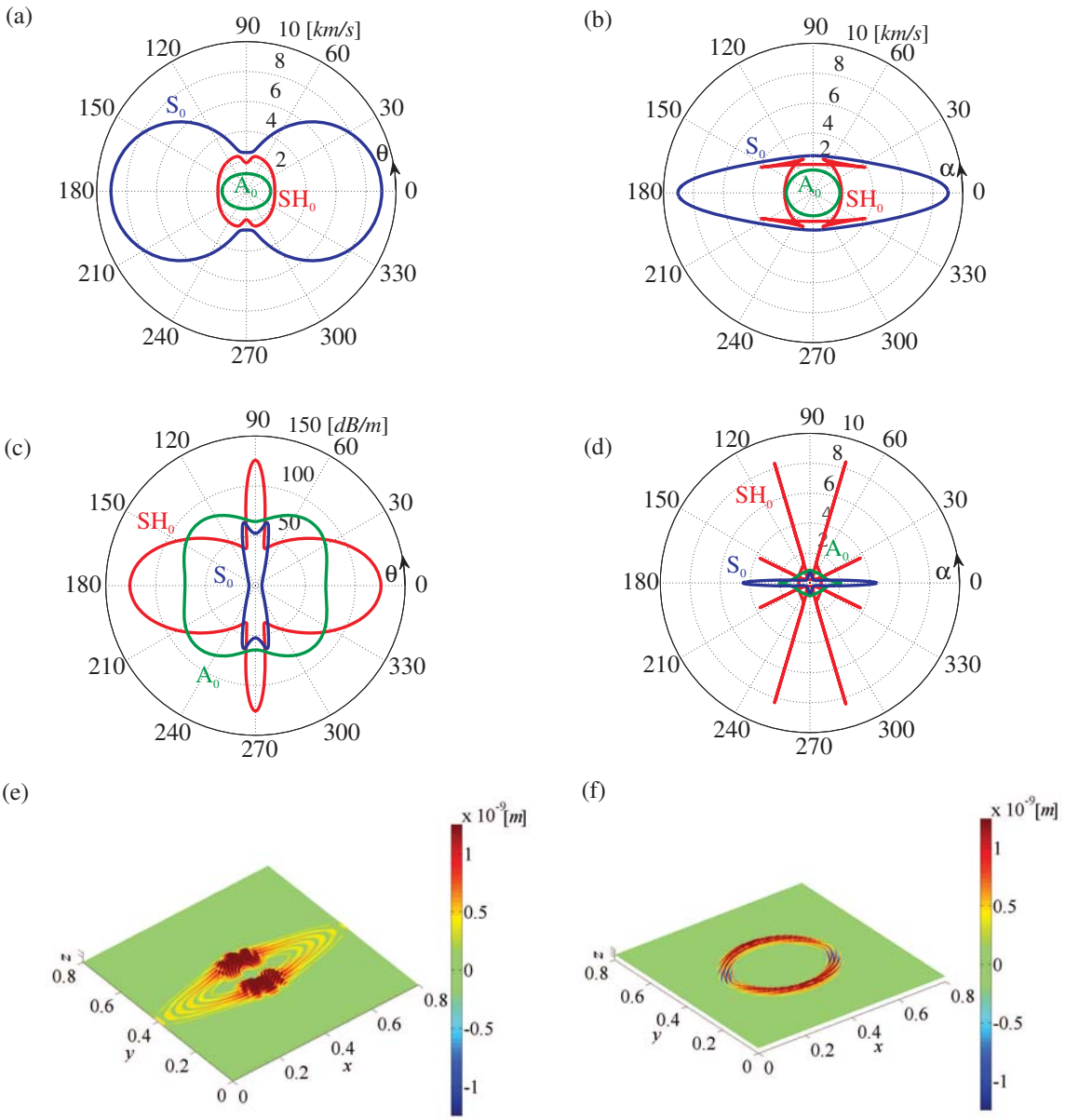

Figure 7.4. *Simulation results for the fundamental modes of propagation: (a) Velocity curves, (b) Wave curves, (c) Attenuation curve with Hysteretic model , (d) Focusing curve, (e) Snapshot of Out-of-Plane motion after* $0.058ms$ *and (f) Snapshot of In-Plane motion after* $0.158ms$.

Table 7.5. *Elastic and viscoelastic properties of a single carbon-epoxy lamina (units in GPa).*

C_{11}	C_{22}	C_{33}	C_{12}	C_{13}	C_{23}	C_{44}	C_{55}	C_{66}
70.0	33.0	14.7	23.9	6.2	6.8	4.2	4.7	21.9
η_{11}	η_{22}	η_{33}	η_{12}	η_{13}	η_{23}	η_{44}	η_{55}	η_{66}
1.8	1.4	0.5	0.9	0.3	0.2	0.17	0.2	0.5

and as scatterers in the perpendicular direction for the A_0 and S_0 modes of propagation. The attenuation is also affected a great deal by the anisotropy of the material. This effect can be observed in Figures 7.4(c), (d) and (e). This is a common characteristic of anisotropic materials where the velocity, attenuation and energy of propagation of the multiple modes are both frequency and angle dependent. This dependence plays a major role in the complexity of the mode shapes of propagating modes, what also affects their detectability. For example at this low frequency, the S_0 fundamental mode is mainly compressional and less attenuated in the direction of the fibres than in the $\theta = 90^\circ$ direction. This is consistent with its mode shape. In an inverse manner, the A_0 mode attenuation is fairly lower at $\theta = 90^\circ$ than at $\theta = 0^\circ$. Figure 7.4(d) shows the capabilities of the phonon focusing factor to precisely track the angular dependent energy concentration effect. The cuspidal regions in the SH_0 mode explain the energy patterns containing caustics. These phenomena are clearly depicted in the simulations of the displacement fields by the SEM depicted in 7.4(e) and (f).

Second, a viscoelastic orthotropic multilayered plate of $4.7mm$ thickness and a density of $1500kg/m^3$ is analysed in this subsection. The elastic and viscoelastic material properties of the plate analysed here are listed in Table 7.5. This viscoelastic CFRP plate is made of 18 equal layers resulting in a total thickness of $4.7mm$ with a stacking of $[-45^\circ 0^\circ 45^\circ 45^\circ 0^\circ -45^\circ -45^\circ 0^\circ 45^\circ]_s$.

Numerical results analysing the effects of material layup on wave propagation, Lamb wave energy focusing and attenuation are presented in Figure 7.5. In a similar fashion as the previous example, the structure is excited by a piezoelectric circular patch located in the middle of the structure using a $12V$ Hanning windowed toneburst with a carrier frequency of $100kHz$ with 5 cycles. The plate is meshed with 80×80 spectral shell elements using 36 nodes per element. The piezopatch has a diameter of $10mm$ and a thickness of $0.25mm$. From Figures 7.5(a) to (c) it can be seen that the mode wave velocities and attenuation are not strongly related to the frequency and orientation of propagation. This affirmation is also in agreement with the displacement fields depicted in Figures 7.5(e) and (f). It can be seen again how the multilayered and multi-oriented composition of the structure mitigates the anisotropic impact of each layer as it was discussed before.

For the A_0 and S_0 fundamental modes of propagation the focusing factor is highest in the direction $\alpha = 0^\circ$; however, a second maximum also occurs at $\alpha = 90^\circ$. Although not depicted here, the focusing effect becomes more pronounced as one moves along the

frequency axis to higher frequencies for the fundamental symmetric modes. This effect is less significant for the fundamental antisymmetric mode. Regarding the experimental calculation of attenuation as a function of the frequency, this is obtained using the ratio of the spectra between two sensors points lying on a single line, i.e. the ratio of the Fourier transforms (FFT) of the signals recorded at the two points allows to determine the reduction in amplitude as a function of frequency for the given distance.

For the present study, the A_0 mode was specially selected in a frequency in which dispersion was low in order to guarantee an accurate measurement of mode attenuation. The attenuation curve together with experimental results for the A_0 mode at a frequency $f = 100kHz$ are depicted in magenta circles in Figure 7.5(c). It can be seen that a good

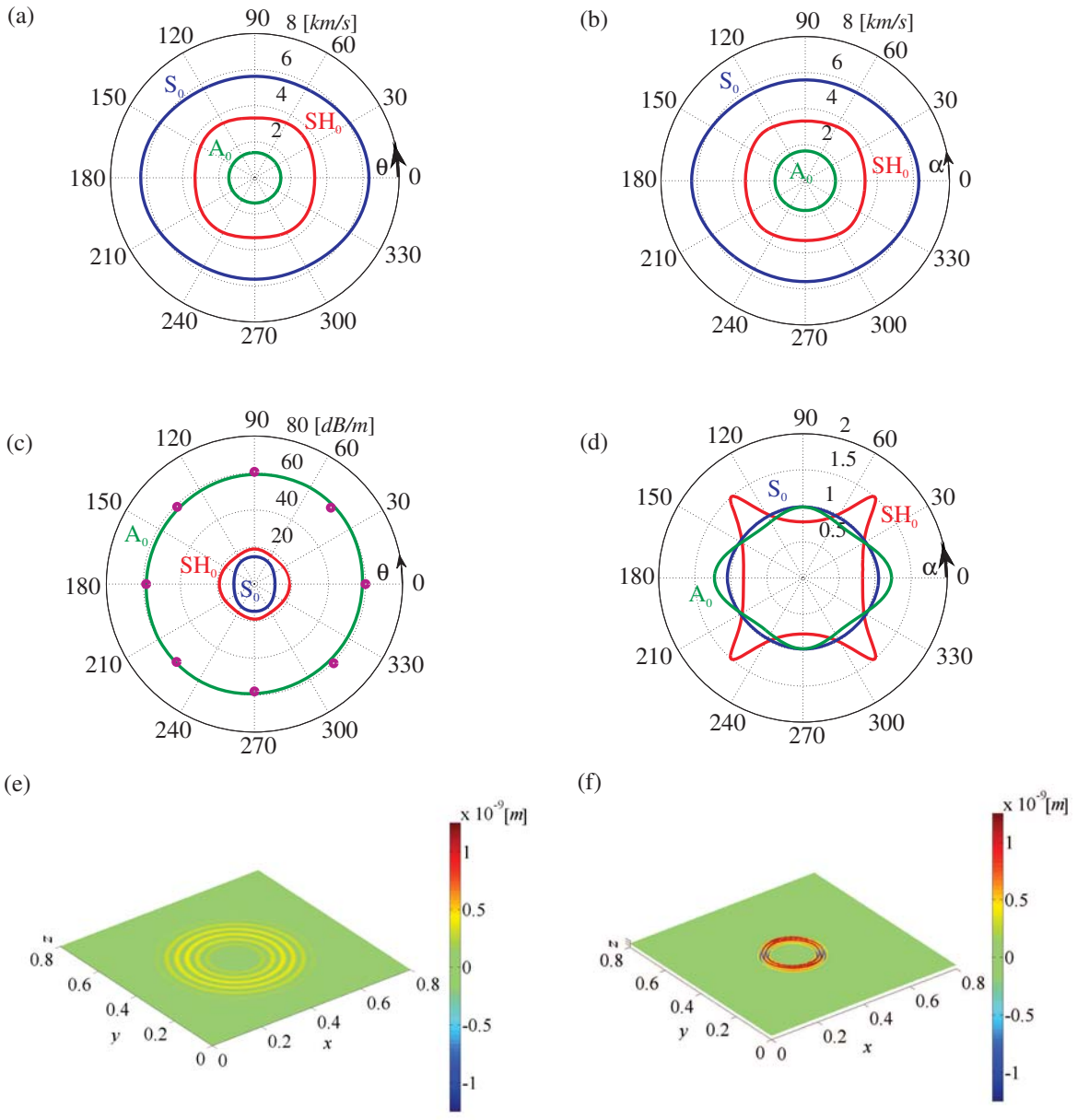

Figure 7.5. *Simulation results for the fundamental modes of propagation: (a) Velocity curves, (b) Wave curves, (c) Attenuation curve with Hysteretic model , (d) Focusing curve, (e) Snapshot of Out-of-Plane motion after* 0.045*ms and (f) Snapshot of In-Plane motion after* 0.113*ms.*

Table 7.6. *Material properties of a single carbon fibre reinforced lamina (units in GPa).*

E_{11}	E_{22}	E_{33}	G_{12}	G_{13}	G_{23}	$\nu_{12} = \nu_{13} = \nu_{23}$
122.0	10	10	7.4	7.4	5.4	0.33

agreement between theoretical and experimental results is obtained. For this material, the caustics present in the SH_0 mode from the previous example are not any more present. However, the cuspidal regions of the SH_0 in the focusing curve from Figure 7.5(d) indicate the energy concentration in the four quadrants at approximately $\alpha = 48°, 138°, 228°$ and 318°.

7.2.4. Temperature Influence on Propagation Modes

As discussed in Section 5.4, changing environmental conditions augment the complexity for the reliable monitoring of a structure. It is well known that temperature as well as damage can have similar effects on the dynamic behaviour of a structure. As a result, dynamic responses obtained for wave propagation-based methods can be affected by these effects and lead to false alarms or wrong damage locations. Therefore, it is very important to understand the impact of these changing conditions and take them into account. Increase in time-of-flight and changes in sensor response magnitude with temperature are analysed and discussed here.

Experimental results are presented here for two different plates. First, a CFRP plate made of 4 equal layers with a total thickness of $1.7mm$, stacking of $[0°\,90°\,90°\,0°]$ and a density of $1500kg/m^3$ is studied. Nominal material parameters of the unidirectional layers are given in Table 7.6. Temperature tests were conducted in a temperature-controlled oven. During the test runs the temperature was raised stepwise from $T = -24 \pm 2°C$ up to $T = 60 \pm 2°C$. The temperature was measured by two PT100 sensors mounted on the plate opposite corners.

Figure 7.6(a) shows the structure with dimensions $200mm \times 250mm$. Nine piezoelectric transducers PIC151 from PI Ceramics were attached to the surface of the structure. The structure was excited by a piezoelectric transducer located in the middle of the structure. The excitation voltage signal is a $12V$ Hanning windowed toneburst with a carrier frequency of $30kHz$ with 5 cycles. Transducer P_5 was used as actuator. The influence of the variation in temperature causes an evident change of the structural dynamics. The dynamic response signal for sensor number two and three decreased monotonically in peak-to-peak magnitude with increasing temperature and it can be seen from Figure 7.6(b) and (c). Interestingly, the inverse effect was seen in sensor number six as depicted in Figure 7.6(d). According to experimental results depicted in Figures 7.6(b) to (d), the increase in the temperature causes a right time-shift of the dynamic responses. Inversely, the decrease in the temperature causes a left shift. The reason of these time-shifts is both

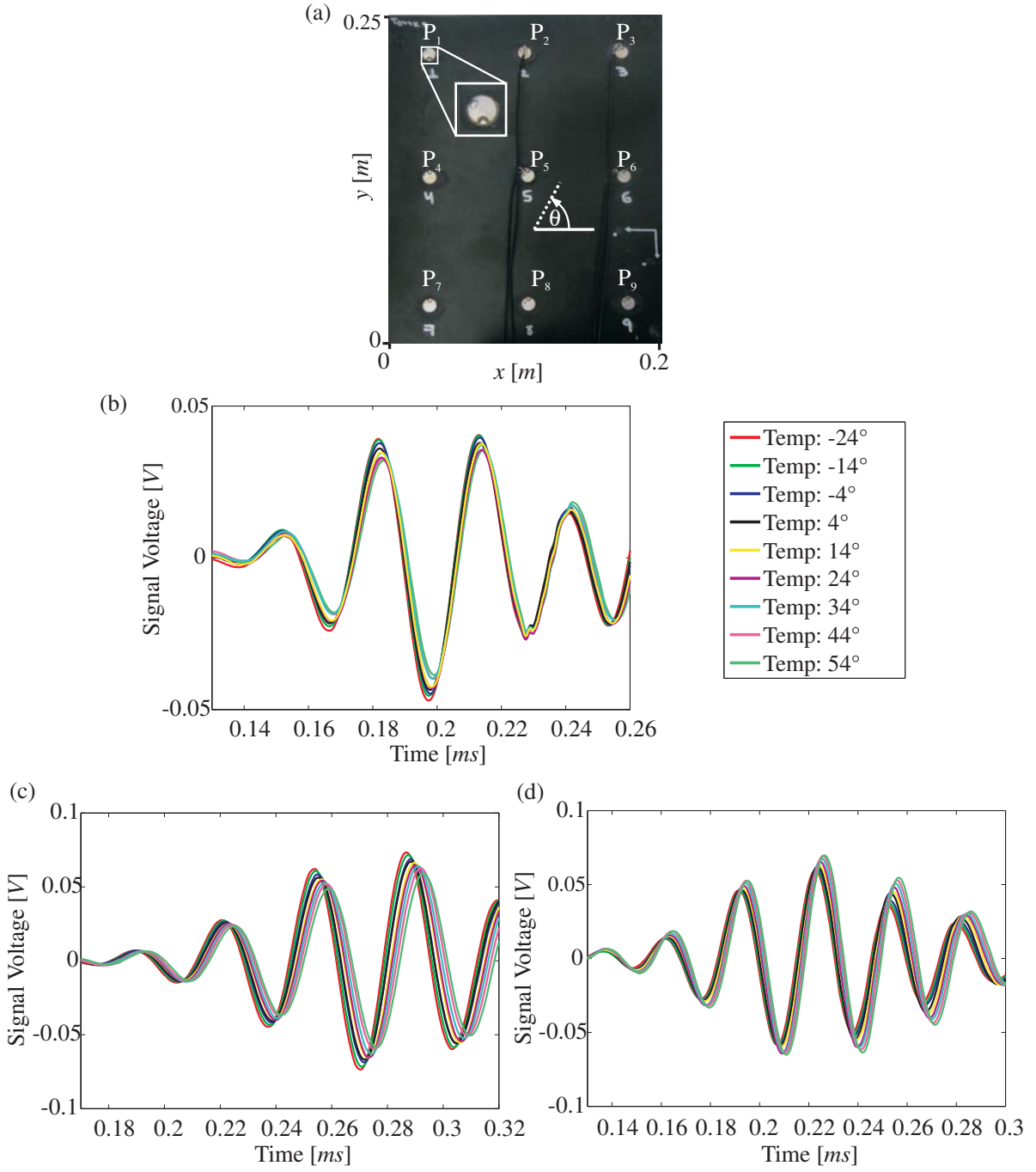

Figure 7.6. *Influence of temperature on the propagated ultrasonic guided waves: (a) Experimental setup, (b) Ultrasonic signals collected at transducer* P_2*, (c) Ultrasonic signals collected at transducer* P_3 *and (d) Ultrasonic signals collected at transducer* P_6*.*

thermal expansion and changes in wave velocities with temperature. The attenuation of Lamb wave can be regarded to both wave dispersion as a result of frequency dependent phase velocities and attenuation loss due to frequency/temperature dependent material damping.

Next, a second plate made of six equal layers with a total thickness of $3mm$ made of roving glass composite laminate from Bond Laminates GmbH is studied. The experimental setup is depicted in Figure 7.7(a) showing the structure with dimensions $200mm \times 250mm$.

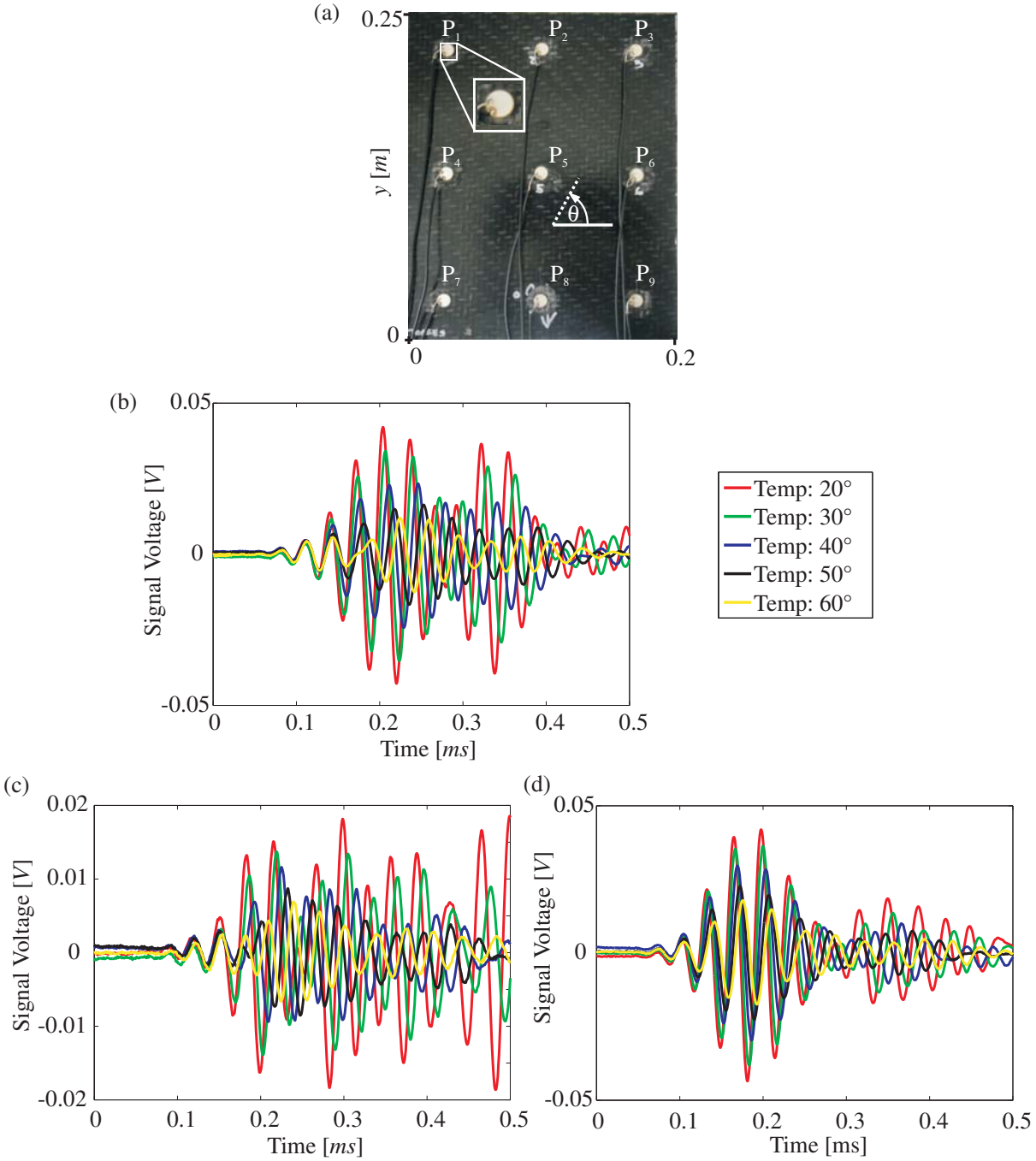

Figure 7.7. *Influence of temperature on the propagated ultrasonic guided waves: (a) Experimental setup, (b) Ultrasonic signals collected at transducer* P_2*, (c) Ultrasonic signals collected at transducer* P_3 *and (d) Ultrasonic signals collected at transducer* P_6*.*

In a similar manner to the first CFRP plate, nine piezoelectric transducers were attached to the surface of the structure. The constitutive laminae is built with woven fibres. The excitation signal was the same as in the previous example and transducer P_5 was used as actuator. From Figure 7.7(b) to (c), in comparison to the previous example, one can notice a notorious influence of temperature variability on the amplitude of the recorded modes, i.e. the higher the temperature, the higher the attenuation of the propagated waves. It can be also observed that the offset of all the ultrasonic signals is dependent on

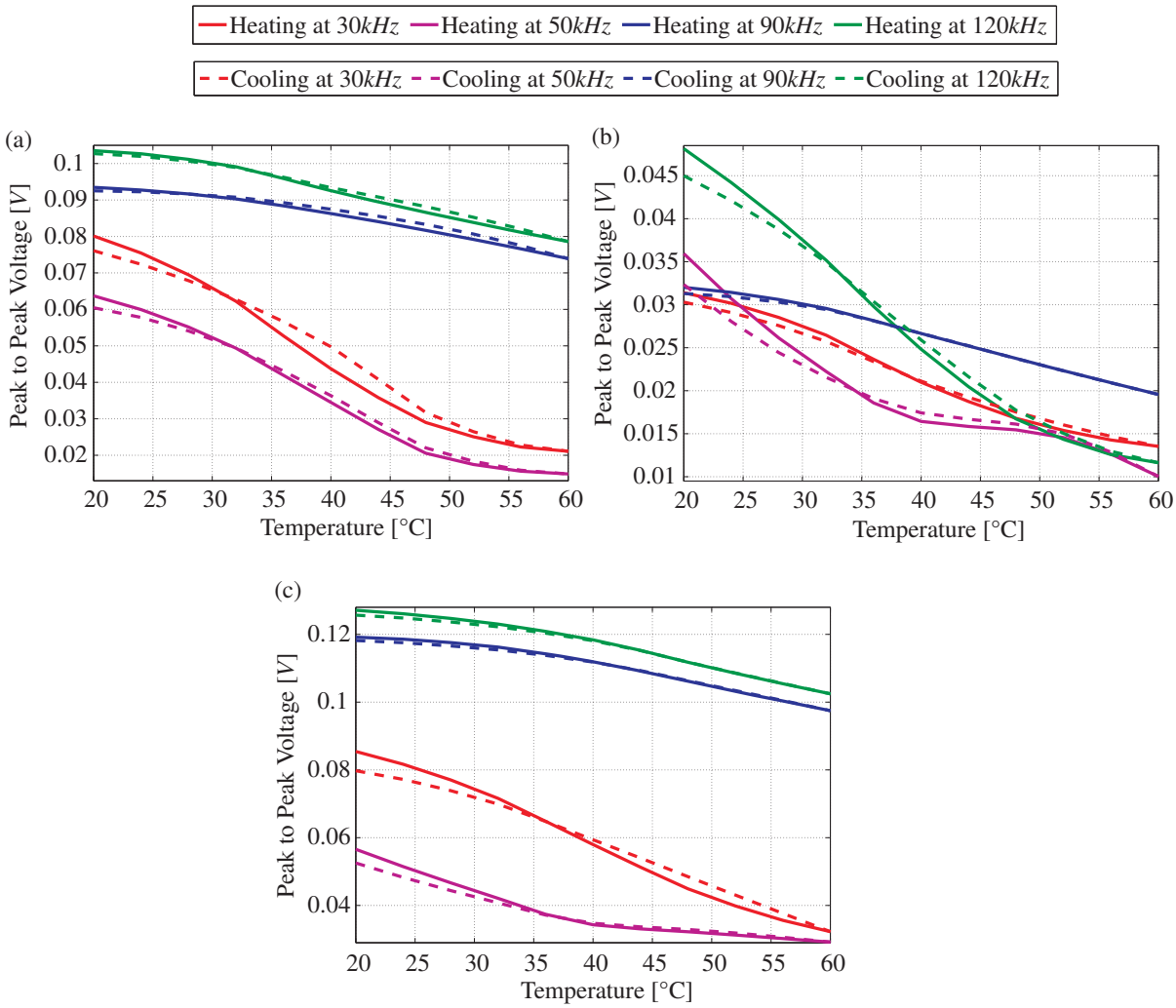

Figure 7.8. *Temperature gradient effect on Peak-to-Peak amplitudes of* A_0 *Mode: (a) Sensor 2, (b) Sensor 3 and (c) Sensor 6.*

the temperature.

The second study carried out with this structure was performed in order to analyse the influence of the temperature cycles under which the structure was subjected at different excitation frequencies. Without loss of generality, the A_0 mode was selected in this study for the analysis of the influence of temperature gradient sign in the mode amplitude changes since this mode is easier to excite with the provided sensor arrangement. Mode identification was accomplished based on dispersion features and energy distribution analysis as proposed in Chapter 4.

The first effect that can be noticed from Figure 7.8(a) to (c) is the change of amplitudes for a given frequency and orientation of the sensor. This effect is explained due to the changing ratio of displacement and stress amplitudes with respect to the frequency and angular orientation for a particular mode along the plate thickness as it was presented in Chapter 5. As it can be inferred from all the results presented till now, the understanding of these wave propagation phenomena plays a critical role in the selection of the optimal inspection frequencies for the improvement of the sensitivity and for the optimization of

sensor networks in terms of sensor placement and number of sensors. It can be observed as well that the temperature gradient has a strong effect on the trajectories of the peak-to-peak amplitudes with respect to the heating or cooling cycles. It is good to bear in mind that the capacitance of piezoelectric materials is known to be temperature sensitive. As temperature increases, the capacitance value of the PZT normally increases and this effect modifies the response of the sensor. Even when not depicted for this plate, the dynamic response signals of all sensors decreased monotonically in peak-to-peak magnitude with increasing temperature for all the tested frequencies.

7.2.5. Applications of the Model for Manufacturing Control

As it has been experimentally validated, the proposed model for guided wave propagation is able of providing accurate estimates of velocities for the different modes of propagation. It is evident that the analytical model would significantly support the understanding and interpretation of experimental results for a great variety of laminate designs. It is well-known that based on the load requirements there are a variety of layups for composite laminates. Consequently, Lamb waves could be used for detecting fibre misorientation or stacking sequence errors in composite laminates.

Using the model developed in Chapter 3, an angular scan has been simulated for different frequencies in order to calculate the phase and group velocities of the fundamental antisymmetric and symmetric modes of propagation. The evaluated structure is a CFRP laminate with a layup of $[0°\,0°\,0°\,0°]$ with a total thickness of $1mm$. Nominal material parameters of the unidirectional layers are given in Table 7.1. The misplacing mistake is simulated by placing the ply number two at $45°$ instead of $0°$.

Figure 7.9 shows the results for the fundamental A_0 mode. By checking the phase velocity surfaces from Figures 7.9(a) and (c), it is very difficult to notice a clear difference between both plots that can indicate a pattern resulting from the misalignment of the second ply. Nevertheless, if one observes and compares the group velocity surfaces from Figures 7.9(b) and (d), one can clearly notice the changes of the angle-frequency patterns caused by the single-ply misorientation. This can be observed specially in the high frequency range along the $0°$ direction where the curved shape changes to an almost flat surface.

Figure 7.10 shows the results for the fundamental S_0 mode of propagation. It can be easily seen from Figures 7.10(a) to (d) that a change not only in the maximum values of both the phase and group velocity surface plots occurs (see the colour bar limits), but also in their shapes. Another interesting change that can be identified is the modification in shape of the group velocity plot along the $90°$ direction (around $1.57\,radians$) where the profile moves from a convex shape to a concave one. These results reflect that the transmitted S_0 mode is very sensitive to the orientation of the ply. As it could be observed from the figures previously discussed, the velocity angular pattern is very sensitive at the different

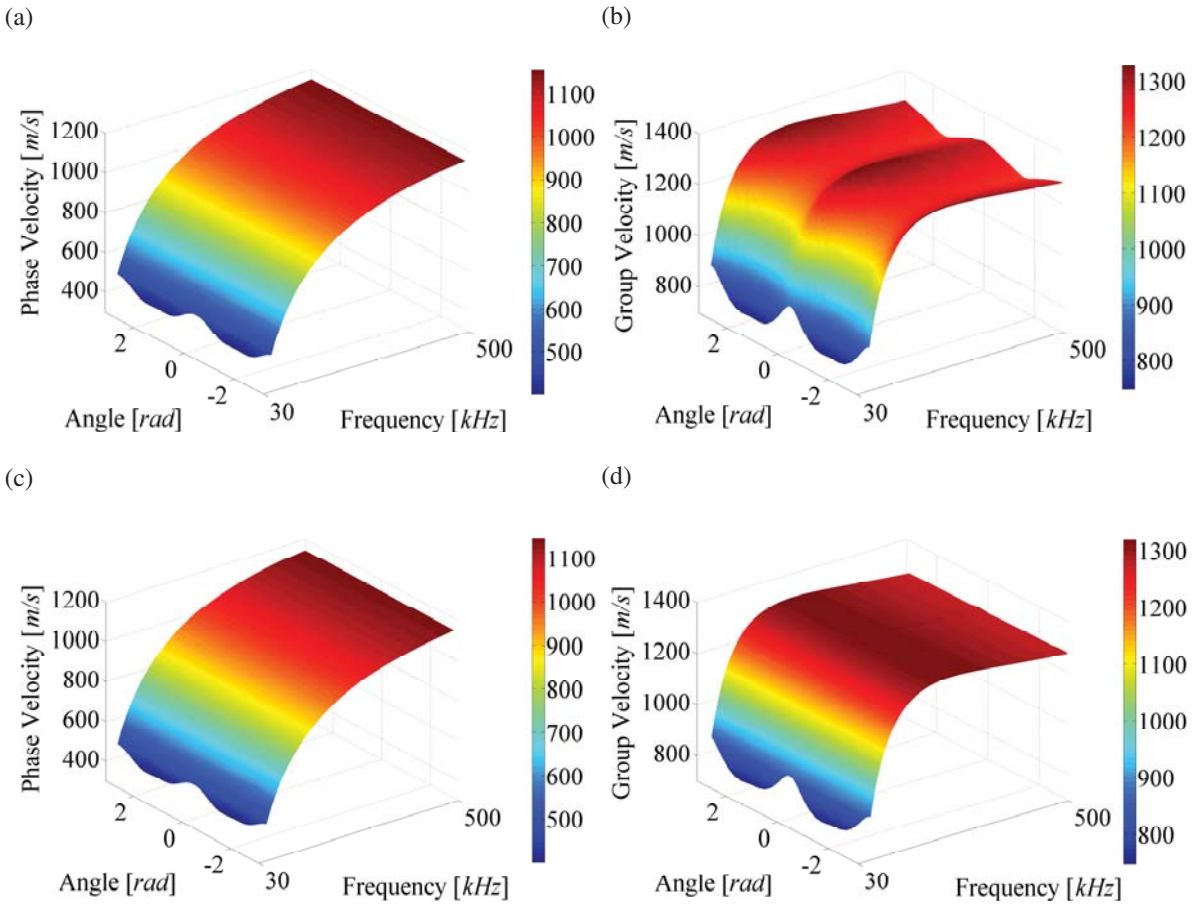

Figure 7.9. *Angle-frequency surface for a* 1*mm thick GFRP plate for the* A_0 *mode of Lamb wave propagation up to a frequency of* 500*kHz: (a) Phase velocity for the correct stacking sequence, (b) Group velocity for the correct stacking sequence, (c) Phase velocity for the wrong stacking sequence and (d) Group velocity for the wrong stacking sequence.*

frequencies allowing to depict the laminate layup differences between both structures. Experimentally, these plots can be generated using a pulse excitation and recording the transmitted wave signals in the time domain at a given angular scan resolution for later mode identification and velocity calculation. Mode identification is the subject of study in the following section.

7.3. Modal Acoustic Emission

This section evaluates the methodologies proposed in Section 4. The goal is to establish a novel deviation from the traditional dependence on statistical-based and parameter-based analysis so that an significant improvement of the monitoring capabilities of acoustic emission can be accomplished. Nevertheless, standard AE analysis are carried out for comparison purposes. The idea behind using modal techniques is to provide an improved understanding of the damage mechanisms which together with the help of the model developed in Chapter 3 could additionally and potentially support sensor reduction and

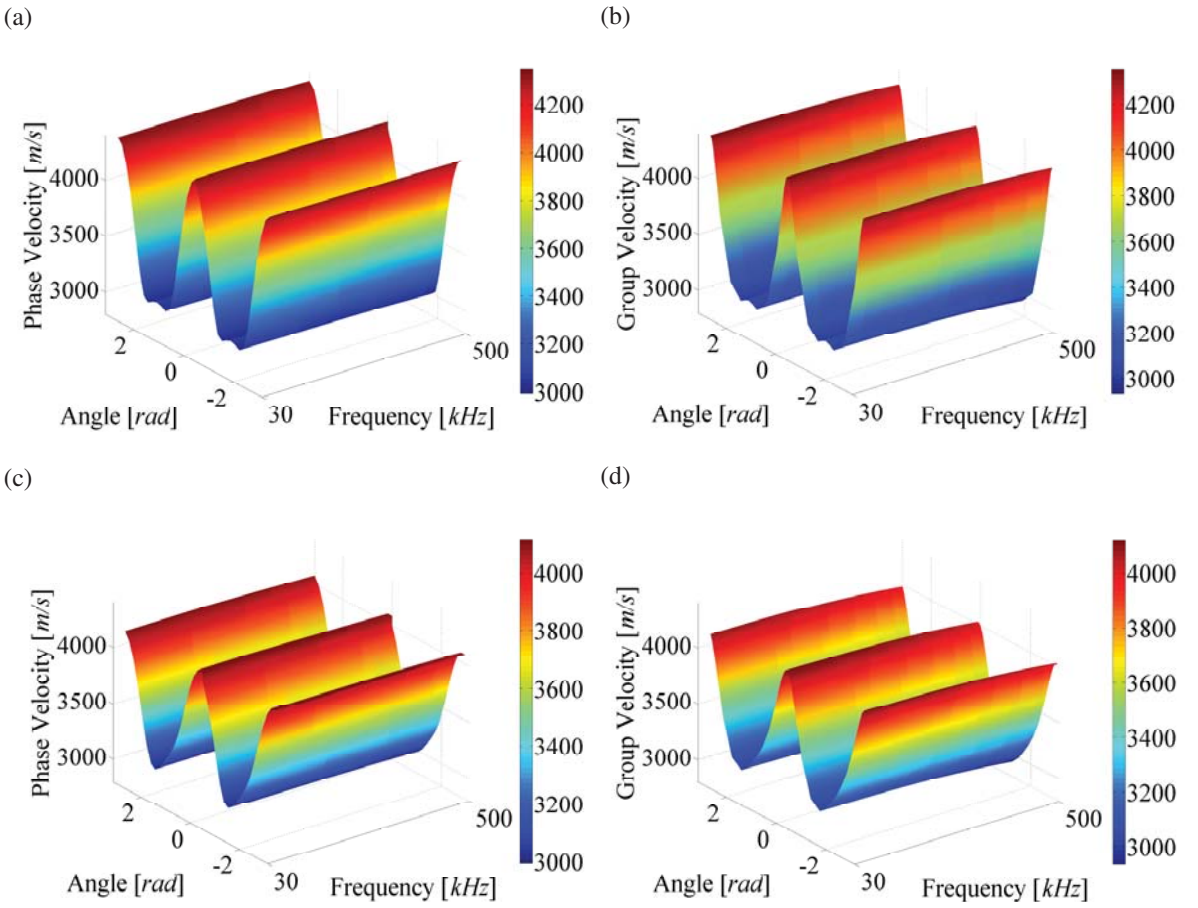

Figure 7.10. *Angle-frequency surface for a* $1mm$ *thick GFRP plate for the* S_0 *mode of Lamb wave propagation up to a frequency of* $500kHz$*: (a) Phase velocity for the correct stacking sequence, (b) Group velocity for the correct stacking sequence, (c) Phase velocity for the wrong stacking sequence and (d) Group velocity for the wrong stacking sequence.*

increased source location accuracy.

7.3.1. Mode Identification with Neural Networks

In order to check the performance of the proposed method for mode identification by means of artificial neural networks, a specimen was made from a $2mm$ aluminium sheet of dimensions $800mm \times 800mm$. Four broadband AE sensors (VS900-M) were installed on the plate and vacuum silicon grease was used to improve the signals transmission between specimen and sensors. The sensors were positioned at an equidistance of $50mm$ from each corner of the plate area and kept in position by means of C-clamps. The experimental setup consisted of AEP3 amplifiers (Vallen Systems), a HS4 handy-scope from TiePie Engineering and a PC. The complete experimental setup is depicted in Figure 7.11(a). The amplifier gain was set to $34dB$, the anti-aliasing low-pass and high-pass cut-off frequencies were adjusted to $95kHz$ and $800kHz$, and the sample frequency was $50MHz$. A database consisting of more than 1500 recorded signals from pencil lead break sources with different pencil lead hardness (2B, 2H, B, H and HB) at different angles of incidence was used for the training, validation and test of the network. The database was composed

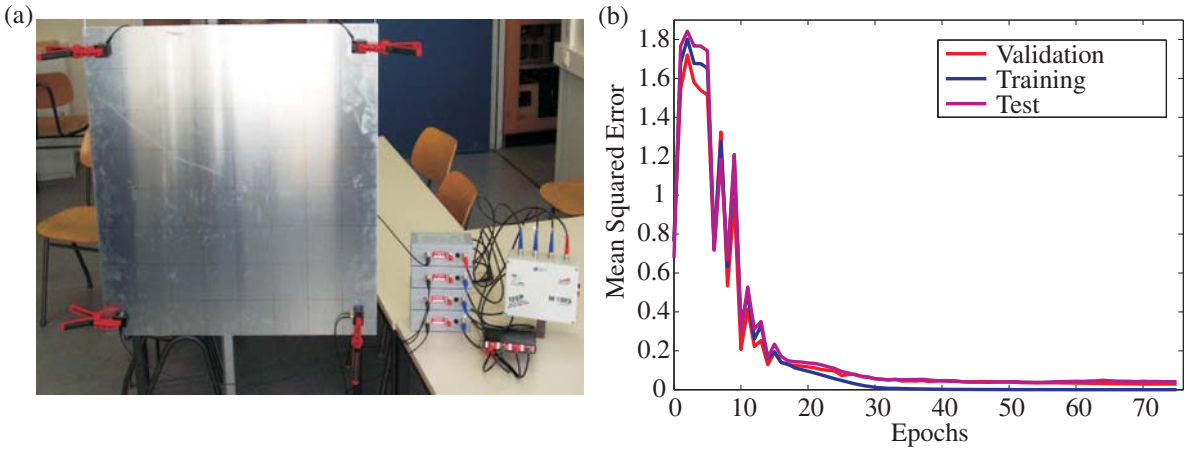

Figure 7.11. *Mode identification experiment by means of artificial neural networks: (a) Experimental setup and (b) Mean squared error plots for validation, training and test data sets.*

of segments representing the fundamental symmetric S_0 and antisymmetric A_0 modes as well as noise segments extracted prior to the wave first arrival. The data fed to the network were normalized. Resilient back-propagation was used as training function and the mean squared error (MSE) as performance function. An early stopping technique was used in order to avoid overfitting of the training set and degradation in the network prediction capabilities. The number of neurons in the hidden layers are selected so that an acceptable classification error is obtained. However, a specific rule was not followed in order to select the dimension of the hidden layers. As it is normally expected, if too few nodes are defined in the hidden layers, the prediction accuracy of the neural network might be poor. However, if too many hidden nodes are defined, the network will be susceptible to overfitting. For the present case, the optimal network consists of one input layer with 300 nodes, one output layer, 45 nodes in the first hidden layer and 29 nodes in the second hidden layer. The training phase used the 1 of M strategy. The best validation performance was obtained at epoch 75 and it was equal to 0.029. The mean squared error plot for the test, validation and training data sets is depicted in Figure 7.11(b).

To test the mode identification method, fifty pencil lead brakes with different hardness were exerted on the surface of the plate with a grid density of $10mm$. The square area limited by the sensors was investigated. The recorded signals were first processed with the DWT in order to obtain denoised signals and later fed into the trained artificial neural network for mode recognition. After the neural network has been trained, examination of the generalization performance of the network revealed that it was possible to predict correctly 94% of the A_0 segments, 98% of the S_0 segments and 95.2% of the noise segments from the signals recorded in the test.

Localisation by means of the different Onset-time Detectors As it has already been discussed, the accuracy of the localisation algorithm depends highly on the performance of the onset-picker. As a part of this thesis, a toolbox comprising the most common

algorithms depicted in Section 4.3 was implemented. The performance of each algorithm is evaluated in this section for the purpose of stress wave localisation by means of using the localisation scheme previously discussed in Section 4.7. This is accomplished by combining the mode identification approach based on artificial neural networks, the time-frequency analysis as introduced in Section 4.4 and the model developed in Chapter 3 so that the necessary parameters could be fed into Eq.(4.17) for the solution of the localisation problem. Figure 7.12 displays the RMSE for every interrogated node in the grid as a three dimensional bar chart.

It can be seen how the methods based on cross-correlation, i.e. Figure 7.12(a) to (c), provide the worst results compared to the picker-based methods. This can be explained by the fact that wave dispersion greatly affects the performance of the algorithms for time of difference calculation. The calculated root mean squared errors for the GCC filter, GCC-PHAT filter and the HT filter are equal to $27.75mm$, $23.25mm$ and $23.22mm$, respectively. The Hinkley picker performed somewhat better with a RMSE equal to $20.64mm$. The optimal parameter ε for this experiment was found to be equal to 100. For the AIC picker, it was found that the root mean square error (RMSE) was of $4.7mm$ for the entire grid, which points out a clear improvement in source location in comparison with traditional methods (see for example [Gaul et al. 2001, Baxter et al. 2007]).

7.3.2. Mode Identification by means of Modal Energy Orientation

In order to check the performance of the proposed methodology for mode identification by means of modal energy orientation, a specimen was made from a $1.46mm$ unidirectional GFRP laminate of dimensions $800mm \times 350mm$. For the present experiment, four broadband AE sensors (VS900-M by Vallen Systems) were installed on the plate and vacuum silicon grease was used to improve the signal transmission between specimen and sensors. The sensors were fixed to the structure by means of magnetic clamps. The nominal material parameters of the layer are the following: $E_{11} = 30.7GPa$, $E_{22} = 15.2GPa$, $G_{12} = 4GPa$, $G_{13} = 3.1GPa$ and $G_{23} = 2.75GPa$. The density is approximately $1700kg/m^3$. The experimental setup consisted of AEP3 amplifiers (Vallen Systems), a four channel HS4 handy-scope from TiePie Engineering and a PC. The amplifier gain was set to $34dB$, the anti-aliasing low-pass and high-pass cut-off frequencies were adjusted to $95kHz$ and $800kHz$, and the signals were recorded with a sample frequency of $50MHz$. The experimental setup for the collection of AE data and a typical signal from a pencil lead break containing wave packets related to the fundamental symmetric and antisymmetric modes of propagation are depicted in Figure 7.13.

In practice larger dictionaries provide better performance for signal processing but the algorithm running time can be excessive. For the implementation procedure in this work a dictionary of chirplet atoms was built, which was small but sufficient by adaptively

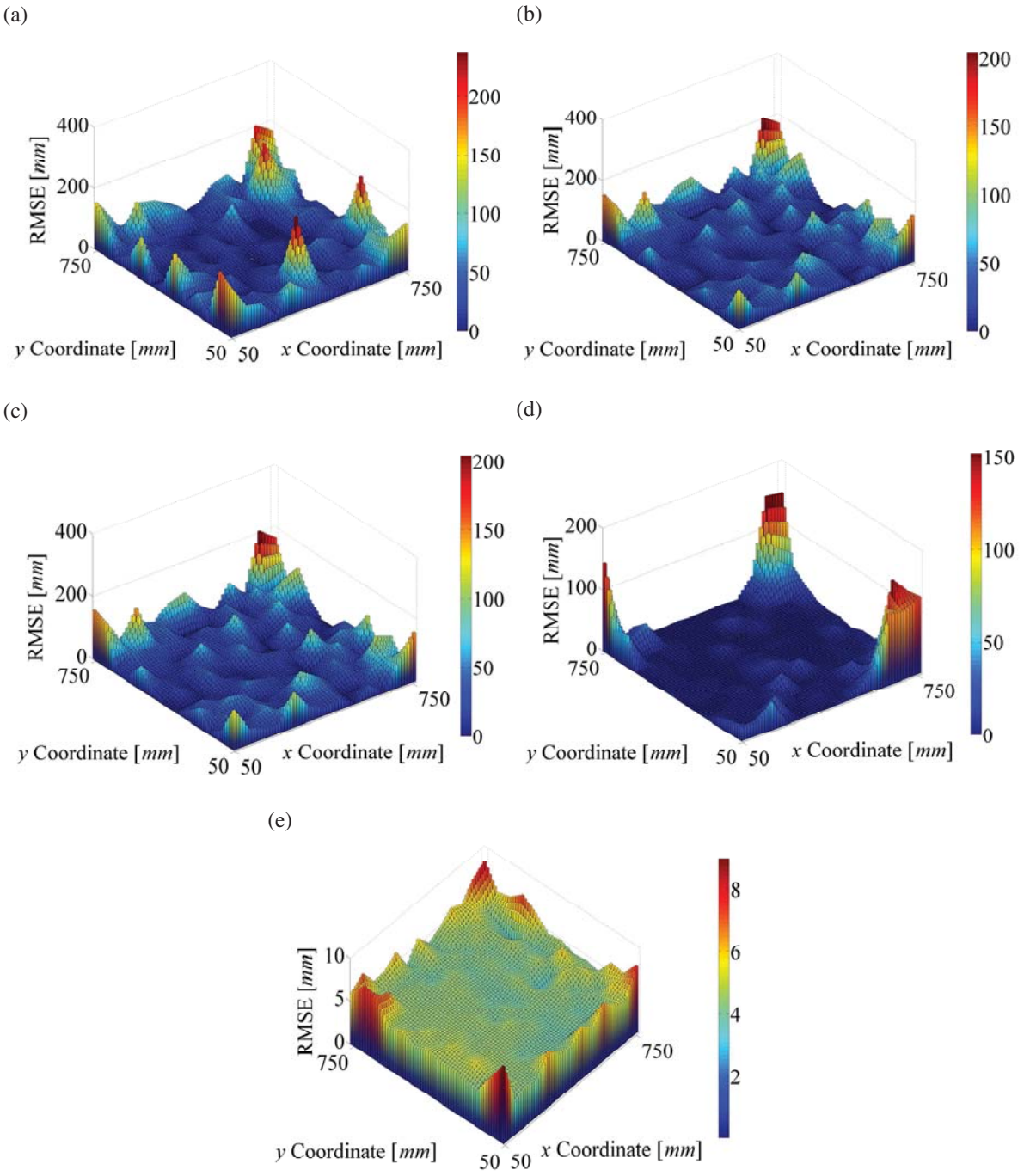

Figure 7.12. *Three-dimensional bar chart for the calculated root mean squared error for every tested node in the defined grid: (a) Localisation results using the GCC filter, (b) Localisation results using the GCC-PHAT filter, (c) Localisation results using the HT filter, (d) Localisation results using the Hinkley picker and (e) Localisation results using the AIC picker.*

choosing the parameter space of the chirplet decomposition based on the spectrum of the signals to be decomposed. This design led to a fast algorithm and reduced the computational cost produced by defining a large redundant dictionary. The decomposition termination was set to a threshold value of 98 per cent of the original signal energy. It is well known that acoustic emissions occur in such a fast succession that signals of different frequencies and amplitudes superpose each other. An example of this effect is given below

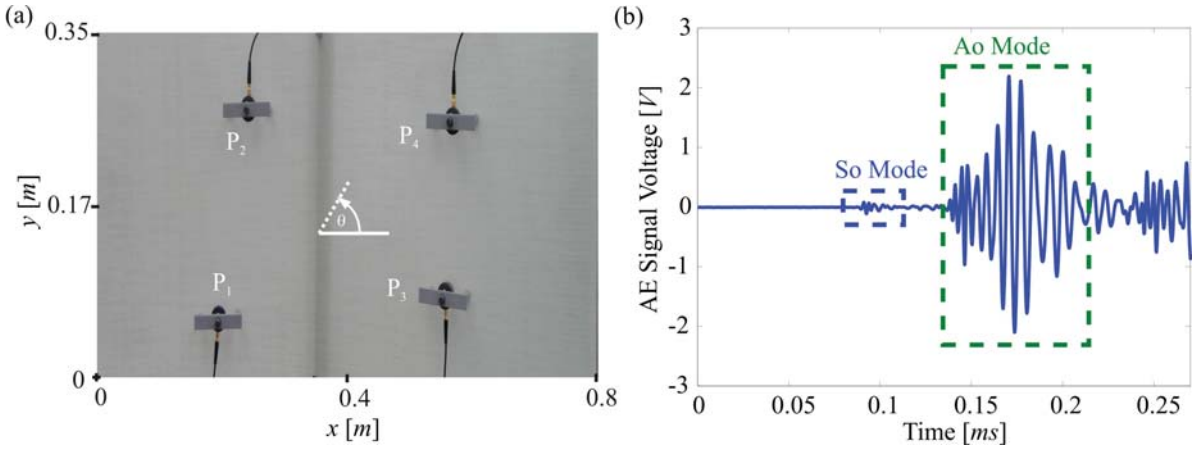

Figure 7.13. *GFRP plate: (a) Experimental setup and (b) Signal generated from a pencil lead brake.*

in Figure 7.14 in order to illustrate the full chirplet decomposition process and its ability to decode overlapping packets in the presence of noise.

The signal was generated by a pencil lead brake at a radial distance of 200*mm* from the

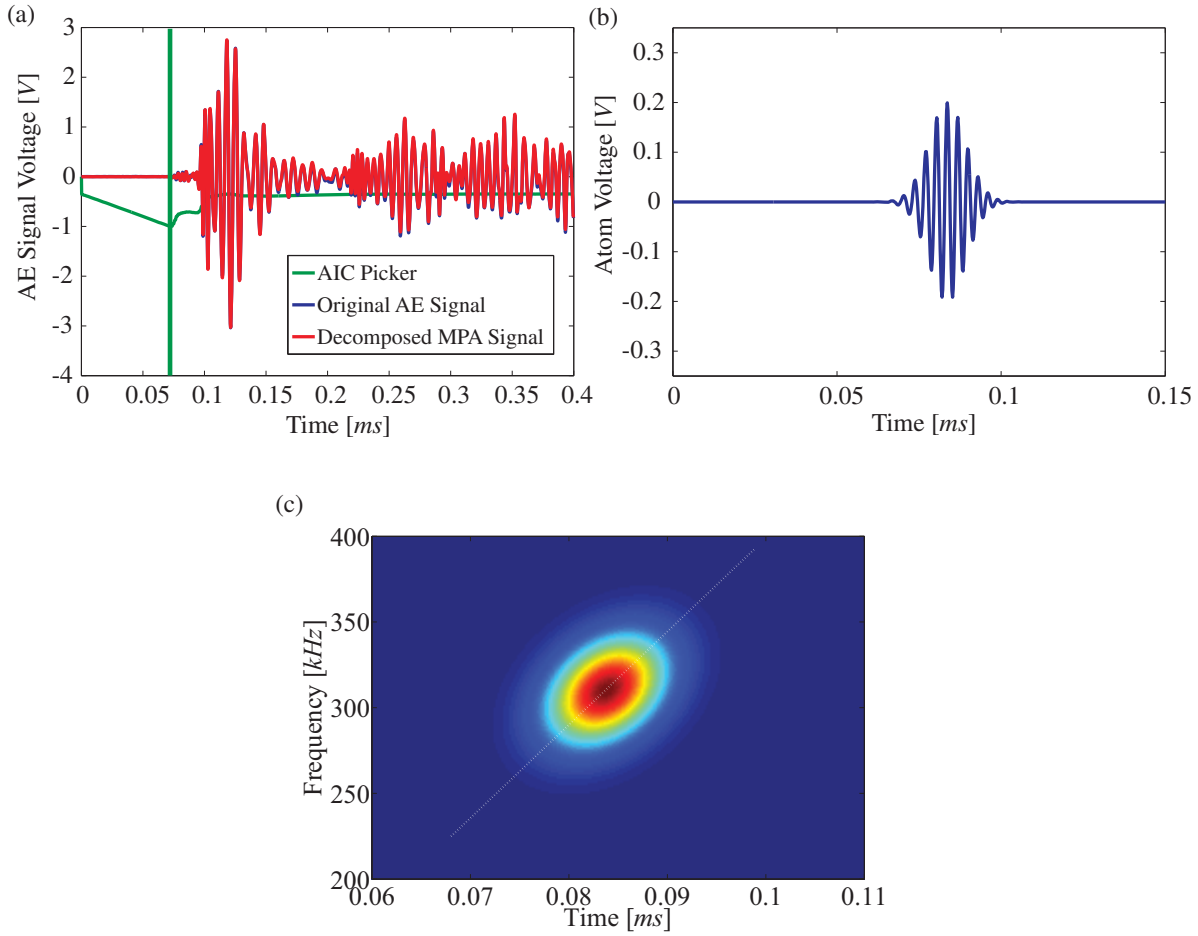

Figure 7.14. *Pencil lead break mode identification in GFRP plate for sensor number one: (a) Matching pursuit algorithm and AIC onset time detector estimate, (b) Atom corresponding to the arrival time of the AE signal and (c) Matched atom energy distribution corresponding to the onset estimation.*

sensor number one. This signal consists of four main components that are (i) a first wave packet representing the S_0 mode of propagation with faster energy velocity, (ii) a second wave packet presenting the slower A_0 mode of propagation, (iii) reflections from the boundaries of the structure and (iv) inherent noise. From this figure, it can be clearly seen the capabilities of the method to properly separate between modes by depressing the effect of overlapping; the difficulty to separate wave packets both in time and frequency and elimination of non-negligible cross-terms using traditional methods was overcome by the proposed approach. The TFR algorithm used in this work was the Wigner-Ville distribution and the matched atoms were considered as analytic signals. The intensity of the plot is proportional to the energy content in the signal at the indicated frequency and time.

From the conclusions obtained in the Section 4.6.2, it can be estimated from the energy distribution and frequency modulation rate sign that the detected mode corresponds to the S_0 mode. Finally, the atomic decomposition on a signal produced by a pencil lead break at 90° with respect to the plane of the CFRP plate is illustrated. It is well-known that for this kind of elastic wave excitation most of the motion is normal to the plate and it normally generates a large flexural mode. For this experiment, the distance between a selected sensor in the network, P1 with no loss of generality, and the source was specially selected in order that the chosen sensor was able to detect a different mode in comparison to the others in the network, i.e. just the A_0 mode, while the S_0 mode amplitude is totally decreased and lost in the background noise. Figure 7.15 depicts the complete chirplet decomposition of the recorded signal at P1 and the quadratic energy distribution related to the matched atom predicted by the onset detector. This signal consists of two main components that are (i) a first wave packet representing the A_0 mode of propagation with (ii) a second train of wave packets related to the reflections from the boundaries of the structure and noise. According to the same previous assumptions from the energy characteristics of the matched atom, it can be concluded that the detected mode was A_0. By interrogating every sensor in the network, it can be found that not all the sensors detected the same mode in this case, and a correction measure must be taken in order to guarantee the selection of a common mode to all the sensors so that potential errors in the localisation algorithm can be avoided. This can be easily done since all the decomposed signals contain well defined atoms in time and frequency, and mode wave packet arrival detection can be automatically implemented based on the energy characteristics of the atoms.

Finally, the analysed characteristics of the recorded signals could be used for the application of advanced source localisation algorithms. The successful application of the present method in the current passive monitoring technique is partially due to the good choice of the matching pursuit dictionary and the optimization method used to find the optimal parameters representing the signal content. Moreover, the proposed method al-

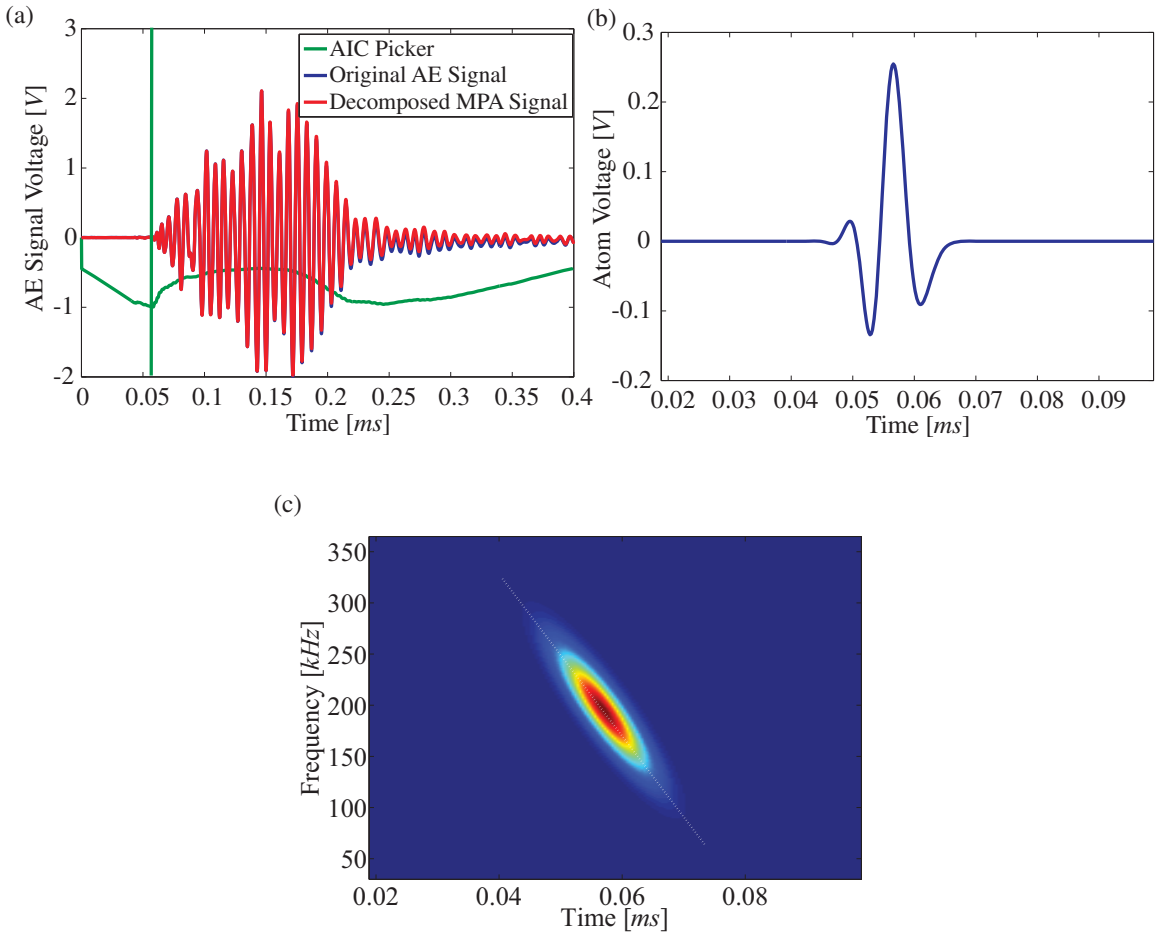

Figure 7.15. *Pencil lead break mode identification in GFRP plate for sensor number one: (a) Matching pursuit algorithm and AIC onset time detector estimate, (b) Atom corresponding to the arrival time of the AE signal and (c) Matched atom energy distribution corresponding to the onset estimation.*

lows a different approach from traditional statistical analysis and enables an improved understanding of the origin of the source.

7.3.3. Mode Identification with Pattern Recognition

The fast analysis and identification of acoustic emission signals is very important for the development of AE-based structural health monitoring systems. By analysing the intrinsic characteristics and rate of occurrence of the types of emissions generated, one would be able to predict the type of damage processes which are occurring at various stages of the life of a structure so that preventive measures can be undertaken for security and economical reasons. For current state of the art AE systems, this is accomplished by extracting various features of acoustic emissions generated during operation for further analyses using pattern recognition techniques. A variety of features such as frequency content, peak amplitude, signal duration, rise time are traditionally used for this purpose. The results depicted here will include traditional standard analysis and the proposed methodology for acoustic emission identification described in Section 4.8.

Table 7.7. *Dimensions of the test specimen (units in mm).*

b_0	L_0	B	r	h	L_c	L_t
20	80	30	20	50	120	250

Tensile Test Experiments were carried out on twenty tensile specimens made out of unidirectional glass fibre reinforced plastic material. This type of material was selected since it is to a certain extent transparent and damage can be identified by visual inspection during the running of the tests. The tensile specimens were prepared according to DIN 50125. The elastic properties in the principal directions of material symmetry provided by the manufacturer are given in Table 7.1. The material constants units are given in *GPa*. Figure 7.16 shows the geometry of a typical specimen. Dimensions are provided in Table 7.7.

The experimental setup consisted of AEP3 amplifiers (Vallen Systems), a HS4 handy-scope from TiePie Engineering and a PC. The amplifier gain was set to $40dB$, the anti-aliasing low-pass and high-pass cut-off frequencies were adjusted to $95kHz$ and $800kHz$, and the sample frequency was $50MHz$. Four broadband AE sensors (VS900-M) were installed on the plate and vacuum silicon grease was used to improve the signals transmission between specimen and sensors. The sensors located near the specimen corners were placed at a distance of $50mm$ from the specimen ends. The remaining sensors were installed at a distance of $30mm$ from each of these sensors. The sensors are numbered from top to bottom. Tensile tests were carried out in an MTS 810 loading machine with a $50kN$ load cell kindly provided by the Research Group for Material Science and Material Testing at the University of Siegen. The crosshead speed was fixed at $0.1mm/min$. The tests were stopped after total failure.

The tests specimens with a unidirectional fibres were loaded along the fibre axis. The fibres are loaded in tension by shear forces transferred from the matrix through the fibre-matrix interface. It is expected that the given composite material consisting of fibres and a polymeric matrix which is subjected to external loading will fail as a result from a combination of damage mechanisms such as matrix cracking, debonding at the fibre-matrix interface and fibre fracture. Ideally, it should be possible to identify individual damage mechanisms by analysing the recorded AE events emitted by the specimen. This is given by the fact that signals arising from events such as matrix cracking, fibre/matrix debonding and fibre breakage are completely different in nature and give rise to different signals. Accordingly, the samples and experiments have been intentionally selected in order to produce this type of damage mechanisms.

For the sake of brevity, only one out of twenty experiments was selected for analysis in this section. However, results were similar for all the tested samples. Figure 7.17 depicts the progressive failure of the specimen where 7.17(a) shows the unloaded specimen. Matrix cracking is normally the first damage mechanism happening in a composite structure

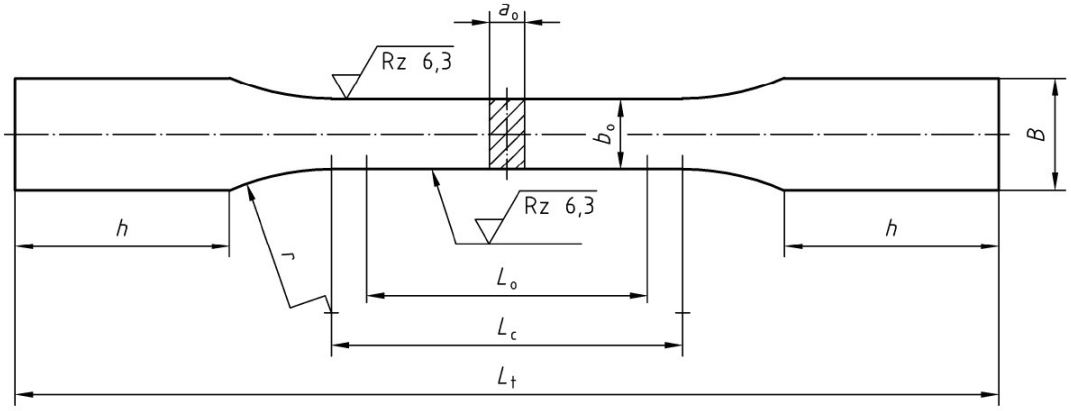

Figure 7.16. *Geometry of the test specimen.*

subjected to a quasi-static or cyclic tensile load (see [Adolfsson and Gudmundson 1997]). Normally, this type of cracks extend across the thickness of the sample and propagate parallel to the fibre direction, and are normally known in the composite materials jargon as ply cracks or transverse cracks. This damage mechanism can be seen in Figures 7.17(b) and (c) by tracking the change in colour of the specimen between sensor 2 and 4. Nevertheless, matrix cracks are rarely critical from a structural failure point of view, but they can lead to possible fibre debonding, fibre fracture and delaminations in case of a laminate. When the matrix fails, the load carried by the matrix is then transferred to the fibres, and given that the breaking stress of the fibres is not exceeded, the fibres will be further extended, leading to multiple cracking of the matrix and possible debonding between the fibres and the matrix. This effect can be observed in Figures 7.17(d) and (f) where one can see how the fibres and matrix are debonded for a certain length. This can also be observed when a strong mechanical bond between the matrix and fibres exists (see [Aveston and Kelly 1973]).

During the experiments, it was observed that cracking still occurred after fibres have debonded. Finally, while the load continues to grow to relatively high load values, fibre breaking starts to happen in the specimen. It can be clearly deducted from the damage evolution phases depicted in Figure 7.17 that keeping track of all of these damage mechanisms and locations is a very complex problem.

The loading curve and accompanying AE parameters, including AE number of hits and AE cumulative sum of signal energy, for the tensile experiment are shown in Figure 7.18. Noise signals coming from specimen slippage in the grips were identified and deleted for the analysis. These signals were characterised by short duration and low amplitude. Additionally, sensors number one and four can be used as guard sensors in order to reject this type of signals. It can be noticed from 7.18(a) that very few acoustic emission events are detected at the lowest loading values. The stable acoustic emission rate in Figure 7.18(a) suggests the irreversible damage accumulation. According to this figure, all sensors appear to have detected almost the same amount of hits per AE event. It can

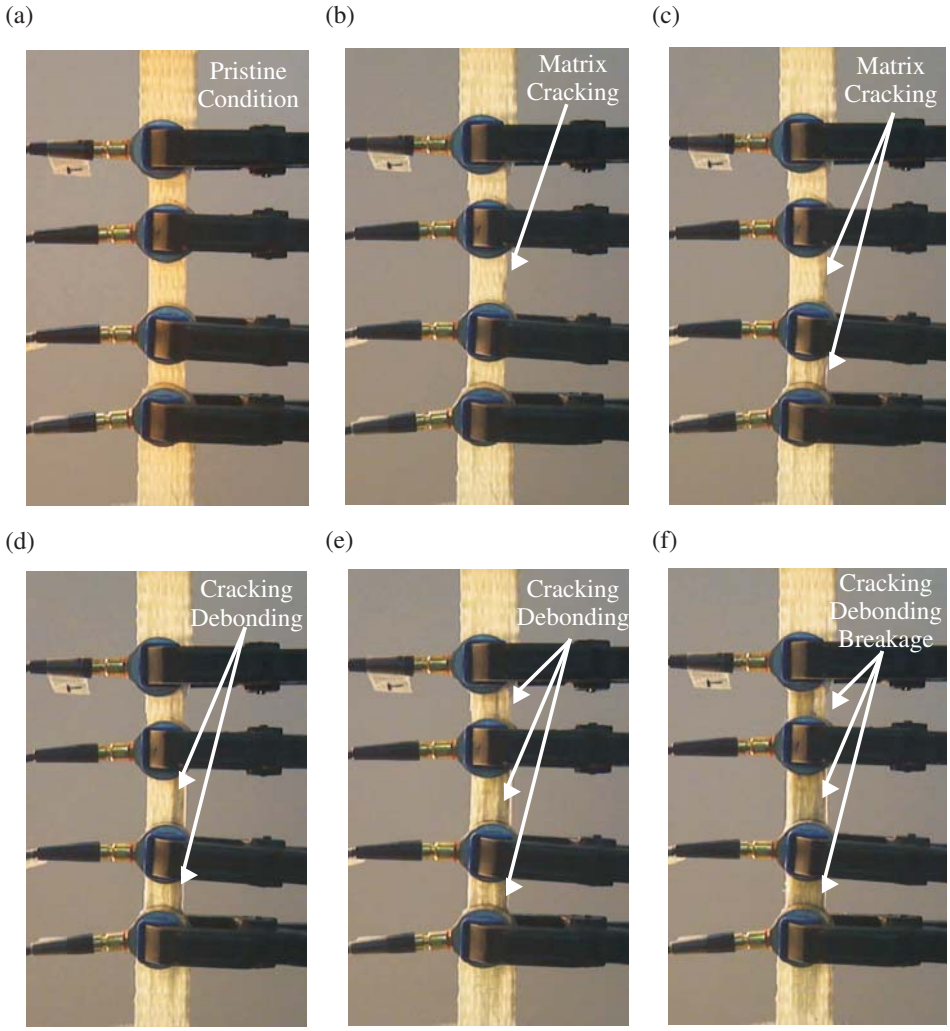

Figure 7.17. *Damage evolution during the tensile test: Progressive failure from undamaged state to total failure is depicted from (a) to (f).*

be seen that AE increased significantly each time the sample was loaded to higher loads. When the load drops and is increased again, AE events do still occur. This appearance of significant acoustic emission events at a load level below the previous maximum applied level is known as the Felicity effect. This effect is typical observed in composite materials. This fact indicates that loads of this magnitude may begin to cause damage to the sample.

The cumulative sum of energy plots depicted in Figure 7.18(b) allow to identify that sensor number four and two were the ones receiving signals with higher amplitudes. It can be additionally observed that after the first drop-off of the load, a drastic increase in the energy of the recorded AE events took place. In this stage, few AE signals with high amplitudes and short durations were detected. For this experiment, no exact source location technique was used in order to try to determine the location of damage.

Figure 7.19 shows the three-dimensional plots relating the amplitude, time of occurrence and number of hits for every sensor in the network. Each sensor output is chosen to $10\mu Volts$ as the $0dB$ reference since it was the lowest detectable voltage above the noise level of the system electronics. The results imply that an observable range of different

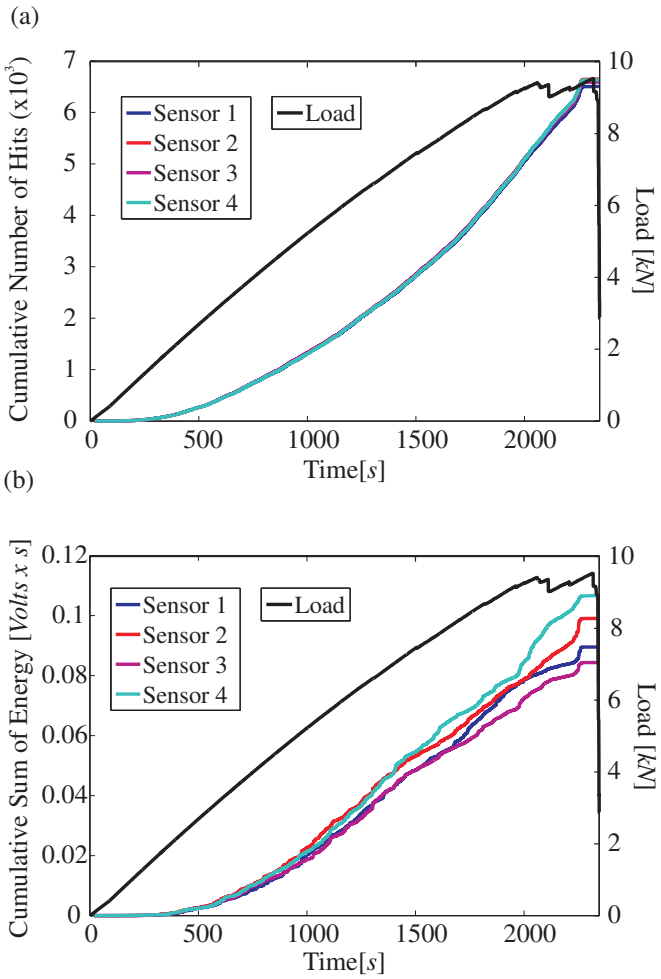

Figure 7.18. *Standard acoustic emission parameter analysis: (a) Cumulative hits plot for every sensor and (b) Cumulative energy plot for every sensor.*

orders of magnitude are detected during the running of the test for the recorded signals. Traditionally, this phenomenon based on the acoustic energy released is used in order to identify the different damage mechanisms.

Based on the analysis and observation of the first appearing damage mechanisms, the first appearing cracks seem to correlate with low amplitude AE events. This is in accordance to existing literature where a typical matrix crack signal is said to be of short duration with a small amplitude and low energy. It can be seen as well from Figure 7.19(a) to (d) that a significant amount of damage signals with low amplitude accumulates before the specimen fails. Nevertheless, this generalization must be done with extreme care since this cannot be generalised for any structure since most composite structures do not exhibit the same plastic-elastic behaviour found in metallic structures. This is supported by the fact that the anisotropic behaviour of the medium causes the wave to propagate with different velocities in different directions and the viscoelastic behaviour of the structure causes damping and dispersion. Thus, the recorded wave arriving at the transducer is a highly distorted and attenuated version of the source waveform. In addition, the frequency response of the transducers and the couplant between the medium and the transducer

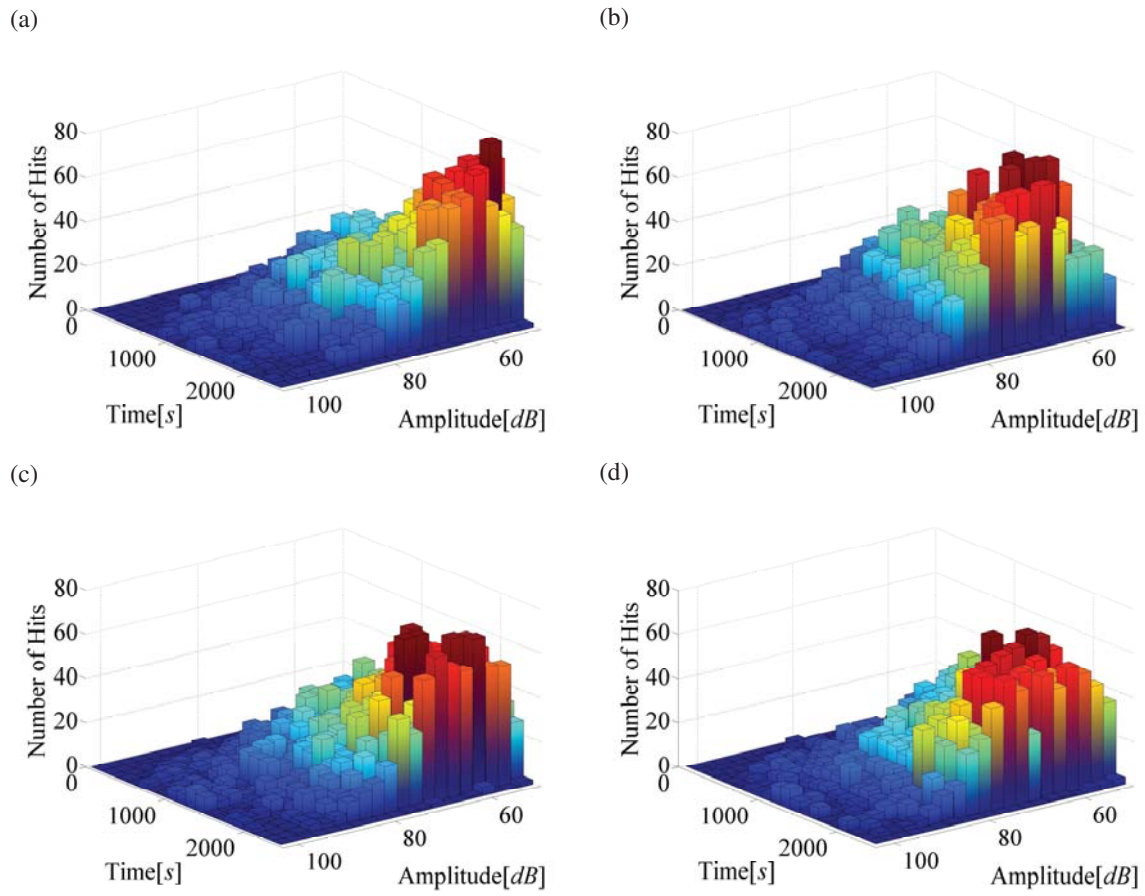

Figure 7.19. *Three-dimensional histograms depicting the time of occurrence and amplitude of the different AE hits in the sensor network: (a) Sensor number one, (b) Sensor number two, (c) Sensor number three and (d) Sensor number four.*

contribute to the general distortion of the recorded signals.

It was observed that large cracks formed just prior to failure and fibre breakage at the last stage before total failure appears to correlate with high amplitude events. The last failure mechanism found during the test, fibre breakage, is typically the most damaging of the mechanisms due to the fact that the fibres are the main load bearing constituents of the structure. Glass fibre breaks have the highest amplitudes of the three primary failure mechanisms. In order to support the statements about the different type of damage mechanisms encounter during the tests, the samples were carefully analysed not only by visual inspection but also by means of a 3D measuring laser microscope. Results are depicted in Figures 7.20, 7.21 and 7.22. A LEXT 3D measuring laser microscope OLS4000 was kindly provided by the Research Group for Material Science and Material Testing at the University of Siegen. The examined samples were covered with gold. It can be seen from Figure 7.20(a) that when the matrix of the continuous fibre reinforced composite fails at a lower strain than the fibres, multiple cracking of the matrix results along the fibre direction. This effect will continue as long as the fibres are strong enough to withstand the additional load.

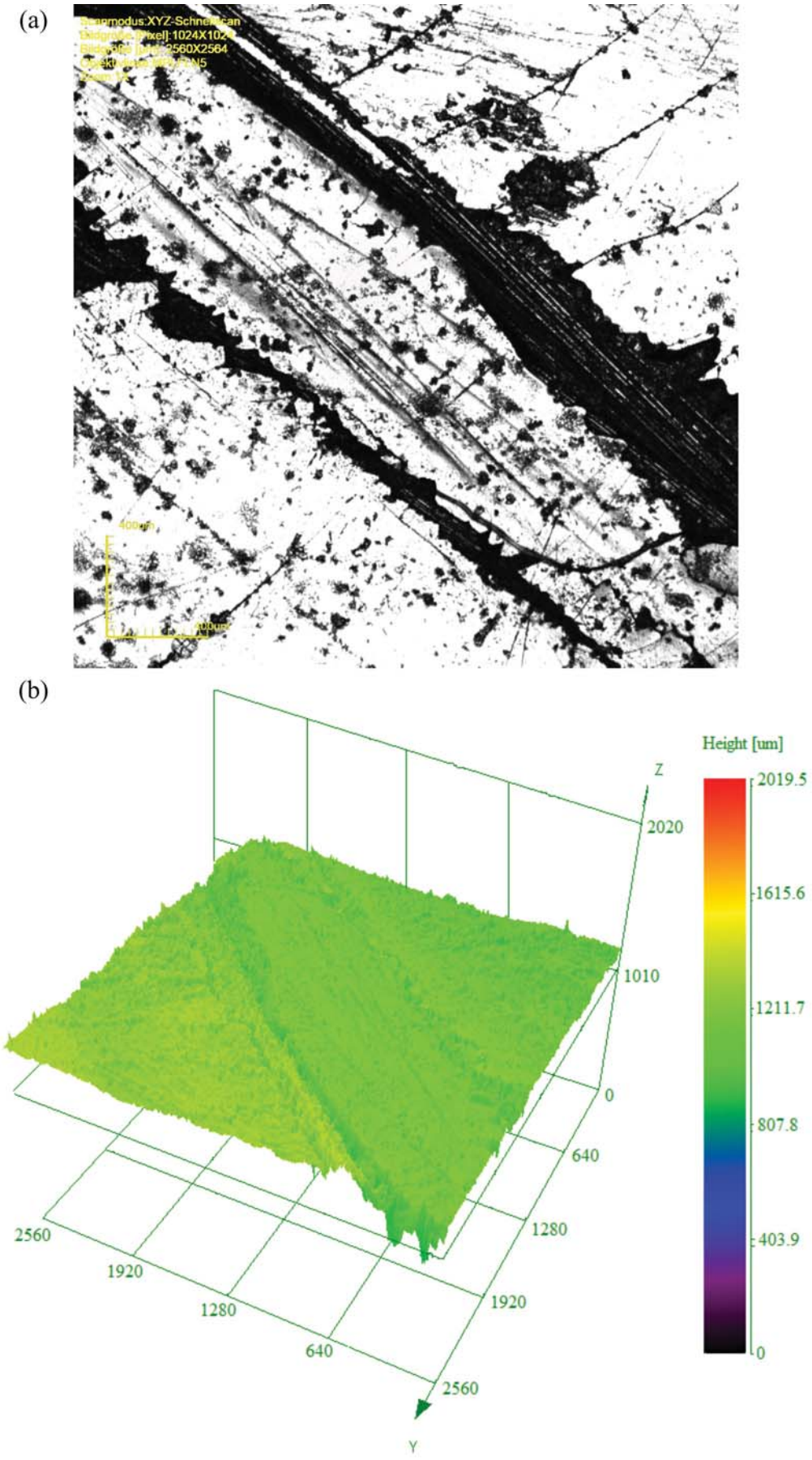

Figure 7.20. *Experimental analysis with the 3D measuring laser microscope for matrix cracking: (a) Top view of the damage and (b) Calculated three-dimensional surface.*

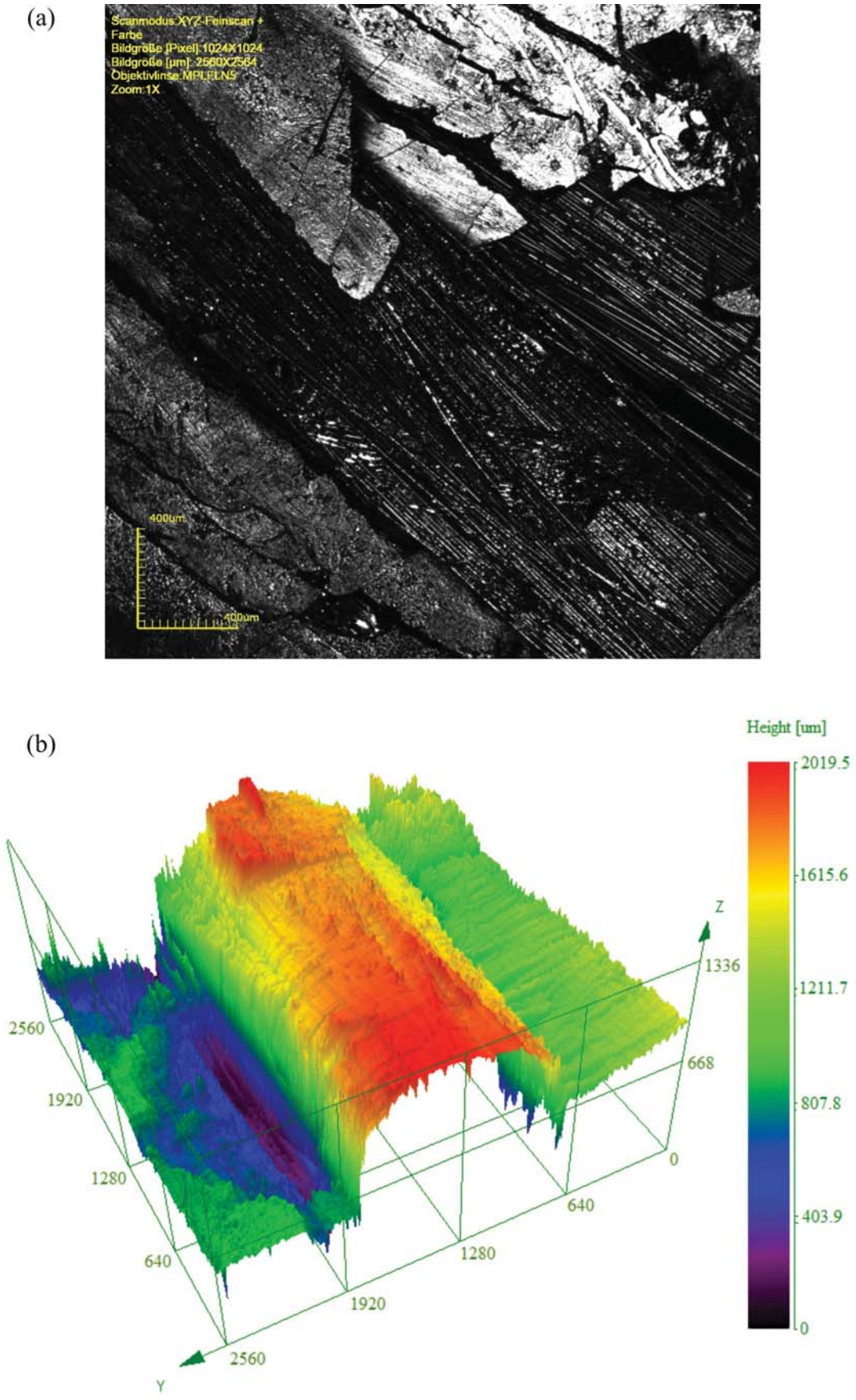

Figure 7.21. *Experimental analysis with the 3D measuring laser microscope for fibre debonding: (a) Top view of the damage and (b) Calculated three-dimensional surface.*

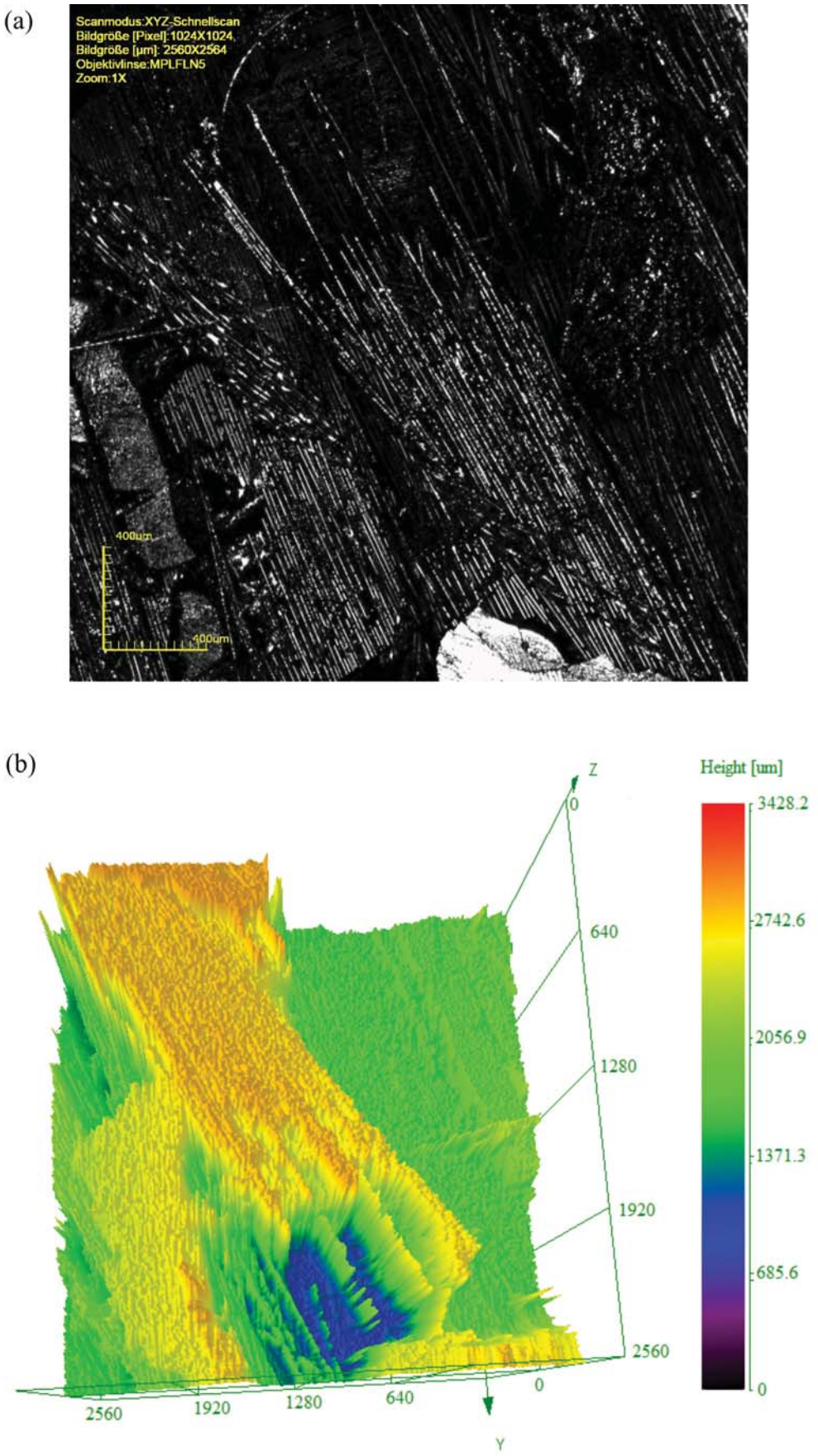

Figure 7.22. *Experimental analysis with the 3D measuring laser microscope for fibre breakage: (a) Top view of the damage and (b) Calculated three-dimensional surface rotated* 180°.

Figure 7.20(b) depicts the calculated three-dimensional surface where one clearly sees how the cracks extend in a direction parallel to fibre orientation in form of a channel. The other type of damage mechanism occurring is fibre debonding as it can be clearly observed from Figure 7.21. Finally, when higher loads are reached, fibre breakage occurs before final failure as it is shown in Figure 7.22. It was observed that the final failure of the specimen was imminent at the onset of fibre breakage. The same experiment was used in order to evaluate the practical performance of the proposed methodology in Section 4.8. If one focuses the attention on the general situations encountered with AE data such as difficulties in generating a training set for analysis, the advantages of using an unsupervised method outweighs the supervised methods. As the first step, the DWT coefficients are calculated from the captured stress waves and fused following the described unfolding procedures. Four levels of decomposition were used for an optimal DWT. Second, a review of the variances retained in the components using standard PCA was performed in order to define the optimal number of principal components required for h-NLPCA. It was found that by selecting 3 components more than 97% of the total variance was retained. The optimal number of units for the mapping and de-mapping layers was calculated using Eq.(2.38). For the experiments depicted here, 84 neurons were used for both layers. In order to define the size of the self-organizing map, the quantization error (QE) and topographic error (TE) were analysed. As a result of the analysis, a map size of 30×10 was defined. Additional to the map size, the map lattice and shape must be specified. The SOM lattice gives the local topology of the map, i.e. the connectivity of the map units. For the present study a hexagonal lattice and a flat sheet shape are considered here. Additionally, a Gaussian neighbourhood function was used.

The correspondence between acoustic emission events and damage mechanisms was validated by comparison between the time of occurrence of the acoustic emission events and the energy distribution analysis explained in the previous section. This is further validated by checking the damage evolution for each tensile test in addition to scanning of the samples. The 3D measuring laser microscope results and careful analysis of the samples during the test showed that the main failure mechanisms of the specimens were matrix cracking and fibre-matrix debonding. In addition, few fibre failures were observed. Fibre breakage and matrix cracking along the fibre direction are characterised by having a highly excited fundamental symmetric mode of propagation, while fibre debonded is characterized by a highly excited antisymmetric mode or propagation. Figure 7.23 depicts an example of the three type of signals identified, each of which was attributed to different damage mechanisms according to the clustering results. The first group is characterised by low amplitude signals believed to represent emissions due to matrix cracking. The second group are high amplitude signals believed to represent emissions due to fibre breakage. The third group are low amplitude signals believed to represent emissions due to fibre-matrix debond-

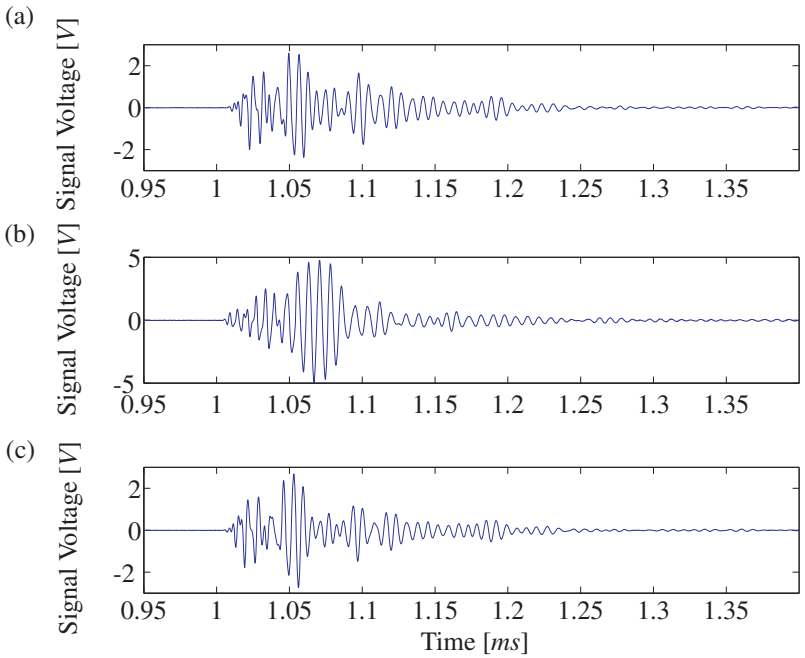

Figure 7.23. *Recorded waveforms for the identified clusters: (a) Matrix cracking, (b) Fibre breakage and (c) Fibre Debonding.*

ing. These results are in good agreement with the relevant literature regarding failure mechanism identification [Guo et al. 1996, Qi 2000, Loutas and Kostopoulos 2009].

The calculated U-Matrix surface is depicted in Figure 7.24 in order to show the formed clusters. As it can be seen from this figure, three clusters are well identified where the zones in lighter colours mark the boundaries. These results further validate the experimental and modal analysis carried out throughout this section. The different clusters have been labelled in Figure 7.24 according to the analysis and explanations given before. One can see how one can increase the understanding and the possibility to interpret the measured AE signals by means of mixing the developed analytical model describing the source mechanism characteristics and pattern recognition approaches.

In addition, even when not discussed here, twelve samples were also loaded with the fibres in a direction parallel to the load. It could be observed that the composites failure in tension resulted as an instantaneous failure for all the samples, being the failure located in the proximity of the sample necks. No clear defined clusters were found for these experiments; only one big cluster seemed to have formed. This could be explained by the fact that only a dominant damage mechanism took place during the failure process, i.e. matrix cracking.

Double Cantilever Beam Tests As it has been shown throughout this thesis, modern structural components are made of materials arranged in layers. Examples are airplanes, ships and large wind turbine blades. Typical examples of damage mechanisms in these structures are delamination of laminates and interface cracks in sandwich structures, ad-

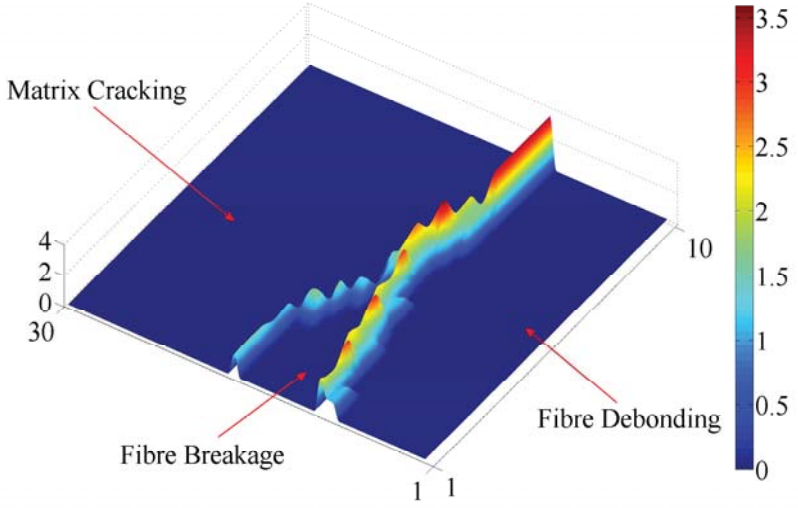

Figure 7.24. *U-Matrix surface for acoustic emission clustering after data-fusion and feature extraction. In-plane axes correspond to the number of neurons.*

hesive joints and multilayered structures [McGowan et al. 2007]. Generally, there are three modes describing different crack surface displacement. Mode I is an opening or tensile mode where the crack surfaces move directly apart. Mode II is sliding in-plane shear mode where the crack surfaces slide over one another in a direction perpendicular to the leading edge of the crack. Mode III is tearing and antiplane shear mode where the crack surfaces move relative to one another and parallel to the leading edge of the crack [Kim 2000]. Cracking of fibre composites frequently occurs together with fibre bridging. Fibres or fibre ligaments continue to be attached to both crack faces and, in consequence, multiple connections between the crack faces behind the crack tip are developed [Soerensen et al. 2004].

The next series of experiments comprised dual cantilever beam (DCB) test series carried out at DTU Wind Risø Campus. The samples were kindly provided by Dr. Helmuth Langmaack Toftegaard. A Laptop based two-channel PAC USB node system with R15-alpha sensors from Physical Acoustics was used for these experiments. The sensors have a resonance frequency at $150kHz$ and use an integral pre-amplifier. The system was calibrated using pencil leadbreaks (Hsu-Nielsen sources) according to the standard ASTM E 976-84. Additionally, the computer program AEwin from Physical Acoustics was used for data acquisition and replay. The sensors were installed at a distance of $90mm$ and $230mm$ away from the upper end of the samples. Sensors were clamped against the outside surface of the specimen without affecting the crack line of the DCB. The amplifier gain was set to $40dB$, the anti-aliasing low-pass and high-pass cut-off frequencies were adjusted to $20kHz$ and $200kHz$, and the sample frequency was $5MHz$. A water based couplant was used to improve energy transfer between sensor and specimen. The AE monitoring proposed here was intended to give information about the initiation and growth

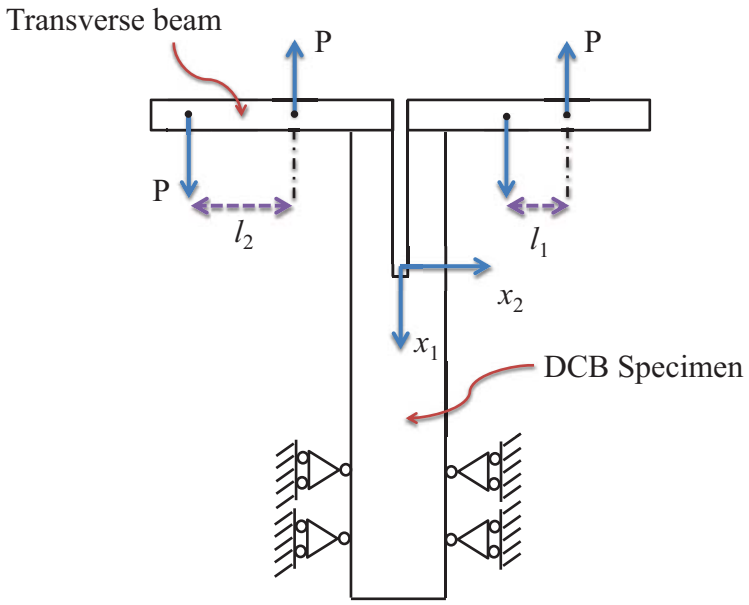

Figure 7.25. *Schematic of the loading method. The mode mixity is controlled by altering the length of one the transverse beam arms.*

of the crack, including localisation information, as well as highlighting differences in the behaviour of the specimen responses when loaded in Mode I and Mode II.

The specimen material used is an E-glass/LPET laminate with the quasi-isotropic lay-up $[(90°45°0° - 45°)_{s2}]_s$. A $13\mu m$ thick release foil was placed with between a layer with 90° orientation (ply 17) and a layer with 45° orientation (ply 18). The foil was placed to help as a pre-crack source and ease crack initiation. The measured fibre and matrix volume fractions are $46.9 \pm 0.1\%$ and $53.1 \pm 0.2\%$, respectively. The volume fractions are given with a 95% confidence interval for the mean. The length, width and depth of the samples were approximately $500mm$, $18mm$ and $30mm$. Details of fibre and matrix properties are proprietary. The principle of creating different bending moments in the two free beams of the double cantilever beam specimen loaded with uneven bending moments (DCB-UBM) specimen is shown schematically in Figure 7.25. Forces of identical magnitude P are applied perpendicular to two transverse arms connected to the end of the beams of the DCB specimen. These are obtained by the use of a wire arrangement. The uncracked end of the specimen is restricted from rotation but can move freely in the x_1-direction. Different moments are obtained if the length of the two moment arms, l_1 and l_2, of the transverse arms are uneven. The applied moments are $M_1 = \mathrm{P}l_1$ and $M_2 = \mathrm{P}l_2$. Further details of the experimental setup can be found in [Soerensen et al. 2006].

The specimens identified as A-01 to A-04 were loaded in mode I (mode mixity 0°) and the specimens B-01 to B-04 were loaded in mixed mode close to mode II (mode mixity 89°). The specimens were loaded at a constant displacement rate of $10mm/min$. The data acquisition frequency for the load control was $20Hz$. During all the tests the applied force was measured with load cells. The damage evolution process during the double

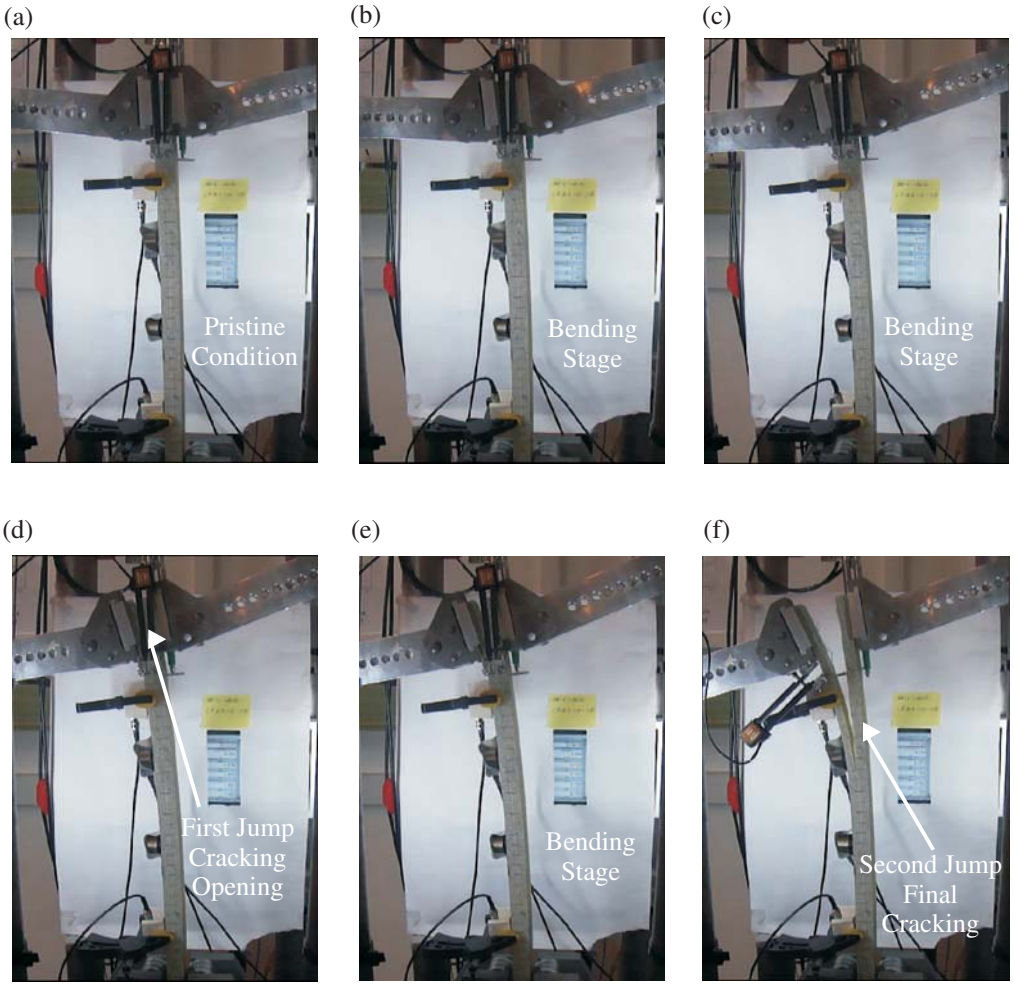

Figure 7.26. *Damage evolution during the double cantilever beam test for Mode II: Progressive failure from undamaged state to total failure is depicted from (a) to (f).*

cantilever beam test for one of the tested samples under Mode II crack growth is depicted in Figure 7.26. A linear localisation array was formed between sensor one (top) and sensor two (bottom) to detect and measure the growth of the crack during both Mode I and Mode II loading. As it could be observed from the test images, in the first part of the experiments, all the samples started to bend without any visual or audible evidence of possible damage initiation, even though, significant AE activity was recorded (see 7.26(a) to (c)). After continuing with the bending phase, a jump in the samples suddenly happened what indicated the initiation of damage, i.e. a initial crack opening which led to further delamination. This is shown in Figure 7.26(d). The crack tip position was located around the top middle position. Following further loading, acoustic events were still recorded and the sample suddenly failed as it is depicted in Figure 7.26(f). No fibre breaks due to fibre bridging could be clearly observed for the tests. The total energy of all the Mode II tests is entirely concentrated in these two bursts related to the main cracking events.

The AE-hit trace recorded for the different types of cracks generated in the samples during the tests are depicted in Figure 7.27. It could be observed that Mode II loading with a

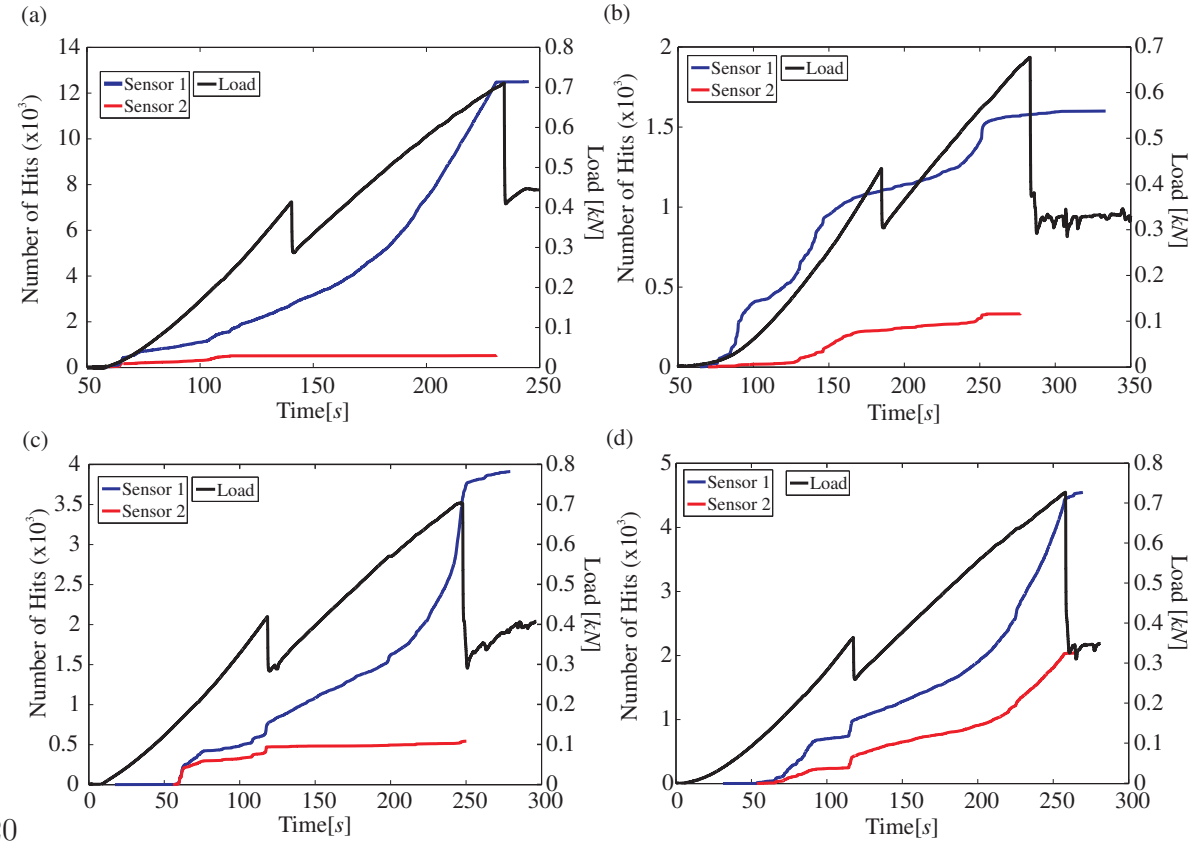

20

Figure 7.27. *Cumulative hits for the four Mode II DCB Tests: (a) Sample B-01, (b) Sample B-02, (c) Sample B-03 and (d) Sample B-04.*

mode mixity of 89 degrees generated a friction dominated crack propagation where the specimen tends to fail in sudden jumps as it can be seen from all plots in Figure 7.27. This effect is very clear if one tracks the load time history in which a significant load drop occurs with crack initiation and final fracture. As previously mentioned, almost of all the recorded AE energy was generated during these two phases. As it was expected due to attenuation of the stress waves and proximity to the damage, sensor number one received the majority of hits for all the experiments. As it was shown before, in composites the high frequency components of stress waves are damped very rapidly, whereas lower frequency components travel much further. It can be seen that The Mode II tests reflected the fact that crack growth is not so steady with exception of the test run with the sample B-01. Table 7.8 summarizes the AE analysis for the calculated AE parameters.

Table 7.8. *Acoustic emission parameter analysis for DCB tests in Mode II.*

Specimen	AE Hits	Counts	Energy	Counts/Hit	Energy/Hit	Energy/Count
B-01	13026	315594	636559	24.2	48.9	2.02
B-02	1934	41466	220445	21.4	114.0	5.33
B-03	4455	107855	217879	24.2	48.9	2.02
B-04	6590	141328	307172	21.4	46.6	2.18
Average	6501	151560	345514	22.8	64.6	2.89

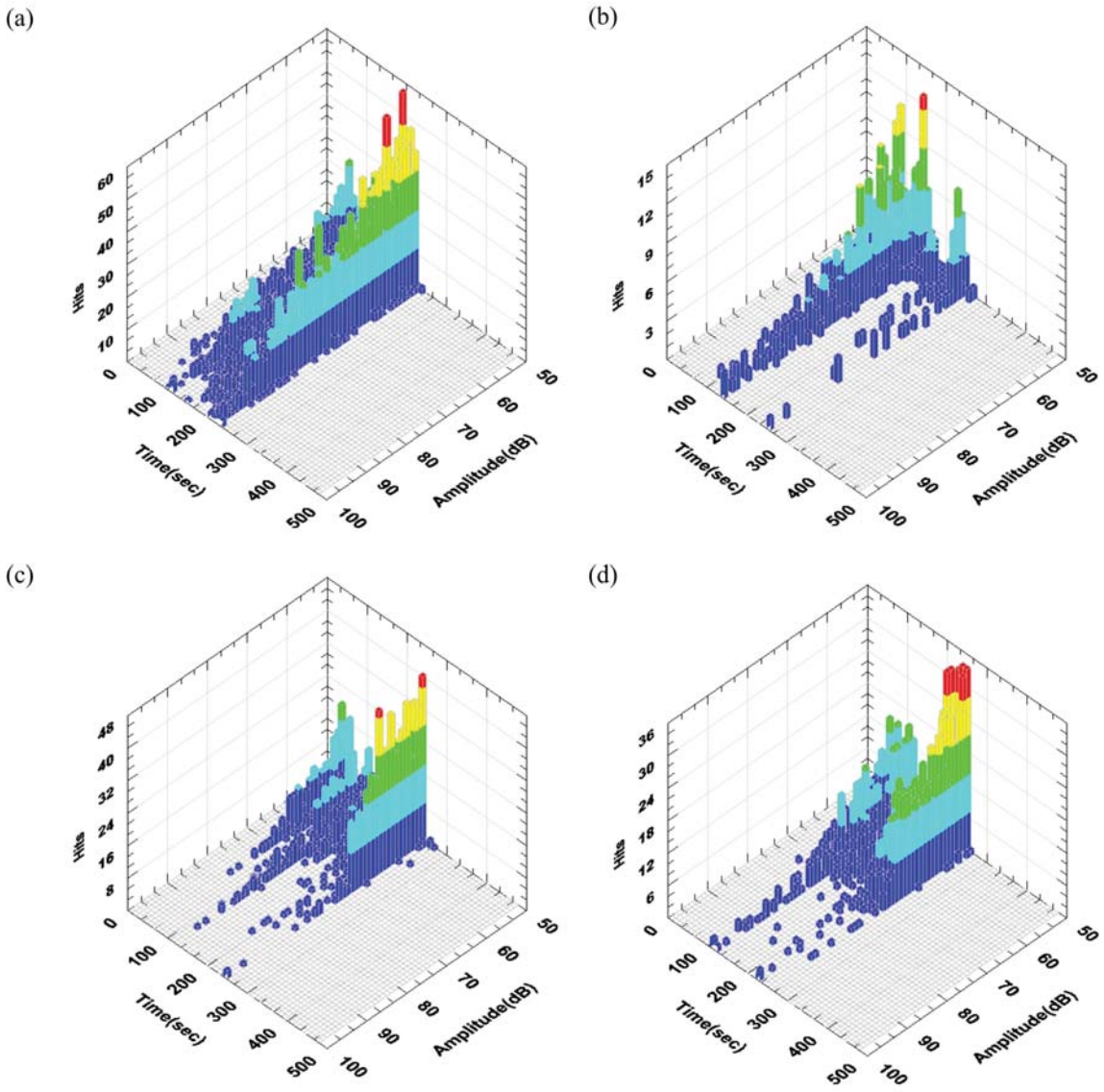

Figure 7.28. *Three dimensional histograms for depicting the time of occurrence and amplitude of the different AE hits in the sensor network: (a) Sample B-01, (b) Sample B-02, (c) Sample B-03 and (d) Sample B-04.*

For all the tested samples, most of the AE events were localised in the close proximity of sensor one. This is further validated by just simply inspecting the deformation and damage evolution of the samples as it is shown in Figure 7.26. The results of hit amplitude distribution with respect to time of occurrence are shown in Figure 7.28. Each sensor output is chosen to $1\mu Volts$ as the $0dB$ reference. At the early stage of loading, it appears to be almost not AE activity. It can be seen from all figures that a few number of low-amplitude AE events are recorded prior to both crack opening and final cracking. These events can be considered as microscale events that do not contain a big amount of energy, however, a huge amount of high amplitude events are produced before the two sudden jumps. These macroscale events, characterised by high amplitudes, can be directly identified during the cracking stages and correlated with the load drops in Figure 7.27.

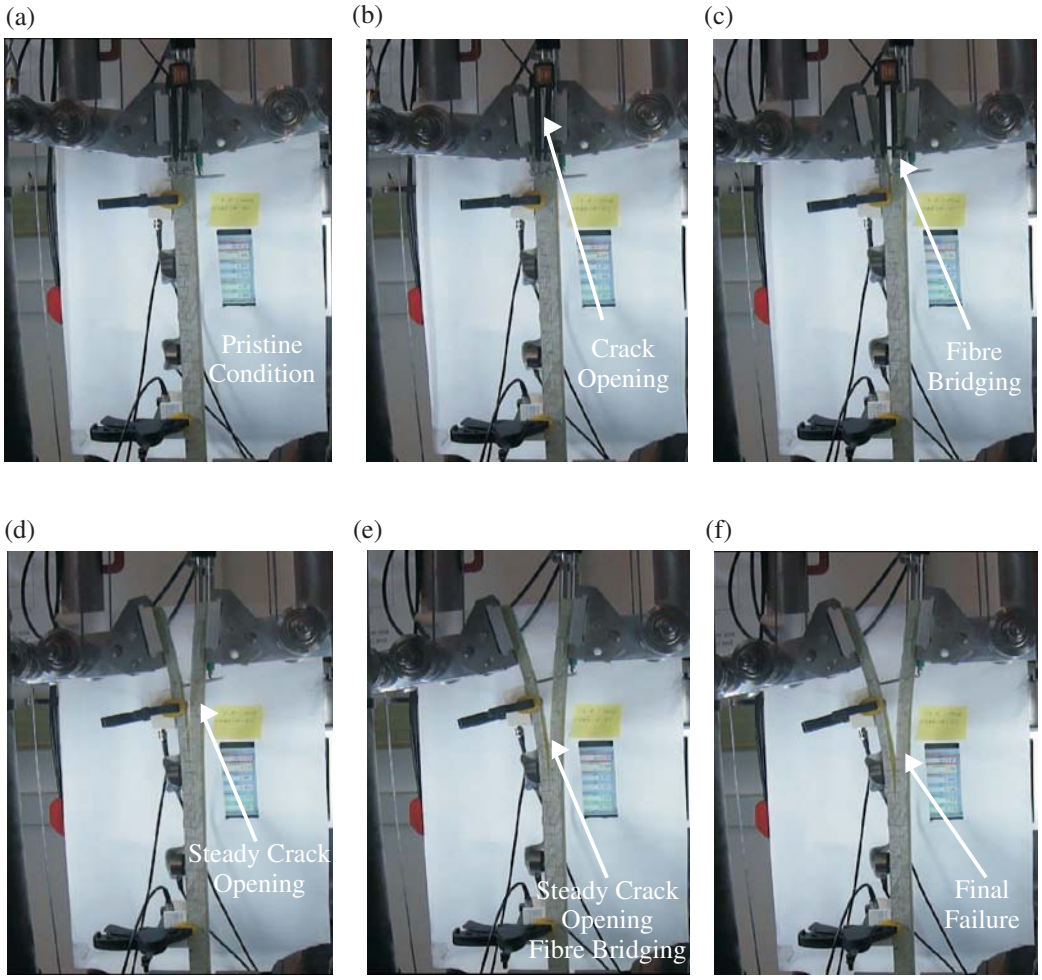

Figure 7.29. *Damage evolution during the double cantilever beam test for Mode I: Progressive failure from undamaged state to total failure is depicted from (a) to (f).*

Mode II tests showed a rapid crack growth with more limited activity behind the crack front. By analysing Figure 7.28, one can infer how the energy release accelerates prior to failure of composite materials. Following this concept, the monitoring of acoustic emission energy would enable to anticipate the failure of the samples as a result of the detection of more energetic signals during the tests. The damage evolution process during the double cantilever beam test for one of the tested samples under Mode I crack growth is depicted in Figure 7.29. Mode I loading with a mode mixity of 0 degrees generates a fibre bridging dominated crack propagation where the crack front develops steadily due to the cohesive zone behind the crack front. For the experiments presented here, the crack growth was controlled and grew very slowly. Delamination propagation was clearly observed during the duration of all the tests. Additionally, fibre breaks could be observed while the delamination process was taking place due to the bridged fibres. No matrix cracks were observed on the delaminated surfaces for the laminates.

The AE-hit traces recorded for the different tested samples are depicted in Figure 7.30. These plots show that the AE activity for the Mode I tests is almost perfectly constant for the entire duration of the crack growth with both sensors responding identically. This

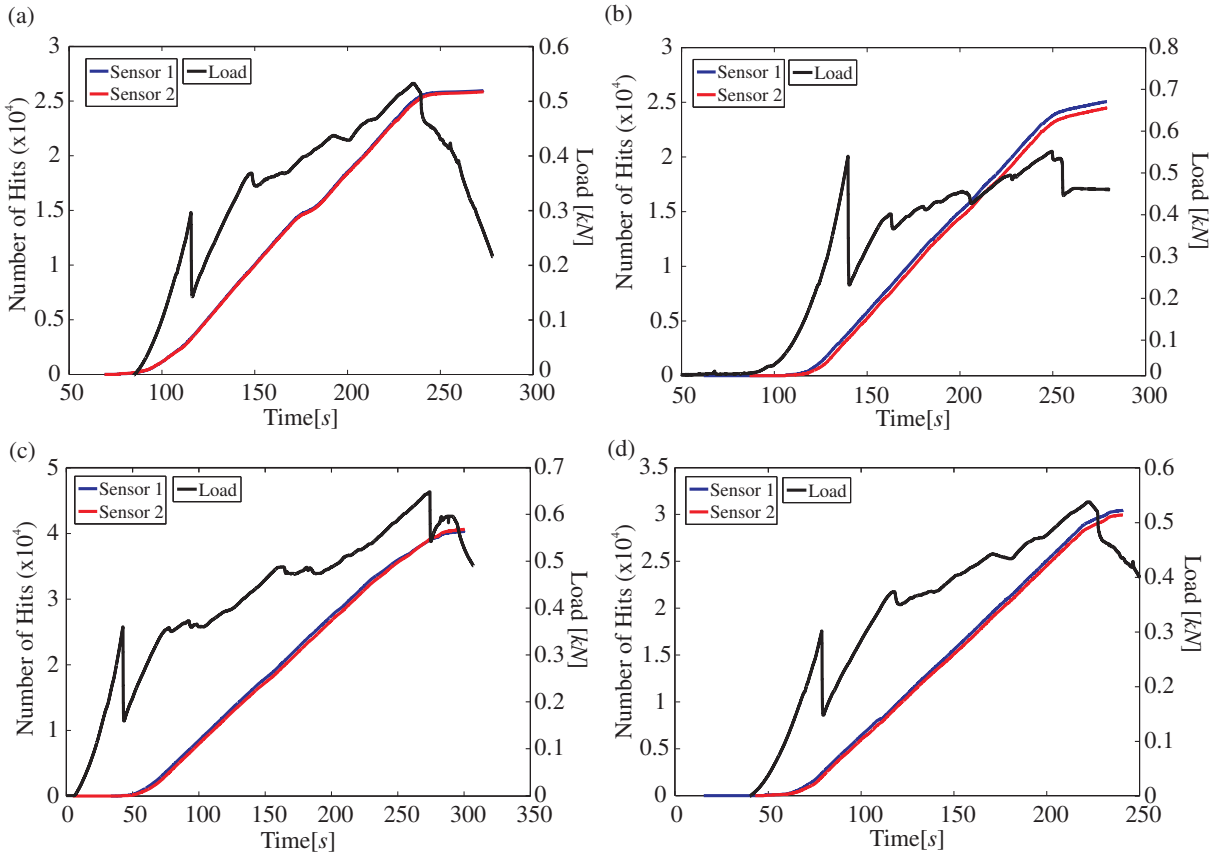

Figure 7.30. *Cumulative hits for the four Mode I DCB Tests: (a) Sample A-01, (b) Sample A-02, (c) Sample A-03 and (d) Sample A-04.*

is in contrast to the Mode II tests showing an unsteady crack growth. A considerable load drop is only seen for the case of crack initiation. Nevertheless, the crack growth took place via a series of small load drops. These load drop points correspond to damage initiation and accumulation, respectively. In comparison to the Mode II tests, a huge number of hits was recorded. As a consequence, more energy is released during the Mode I tests. Additionally, a crack propagation process involving fibre bridging would be expected to have many microscale AE events than one that does not [McGugan et al. 2006]. Table 7.9 summarizes the AE parameters calculated for the specimens under Mode I crack growth.

The character of the AE is significantly different between the tested samples under Mode I and Mode II crack growth, with the Mode I tests showing longer duration hits with greater energy content, but the Mode II acoustic emission has a slightly higher energy

Table 7.9. *Acoustic emission parameter analysis for DCB tests in Mode I.*

Specimen	AE Hits	Counts	Energy	Counts/Hit	Energy/Hit	Energy/Count
A-01	51805	3280766	5138185	63.3	99.2	1.57
A-02	49536	3615485	7182435	73.0	145.0	1.99
A-03	80969	6232135	11612661	77.0	143.4	1.86
A-04	60369	4910615	8849783	81.3	146.6	1.80
Average	60670	4509750	8195766	73.6	133.6	1.80

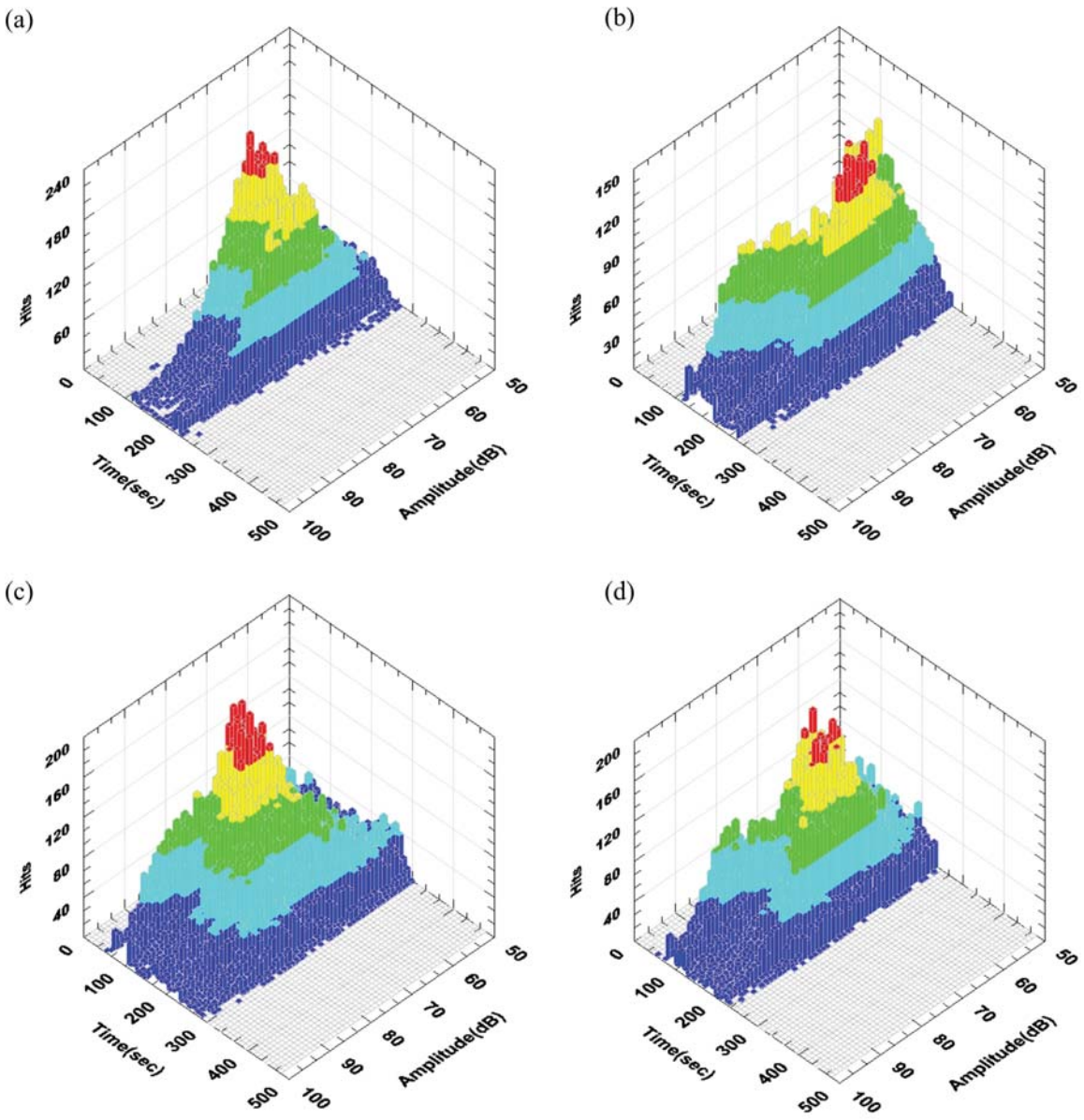

Figure 7.31. *Three dimensional histograms for depicting the time of occurrence and amplitude of the different AE hits in the sensor network: (a) Sample A-01, (b) Sample A-02, (c) Sample A-03 and (d) Sample A-04.*

density, i.e. the Energy/Count value. An analysis of the hit amplitude distribution with respect to time of occurrence between the samples shows a great similarity between the tests. These results are depicted in Figure 7.31. It can be seen that a huge number of hits with medium amplitude occurred during the tests (around $60dB$ to $75dB$). This intense activity appears to show around the same experiment time for all the tests. The AE amplitudes increased to a maximum value and steeply decreased before final failure. This evolution is observed for all the tests. This behaviour of AE activity and energy seems to be an interesting way of anticipating the final failure. Here again, the AE energy released during the tests was found to accelerate before ultimate failure.

For the localisation calculations, the longitudinal and transverse velocities are defined

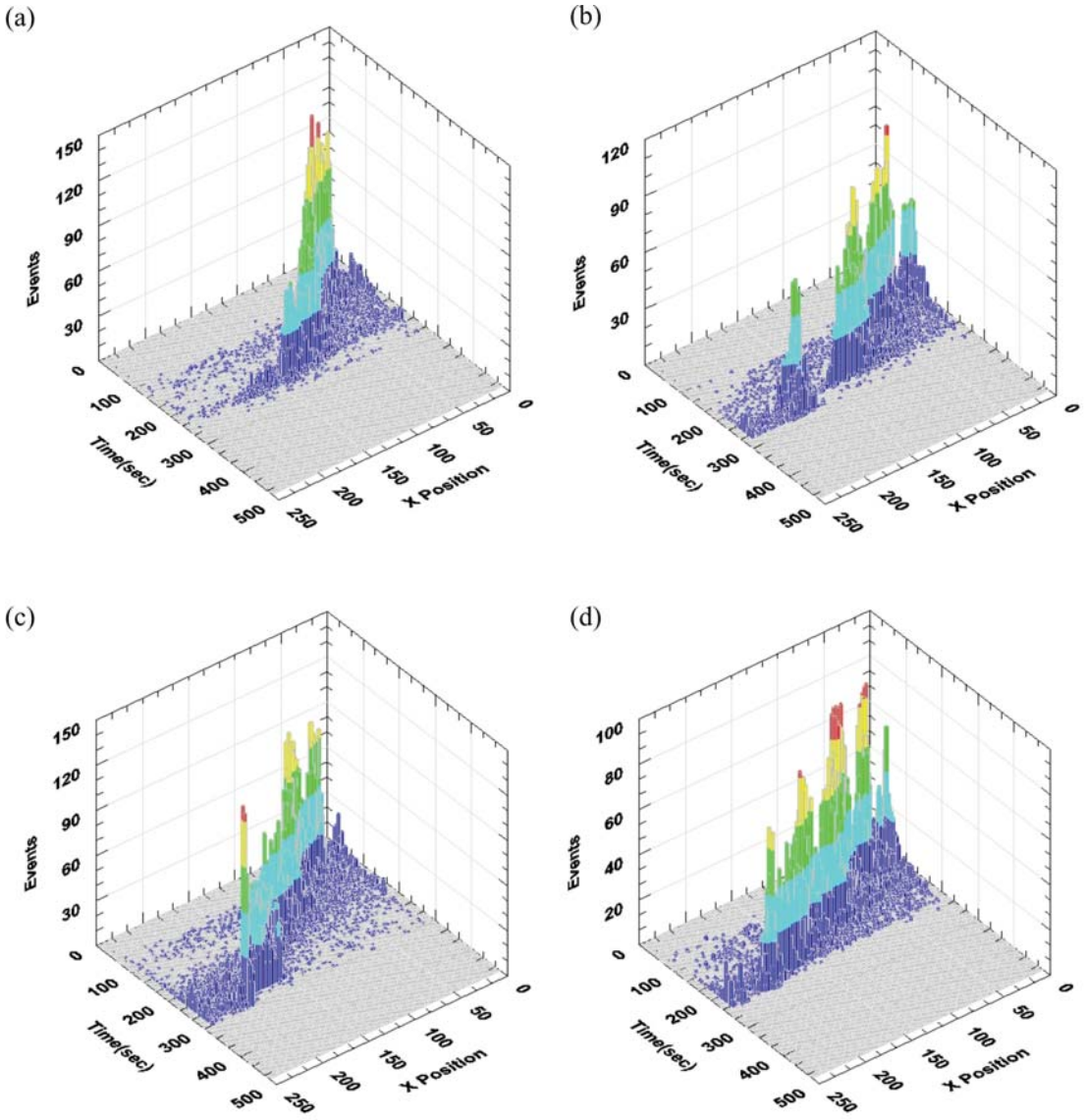

Figure 7.32. *Linear localisation results: (a) Sample A-01, (b) Sample A-02, (c) Sample A-03 and (d) Sample A-04.*

as $C_L = 2.73km/s$ and $C_T = 1.43km/s$, respectively. Linear localisation results for all the tested samples are shown in Figure 7.32. It can be observed that the Mode I localisation shows the crack front progressing with a large amount of AE activity taking place behind it, i.e. in the fully developed bridging zone. According to the obtained results, all the detected AE events seemed to have been well localised.

The succeeding damage processes were quite different for both samples; accumulation and sudden growth of delaminations were observed in samples subjected to Mode II failure, while fibre bridging, sudden fibre fractures and delaminations occurred in samples under Mode I failure. In order to find correlation between the recorded AE signals and the observed damage mechanisms, the methodology proposed in Section 4.8 is evaluated. As it is performed with the proposed methodology, following the calculation of the DWT coefficients calculated from the captured stress waves and the unfolding procedure for

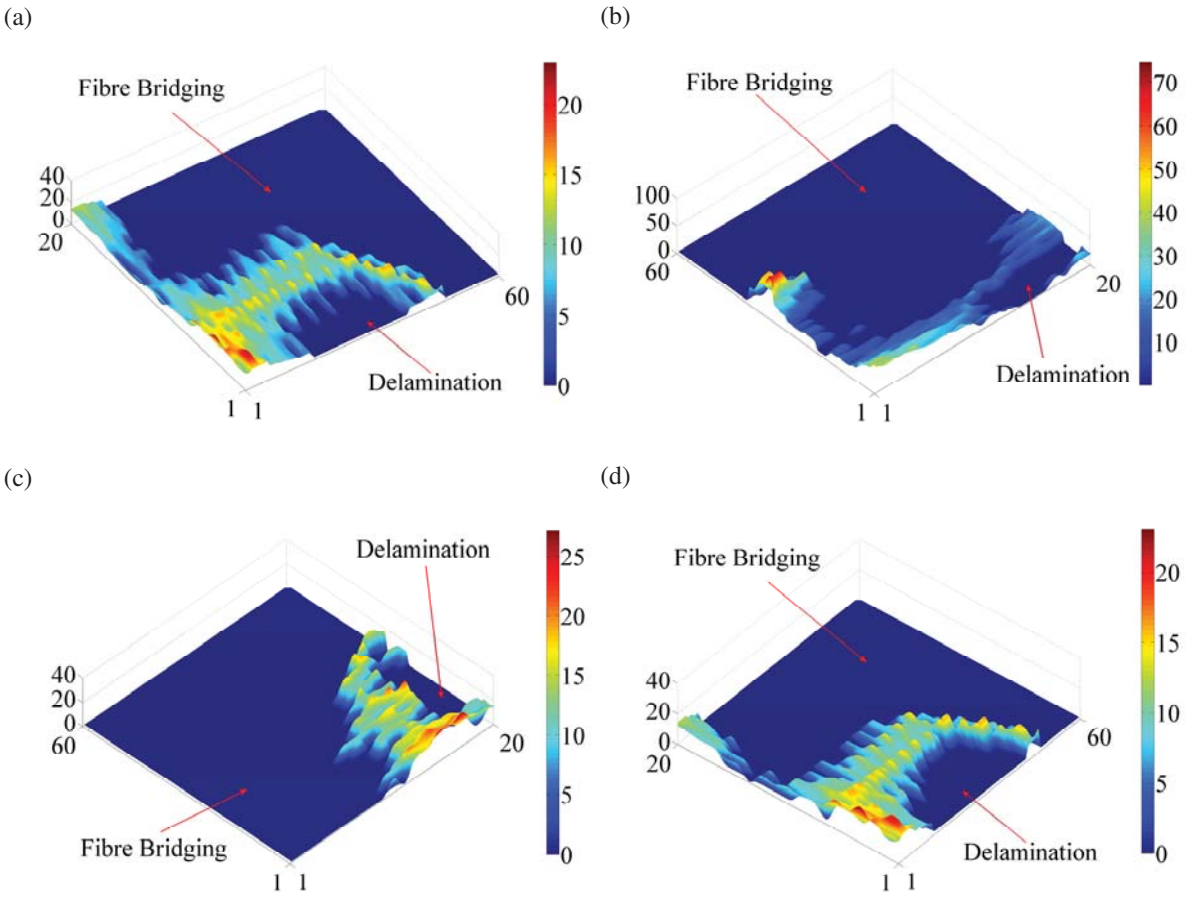

Figure 7.33. *U-Matrix surface for acoustic emission clustering after sensor data-fusion and feature extraction: (a) Sample A-01, (b) Sample A-02, (c) Sample A-03 and (d) Sample A-04. In-plane axes correspond to the number of neurons.*

sensor-data fusion, a review of the variances retained in the components using standard PCA is performed. It was found that by selecting 10 components more than 95% of the total variance was retained. This number of components was selected for h-NLPCA. Four levels of decomposition were used for the DWT. The optimal number of units for the mapping and de-mapping layers was calculated using Eq.(2.38). For the experiments depicted here, 120 neurons were used for both layers. In order to define the size of the self-organizing map, the quantization error (QE) and topographic error (TE) were analysed. As a result of the analysis, a map size of 60×20 was defined. For the present study a hexagonal lattice and a flat sheet shape are considered here. Additionally, a Gaussian neighbourhood function is used. For the specimens loaded under Mode II, following similar clustering results to the tensile tests with load normal to the fibre direction, no clear defined clusters were found. For these tests one big cluster seemed to have formed with no identifiable boundaries. This again could be possibly explained since only one dominant and discrete type of damage mechanism governed the failure process. However, results for the samples loaded under Mode I provided more detailed information regarding the clustering of AE events. The calculated U-Matrix surfaces for the Mode I tests are depicted in Figure 7.33.

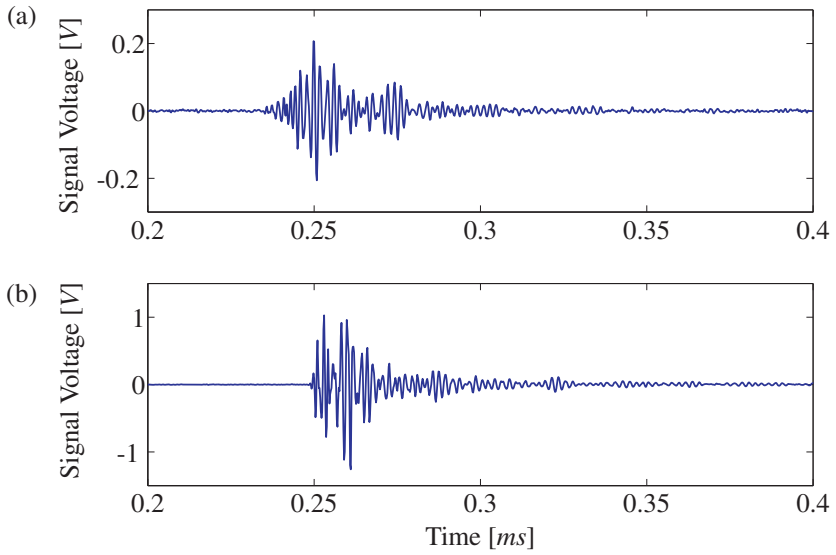

Figure 7.34. *Recorded waveforms for the identified clusters: (a) Fibre Bridging related damage and (b) Delamination.*

As it can be seen from this figure, two clusters are well identified where the zones in lighter colours mark the boundaries. With exception of the case for the second sample, i.e. A-02, all the clusters were separated by well-defined boundaries. Additionally, it is very interesting to see that the cluster shape keeps a good similarity for the tests, specially for the case of samples A-01 and A-04. Conclusively in all samples, the correlation between the resulted clusters from the pattern recognition of experimentally recorded AE events and damage mechanisms is delamination between the middle plies and fibre bridging-related events such as fibre breakage. Figure 7.34 depicts typical signals coming from these clusters. One can observe how the signals generated by fibre bridging effect have a small amplitude compared to the energetic signals produced by the delamination process. It can be also seen that not only the number of AE hits, amplitude distribution and energy content but also the feature extraction and patter recognition approaches provide a solid insight for the way damage develops. For all the experiments carried out in this section, the analysing parameters peak definition time (PDT), hit definition time (HDT) and hit lockout time (HLT) were set to the following values: $\mathrm{PDT} = 35\mu s$, $\mathrm{HDT} = 150\mu s$ and $\mathrm{HLT} = 300\mu s$, whereas the recording threshold was set at $40dB$.

7.4. Damage Assessment with Acousto-Ultrasonics

This section presents the evaluation of the data-driven multivariate methodology proposed in Chapter 5 as a reliable method for damage detection. The proposed structural health monitoring (SHM) methodology is based on a network of piezoelectric transducers operating in pitch-catch mode to excite and record information on the structural condition and inform the user of the presence of any damage. A combination of time-frequency analysis, auto-associative neural networks for data-driven system modelling, squared pre-

Table 7.10. *Material properties of a single carbon fibre reinforced lamina (units in GPa).*

E_{11}	E_{22}	G_{12}	G_{13}	ν_{12}	ν_{13}	ν_{23}
142.6	9.65	6.0	6.0	0.334	0.328	0.54

diction errors and self-organizing maps is developed to automate the damage detection and identification problem. The problem is then treated as one of pattern recognition. For the creation of the self-organizing maps, all the studies presented used a hexagonal lattice and a flat sheet shape was considered for ease of visualization. Additionally, a Gaussian neighbourhood function is used. For all the experiments depicted in this section, the processing engine for transmitting the waveform signal and acquiring the dynamic responses was written in Matlab® 7.9 using the DLLs provided by TiePie Engineering running under Windows operating system. The input signal to the selected actuators was generated using the arbitrary signal generation capability of a HandyScope HS3. The receiver sensors are connected to the input channels of auxiliary HS4-HandyScopes. The time histories are digitised at a sampling frequency of $50MHz$ and transferred to a portable PC for post-processing. The record length was set to 30000 points and the recording triggering source was defined as the generator.

7.4.1. Aircraft Composite Skin Panel

The first structure to be studied is a simplified aircraft composite skin panel made of carbon fibre reinforced plastic. The structure is depicted in Figure 7.35(a). The overall size of the plate is $500mm \times 500mm \times 1.9mm$ and its weight is about $1.125kg$. The stringers are $36mm$ high and $2.5mm$ thick. The properties of the unidirectional (UD) material are given in Table 7.10. The fibre volume is equal to $V_{Fiber} = 60\%$. The plate and the stringers consist of 9 plies. Four piezoelectric transducers PIC-151 from PI Ceramics are attached to the surface of the structure with equidistant spacing. The piezoelectric transducers have a diameter of $10mm$ and a thickness of $0.5mm$.

Localized Mass Problem Firstly, damage on the multilayered composite plate is simulated by placing magnets with the same mass at random orientations on both surfaces of the structure as artificial damage as it is depicted in Figure 7.35(b). The magnets have a disk shape and their diameter, height and mass are $12mm$, $5.26mm$ and $0.004kg$, respectively. The reason for using this approach for damage simulation is that local stiffness reductions will reduce the natural frequencies and an alternative way of reducing the frequencies might be to locally increase mass [Worden and Manson 2007]. Additionally, the contact area of the magnets and the structure surface will help for energy leakage of the interacted guided wave. For the case of this study, the aim of this form of artificial damage was to introduce reversible changes in the structure along the wave propagation

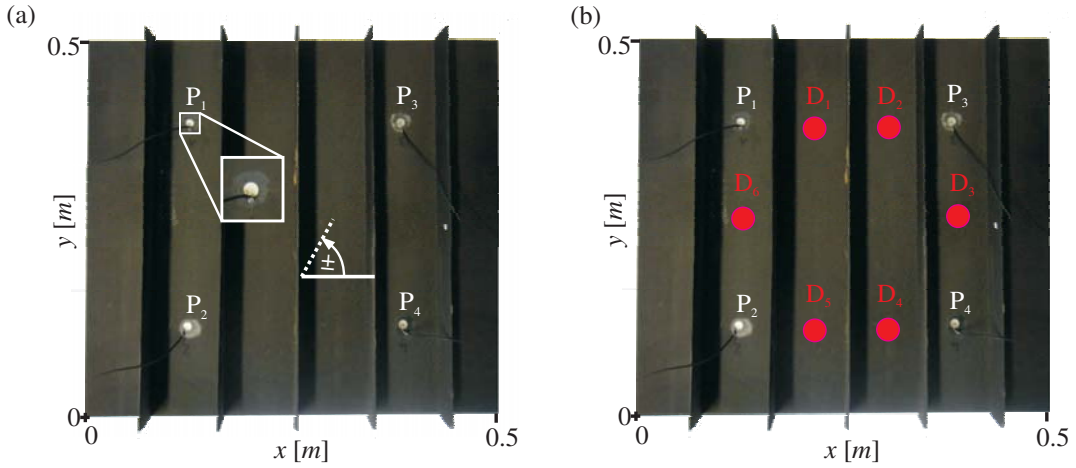

Figure 7.35. *Simplified aircraft composite skin panel: (a) Setup and (b) Damage Positions.*

paths without destroying the structure.

The excitation voltage signal is a $12V$ Hanning windowed cosine train signal with 5 cycles; 150 experiments were recorded per sensor-actuator configuration. To determine the carrier central frequency for the actuation signal in the structure, a frequency sweep was performed and the spectral content of each signal was analysed. The optimal carrier frequency was found to be $50kHz$ for the structure. The carrier frequency was chosen to maximize the propagation efficiency. This type of excitation generates a dominant A_0 mode that is propagated along the structure allowing a better interaction of the guided wave with the simulated damage. In order to evaluate the identification capabilities of the SOM with regard to the input feature vectors generated by the proposed methodology, seven different states of the structures were tested, i.e. the undamaged structure and six localized and independent damages. Table 7.11 outlines the coordinates for the simulated damages on the composite skin panel.

As it was introduced in Section 5, auto-associative neural networks (h-NLPCA) are trained independently using the calculated DWT approximation coefficients extracted from the healthy system in order to build the models. The details coefficients are not taken into account in this study since they are going to be discussed in the next subsection in detail. For the current example, a level eight decomposition was accomplished as the optimal decomposition level. However, before training the network, the data gathered in each

Table 7.11. *Damage locations in the simplified aircraft composite skin panel.*

Damage Number	x position (mm)	y position (mm)
1	208.25	400
2	291.55	400
3	374.55	250
4	291.55	100
5	208.25	100
6	124.95	250

actuation step were fused following unfolding procedures.

As a first step, an outlier analysis is performed using standard PCA and h-NLPCA as it is explained in Section 5.6.3. A review of the variances retained in the components was performed in order to define the optimal number of components required for building the models from the pristine structural condition. For this purpose, standard PCA was performed first. It was found that the first three components included around 80% of the total variance into the reduced model. This previous analysis is important in order to ensure that enough variance is retained in the model that allows performing an optimal reduction. A similar analysis was performed for each actuation step and finally, three components were selected as a good representation of the input data for the h-NLPCA. This a reasonable option since it is expected that h-NLPCA will describe the data with greater accuracy and/or by fewer factors than standard PCA. The optimal number of units for the mapping and de-mapping layers was calculated using Eq.(2.38). For the experiments depicted here, 32 neurons were used for both layers.

In this work, the threshold is calculated from the baseline data. As it was explained in Section 5.6.3, the threshold is adjusted to $\mu + \varsigma\sigma$, where μ is the mean value, σ is the standard deviation value of the novelty index over the baseline, i.e. the undamaged structure, and the factor ς controls the degree of confidence. The confidence level is defined to be 99.99% in this study. For the experiments presented here, not all the baseline data were used for building the models. The models were built with 35% of the total data and the remaining percentage was used for validation purposes. The results of applying PCA and outlier analysis as explained before show that damage can be separated from the pristine state using only the first three linear components for all the actuation steps as it is depicted Figure 7.36(a) to (d).

Nevertheless, it can also be observed that when the different simulated damages are projected into the baseline and the discordance index is calculated, these damages cannot be clearly distinguished. Additionally, one can notice how the first two actuation steps, i.e. the actuation for transducer one and two, provide a more compact representation of the novelty index in which this value is concentrated in a well-defined cloud around the value of one. This is not case for the last two actuation steps, i.e. the actuation for transducer three and four, where a clear higher deviation of the novelty index around the value of one is present. The explanation for this effect is not clear and require further study. However, theoretically, one would expect to obtain a similar behaviour in all the actuation steps due to the geometrical symmetry of the structure.

Following the outlier analysis with the help of h-NLPCA, the results are similar to the ones obtained by applying PCA. In this case again, damage can be separated from the pristine state using only the first three non-linear components for all the actuation steps. Results are depicted in Figure 7.37. In comparison to the previous case, the distribution of the novelty index value seems to be relatively better concentrated around the value

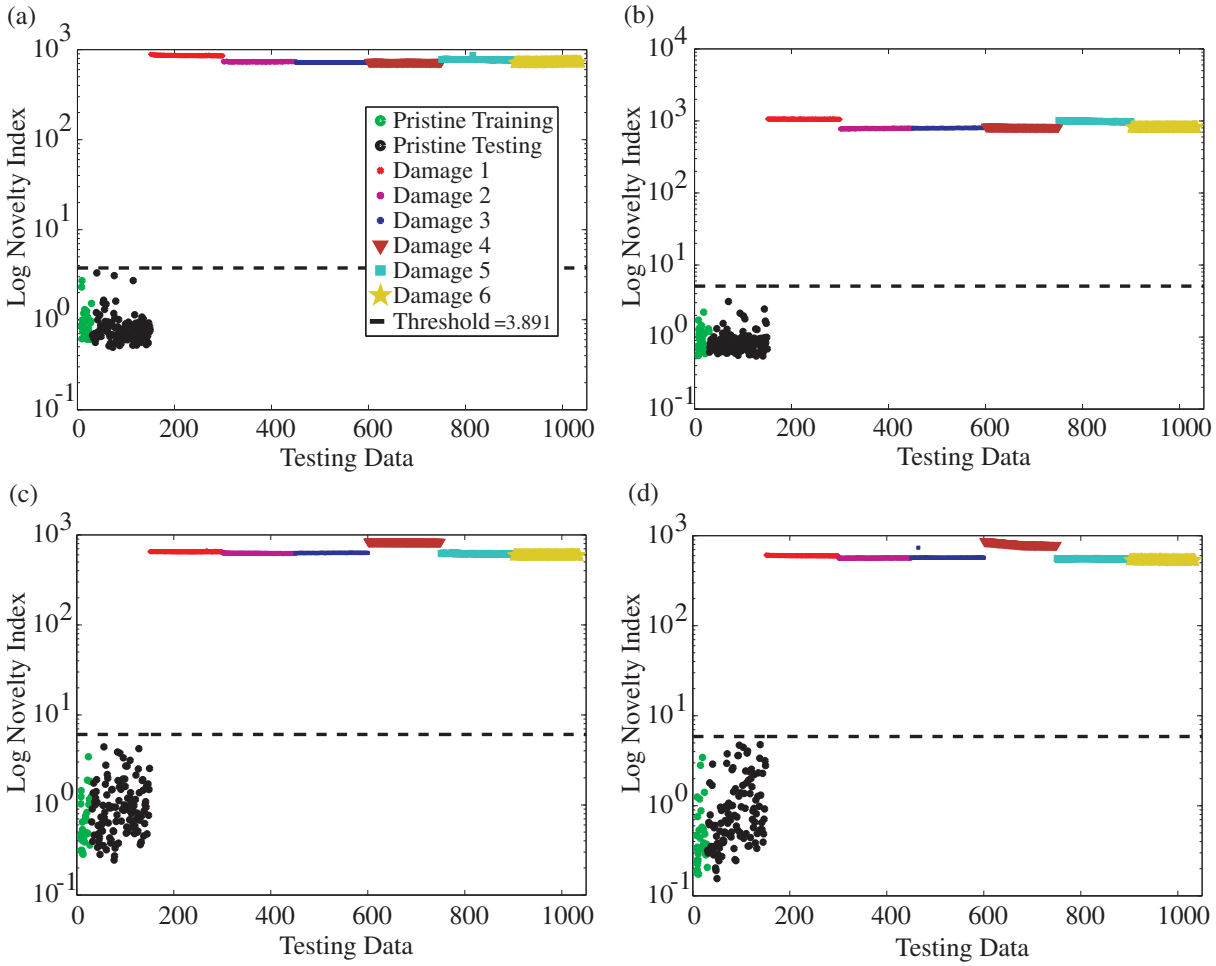

Figure 7.36. *Outlier analysis by means of PCA: (a) Actuator 1, (b) Actuator 2, (c) Actuator 3 and (d) Actuator 4.*

of one in almost all of the actuation steps. Nevertheless, there seems to be almost no considerable differences between both algorithms for the outlier analysis results.

One disadvantage of using the outlier analysis is that, even when unfolding procedures are taken and the sensor data are fused, the information from all the actuation steps (models) must be analysed independently. This is not the case for the methodology proposed in this thesis. The advantage of the proposed methodology is the ability to fuse all the information contained in the different actuation steps for the analysis rather than just analysing each actuation step one by one. The results obtained applying the proposed methodology with help of PCA, SPE measures and SOM are presented in Figure 7.38.

The SOM training algorithm used here is implemented in a Matlab®-Toolbox created by [Vesanto et al. 2000]. To find the optimal map size, a control run is repeated by changing the map size. In order to accomplish the selection of the optimal map size, the average quantization error (QE) and topographic error (TE) were analysed. As a result, a map size of 30×10 was defined. Nonetheless, for a proper understanding of the figures, some properties of the U-Matrix must be discussed. It is good to bear in mind that the mountain-like surfaces formed on a U-Matrix surface define the cluster boundaries. Valleys

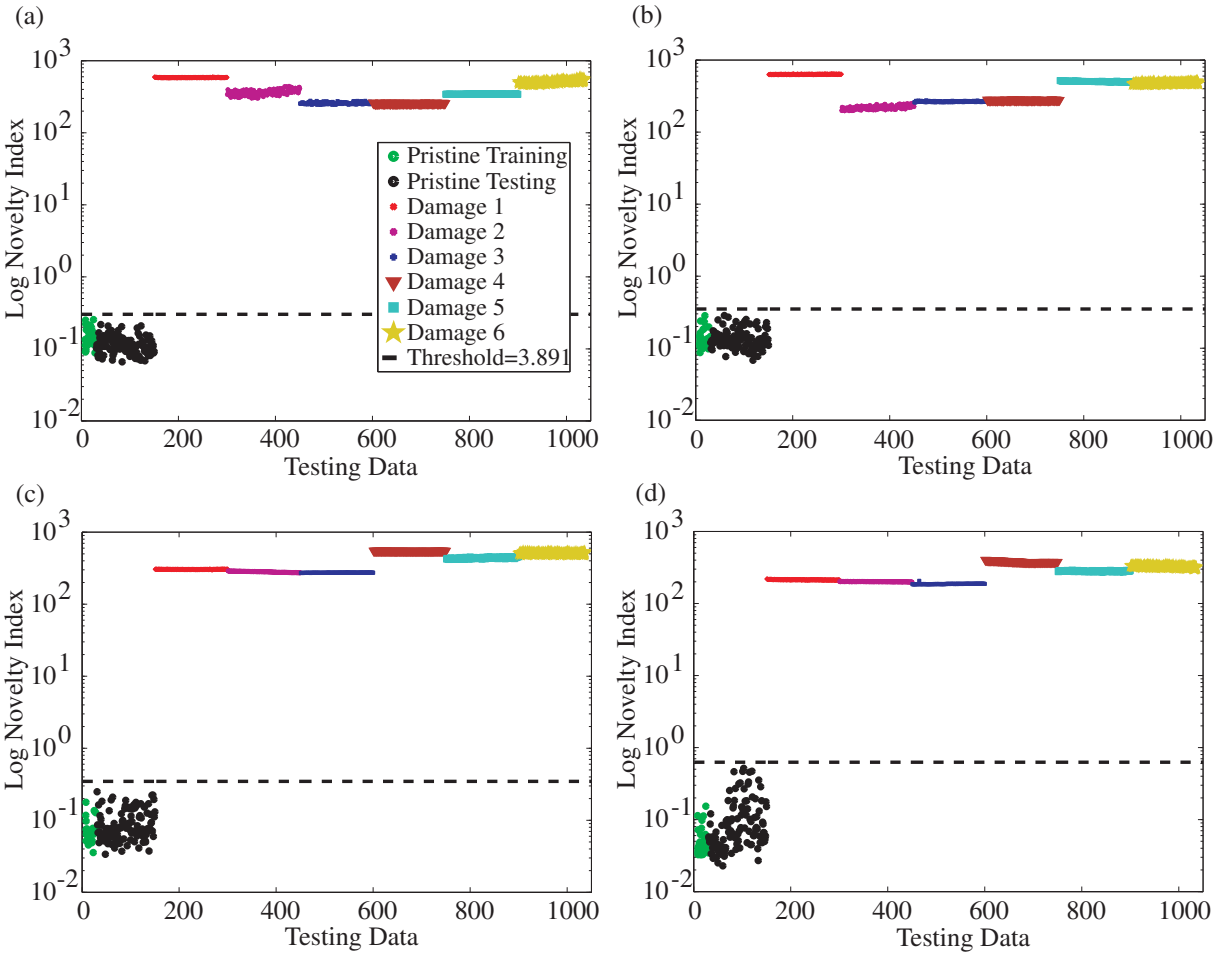

Figure 7.37. *Outlier analysis by means of h-NLPCA: (a) Actuator 1, (b) Actuator 2, (c) Actuator 3 and (d) Actuator 4.*

on a U-Matrix surface point to cluster centres. The cluster maps in Figure 7.38(a) can be used as a tool to show the different data sets grouped with similar characteristics showing the clustering tendency. However, in this specific case, no clear cluster separation between all the damage scenarios can be identified in the corresponding U-Matrix surface as it is shown in Figure 7.38(b). This can be clearly seen since the simulated damage number two, three and six cannot be differentiated in the U-Matrix surface, i.e. mountain-like surfaces were not formed for allowing a separation between all the damage types. Nevertheless, the undamaged state can be separated very well from the other simulated damage states. This result is sufficient if the objective is just to identify if the system departs from normal condition. However, if one wishes to address the problem of damage identification, the obtained results cannot provide much information about the damage type.

In a similar manner as the one discussed before, analysis were carried out by means of h-NLPCA, SPE measures and SOM. Figure 7.39(a) shows the cluster map. In this case, seven clusters seem to have been well identified. This is the case for the U-Matrix surface as well as it is shown in Figure 7.39(b). Additionally, the boundaries are more clearly formed when compared with the previous example. It is also visible that a more compact

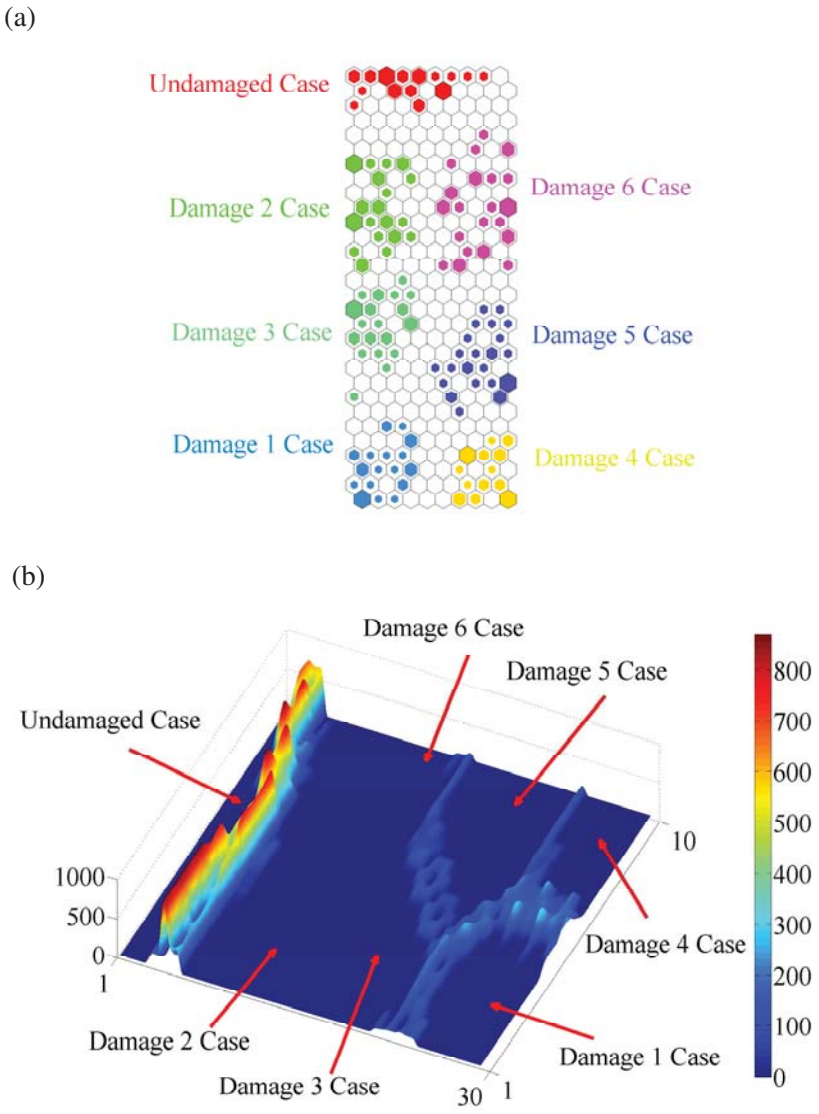

Figure 7.38. *Analysis with fused PCA, SPE and SOM: (a) Cluster map and (b) U-Matrix surface. In-plane axes correspond to the number of neurons.*

representation of the clusters with a lesser variance around the cluster centre is present for the undamaged scenario as it can be seen from Figure 7.39(a).

In this case, the proposed methodology and algorithms seem to outperform the results obtained with the previous methodology based on standard principal component analysis. The main advantage of using the processing approach presented here is to provide robustness in the analysis by the use of data fusion using the projections obtained by each model together with the square prediction errors measurements as inputs to a self-organizing map.

Localised Increasing Mass Problem As it was previously discussed, it has been shown that the proposed methodology was able to detect damage and the different damage cases. Nevertheless, since the type of damages which were simulated in the previous example are not very realistic with respect to a growing damage process, a second series of experiments

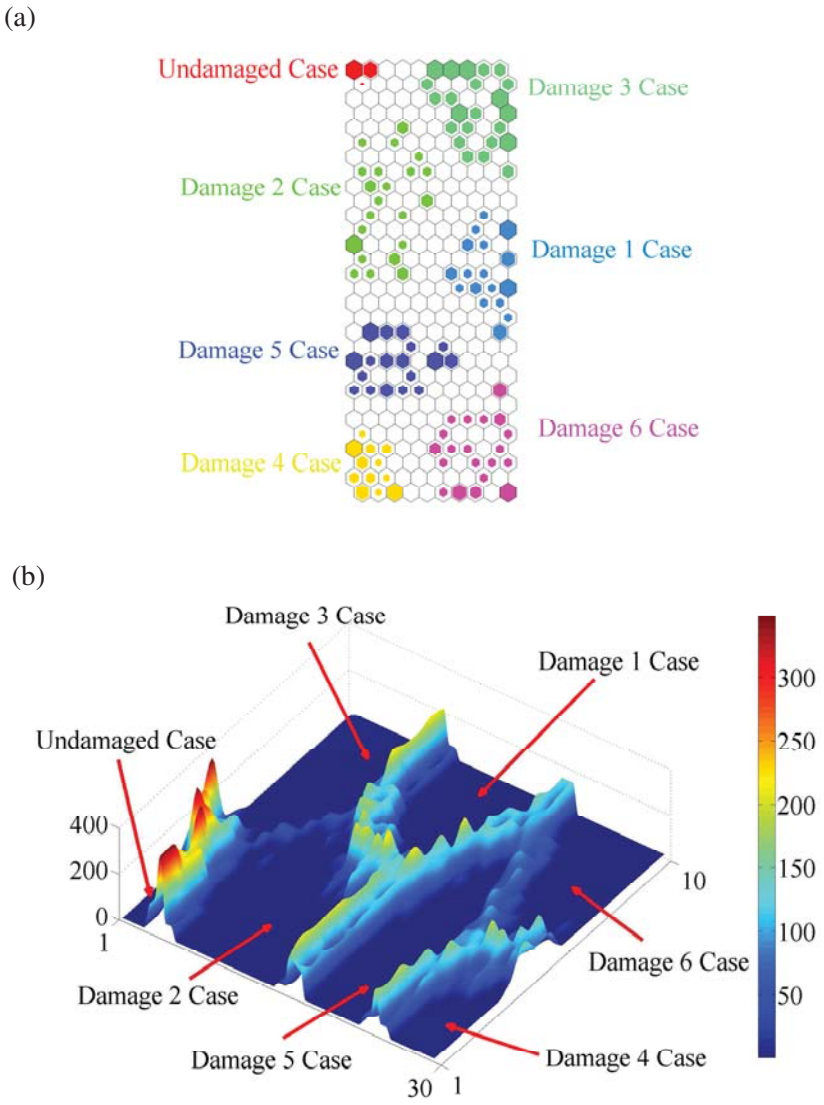

Figure 7.39. *Analysis with fused h-NLPCA, SPE and SOM: (a) Cluster map and (b) U-Matrix surface. In-plane axes correspond to the number of neurons.*

were undertaken. In these experiments damage is simulated again by a localised mass, but the difference resides in that damage increase is simulated by locally increasing the mass at the same damage location by steps so that damage states could be realistically simulated. The magnets employed have a disk shape and their diameter, height and mass of the magnets are $25mm$, $10mm$ and $0.012kg$, respectively. The magnets were placed on both sides of the structure. A combination of magnets was used to get different mass values. Four damage evolution steps were simulated using the following mass increase:

1. Damage state one corresponds to a localized mass of $0.024kg$.
2. Damage state two corresponds to a localized mass of $0.048kg$.
3. Damage state three corresponds to a localized mass of $0.072kg$.
4. Damage state four corresponds to a localized mass of $0.096kg$.

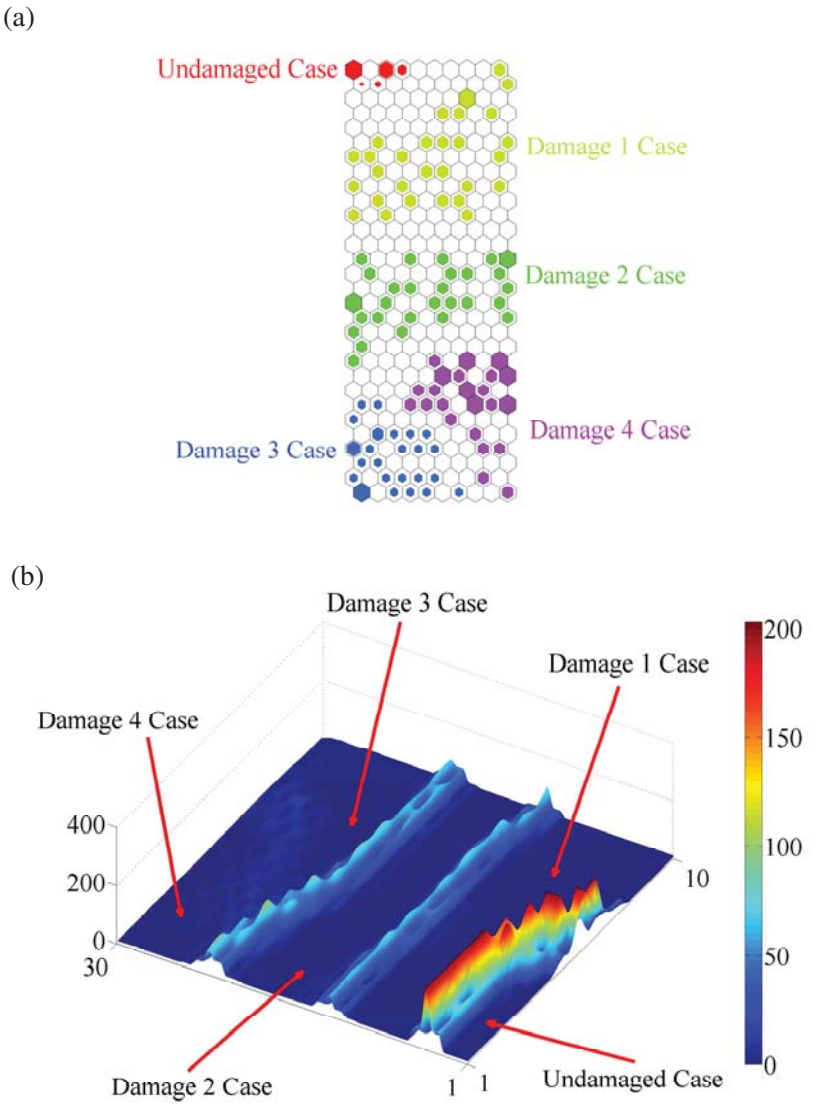

Figure 7.40. *Analysis with fused h-NLPCA, SPE and SOM for the localised increasing mass problem: (a) Cluster map and (b) U-Matrix surface. In-plane axes correspond to the number of neurons.*

The damages were located in the middle position between P_1 and P_2. For the current example, a level eight decomposition was accomplished as the optimal decomposition level as with the previous example. The size of the mapping and demapping layer are kept the same as well as the map parameters and number of retained components. For comparison reasons, analyses are carried out by means of h-NLPCA, SPE measures and SOM as presented before. Figure 7.40(a) shows the cluster map. In this case, four clusters seem to have been identified. Nevertheless, the distance in the map between the clusters associated to damage three and four is not significant. As it is shown in Figure 7.40(b), this effect is also reflected in the U-Matrix surface as well. One can observed that for the first two damage states the boundaries are very well-defined. However, the boundaries separating the clusters for damage states three and four have very low values making an separation between the states not so visibly clear and straight-forward to be identified.

It seems from that from Figure 7.40 one could relate the damage severity with respect to the distance between the cluster centres to the undamaged case. Nevertheless, as it is going to the shown in the following subsections, where real damage is introduced to a structure, this principle does not seem to always hold.

Temperature Influence on Damage Assessment Capabilities In order to conclude the analyses with this structure, a final experiment was performed. As it was done previously done, all the controlling parameters are kept the same for comparison purposes, i.e. DWT decomposition levels, number of retained components, etc. The idea behind the experiments carried out here is to depict the influence of changing environmental conditions, i.e. temperature changes, in the assessment capabilities of the method. For this purpose, baseline measurements are taken at different temperature levels. Temperature is varied from $T = 25°\text{C}$ to $T = 75°\text{C}$ in increments of $10°\text{C}$. The temperature was measured by two PT100 sensors mounted on opposite corners of the aircraft composite skin panel. Results are depicted in Figure 7.41.

These results are obtained by projecting the new measurements recorded at different temperatures into the baseline models at $T = 25°\text{C}$, similarly to all the previous cases. Figure 7.41(a) clearly shows how the recorded data are properly clustered according to the temperature of measurement. It can be observed how the baseline measurements at $T = 25°\text{C}$ fall into a single and compact cluster around a neuron. The other clusters appear to have a larger deviation around their cluster centres, even though, they are well separated. This can be explained by the fact that during the temperature measurements there was a temperature variation of $\pm 3.5°C$ around the desired reference temperature. Figure 7.41(b) shows that at higher temperatures, that is to say at $T = 55°\text{C}$, $65°\text{C}$ and $75°\text{C}$, the boundary values between the clusters formed at these temperature levels are very high. Even when it is not visually evident at first sight, the separation of the measurements between the baseline model at $T = 25°\text{C}$ and the measurements at $T = 35°\text{C}$ and $T = 45°\text{C}$ have also well defined boundaries. As it was depicted before, special measures must be taken into account in order to avoid false-positive indication of damage. As a result, it is very important to collect training datasets over a wide range of environmental conditions of the system so that the minimization of false indications of damage are accomplished and in order to develop a robust monitoring system.

7.4.2. Pipe Structure

An experiment was performed in order to evaluate the practical performance of the proposed methodology in pipework. Figure 7.42(a) depicts the experimental setup used for testing. The pipes were kindly donated by Prof. Dr.-Ing. Bernd Engel, chair of the Forming Technology Department at the University of Siegen. Four piezoelectric transducers

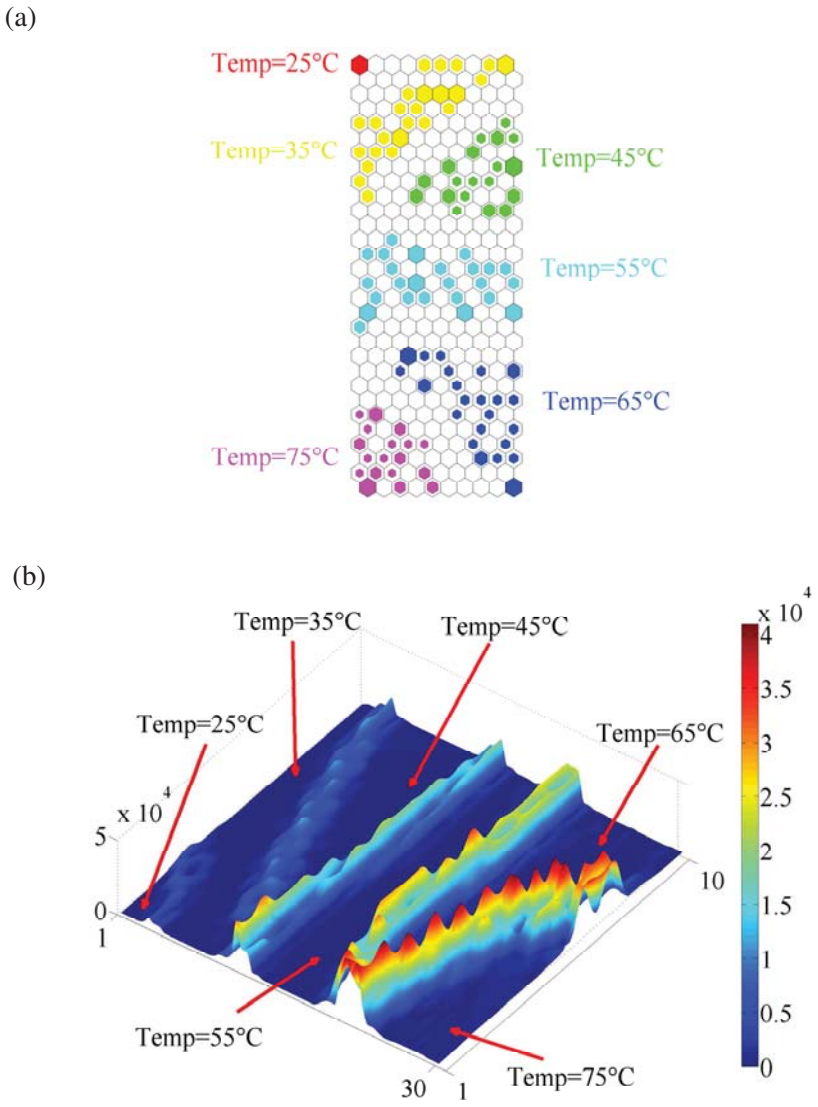

Figure 7.41. *Analysis with fused h-NLPCA, SPE and SOM for the temperature problem: (a) Cluster map and (b) U-Matrix surface. In-plane axes correspond to the number of neurons.*

PIC-151 from PI Ceramics are attached to the surface of the structure with equidistant angular spacing on both sides at a distance of approximately $35mm$ from the flanges. The piezoelectric transducers have a diameter of $10mm$ and a thickness of $2.5mm$. The monitored pipe has a length of approximately $850mm$. It was made of stainless steel with an outer radius of $20mm$ and $2.15mm$ wall thickness. Damage was introduced into the structure in several steps. It was executed as a cut with an angular grinder. The depth and its vertical extension are enlarged in four steps, starting with a cut of $0.75mm$ depth. This cut is increased in depth in a second step until the wall is almost penetrated, followed by an increase in vertical direction. Finally the pipe wall is penetrated, increasing the depth in the middle of the former notch. The different states can be found in Figure 7.42(b) to (e).

It is well-known that each of the possible excited modes will produce different deformation fields along the wall thickness, i.e. the particle displacements and velocities as well as the

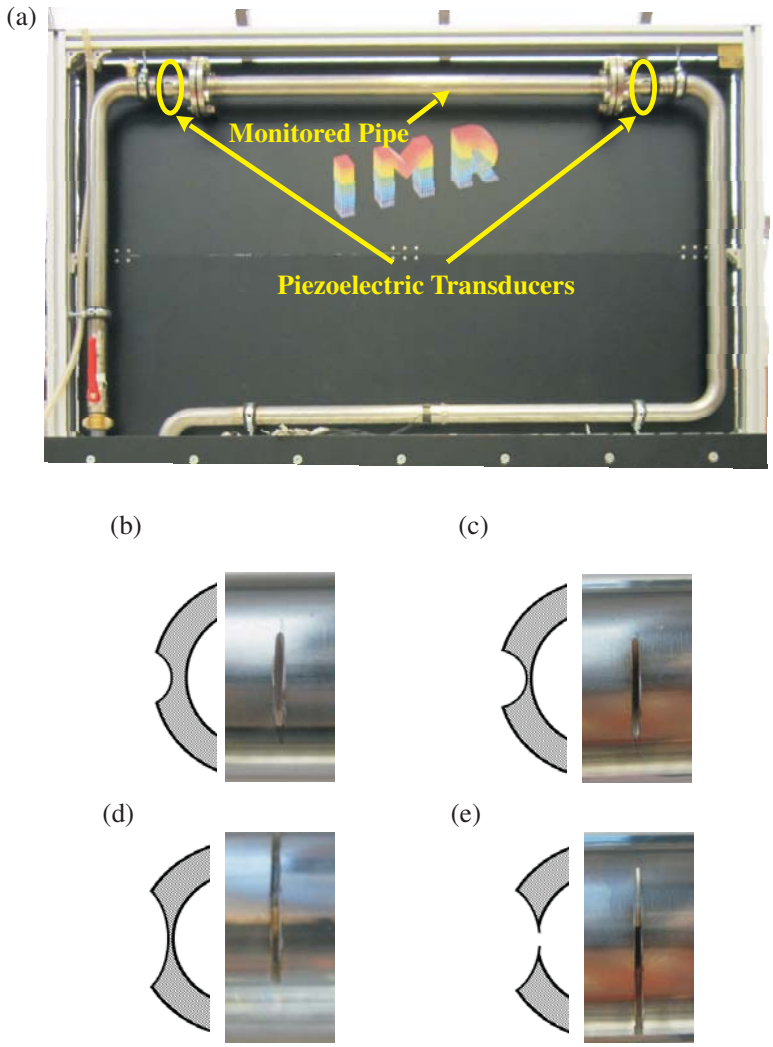

Figure 7.42. *Pipe structure used for evaluating the acousto-ultrasonics methodology: (a) Experimental setup, (b) Damage 1, (c) Damage 2, (d) Damage 3 and (e) Damage 4 cross sections.*

stress and strain fields will all vary for each mode. Therefore, it is desired to select a mode with greater penetration power across the wall thickness in the pipeline. Previous works have shown that the second order longitudinal mode $\mathrm{L}(0,2)$ is very attractive to use for long-range testing since it is practically non-dispersive and it is also the fastest mode [Alleyne et al. 1998]. Additionally, this mode has most of its energy flow proportionally located across the wall thickness. For this reason, special attention was paid in order to excite this mode. In order to assure the selection of the mode, dispersive characteristics and energy distribution analysis is carried out. To guarantee this requirement, the excitation voltage signal was a $12V$ Hanning windowed cosine train signal with 5 cycles and carrier frequency of $180kHz$. The carrier frequency was chosen not only to maximize the propagation efficiency but also to specially excite the $\mathrm{L}(0,2)$ mode [Torres Arredondo et al. 2012]. Figure 7.43(a) shows the group velocity dispersion curves representing the velocity of propagation of the wave energy. The normalized amplitude spectrum is also shown in order to depict the frequency bandwidth of the pulse excitation signal used in this study, i.e. toneburst with 5 cycles and carrier frequency of $180kHz$. Moreover,

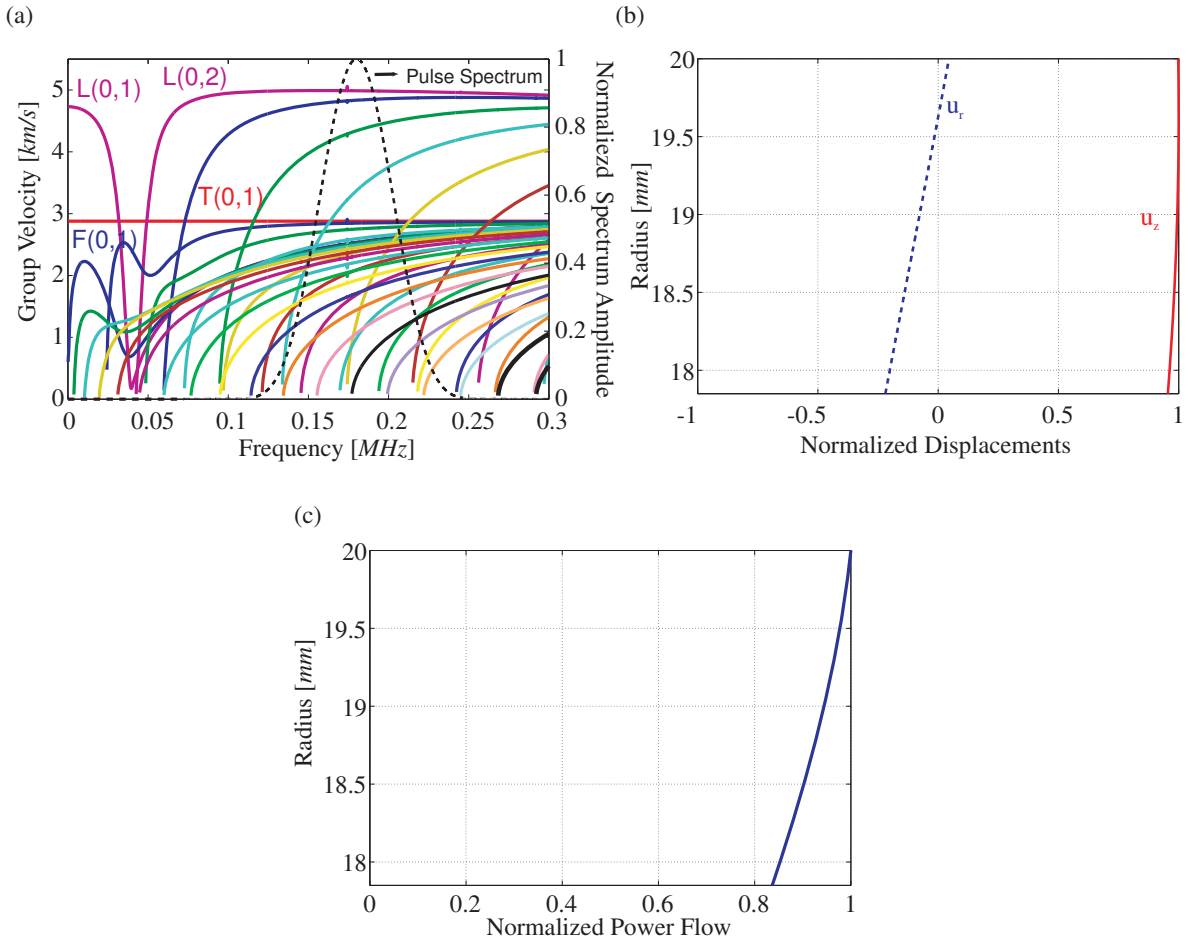

Figure 7.43. *Guided wave dispersive characteristics: (a) Group velocity dispersion curves and pulse spectrum, (b) Displacement fields and (c) Normalised power flow.*

the normalised displacement fields and power flow for the $\mathrm{L}(0,2)$ mode at a frequency of $180kHz$ are shown in Figure 7.43(b) and (c).

As it has been done previously, an outlier analysis is performed first. Nevertheless, in this part both the detail and approximation coefficients at the optimal level of decomposition are studied for the purpose of damage detection and possible identification of the damage process. Furthermore, and according to the previous example conclusions, the analyses are going to be done based solely on h-NLPCA built models. A level eight of decomposition was found to be the optimal decomposition level. A review of the variances retained in the components is performed in order to define the optimal number of components required for building the non-linear model by means of standard PCA. For both models, i.e. models built either with the approximation or detail coefficients calculated from the pristine structure data, it was computed that the first three components included around 95% of the total variance into the reduced model. In the present work, auto-associative neural networks with different dimensions in the mapping and de-mapping layers are applied to this training data to determine the best network architecture. For the experiments depicted here, 178 neurons were used for both layers. The threshold for the novelty index is calculated from the baseline data and the confidence level is

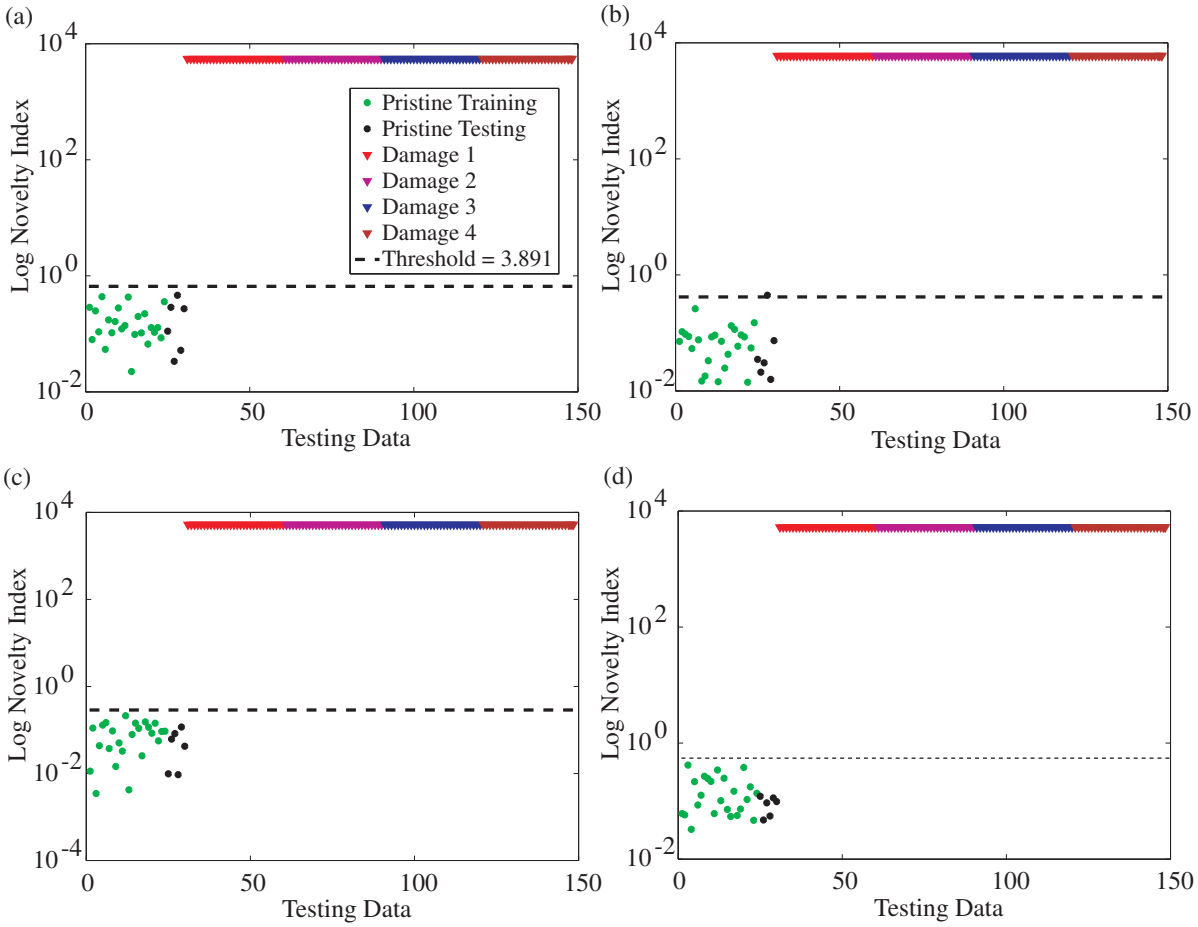

Figure 7.44. *Outlier analysis by means of h-NLPCA from the detail coefficients: (a) Actuator 1, (b) Actuator 2, (c) Actuator 3 and (d) Actuator 4.*

defined to be 99.99%. For the present study, 80% of the recorded baseline data were used for building the template models for each actuation step. The actuation signals were generated in one of the ends near the pipe flanges for each transducer and then the propagated guided waves were collected in the other side of the structure (see Figure 7.42(a)). Figure 7.44 shows the outlier analysis results obtained from the non-linear modelling from the calculated details DWT coefficients and h-NLPCA modelling. It can be observed that all damage cases were correctly identified for all the actuation steps. However, as it can be seen from Figure 7.44(b), one undamaged data point appears to be incorrectly identified during the actuation step number two. One additional point to discuss is that the novelty index value is almost the same for all the damage cases. This is a non-optimal result if one desires to track the dissimilarity between the different damage evolution steps. Moreover, it can be seen that the novelty index values have a big deviation for the baseline data. This can be explained by the fact that data-driven modelling techniques are very sensitive to data which do no appear to be consistent to the process to be modelled. This kind of inconsistent results can be introduced by experimental errors, noise sources, small deviations during the recording of the guided waves due to the internal clock synchronization differences between experiments, etc.

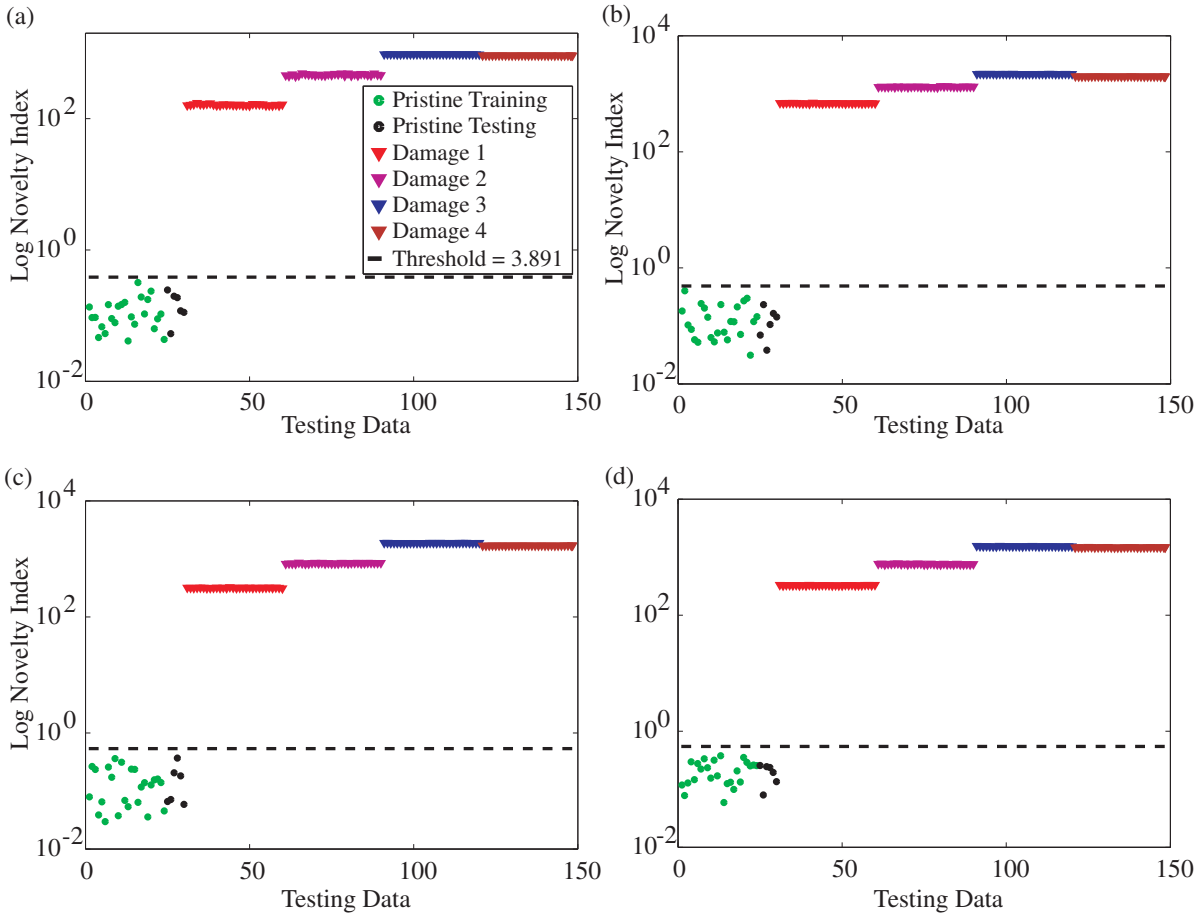

Figure 7.45. *Outlier analysis by means of h-NLPCA from the approximation coefficients: (a) Actuator 1, (b) Actuator 2, (c) Actuator 3 and (d) Actuator 4.*

The outlier analysis results obtained from the non-linear modelling from the calculated approximation DWT coefficients and the h-NLPCA modelling are depicted in Figure 7.45. The analysis shows that damage can be well separated from the pristine state using only the first three non-linear components for all the actuation steps. It can also be observed that the damage cases can be relatively well distinguished by just using the novelty index. Interestingly, it appears to be that the novelty index correlates well with the damage severity for the first three damage cases, i.e. the values increase as the damage severity increases. However, this correlation breaks down for the case of damage four where the novelty index values decrease. For the case of the h-NLPCA models, one can see that the novelty index values for the baseline measurements turn up to be somewhat more compact in contrast to the values previously discussed using the detail DWT coefficients.

Finally, the proposed methodology is evaluated for both the detail and approximation coefficients. As it has continuously done throughout this section, a control run is repeated by changing the map size in order to find the optimal map size by analysing the average quantization error and topographic error. As a result, an optimal map size of 30×10 was obtained. Results are quite similar to the ones obtained with the outlier analysis. For this analysis, only the U-Matrix surface plots are depicted. It can be seen from Figure 7.46(a)

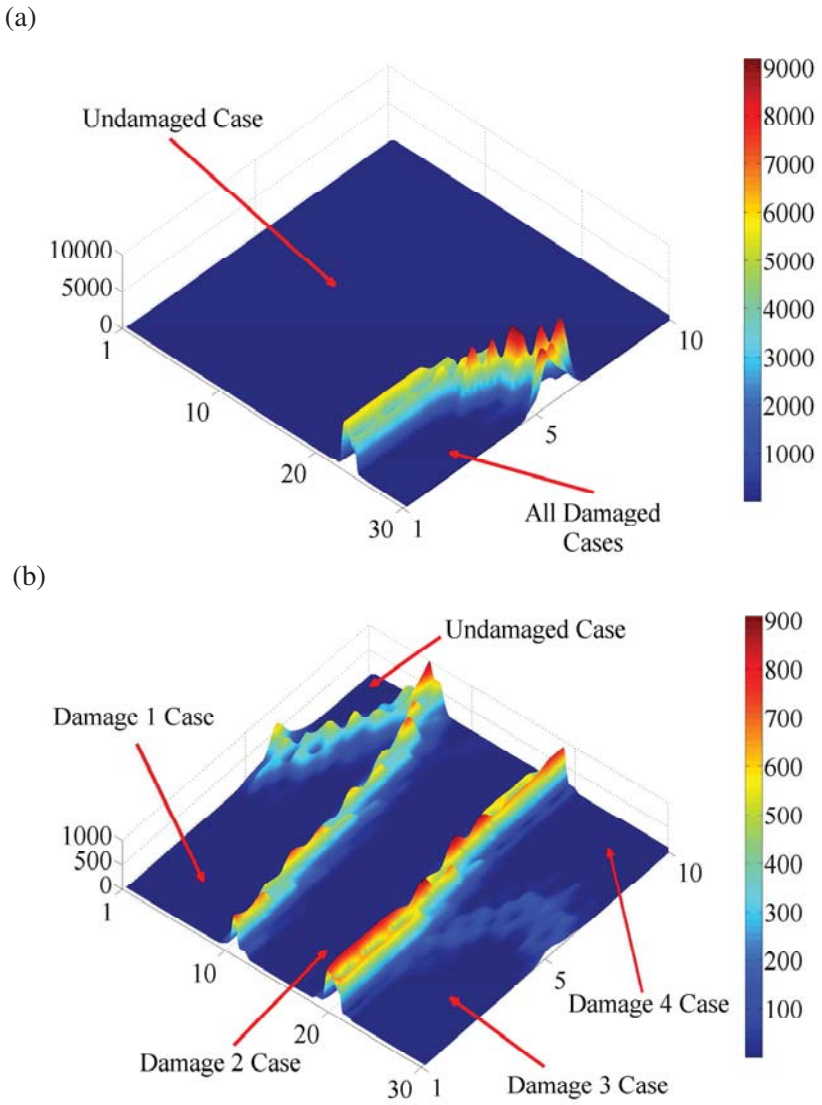

Figure 7.46. *Analysis with fused h-NLPCA, SPE and SOM for the pipe damage detection problem: (a) U-Matrix surface from detail coefficients and (b) U-Matrix surface from approximation coefficients. In-plane axes correspond to the number of neurons.*

that all damage cases can be clearly identified but not separated for the case of the detail coefficient-based models. For the case of the approximation coefficient-based models, it can be observed from Figure 7.46(b) that five clusters seem to have been well formed. In particular, it can be observed that the undamaged state can be properly separated from the rest of damage cases. A separation between the different damaged cases is also possible due to the well-defined boundaries in the U-Matrix surface.

As it has been shown, in this particular case, the coefficients of the details, i.e. the high frequency part of the signal, also provide good results. This could probably be explained by higher harmonic generation of guided Lamb waves. It has been shown that nonlinear materials depict power-dependent transmission and selective generation of higher harmonics [Bermes et al. 2007, Shadrivov et al. 2008, Srivastava and Scalea 2009]. A study of the applicability of DWT coefficients for damage detection is presented under

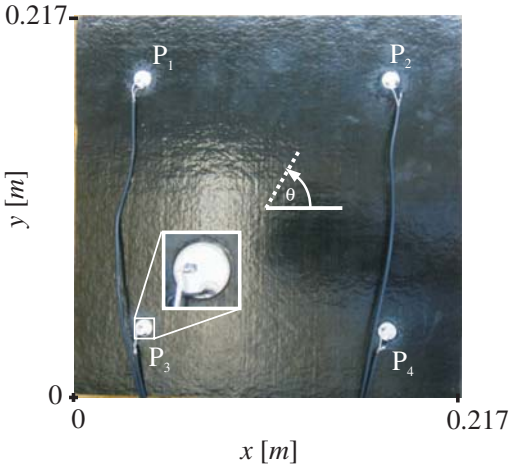

Figure 7.47. *Experimental setup for the CFRP sandwich structure.*

joint research by the author in [Tibaduiza et al. 2013]. Nevertheless, this topic requires further research.

7.4.3. Carbon Fibre Reinforced Plastic Sandwich Structure

The next experiment to be performed is done in a CFRP sandwich structure. The sample was kindly provided by Dr. Kaj Kvisgaard Borum from the Risø National Laboratory for Sustainable Energy at the Technical University of Denmark. The overall size of the structure is $217mm \times 217mm \times 31mm$. The skin is made of carbon/ epoxy material with a $0.5mm$ thickness. The stacking sequence is $[0°90°]$. The core is made of polyether imide foam with a $30mm$ thickness. Four piezoelectric transducers PIC-151 from PI Ceramics are attached to the surface of the structure with equidistant spacing. The piezoelectric transducers have a diameter of $10mm$ and a thickness of $0.5mm$. The sensors were positioned at an equidistance of $40mm$ from each corner. Figure 7.47 depicts the experimental setup used for testing.

Damage on the multilayered composite sandwich structure was intentionally produced in order to simulate different damage mechanisms, i.e. delamination and cracking of the skin. The damages were carefully introduced and measured. Table 7.12 outlines the descriptions for the six simulated damages on the composite skin panel. The excitation voltage signal is a $12V$ Hanning windowed cosine train signal with 5 cycles and carrier frequency of $50kHz$. The carrier frequency was chosen to maximize the propagation efficiency.

For the current experiment and according to the conclusions drawn from the previous example, only the approximation coefficients are evaluated. A level eight of decomposition was found to be the optimal decomposition level. A review of the variances retained in the components by means of standard PCA is performed in order to define the optimal number of components required for building the non-linear model. It was calculated that the first fifteen components included around 80% of the total variance into the reduced

Table 7.12. *Damage description for the generated damages in the CFRP sandwich structure.*

Damage Number	Damage Description
1	Delamination: Started symmetrically from the right side of the sample at its middle position along the y-axis. Its width along the y-axis is $16mm$ and depth along the x-axis is $10mm$
2	Extended the previous damage to a width of $33mm$ and depth of $42mm$
3	A crack of $25mm$ length initiated at the middle position along the vertical y-axis and in parallel direction to the x-axis
4	Extended the previous crack to a length of $30mm$
5	Extended the previous crack to a length of $45mm$
6	Extended the previous crack to a length of $70mm$

model. This number of components was selected for h-NLPCA. The optimal number of units for the mapping and de-mapping layers was calculated using Eq.(2.38). For the experiments depicted here, 80 neurons were used for both layers. The optimal map size was found by analysing the average quantization error and topographic error. As a result, an optimal map size of 30×15 was obtained. Results are depicted in Figure 7.48.

Figure 7.48(a) show the clusters map using the fused data from the h-NLPCA models and the SPE measures calculated from the approximation coefficients. As it is possible to observe by means of the separations between the groups in the Figure 7.48(a), seven clusters seem to have been well identified. Nevertheless, if one observes carefully 7.48(b), only six clusters appear to be formed in the U-Matrix surface. It can be seen that there is no a clear visible boundary separating damage three and four. This could be probably explained due to the fact that there is no a significant increase in the crack length between both damages. Additionally, it can be observed that the boundaries values are higher for the last two damage cases. This is probably given by the fact that these damages are located inside of the area covered by the sensor network which provides a higher interaction of the waves with the damage and less disturbing effects introduced by the boundaries of the structure. Nevertheless, the results obtained with the first four damage cases are also very satisfactory.

7.5. Impact Load Monitoring

In this section, the Bayesian framework within the context of Gaussian Processes for the purpose of impact magnitude estimation and localisation presented in Chapter 6 is demonstrated experimentally and discussed. Following this concept, a probabilistic model is constructed either for impact load or impact location estimation and predictions are then expressed in terms of a predictive distribution that gives the probability distribution over the predicted targets, rather than simply a point estimate. The training algorithm

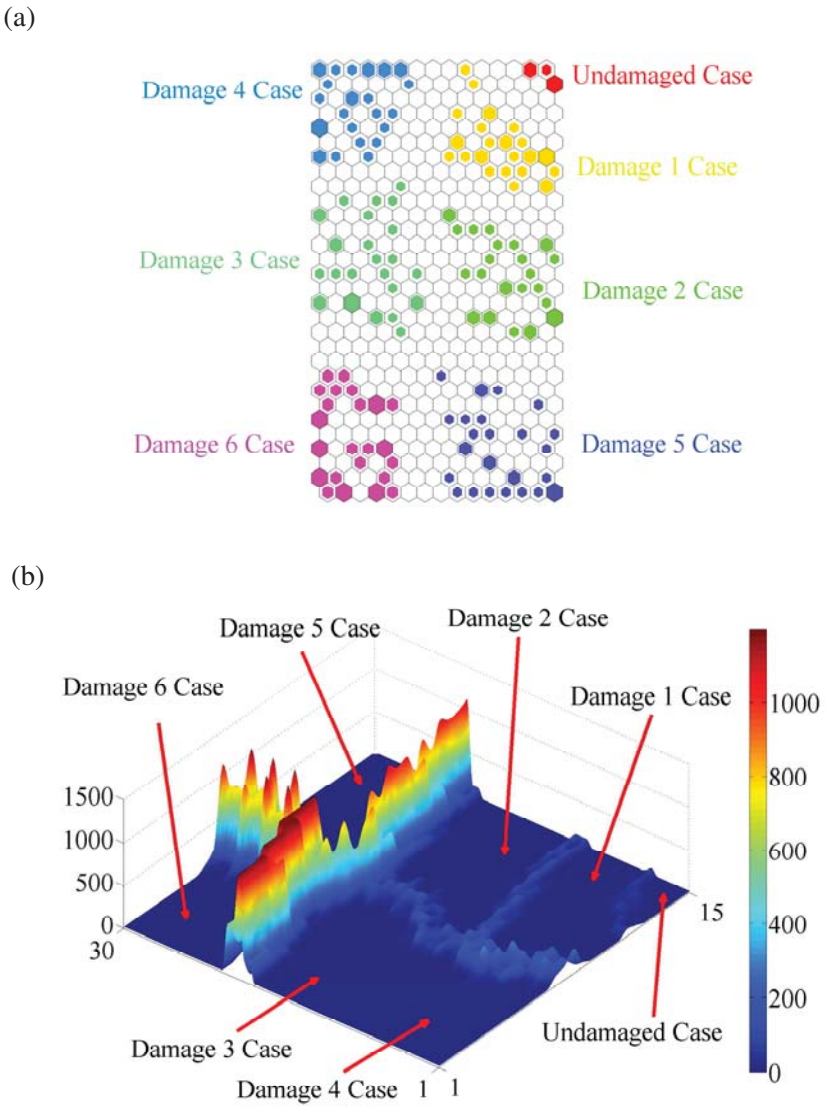

Figure 7.48. *Analysis with fused h-NLPCA, SPE and SOM for the pipe damage detection problem: (a) Cluster map and (b) U-Matrix surface. In-plane axes correspond to the number of neurons.*

used here for regression is implemented in a Matlab®-Toolbox created by [Rasmussen and Williams 2006].

7.5.1. Impact on an Isotropic Plate

A specimen was made from a $2mm$ aluminium sheet of dimensions $800mm \times 800mm$. For the present experiment, six broadband piezo-transducers PIC-255 from PI Ceramics were installed on the surface of the plate. The piezoelectric transducers have a diameter of $10mm$ and a thickness of $0.5mm$. Figure 7.49 displays the evaluated structure. The sensor positions are given in Table 7.13.

The experimental setup consisted of two HS4 handy-scopes from TiePie Engineering, an impulse force hammer from Kistler Holding AG and a PC. The time histories are di-

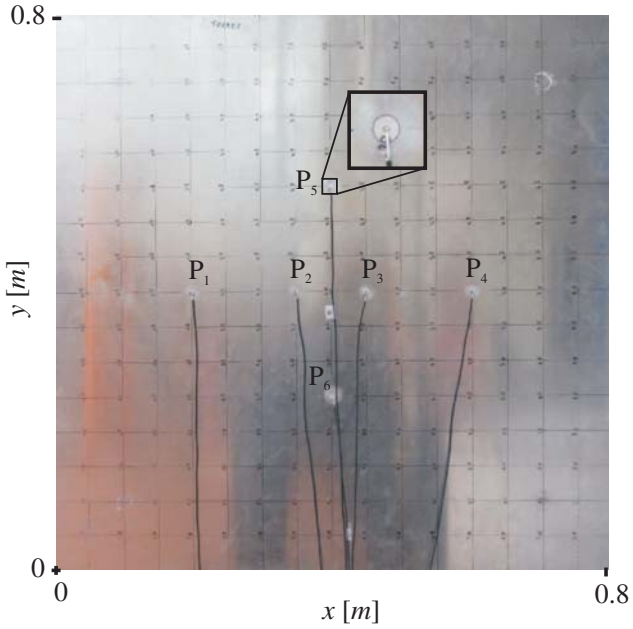

Figure 7.49. *Experimental setup for the aluminium plate.*

gitised at a sampling frequency of $10MHz$. For the impact magnitude estimation, the Gaussian process had a single output target whose inputs were the area under the curve of the power spectral density from each sensor and the non-linear principal components extracted from the calculated approximation coefficients obtained by the DWT. A level six of decomposition was found to be the optimal decomposition level. Standard PCA was used in order to define the number of principal components used in the h-NLPCA. Principal components contributing less than 2% to the total variation of the data set were eliminated for this task. Accordingly, ten components were selected for the purpose of dimensionality reduction. The optimal number of units for the mapping and de-mapping layers was defined as thirty following the same procedures depicted in the previous examples. To test the proposed method, more than 800 impacts of different magnitudes were exerted on the surface of the plate with a grid density of $50mm$ in order to create the database. The data were then divided into training and test sets. Twenty percent of the total amount of data was used for testing purposes.

Figure 7.50 shows the results of impact magnitude estimation for 30 randomly selected

Table 7.13. *Sensor locations in the aluminium plate.*

Sensor	x position (mm)	y position (mm)
1	200	400
2	350	400
3	450	400
4	600	400
5	400	550
6	400	250

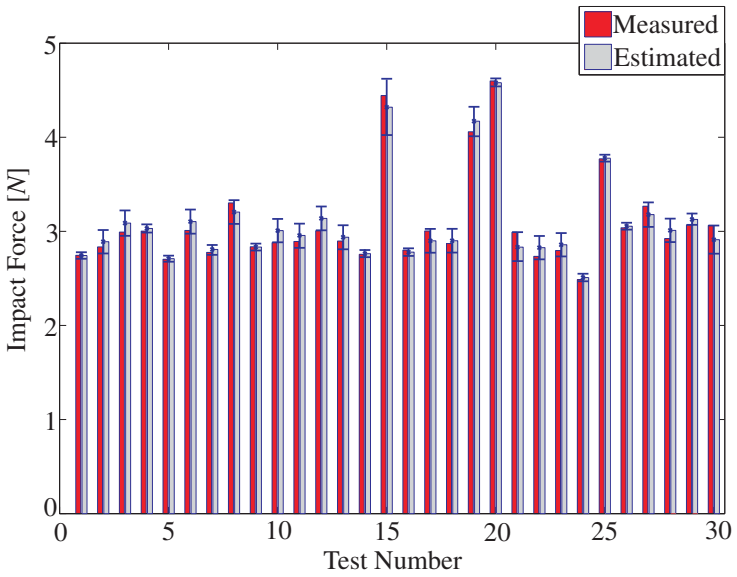

Figure 7.50. *Estimated and measured impact forces on the plate.*

testing events. The grey bars represent the means provided by the Gaussian process predictive distribution, and the error bars corresponds to plus and minus two standard deviations. For the testing set, the Gaussian process was able to estimate the impact magnitude force with an average percentage error of 3.3%. This result reflects an improvement in comparison with traditional methods based on neural networks and traditional descriptors when it is compared to results obtained from a similar structure [Jones et al. 1997]. It is worth noting that since the input force spectrum exerted in the structure is a combination of the stiffness of the hammer tip and the stiffness of the structure, the Gaussian process ability to provide accurate estimates between different types of impacts is highly dependent on the provided training data covering all the possible ways an impact may occur. To generate the database experimentally under these conditions can be a very expensive and almost an impractical task, therefore, the use of computer modelling tools is suggested for this purpose. Here, only hard tip impacts are studied.

For the impact localisation, two independent Gaussian processes with outputs corresponding to x and y coordinates of the impact were implemented. The inputs were the differences in time of flight between the sensors and the frequency content of the first wave arrival in every sensor of the network. The Wigner-Ville time-frequency analysis was evaluated for the analysis of the MAP decomposed stress waveforms.

Figure 7.51(a) and (b) depict the impact positions estimated by the algorithm and the known positions in every test. The root mean squared errors (RMSE) on the test set were found to be $2mm$ and $3.2mm$ for the x and y coordinates, respectively. As it can be seen, the results obtained are very accurate. It can be noticed from the previous figures how the uncertainty increases in the regions where the estimates deviate from the true values. However, this is not always true and sometimes the algorithm provides poor results with high confidence. This is a common case and criticism in Bayesian methods where

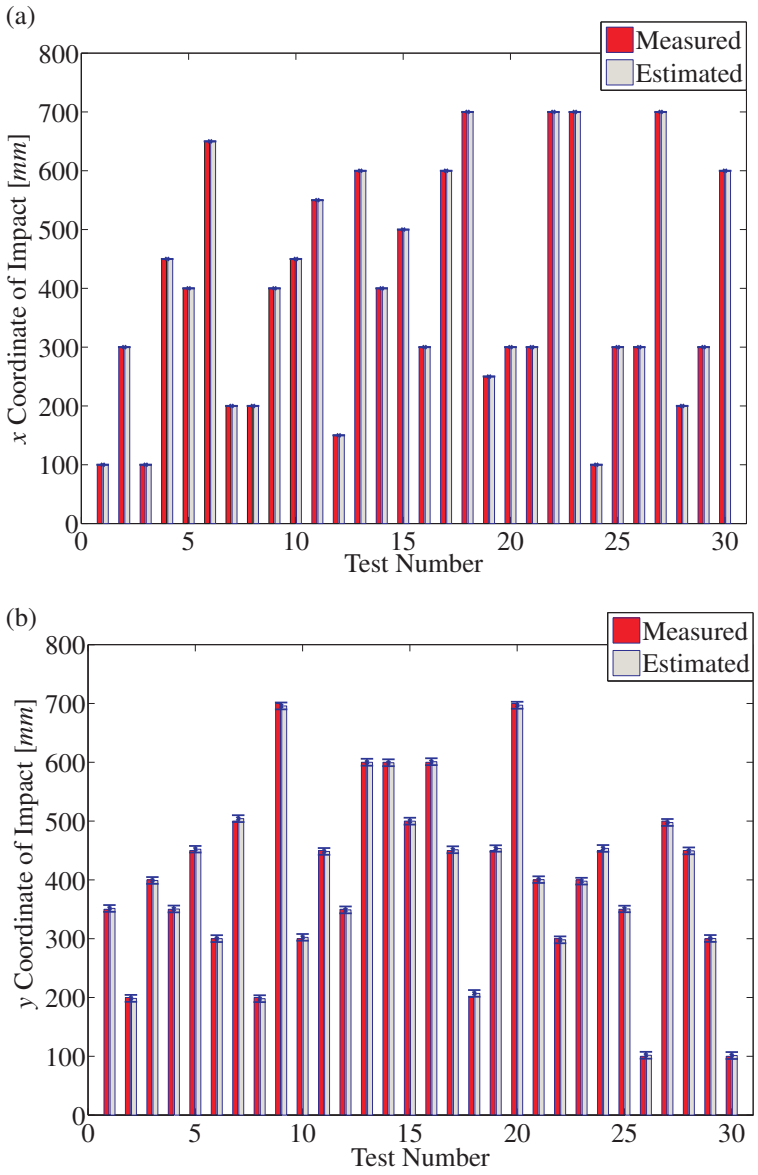

Figure 7.51. *Estimated and real impact locations on the plate: (a) x coordinate and (b) y coordinate.*

poor choices of priors lead to these results [Bishop 2007]. Another general shortcoming of the proposed methodology is that it depends on the quality of inputs, i.e. onset-time estimation, principal components, etc. These inputs must be determined precisely and with a high degree of automation.

7.5.2. Impact on an Airbus A320 Fuselage

An aircraft fuselage from an Airbus A320 is used in order to investigate the effectiveness of the method in a more complex and realistic structure. The structure includes a curved plate, four vertical stringers and seven horizontal ribs. The fuselage was instrumented with nine broadband piezo-transducers PIC-255 from PI Ceramics bonded on the curved plate surface. The piezoelectric transducers have a diameter of $10mm$ and a thickness of

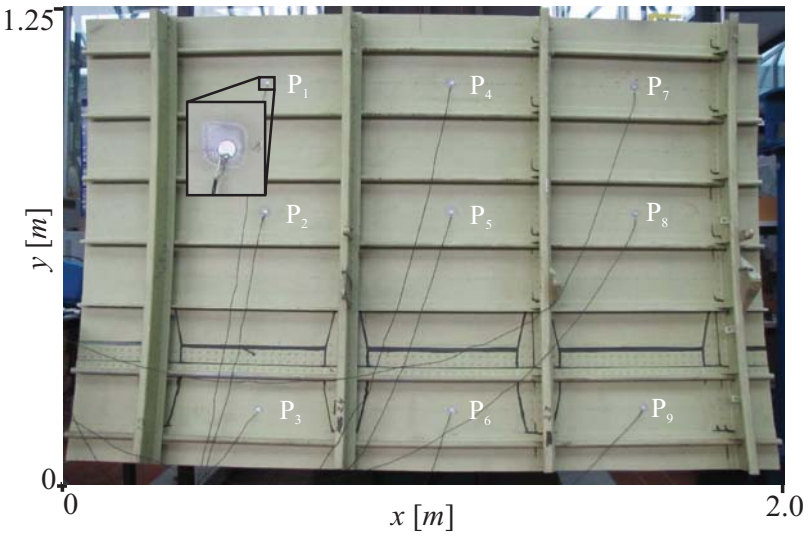

Figure 7.52. *Experimental setup for the Airbus A320 fuselage.*

0.5*mm*. The structure and transducers configuration are shown in Figure 7.52.

The hardware used for this experiment is the same as the one used in the previous example. The time histories are digitised at a sampling frequency of 2*MHz*. To test the proposed method with this structure, more than 1500 impacts of different magnitudes were exerted on the surface of the fuselage in order to create the database. Impacts were executed with four different types of hammer tips, i.e. one soft, one medium and two hard tips. A level four of decomposition for the wavelet transform algorithm was found to be the optimal decomposition level. In order to define the number of principal components used in the h-NLPCA, an analysis by means of standard PCA was carried out. Principal components contributing less than 2% to the total variation of the data set were eliminated for this task. As a result, ten components were selected for the purpose of dimensionality reduction. The optimal number of units for the mapping and de-mapping layers was defined as eighty. The data were then divided into training and test sets. Twenty percent of the total amount of data was used for testing purposes. Figure 7.53 shows the results of impact magnitude estimation for 30 randomly selected testing events.

Here again, the grey bars represent the means provided by the Gaussian process predictive distribution, and the error bars corresponds to plus and minus two standard deviations. For the testing set, the Gaussian process was able to estimate the impact magnitude force with an average percentage error of 9.3%. This result is not so unsatisfactory if one considers the high complexity of the structure in comparison to the plate-like structure analysed before. It can be noticed from this figure how the uncertainties are higher in this example. This result provides an idea about the uncertainty and reliability of the developed model predictions.

For the impact localisation, the structure is divided into eighteen sections (see Figure 7.52) where one is interested in determining the section where the impact occurred instead of the exact impact coordinate. One independent Gaussian process is implemented for

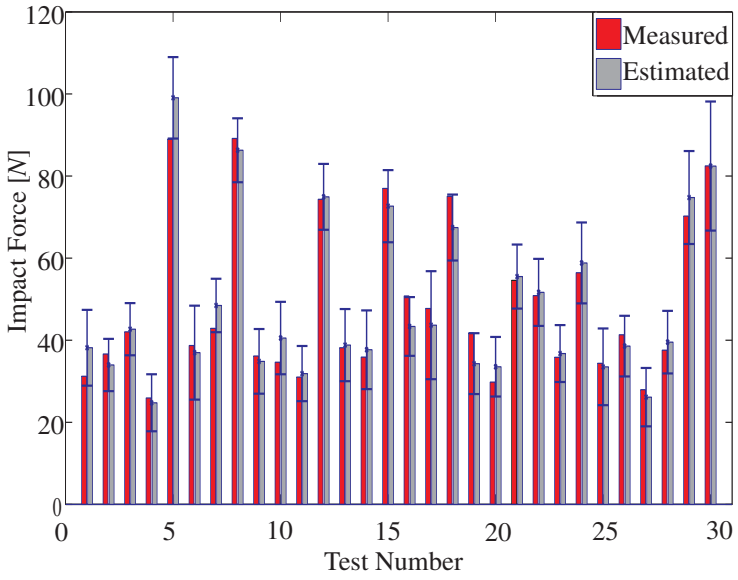

Figure 7.53. *Estimated and measured impact forces on the Airbus A320 fuselage.*

classification. The training phase used a 1 of M strategy, i.e. the Gaussian process is required to produce a value of 1 at the output corresponding to the desired class and 0 at all other outputs. As it was explained before, this actually estimates the Bayesian posterior probabilities for the classes with which the outputs are associated. Due to the long time taken to run the multi-class code and as it is done in [Williams and Barber 1998], a maximum penalised likelihood approach was undertaken in which the gradient is used as input to a scaled conjugate gradient optimizer attempting to find a mode of the class posterior rather than to average over the posterior distribution. A part of the codes implemented here for the multiple class problem were kindly provided by Professor Christopher K. I. Williams from the School of Informatics at University of Edinburgh. An average percentage error of 3.33% was obtained for the multi-class problem. Due to the big size of the confusion matrix, this one is not depicted here. A classification approach based on a standard multilayer perceptron network was further pursued due to the long processing time required with the Gaussian process. It was found that similar results were obtained with the neural network within a processing time of few seconds in comparison to several hours required using the Gaussian process. This fact clearly depicts a disadvantage of using Gaussian processes for classification purposes when one takes into account the computational cost and time required.

8. Conclusions and Future Work

This thesis has examined and proposed possible solutions to several research issues which are still opened in guided wave structural health monitoring applications which perform their tasks under the principles of acoustic emission and acousto-ultrasonics. It has been shown throughout this thesis that these technologies have a broad area of application for aeronautic, aerospace, civil and mechanical structures. This is explained by the fact that guided waves are able to propagate over relative long distances, interact sensitively with and/or being related to different types of defects. Examples of the proposed methodologies have been experimentally evaluated and their advantages and limitations identified.

Firstly, Chapter 1 described the concepts of structural health monitoring as well as the impact of the implementation of an SHM methodology for life-safety, economic and ecological benefits. Additionally, this chapter introduced a review in literature together with the subject of research and the framework under which it was accomplished. Within this, it was proposed to tackle the different problems presented in this thesis using a data-based approach combining both the physical understanding of the wave propagation problem and advanced signal processing and pattern recognition approaches. After the introduction, Chapter 2 reviewed the fundamentals of guided wave propagation in solid media for pipe-like and plate-like structures. This is motivated by the fact that many structures have this type of geometry in practice. The mathematical modelling of these waves in such type of structures and an analysis of the dispersive nature of guided waves as a function of the frequency-thickness product have been depicted. Discussion regarding the variation of wave velocities and effects of guided wave attenuation have been brought into attention in order to aid for a better understanding of the physical problem which allowed an improved inspection of complex structures. This is followed by an introduction to ultrasonic guided wave analysis techniques in conjunction to an explanation of the sensors and actuators used in this thesis. Finally, different techniques for signal processing and analysis are presented. These techniques are introduced for the purpose of signal conditioning, extraction and selection of damage-sensitive features, sensor-data fusion, pattern recognition and visualisation. It is known that structures normally contain structural features such as reinforcements, holes, thickness changes, rivets, welds, etc. This structural features influences the path of ultrasound from source to sensor and make the interpretation and

analysis of the recorded guided waves a challenge. For that reason, it is expected that the use of robust signal processing and patter recognition techniques lead to the development of efficient SHM methodologies.

In Chapter 3 a coupling between viscoelasticity theory and a laminated plate theory has been suggested which is applicable to viscoelastic fibre reinforced composite materials for the calculation of wave velocities, attenuation and energy focusing for the different modes of propagation. It is believed that one can only possible benefit from the advantages of guided waves once the complexity of guided wave propagation is disclosed. Given this reason, an understanding of the behaviour of wave propagation in solid structures would greatly help to improve the accuracy and applicability of the techniques implemented in this thesis. The motivation of using an approximate theory is given by the fact that exact solutions from the three-dimensional elasticity theory require very sophisticated and computational expensive procedures for tracing the dispersive solutions in complex multilayered and viscoelastic media. The proposed model is intended to shorten time consumption in calculations, allow to study wave propagation phenomena with a higher efficiency while maintaining good accuracy in the results. Additionally, the computational requirements of the proposed model are reasonably modest. This chapter presented the complete mathematical development of the theory, introduced the standard material viscoelastic damping models, and provided a guideline for the computer implementation of the model.

According to the results presented in Section 7.2, comparisons to experimental data showed that the proposed model provided accurate estimates of velocity and attenuation in anisotropic laminates in the frequency range of guided wave applications. Furthermore, the focusing of guided waves has been numerically depicted and its importance brought into consideration for the development SHM systems. From numerical calculations it was illustrated that this phenomenon rendered a superposition of waves into a flux pattern containing caustics. Additionally, a computer program for the modelling of guided wave-based SHM systems for thin shells developed at the University of Siegen was used to further validate the proposed model and depict visually in a clear manner the wave propagation phenomenon [Schulte 2010]. Section 7.2.5 presented a possible application example of the developed model for manufacturing control where lamb waves could be used for detecting fibre misorientation or stacking sequence errors in composite laminates.

Nevertheless, it is also worth mentioning that the model suffers from some limitations that prevent it from being used to solve the whole spectrum of composite laminate problems, i.e. for high frequency-thickness products. By increasing the complexity of the structure, that is to say as the number of constitutive layers increases, the solutions obtained with the plate theories start to highly deviate from the exact solutions and render to incorrect results. It is well known from literature that higher order theories accuracy deteriorates as the laminate becomes thicker; in the case of the developed model an error below 3% in

comparison to the exact three-dimensional elasticity theory was obtained for a frequency-thickness product of $1.2MHz \times mm$. Moreover, plate theories require the calculation of correction factors, as it was depicted in Chapter 3, in order to match frequencies from the approximate theory to frequencies obtained from the exact theory. As it was concluded there, for the general case of a laminate, this procedure becomes burdensome as the value of the correction factors depends on the number, stacking sequence and properties of the constitutive plies [Whitney and Sun 1973].

Despite these limitations, it has been demonstrated that the knowledge of factors like attenuation, wave velocity and energy focusing of Lamb waves provides a better understanding of the wave propagation phenomena and allows to analyse in depth the influence of important parameters like actuator/sensor positions, the determination of the inspection range of the sensor network and to improve the probability of detection of guided waves.

Chapter 4 was fully dedicated to modal analysis of acoustic emission. It is emphasized here that the selection of AE in this thesis is due to its ability to detect evolving damages during in-service life of structures. Source characteristics of acoustic emissions are investigated first on the basis of mode excitability based on elastodynamic reciprocity. This allows to understand and provide a quantitative measure of the radiation pattern of guided wave energy which is separated between the various modes of propagation being excited. Furthermore, these calculations provide a mean to get an insight into the source mechanism in relation to the modes present in an AE signal by correlating the direction of displacement from damage sources to the excited modes. As it was mentioned in Chapter 4, the antisymmetric wave modes with dominant out of plane motion will be more strongly related with damages lying parallel to the plane of the wave propagation such as delaminations, fibre, skin or core debonding, and impact damage. Alternatively, the symmetric wave modes with dominant in-plane motion will be more strongly related with damages lying perpendicular to the plane of wave propagation such as matrix cracking, matrix splitting, fibre breakage and core crushing [McGugan et al. 2006]. Furthermore, an introduction to time delay estimators, onset time detectors and frequency analysis is given. These topics are of great interest since they are one of the most important steps required for the localisation of acoustic emission events.

At the end, three automatic methods are proposed for the analysis of AE signals. The first two methods are used for the identification of propagating modes in acoustic emission signals. They are based on artificial neural network classification of the recorded waveforms and a combined methodology used for the characterisation and classification of modes based on dispersion features and energy distribution analysis. The third method proposes a scheme where feature extraction, sensor-data fusion and pattern recognition based on unsupervised clustering is used to find different patterns among the input data.

Based on the results presented in Section 7.3.1, the first methodology based on neural net-

works was successfully used to classify the fundamental modes of propagation contained in the recorded AE data with great accuracy for the evaluated structure. Additionally, a comparison of the performance of the localisation algorithm presented in Section 4.7 together with the proposed technique was shown by evaluating the different time delay estimators and onset detectors presented in Section 4.3. It could be seen that the performance of the methods based on the cross-correlation technique was greatly affected by the dispersive effects of the recorded signals which led to big inaccuracies in the localisation results. The methods based on the Hinkley criterion and the AIC proved to provide more accurate results for localisation. However, it is recommended to use the AIC picker since this algorithm does not require any parameters to be adjusted as it is the case for the Hinkley method where the parameter ε is selected according to the material tested. Nevertheless, some issues with the proposed techniques must be discussed. First, a possible source of error leading to the incorrect identification of modes can happen when they overlap and interfere which will further induce errors in the source localisation. Moreover, the selected length of the signal characterising the different modes will vary according to the structure and its features. These effects can generate some difficulties in the practical application of this method. Moreover, real AE data from evolving damages will be rarely available in practice in order to successfully implement the supervised learning algorithm. A way to possibly tackle this problem would be the creation of computer models from which the AE could be generated, but this could be a very complicated and expensive tasks.

In order to overcome this problem, the second approach based on a special decomposition technique and dispersive/energy analysis was proposed. This approach was specially developed in order to be able to identify the different modes recorded in the AE signals and guarantee that the onset time predictions corresponded to the same picked mode in the sensor network for the improvement of the localisation of the source. As it has been stated continuously all over this thesis, a major difficulty in acoustic emission is the analysis of broad-banded signals and discrimination of the modes contained in the recorded signals. Here, a chirplet atomic decomposition was developed to accurately classify wave packets pertaining to different modes of propagation based on dispersive energy characteristics.

As it was depicted in Section 7.3.2, the proposed decomposition automatically finds the atoms describing the content of the AE signals and provides an optimized representation of the acoustic emission waveforms. Additionally, in contrast to previous studies implementing the matching pursuit algorithm for the analysis of ultrasonic waves [Zhang et al. 2000, Hong et al. 2005], the atoms contained in the dictionary of the proposed technique are well-suited for analysing the dispersive signals with a non-stationary time-frequency behaviour. A matching pursuit decomposition in a given dictionary defines a system of interpretation for signals. The algorithm isolates the signal structures that are coherent with respect to a given dictionary. For this reason, the atoms contained in the dictionary

must be coherent with the physics of the signals to be decomposed. The dispersion knowledge gained with the proposed plate theory in combination with spectral analysis in the frequency domain and the knowledge of excitability functions helped in the development of a dictionary with optimal control parameters for the signals contained in it. This strategy significantly improves the resolution of the decomposition without increasing the size of the dictionary and speeding up the computation time. From a statistical point of view, this method is closely related to projection pursuit strategies developed by [Friedman and Stuetzle 1981] for statistical parameter estimation. In addition, a time-frequency energy distribution allowed the complete investigation of the frequency content evolution from complex ultrasonic signals of interest to structural health monitoring.

The third proposed methodology is motivated for the purpose of automating a procedure for acoustic emission clustering based on self-organizing maps where the inputs to the neural network are obtained from the processed stress waves. The processing steps included feature extraction, feature selection, sensor-data fusion and dimensionality reduction as it is explained in Section 4.8. Within this methodology, a fundamental understanding of guided waves and the characterisation of their nature were essential for the correct identification of the formed clusters. Additionally, it is expected to benefit from the capabilities of unsupervised learning such as the ability to find the hidden structures in the recorded data without any previous knowledge. It was assumed here that damage mechanisms will generate AE signals with different waveform characteristics so that the pattern recognition methodology can exploit this fact for the proper clustering of the recorded AE events. In order to validate this methodology, the first case study consisted of analysing the AE waves detected during tensile testing of a unidirectional GFRP sample with fibres parallel to the load whose damage sequence was well established as it is shown in Section 7.3.3. This fact allowed to further validate the correlation of the formed clusters with the damage mechanisms. Additionally to the application of the proposed methodology, standard AE analyses were also performed.

As it was expected from the standard AE analyses, the number of hits increased with the load due to the succession of the different damage mechanisms. The number of cumulative AE hits was very repeatable for all the tested specimens. Using the proposed methodology three clusters of damages were clearly identified for the tests. The relations of the clusters to the respective damage mechanisms were done based on modal analysis of the signals by analysing their dispersive characteristics and their energy distribution in time and frequency. This was additionally validated by inspecting the samples both during the tests and careful analysis using a 3D measuring laser microscope. As the samples were transparent, visual identification and correlation to the damage mechanisms was as well facilitated. The first cluster was characterized by low amplitude signals representing emissions due to matrix cracking. The second cluster were high amplitude signals representing emissions due to fibre breakage. The third cluster were low amplitude signals representing

emissions due to fibre-matrix debonding. The results are similar to the ones presented in the reviewed literature regarding damage mechanism identification [Hallett and Wisnom 2006, Emery 2007, Bussiba et al. 2008, Paipetis and Aggelis 2012]. The samples loaded with the fibre direction perpendicular to the load suffered from sudden failure, generated very few AE activity and did not provide valuable information for analysis.

The second configuration tested was a double cantilever beam configuration where the samples were forced to fail either in Mode I or Mode II of failure. For the specimens under Mode II failure, a similar behaviour to the one observed with the tensile samples with the fibres perpendicular to the load direction was obtained. The samples failed during two sudden jumps which could be easily observed from the load time histories. The amount of collected AE hits was high but, in a similar manner, no visible clusters were identified using the proposed methodology. In contrast, the specimens under Mode I failure presented a quite different behaviour. The samples showed higher AE activity and a steady crack growth. Using the proposed methodology two clusters of damages were clearly identified for all the tests. The correlation between the formed clusters from the pattern recognition of experimentally recorded AE events and damage mechanisms were believed to correspond to delamination between the middle plies and fibre bridging-related events such as fibre breakage according to the occurrence of the damages and the modal analysis performed on the clustered signals. It could be seen as well that the localisation of AE events was successfully accomplished.

The methodology developed in this thesis seems to satisfactorily work for the purpose of identification of failure mechanisms. However, there were many influencing effects that were not taken into consideration and that could influence the performance and clustering capabilities of the method and which deserve further discussion. For example, it is known that boundary reflections, transducer response and transducers sensitivity could affect the waveforms used to characterise the damage mechanisms and this could lead to possible wrong characterisation. These effects were omitted in the proposed methodology. It has also been shown in [Hamstad et al. 2001] that the close proximity of the specimen edges can influence measurements giving waveform observations that differ depending on the test specimen size. For the reasons given before, it is highly desirable in many cases to complement AE analysis with confirmation of the damage mechanisms by another technique. It would be also interesting to evaluate the concept of moment tensor inversion used for modelling the source mechanisms. This theory is based on the fact that displacement discontinuities can be represented by equivalent volume forces [Ohtsu and Ono 1986, Grosse and Ohtsu 2008]. However, this concept can only be applied in case that the size of the defect is much smaller than the dimensions of the structure and the shortest wavelength being studied [Johnson and Gudmundson 2000]. Moreover, additional testing and data analysis would be of great importance for the further validation of the method so that it could be employed for the quasi real-time classification of damage mechanisms

during AE monitoring.

Chapter 5 was completely dedicated to the application of acousto-ultrasonics for damage assessment. Firstly, an introduction to the transducers configuration and the criteria for the selection of the optimal excitation signal was presented. The selection of parameters such as the optimal number of cycles and excitation frequency together with an analysis of spreading of ultrasonic guided waves in space and time were discussed in detail. The mode shapes of different guided wave modes have been analysed in order to depict the importance of the selection of the actuation signal for an optimized damage detection strategy. This is explained by the fact that it is possible that the modes that are excited in the structure could not be able to interact with damage. This is given due to the changing ratio of displacement and stress amplitudes along the wall thickness as it was depicted in Section 5.3. As it was explained there, the behaviour of guided waves and their interaction with damage is very complex where the sensitivity to damages is a function of the type of mode being excited, the frequency-thickness product and not only of the used wavelength [Alleyne 1991]. This behaviour of mode interaction is exploited in the study case undertaken with the pipe-like structure introduced in Section 7.4. Moreover, several factors affecting the damage detection performance such a variable temperature, changing operational conditions and sensor damage were treated and their effects on the wave propagation were experimentally depicted. At the end, a methodology for damage assessment was developed on the basis of data-driven modelling.

According to the results presented in Section 7.4, an efficient way to detecting and identifying damages was developed in this thesis. A comparison of data-driven modelling using both multi-way PCA and multi-way h-NLPCA by means discrete wavelet transform coefficients, squared prediction error measures and self-organizing maps was presented. Results were shown that illustrated the application of the proposed methodology to isotropic and anisotropic composite structures. The coefficients from the DWT allowed a reduction in the computational cost by decreasing the size of the unfolded matrices by each actuation step since the whole recorded time histories are not used. This step allowed to lessen the difficulty of analysing directly the complex time traces by extracting relevant damage-related information and reducing the dimensionality of the problem. Similarly, the identification of the data set from different structural states was improved. The results showed that the proposed methodology outperformed the analysis accomplished with PCA. This is given by the fact that the method allowed securing the separability of the data classes and permitted a lower dimensional representation. In addition, it was shown how the SOM algorithm by means of the U-matrix surface allowed the identification of the different structural states. Nevertheless, it is good to bear in mind that for the method to be functioning, reliable models for the healthy and damage conditions must be available as with any physical or data-driven models. The analyses showed how the damage detection and identification should be performed by reviewing the cluster maps and the

U-matrix surfaces. Using the cluster map, the clustering tendency can be evaluated and the identification of the data sets can be performed. The U-matrix surface allowed to identify the sparser regions between the map. A comparison of the use of either the approximation or details coefficients from the DWT showed that both methods allowed the detection of damage. However, the results obtained from the detail coefficients did not allow to identify the different damage scenarios. It is very interesting to see how the high frequency bands of the recorded signals provided valuable damage-related information. This could be probably explained by the possible presence of high order harmonics in the spectrum of the transmitted signals which could be an indication of non-linearity inside the material. This effect could potentially lead to significant enhancement in the sensitivity to structural defects.

The effects of temperature and surface wetting on guided wave propagation were also addressed. From Section 7.2.4 it could be observed that the main effects where increase in time-of-flight and changes in sensor response magnitude. It can be concluded that influences such as temperature and changing operational conditions, which modify the structural dynamic responses, can be sufficient to disguise any changes correlated to damage to a level that it might not be detected. These changes can be considered as one of the main disadvantages for implementing active guided waves based techniques in real world applications. This is of special attention in baseline-based methods where the detection and characterisation of damage is performed normally by means of metric indices by comparison of two dynamic response signatures. It was shown in Section 7.4 that the influence of temperature must be compensated so that the damage assessment capabilities are not degraded. It is good to bear in mind that the effects of temperature on the transducer performance were not studied here. Nevertheless, it has been shown that these effects are significantly less than the effect of temperature on wave propagation within the structure. According to the authors opinion, the development of an improved modelling technique incorporating the effects of variable temperature in wave propagation and sensor response as well as the analysis of sensor fault detection would be of great support for the design of a virtual SHM system. It was suggested to collect a baseline related to these environmental conditions over a large range of these changing conditions so that they can be characterized to reflect the different environmental states. However, this approach can be an expensive process and other methods such as the optimal baseline selection and/or the optimal signal stretch are recommended [Konstantinidis et al. 2007, Clarke et al. 2009, Croxford et al. 2010].

An advantage of the approach presented here is to provide robustness in the analysis by the use of sensor-data fusion using the projections obtained by each actuation step together with the squared prediction errors measurements as inputs to a self-organizing map. Additionally, the self-organizing maps visualization capabilities makes this approach interesting, especially for larger amount of data with high dimensional feature vectors.

From the results it can be seen that the multi-way extension of the method proved to be very useful in systems involving several sensors since it allowed building a model for the whole system instead of one by each sensor.

However, there are as usual limitations attached to the proposed methodology. The proposed scheme is a qualitative method which is not capable of multi-site damage detection and identification. If several damages appear in the structure, they will emerge as a new cluster inside the map. Moreover, damage localisation with the acousto-ultrasonics technique has not been proposed in this study. A possible solution for damage localisation is the use of statistical indices and contributions based on PCA as it is proposed in [Tibaduiza-Burgos et al. 2011]. However, this technique can only provide a very rough estimate of the area where damage can be located and the implementation of a very dense sensor network would be required in order to provide more accurate locations of damage. More advanced and reliable techniques are discussed by the author in [Moll et al. 2012].

Chapter 6 was dedicated to the topic of impact load monitoring. The chapter started with a description of the type of loads and the different approaches available for load monitoring. In this section the motivation of using a machine learning techniques is stated. This is motivated by the fact that for structures of high complexity with complicated geometrical profiles and material non-uniformity, it is a very difficult task to achieve a reliable inverse model from physical laws-based models. This is followed by a description of the procedures used for sensor-data fusion, feature extraction and selection together with the introduction of Gaussian processes for the purposes of regression and classification. A unique combination of time-frequency analysis, auto-associative neural networks for dimension reduction and Gaussian processes is developed to automate the impact identification problem. This process involved the passive monitoring of stress waves induced by impacts and evaluated the proposed automatic approach for impact magnitude estimation and localisation based on Bayesian analysis with single target Gaussian processes.

Results from Section 7.5 demonstrated the success of the adopted scheme to provide accurate estimates of position and impact magnitude in two structures. Analysis of the experimental results have depicted that the selection of training data able to reflect the physics of the system under study is a decisive factor in order to obtain an accurate and reliable Gaussian process model for regression and classification. The application of advanced signal processing techniques allowed the extraction of non-linear components from signals of interest to structural health monitoring providing a noise reduced model of the investigated process and improving the performance in regression and classification of the implemented Gaussian processes. As with the supervised neural network approach, the limitations of the method are given by the collection of data representing the different impact loads which could happen in reality. The Gaussian process model should be trained with data representative of the complete possible scenarios in order to be a robust method able of providing reliable estimations. As it was already mentioned in Section 6.2.2,

machine learning algorithms can require large training data sets in which the collection of training data can be an expensive process. In the case of very high value structures, the expense of collecting the training data would be compensated by the advantage of getting a more accurate predictive model. In order to try to cope with this problem, numerical simulations of the system behaviour could be carried out in order to help in the process of collecting training data as it was discussed by the author in [Yang et al. 2011]. Additionally, a detailed evaluation of the use of Gaussian processes for multi-class classification showed that this technique proved to be a very expensive method in both computational resources and elapsed calculation time. A neural network trained with a 1 of M strategy showed to provide similar results in a fraction of the time required with the Gaussian process classification.

Within the framework of future developments, the objective analysis of the developed methodologies and their experimental results depicted that there were several areas which could be improved through further research before implementing them in operative SHM systems. For example, the methods proposed in this thesis must be evaluated on a wider variety of practical structures under real operating conditions since the structures tested during this work only represent a small part of those encountered in reality. It is expected to meet additional challenges while implementing these methods on more complex structures and variable conditions. Additional studies must be also carried out for the design of sensor networks and the sensors themselves based on all the considerations depicted throughout this thesis. The consideration of higher order modes of propagation would be also very useful as a mean for the possible improvement of damage sensitivity for active-sensing technologies. In the case of AE technologies, additional testing must be implemented in order to be able to design robust methods for damage mechanism characterisation. As it was proposed in [Ono 2006], the development of regional or global databases for AE under international cooperation will greatly help researchers in order to tests their algorithms.

Bibliography

Aarabi, P., 2003: The fusion of distributed microphone arrays for sound localization. *EURASIP Journal on Applied Signal Processing*, **4**, 338–347.

Abdelghani, M. and M. Friswell, 2007: Sensor validation for structural systems with multiplicative sensor faults. *Mechanical Systems and Signal Processing*, **21**(1), 270–279.

Achenbach, J., 1984: *Wave Propagation in Elastic Solids*. North-Holland, New York.

Achenbach, J. D. and Y. Xu, 1999: Wave motion in an isotropic elastic layer generated by a time harmonic point load of arbitrary direction. *The Journal of the Acoustical Society of America*, **106**(1), 83–90.

Adolfsson, E. and P. Gudmundson, 1997: Thermoelastic properties in combined bending and extension of thin composite laminates with transverse matrix cracks. *International Journal of Solids and Structures*, **34**(16), 2035–2060.

Aggelis, D. G., N. M. Barkoula, T. E. Matikas, and A. S. Paipetis, 2010: Acoustic emission monitoring of degradation of cross ply laminates. *Journal of the Acoustical Society of America*, **124**(6), 1–6.

Alleyne, D., M. Lowe, and P. Cawley, 1996: The inspection of chemical plant pipework using lamb waves: defect sensitivity and field experience. *Review of Progress in QNDE*, **15**, 1859–1866.

Alleyne, D. N., 1991: *The non-destructive testing of plates using ultrasonic Lamb waves*. Phd thesis.

Alleyne, D. N. and P. Cawley, 1992: The interaction of lamb waves with defects. *IEEE Transactions on Ultrasonics, Ferroelectrics and Frequency Control*, **39**(3), 381–397.

Alleyne, D. N., M. J. S. Lowe, and P. Cawley, 1998: The reflection of guided waves from circumferential notches in pipes. *Journal of Applied Mechanics*, **65**(3), 635–641.

Altenbach, H., J. Altenbach, and W. Kissing, 2004: *Mechanics of Composite Structural Elements*. Springer, Berlin.

Alvarez, M. and N. D. Lawrence, 2009: Sparse convolved gaussian processes for multi-output regression. In *NIPS*, volume 21. MIT Press, Cambridge, MA, 57-64.

Anastassopoulos, A. A., D. A. Kouroussis, V. N. Nikolaidis, A. Proust, A. G. Dutton, M. J. Blanch, L. E. Jones, P. Vionis, D. J. Lekou, D. R. V. v. Delft, P. A. Joosse, T. P. Philippidis, T. Kossivas, and G. Fernando, 2002: Structural integrity evaluation of wind turbine blades using pattern recognition analysis on acoustic emission data. In *Proceedings of the 25th European Conference on Acoustic Emission Testing - EWGAE 2002,*, Prague, Czech Republic, 1-8.

ASTM, 1982: Standard definition of terms relating to acoustic emission.

Ativitavas, N., T. Pothisiri, and T. J. Fowler, 2006: Identification of fiber-reinforced plastic failure mechanism from acoustic emission data using neural networks. *Journal of Composite Materials*, **40**(3), 193–226.

Auger, F. and P. Flandrin, 1995: Improving the readability of time-frequency and time-scale representations by the reassignment method. *IEEE Transactions on Signal Processing*, **43**(5), 1068–1089.

Auger, F., O. Lemoine, P. Goncalves, and P. Flandrin, 1995: Time-frequency toolbox.

Auld, B., 1973: *Acoustic Fields and Waves in Solids*, volume 1. Wiley-Interscience, New York.

Auld, B., 1990: *Acoustic Fields and Waves in Solids*, volume 2. Wiley-Interscience, New York, 2nd edition.

Aveston, J. and A. Kelly, 1973: Theory of multiple fracture of fibrous composites. *Journal of Material Science*, **8**(3), 352–362.

Bank, L. C., T. R. Gentry, B. P. Thompson, and J. S. Russell, 2003: A model specification for frp composites for civil engineering structures. *Construction and Building Materials*, **17**(6-7), 405–437.

Barnett, V. and T. Lewis, 1994: *Outliers in Statistical Data*. John Wileyand Sons, Chichester, 3rd edition.

Bartoli, I., A. Marzani, F. L. d. Scalea, and E. Viola, 2006: Modeling wave propagation in damped waveguides of arbitrary cross-section. *Journal of Sound and Vibration*, **295**(3-5), 685–707.

Baxter, M. G., R. Pullin, K. M. Holford, and S. L. Evans, 2007: Delta t source location for acoustic emission. *Mechanical Systems and Signal Processing*, **21**(3), 1512–1520.

Bentahar, M. and R. E. Guerjouma, 2008: Monitoring progressive damage in polymer-based composite using nonlinear dynamics and acoustic emission. *Journal of the Acoustical Society of America*, **125**(1), 1–6.

Bermes, C., J. Kim, J. Qu, and L. Jacobs, 2007: Experimental characterization of material nonlinearity using lamb waves. *Applied Physics Letters*, **90**(2), 021901.

Bishop, C. M., 1995: *Neural Networks for Pattern Recognition*. Clarendon Press, Oxford.

Bishop, C. M., 2007: *Pattern Recognition and Machine Learning*. Information Science and Statistics. Springer, Singapore, 1st edition.

Bonilla, E., K. M. Chai, and C. Williams, 2008: Multi-task gaussian process prediction. In *Advances in Neural Information Processing Systems 20*, Platt, J. C., Koller, D., Singer, Y., and Roweis, S., editors. MIT Press, Cambridge, MA, 153-160.

Boyle, P. and M. Frean, 2004: Multiple output gaussian process regression. Technical report, Victoria University of Wellington.

Brandt, J., 2004: Part i: The composite material research requirements of the aerospace industry. Technical report, EADS.

Bray, D. and D. Mcbride, 1992: *Nondestructive testing techniques*. John Wiley Sons, Inc., New York.

Brio, B. M. d. and A. S. Molina, 2002: *Redes Neuronales y Sistemas Difusos*. Alfaomega, Colombia, 2nd edition.

Brownjohn, J., 2007: Structural health monitoring of civil infrastructure. *Phil. Trans. R. Soc. A*, **365**(1851), 589–622.

Buethe, I., M. A. Torres Arredondo, L. E. Mujica, J. Rodellar, and C.-P. Fritzen, 2012: Damage detection in piping systems using pattern recognition techniques. In *Proceedings of the 6th European Workshop in Structural Health Monitoring, EWSHM 2012*, volume 1, Dresden, Germany, 624-631.

Bussiba, A., M. Kupiec, S. Ifergane, R. Piat, and T. Boehlke, 2008: Damage evolution and fracture events sequence in various composites by acoustic emission technique. *Composite Science and Technology*, **68**, 1144–1155.

Calomfirescu, M., 2008: *Lamb Waves for Structural Health Monitoring in Viscoelastic Composite Materials*. Phd thesis.

Calomfirescu, M. and A. S. Herrmann, 2007: On the propagation of lamb waves in viscoelastic composites for shm applications. *Key Engineering Materials*, **347**, 543–548.

Carlsson, L. and B. Norrbom, 1983: Acoustic emission from graphite/epoxy composite laminates with special reference to delamination. *Journal of Materials Science*, **18**(8), 2503–2509.

Carlyle, J., 1989: Acoustic emission testing the f-111. *NDT International*, **22**(2), 67–73.

Carreno, I. R. and M. Vuskovic, 2005: Wavelet transform moments for feature extraction from temporal signals. In *2nd International Conference in Control, Automation and Robotics, ICINCO 2005*, Barcelona, Spain, 1-8.

Castaings, M., 2007: Characterization of viscoelastic properties of composite materials. Technical report, Laboratoire de Mecanique Physique, UniversitÃ© Bordeaux.

Chang, F.-K., 2002: Ultra reliable and super safe structures for the new century. In *Proceeding of the 1st European Workshop on Structural Health Monitoring*, Balageas, D. L., editor, Paris, France, 3-12.

Chapuis, B., N. Terrien, and D. Royer, 2011: Modeling and experimental investigations of lamb waves focusing in anisotropic plates. *Journal of Physics: Conference Series*, **269**(1), 012020.

Chen, H., x, Yang, C. Man, and Sing, 1994: Radiation and focusing of sh0 elastic waves in anisotropic sheets. *Applied Physics Letters*, **64**(8), 966–968.

Chree, C., 1889: The equations of an isotropic solid in polar and cylindrical coordinates, their solutions and applications. *Trans. Cambridge Philos. Soc.*, **14**, 250–369.

Ciang, C. C., J.-R. Lee, and H.-J. Bang, 2008: Structural health monitoring for a wind turbine system: a review of damage detection methods. *Measurement Science and Technology*, **19**(12), 1–20.

Cicero, T., P. Cawley, M. J. S. Lowe, and F. Simonetti, 2009: Effects of liquid loading and change of properties of adhesive joints on subtraction techniques for structural health monitoring. *Review of Progress in Quantitative NDE*, **28A**, 1006–1013.

Clarke, T., 2009: *Guided wave health monitoring of complex structures*. Phd thesis.

Clarke, T., F. Simonetti, and P. Cawley, 2009: Guided wave health monitoring of complex structures by sparse array systems: Influence of temperature changes on performance. *Journal of Sound and Vibration*, **329**(12), 2306–2322.

Coifman, R. R. and M. V. Wickerhauser, 1992: Entropy-based algorithms for best basis selection. *IEEE Transactions on Information Theory*, **38**(2), 713–718.

Coverley, P. T. and W. J. Staszewski, 2003: Impact damage location in composite structures using optimized sensor triangulation procedure. *Smart Materials and Structures*, **12**(5), 795–803.

Croxford, A. J., J. Moll, P. D. Wilcox, and J. E. Michaels, 2010: Efficient temperature compensation strategies for guided wave structural health monitoring. *Ultrasonics*, **50**(4-5), 517–528.

Dai, H. and C. MacBeth, 1997: The application of back-propagation neural network to automatic picking seismic arrivals from single-component recordings. *Geophysical Journal International*, **120**(B7), 105–113.

Das, S., A. Chattopadhyay, and X. Zhou, 2009: Acoustic based structural health monitoring for composites using optimal sensor placement: Analysis and experiments. *Journal of Reinforced Plastics and Composites*, **28**(1), 83–97.

Deschamps, M. and B. Hosten, 1992: The effects of viscoelasticity on the reflection and transmission of ultrasonic waves by an orthotropic plate. *The Journal of the Acoustical Society of America*, **91**(4), 2007–2015.

Ditri, J. J., J. L. Rose, and G. Chen, 1992: Mode selection criteria for defect detection optimization using lamb waves. *Review of Progress in QNDE*, **11**(1), 2109–2115.

Doebling, S., C. Farrar, and M. Prime, 1998: A summary review of vibration-based damage identification methods. *The Shock and Vibration Digest*, **30**(1), 91–105.

Doyle, J. F., 1997: *Wave Propagation in Structures: Spectral Analysis Using Fast Discrete Fourier Transforms*. Springer, New York.

Dunegan, H. L., 1998: Modal analysis of acoustic emission signals. *Journal of Acoustic emission*, **15**, 1–11.

Eaton, M., K. M. Holford, C. Featherston, and R. Pullin, 2006: Acoustic emission monitoring of defects in buckling cfrp composite panels. *Advanced Materials Research*, **13-14**, 259–266.

Emery, T. R., 2007: *Identification of Damage in Composite Materials using Thermoelastic Stress Analysis*. Phd thesis.

Englehart, K., B. Hudgins, P. Parker, and M. Stevenson, 1999: Improving myoelectric signal classification using wavelet packets and principal components analysis. In *Proceedings of the 21st Annual Conf. and the 1999 Annual Fall Meeting of the Biomedical Engineering Society*, volume 1, Atlanta.

Every, A. G., W. Sachse, K. Y. Kim, and M. O. Thompson, 1990: Phonon focusing and mode-conversion effects in silicon at ultrasonic frequencies. *Physical Review Letters*, **65**(12), 1446.

Farrar, C. R. and K. Worden, 2007: An introduction to structural health monitoring. *Philosophical Transactions of the Royal Society A: Mathematical, Physical and Engineering Sciences*, **365**(1851), 303–315.

Finlayson, R. D., M. Friesel, M. Carlos, P. Cole, and J. Lenain, 2001: Health monitoring of aerospace structures with acoustic emission and acousto-ultrasonics. *Insight: Non-Destructive Testing and Condition Monitoring*, **43**(3), 155–158.

Flynn, E. B. and M. D. Todd, 2010: Optimal placement of piezoelectric actuators and sensors for detecting damage in plate structures. *Journal of Intelligent Material Systems and Structures*, **21**(1), 265–274.

Friedman, J. . H. and W. Stuetzle, 1981: Projection pursuit regression. *Journal of the American Statistical Association*, **76**(376), 817–823.

Fritzen, C.-P., 2005: Recent developments in vibration-based structural health monitoring. In *Proceedings of the 5th International Workshop on Structural Health Monitoring*, Chang, F.-K., editor, DEStech, Stanford, CA, 42-60.

Fritzen, C.-P., G. Mengelkamp, and A. Guemes, 2003: Elimination of temperature effects on damage detection within a smart structure concept. In *Proceedings of the 4th Inter-*

national Workshop on Structural Health Monitoring, Chang, F.-K., editor, volume 1, DEStech Publications, Inc., Stanford, CA, 1530-1538.

Fritzen, C.-P., R. T. Schulte, and H. Jung, 2011: A modelling approach for virtual development of wave based shm systems. *Journal of Physics: Conference Series*, **305**(1), 012071.

Fucai, L., M. Guang, Y. Lin, L. Ye, and K. Kazuro, 2009: Dispersion analysis of lamb waves and damage detection for aluminum structures using ridge in the time-scale domain. *Measurement Science and Technology*, **20**(9), 1–11.

Gao, H. and J. L. Rose, 2006: Ultrasonic sensor placement optimization in structural health monitoring using evolutionary strategy. *Quantitative Nondestructive Evaluation*, **25**(1), 1687–1693.

Gaul, L., S. Hurlebaus, and L. J. Jacobs, 2001: Localization of a synthetic acoustic emission source on the surface of a fatigue specimen. *Research in Nondestructive Evaluation*, **13**(2), 105–117.

Gazis, D. C., 1959a: Three-dimensional investigation of the propagation of waves in hollow circular cylinders. i. analytical foundation. *The Journal of the Acoustical Society of America*, **31**(5), 568–573.

Gazis, D. C., 1959b: Three-dimensional investigation of the propagation of waves in hollow circular cylinders. ii. numerical results. *The Journal of the Acoustical Society of America*, **31**(5), 573–578.

Gibbs, M. and D. Mackay, 2000: Variational gaussian process classifiers. *IEEE Transactions on Neural Networks*, **11**(6), 1458–1464.

Gibbs, M. N., 1997: *Bayesian Gaussian Processes for Regression and Classification*. Phd thesis.

Giordano, M., A. Calabro, C. Esposito, C. Salucci, and L. Nicolais, 1999: Analysis of acoustic emission signals resulting from fiber breakage in single fiber composites. *Polymer Composites*, **20**(6), 758–770.

Girard, A., 2004: *Approximate methods for propagation of uncertainty with gaussian process models*. Phd thesis.

Godin, N., S. Huguet, R. Gaertner, and L. Salmon, 2004: Clustering of acoustic emission signals collected during tensile tests on unidirectional glass/polyester composite using supervised and unsupervised classifiers. *NDT&E International*, **37**, 253–264.

Gorman, M. R., 1991: Plate wave acoustic emission. *Journal of the Acoustical Society of America*, **90**(1), 358–364.

Graff, K. F., 1975: *Wave Motion in Elastic Solids*. University Press, London: Oxford.

Grosse, C. U., F. Finck, J. H. Kurz, and H. W. Reinhardt, 2004: Improvements of ae technique using wavelet algorithms, coherence functions and automatic data analysis. *Construction and Building Materials*, **18**(3), 203–213.

Grosse, C. U. and M. Ohtsu, 2008: *Acoustic Emission Testing*. Basics For Research - Applications in Civil Engineering. Springer, Leipzig, 1 edition.

Grosse, C. U. and H. W. Reinhardt, 2002: Signal conditioning in acoustic emission analysis using wavelets. *Journal of NDT*, **7**(9).

Guo, D., A. Mal, and K. Ono, 1996: Wave theory of acoustic emission in composite laminates. In *Materials Research with Advanced Acoustic Emission Techniques*, volume 14, Rottach-Egern, Germany, 19-46.

Hallett, S. R. and M. R. Wisnom, 2006: Experimental investigation of progressive damage and the effect of layup in notched tensile tests. *Journal of Composite Materials*, **40**(2), 119–141.

Halpin, J. C., 1969: Effects of environmental factors on composite materials. Technical report, Air Force Materials Laboratory.

Hamstad, M., A. OGallagher, and J. Gary, 2001: Effects of lateral plate dimensions on acoustic emission signals from dipole sources. *Journal of Acoustic Emission*, **19**, 258–274.

Hardy, H. R., 2003: *Acoustic emission / microseismic activity*. A.A. Balkema Publishers, New York.

Hayashi, T. and K. Kawashima, 2002: Multiple reflections of lamb waves at a delamination. *Ultrasonics*, **40**(1-8), 193–197.

Hearn, E. J., 1977: *Mechanics of Materials: An Introduction to the Mechanics of Elastic and Plastic Deformation of Solids and Structural Components*, volume 19 of *International Series on Materials Science and Technology*. Pergamon, New York, 1st edition.

Hensman, J., R. Mills, S. Pierce, K.Worden, and M. Eaton, 2008: Locating acoustic emission sources in complex structures using gaussian processes. *Mechanical Systems and Signal Processing*, **24**(1), 211–223.

Holford, K. M., 2000: Acoustic emission-basic principles and future directions. *Strain*, **36**(2), 51–54.

Hong, J.-C., K. Sun, and Y. Kim, 2005: The matching pursuit approach based on the modulated gaussian pulse for efficient guided wave inspection. *Smart Materials and Structures*, **14**(4), 548–560.

Hosten, B., 1991a: Bulk heterogeneous plane waves propagation through viscoelastic plates and stratified media with large values of frequency domain. *Ultrasonics*, **29**(6), 445–450.

Hosten, B., 1991b: Reflection and transmission of acoustic plane waves on an immersed orthotropic and viscoelastic solid layer. *The Journal of the Acoustical Society of America*, **89**(6), 2745–2752.

Hua, J. and J. L. Rose, 2010: Guided wave inspection penetration power in viscoelastic coated pipes. *Insight NonDestructive Testing and Condition Monitoring*, **52**(4), 195–200.

Jeong, H. and Y.-S. Jang, 2000: Wavelet analysis of plate wave propagation in composite laminates. *Composite Structures*, **49**(4), 443–450.

Jia, N. and V. Kagan, 2003: Mechanical performance of polyamides with influence of moisture and temperature - accurate evaluation and better understanding. Technical report, BASF Corporation.

Johnson, M., 2002: Waveform based clustering and classification of ae transients in composite laminates using principal component analysis. *NDT and E International*, **35**(6), 367–376.

Johnson, M. and P. Gudmundson, 2000: Broad-band transient recording and characterization of acoustic emission events in composite laminates. *Composites Science and Technology*, **60**(15), 2803–2818.

Jollife, I. T., 2002: *Principal Component Analysis*. Springer Series in Statistics. Springer.

Jones, R. T., J. S. Sirkis, and E. J. Friebele, 1997: Detection of impact location and magnitude for isotropic plates using neural networks. *Journal of Intelligent Material Systems and Structures*, **8**(1), 90–99.

Kaiser, J., 1950: *A study of acoustic phenomena in tensile tests*. Phd thesis.

Kalogiannakis, G. and D. v. Hemelrijck, 2011: Classification of wavelet decomposed ae signals based on parameter-less self organized mappig. *International Journal of Materials and Product Technology*, **41**(1-4), 89–104.

Kaski, S., J. Nikklia, and T. Kohonen, 1998: Methods for interpreting a self-organized map in data analysis. In *Proceedings of the 6th European Symposium of Artificial Neural Networks (ESANN98)*, Brussels, Belgium, 185-190.

Kaw, A. K. and E. E. Kalu, 2008: *Numerical Methods with Applications*. Lulu, 2nd edition.

Kerschen, G., P. D. Boe, J.-C. Golinval, and K. Worden, 2005: Sensor validation using principal component analysis. *Smart Materials and Structures*, **14**, 36–42.

Kim, J. K., 2000: Stress intensity. Technical report, Virginia Tech Materials Science and Engineering.

Kishimoto, K., H. Inoue, M. Hamada, and T. Shibuya, 1995: Time frequency analysis of dispersive waves by means of wavelet transform. *Journal of Applied Mechanics*, **62**, 841–846.

Klinkov, M., 2011: *Identification of Unknown Structural Loads from Dynamic Measurements Using Robust Observers*. Phd thesis.

Knapp, C. H. and C. Carter, 1976: The generalized correlation method for estimation of time delay. *IEEE Transactions on Acoustics, Speech and Signal Processing*, **24**(4).

Kohonen, T., 2001: *Self Organizing Maps*. Springer.

Kolomenskii, A. A. and A. A. Maznev, 1993: Phonon-focusing effect with laser-generated ultrasonic surface waves. *Physical Review B*, **48**(19), 14502.

Komai, K., K. Minoshima, and T. Shibutani, 1991: Investigations of the fracture mechanism of carbon/epoxy composites by ae signal analyses. *JSME International Journal*, **34**(3), 381–388.

Konstantinidis, G., P. D. Wilcox, and B. W. Drinkwater, 2007: An investigation into the temperature stability of a guided wave structural health monitoring system using permanently attached sensors. *IEEE Sensors Journal*, **7**(5), 905–912.

Kraemer, P., I. Buethe, and C.-P. Fritzen, 2011: Damage detection under changing operational and environmental conditions using self organizing maps. In *Proceedings of SMART 11*, Saarbruecken, Germany.

Kramer, M. A., 1991: Nonlinear principal component analysis using autoassociative neural networks. *AIChE Journal*, **37**(2), 233–243.

Kumar, B. G., R. P. Singh, and T. Nakamura, 2002: Degradation of carbon fiber-reinforced epoxy composites by ultraviolet radiation and condensation. *Journal of Composite Materials*, **36**(24), 2713–2733.

Kundu, T., 2003: *Ultrasonic Nondestructive Evaluation: Engineering and Biological Material Characterization*. CRC Press, London, 1st edition.

Kundu, T., 2012: A new technique for acoustic source localization in an anisotropic plate without knowing its material properties. In *Proceedings of the 6th European Workshop in Structural Health Monitoring, EWSHM 2012*, Dresden, Germany, 37-45.

Kurokawa, Y., Y. Mizutani, and M. Mayuzumi, 2005: Real-time executing source location system applicable to anisotropic thin structures. *The Journal of the Acoustical Society of America*, **23**, 224–232.

Kurz, J. H., C. U. Grosse, and H. W. Reinhardt, 2005: Strategies for reliable automatic onset time picking of acoustic emissions and of ultrasound signals in concrete. *Ultrasonics*, **43**(7), 538–546.

Lamb, H., 1917: On waves in an elastic plate. *Proceedings of the Royal Society of London*, **93**(648), 114–128.

LeClerc, J., K. Worden, W. Staszewski, and J. Haywood, 2007: Impact detection in an aircraft composite panel - a neural-network approach. *Journal of Sound and Vibration*, **299**(3), 672–682.

Lee, B. C. and W. J. Staszewski, 2007a: Lamb wave propagation modelling for damage detection: Ii. damage monitoring strategy. *Smart Materials and Structures*, **16**(2).

Lee, B. C. and W. J. Staszewski, 2007b: Sensor location studies for damage detection with lamb waves. *Smart Materials and Structures*, **16**(2), 399–408.

Lee, C., J. J. Scholey, P. D. Wilcox, M. Wisnom, M. I. Friswell, and B. Drinkwater, 2006: Guided wave acoustic emission from fatigue crack growth in aluminium plate. *Advanced Materials Research*, **13-14**, 23–28.

Li-Fei, L., S. Gong-Tian, Z. Zheng, and W. Zhan-Wen, 2012: Study on crack detection in cast iron plates using the acousto-ultrasonic technique. *Insight - Non-Destructive Testing and Condition Monitoring*, **54**(4), 204–207.

Liang, C., F. Sun, and C. A. Rogers, 1996: Electro-mechanical impedance modeling of active material systems. *Smart Materials and Structures*, **5**(2), 171–186.

Liu, G. and J. Qu, 1999: Guided circumferential waves in a circular annulus. *Journal of Applied Mechanics*, **65**(3), 424–429.

Loutas, T. and V. Kostopoulos, 2009: Health monitoring of carbon/carbon, woven reinforced composites. damage assessment by using advanced signal processing techniques. part i: Acoustic emission monitoring and damage mechanisms evolution. *Composite Science and Technology*, **69**(2), 265–272.

Lowe, M. J. S., 1995: Matrix techniques for modeling ultrasonic waves in multilayered media. *IEEE Transactions on Ultrasonics, Ferroelectrics and Frequency Control*, **42**(4).

Lu, Y. and J. E. Michaels, 2009: Feature extraction and sensor fusion for ultrasonic structural health monitoring under changing environmental conditions. *IEEE Sensors Journal*, **9**(11), 1462–1471.

Lundsgaard-Larsen, C., C. Berggreen, A. Quispitupa, and L. A. Carlsson, 2009: Improved damage tolerant face/core interface design in sandwich structures. In *Proceedings of the International Conference on Composite Materials*, Edinburg.

MacKay, D. J., 1997: Gaussian processes: A replacement for supervised neural networks? In *Proceedings of NIPS: Neural Information Processing Systems*.

Maeda, N., 1985: A method for reading and checking phase times in auto-processing system of seismic wave data. *Journal of the Seismological Society of Japan*, **38**, 365–379.

Mal, A. K., 1988: Wave propagation in layered composite laminates under periodic surface loads. *Wave Motion*, **10**, 257–266.

Mallat, S., 1989: A theory for multiresolution signal decomposition: the wavelet representation. *IEEE Transactions on Pattern Analysis and Machine Intelligence*, **11**(7), 674–693.

Mallat, S., 1997: *A Wavelet Tour of Signal Processing*. Academic Press, San Diego, 2 edition.

Mallat, S. G. and Z. Zhang, 1993: Matching pursuits with time-frequency dictionaries. *IEEE Transactions on Signal Processing*, **41**(12), 3397–3415.

Manson, G., 2002: Identifying damage sensitive, environment insensitive features for damage detection. In *Proceedings of the Third International Conference on Identification in Engineering Systems*, Institute of Physics Publishing, Swansea, 187-197.

Manson, G., S. G. Pierce, and K. Worden, 2001: On the long-term stability of normal condition for damage detection in a composite panel. *Key Engineering Materials*, **204-205**, 359–370.

Marec, A., J.-H. Thomas, and R. E. Guerjouma, 2008: Damage characterization of polymer-based composite materials: Multivariable analysis and wavelet transform for clustering acoustic emission data. *Mechanical Systems and Signal Processing*, **22**(6), 1441–1464.

Maris, H. J., 1971: Enhancement of heat pulses in crystals due to elastic anisotropy. *The Journal of the Acoustical Society of America*, **50**(3B), 812–818.

Masri, S. F., A. G. Chassiakos, and T. K. Caughey, 1993: Identification of nonlinear dynamic systems using neural networks. *Journal of Applied Mechanics*, **60**(1), 123–133.

Maznev, A. and A. Every, 1995: Focusing of acoustic modes in thin anisotropic plates. *Acta Acustica*, **3**(25), 387–391.

Maznev, A. A., A. M. Lomonosov, P. Hess, and A. l. A. Kolomenskii, 2003: Anisotropic effects in surface acoustic wave propagation from a point source in a crystal. *The European Physical Journal B - Condensed Matter and Complex Systems*, **35**(3), 429–439.

McGowan, J. G., R. W. Hyers, K. L. Sullivan, J. F. Manwell, S. V. Nair, B. McNiff, and B. C. Syrett, 2007: A review of materials degradation in utility scale wind turbines. *Energy Materials: Materials Science and Engineering for Energy Systems*, **2**(1), 41–63.

McGugan, M., B. F. Soerensen, R. Oestergaard, and T. Bech, 2006: Detecting and identifying damage in sandwich polymer composite by using acoustic emission. Technical report, Riso National Laboratory.

Mengelkamp, G., 2006: *Entwicklung einer intelligenten Struktur: eine Kombination globaler und lokaler Verfahren zur Schadensdiagnose*. Phd thesis.

Merkl, D. and A. Rauber, 1997: Cluster connections - a visualization technique to reveal cluster boundaries in self-organizing maps. In *Proceedings of the 9th Italian Workshop on Neural Nets (WIRN97)*, Springer.

Meyendorf, N., B. Frankenstein, and L. Schubert, 2012: Structural health monitoring for aircraft, ground transportation vehicles, wind turbines and pipes - prognosis. In *Emerging Technologies in Non-Destructive Testing V*, Paipetis, A. S., Matikas, T. E., Aggelis, D. G., and Hemelrijck, D. V., editors. Taylor and Francis Group, London.

Michaels, J. E., 2008: Detection, localization and characterization of damage in plates with an in situ array of spatially distributed ultrasonic sensors. *Smart Materials and Structures*, **17**(3).

Mindlin, R., 1951: Influence of rotary inertia and shear on flexural motion of isotropic elastic plates. *Journal of Applied Mechanics Transactions of the ASME*, **18**, 31–38.

Miranda, A. A., Y.-A. Borgne, and G. Bontempi, 2008: New routes from minimal approximation error to principal components. *Neural Processing Letters*, **27**(3), 197 – 207.

Moll, J., 2011: *Strukturdiagnose mit Ultraschallwellen durch Verwendung von piezoelektrischen Sensoren und Aktoren*. Phd thesis.

Moll, J., R. T. Schulte, B. Hartmann, C.-P. Fritzen, and O. Nelles, 2010: Multi-site damage localization in anisotropic plate-like structures using an active guided wave structural health monitoring system. *Smart Materials and Structures*, **19**(4).

Moll, J., M. A. Torres Arredondo, and C.-P. Fritzen, 2012: Computational aspects of guided wave based damage localization algorithms in flat anisotropic structures. *Smart Structures and Systems*, **10**(3), 229–251.

Mujica, L., D. Tibaduiza-Burgos, and J. Rodellar, 2010: Data-driven multiactuator piezoelectric system for structural damage localization. In *Proceedings of the Fifth World Conference on Structural Control and Monitoring*, Tokyo, Japan.

Mujica, L. E., J. Rodellar, A. Fernandez, and A. Guemes, 2010: Q-statistic and t2-statistic pca-based measures for damage assessment in structures. *Structural Health Monitoring*, **10**(5), 539–553.

Mujica, L. E., J. Rodellar, J. Vehi, K. Worden, and W. Staszewski, 2009: Extended pca visualisation of system damage features under environmental and operational variations. In *Proceedings of the 16th SPIE conference: Smart Structures and Materials & Nondestructive Evaluation and Health Monitoring*, San Diego, CA, USA.

Mujica, L. E., J. Vehi, M. Ruiz, M. Verleysen, W. Staszewski, and K. Worden, 2008: Multivariate statistics process control for dimensionality reduction in structural assessment. *Mechanical Systems and Signal Processing*, **22**, 155–171.

Murthy, C. R. L., B. Dattaguru, and A. Rao, 1987: Application of pattern recognition concepts to acoustic emission signals analysis. *Journal of Acoustic Emission*, **6**(1), 19–28.

Mustapha, F., G. Manson, K. Worden, and S. G. Pierce, 2007: Damage location in an isotropic plate using a vector of novelty indices. *Mechanical Systems and Signal Processing*, **21**(4), 1885–1906.

Nayfeh, A. H., 1991: The general problem of elastic wave propagation in multilayered anisotropic media. *The Journal of the Acoustical Society of America*, **89**(4), 1521–1531.

Nayfeh, A. H., 1995: *Wave Propagation in Layered Anisotropic Media with Applications to Composites*, volume 39 of *Applied Mathematics and Mechanics*. Elsevier, Amsterdam.

Neal, R. M., 1995: *Bayesian Learning for Neural Networks*. Phd thesis.

Neau, G., 2003: *Lamb waves in anisotropic viscoelastic plates. Study of the wave fronts and attenuation*. Phd thesis.

Nomikos, P. and J. F. MacGregor, 1994: Monitoring batch processes using multiway principal component analysis. *AIChE Journal*, **40**(8), 1361–1375.

Odell, J. H., 1991: Monitored proof testing: a method of insuring structural integrity. *Air Clues: The Royal Airforce Safety Magazine*, **13-14**, 416–419.

Ohtsu, M. and K. Ono, 1986: The generalized theory and source representations of acoustic emission. *Journal of Acoustic Emission*, **5**(4), 124–133.

Oliveira, R. d. and A. T. Marques, 2006: Damage mechanisms identification in frp using acoustic emission and artificial neural networks. *Materials Science Forum*, **214-516**, 789–793.

Ono, K., 2006: Ae methodology for the evaluation of structural integrity. *Advanced Materials Research*, **13-14**, 17–22.

Oskouei, A. R., M. Ahmadi, and M. Hajikhani, 2009: Wavelet-based acoustic emission characterization of damage mechanism in composite materials under mode i delamination at different interfaces. *eXPRESS Polymer Letters*, **13**(12), 804–813.

Overly, T. G., G. Park, K. M. Farinholt, and C. R. Farrar, 2009: Piezoelectric active-sensor diagnostics and validation using instantaneous baseline data. *IEEE Sensors Journal*, **9**(11), 1414–1421.

Paipetis, A. and D. Aggelis, 2012: Damage assessment in fibrous composites using acoustic emission. In *Acoustic Emission*, Sikorski, W., editor. InTech.

Pao, Y.-H., 1978: Theory of acoustic emission. In *Elastic Waves and non-destructive testing of materials*, pao, Y. H., editor. American Society of Mechanical Engineers, San Francisco. California, 107-127.

Park, G., C. R. Farrar, F. L. Di Scalea, and S. Coccia, 2006: Performance assessment and validation of piezoelectric active-sensors in structural health monitoring. *Smart Materials and Structures*, **15**, 1673–1683.

Park, J., S. Ha, and F.-K. Chang, 2009: Monitoring impact events using a system-identification method. *AIAA Journal*, **47**(9), 2011–2021.

Patera, A. T., 1984: A spectral element method for fluid dynamics: Laminar flow in a channel expansion. *Journal of Computational Physics*, **54**(3), 468–488.

Pavlakovic, B. and M. Lowe, 2003: Disperse: A general purpose program for creating dispersion curves. user's manual. Technical report, Imperial College London.

Pavlakovic, B., M. Lowe, D. N. Alleyne, and P. Cawley, 1997: Disperse: A general purpose program for creating dispersion curves. *Review of Progress in QNDE*, **16**, 185–192.

Peairs, D. M., G. Park, and D. J. Inman, 2004: Improving accessibility of the impedance-based structural health monitoring method. *Journal of Intelligent Material Systems and Structures*, **15**(2), 129–139.

Pochhammer, L., 1876: Ueber die fortplanzungsgeschwindigkeiten schwingungen in einemunbegrentzten isotropen kreiscylinder. *Journal fuer die reine angewandte Mathematik*, **81**, 324–336.

Pohl, J. and G. Mook, 2010: Shm of cfrp-structures with impedance spectroscopy and lamb waves. *International Journal of Mechanics and Materials in Design*, **6**(1), 53–62.

Pollock, A. A., 1981: Acoustic emission amplitude distributions. *International Advances in Nondestructive Testing*, **7**, 215–239.

Pollock, A. A., 1989: Acoustic emission inspection. In *ASM Handbook. Nondestructive Evaluation and Quality Control. ASM International*, volume 17. 278-294.

Potel, C., S. Baly, J. F. de Belleval, M. Lowe, and P. Gatignol, 2005: Deviation of a monochromatic lamb wave beam in anisotropic multilayered media: asymptotic analysis, numerical and experimental results. *IEEE Transactions on Ultrasonics, Ferroelectrics and Frequency Control*, **52**(6), 987–1001.

Price, K., R. M. Storn, and J. A. Lampinen, 2005: *Differential Evolution: A Practical Approach to Global Optimization*. Natural Computing. Springer, Heidelberg, 1 edition.

Prosser, W. H., K. E. Jackson, S. Kellas, B. T. Smith, J. McKeon, and A. Friedman, 1995: Advanced waveform-based acoustic emission detection of matrix cracking in composites. *Materials Evaluation*, **53**(9), 1052–1058.

Prosser, W. H., D. Seale Michael, and T. Smith Barry, 1999: Time-frequency analysis of the dispersion of lamb modes. Technical report, NASA Langley Technical Report Server. 888321.

Pullin, R., M. Eaton, M. R. Pearson, C. Pollard, and K. M. Holford, 2012: Assessment of bonded patch bridge repairs using acoustic emission and acousto-ultrasonics. *Key Engineering Materials*, **518**, 57–65.

Pullin, R., K. Holford, and M. Baxter, 2005: Modal analysis of acoustic emission signals from artificial and fatigue crack sources in aerospace grade steel. *Key Engineering Materials*, **293-294**, 217–226.

Qazaz, C. S., C. K. I. Williams, and C. M. Bishop, 1996: An upper bound on the the bayesian error bars for generalized linear regression. In *Mathematics of Neural Networks and Applications: Models, Algorithms and Applications*. Kluwer Academic Publishers, Boston.

Qi, G., 2000: Wavelet-based ae characterization of composite materials. *NDT and E International*, **33**(3), 133–144.

Qin, S. J., 2003: Statistical process monitoring: basics and beyond. *Journal of Chemometrics*, **17**(8-9), 480–502.

Raghavan, A. and C. E. S. Cesnik, 2005: Finite-dimensional piezoelectric transducer modeling for guided wave based structural health monitoring. *Smart Materials and Structures*, **14**(6), 1448–1461.

Raghavan, A. and C. E. S. Cesnik, 2007: Guided wave signal processing using chirplet matching pursuits and mode correlation for structural health monitoring. *Smart Materials and Structures*, **16**(2), 355–366.

Ramirez-Jimenez, C., N. Papadakis, N. Reynolds, T. H. Gan, P. Purnell, and M. Pharaoh, 2004: Identification of failure modes in glass/polypropylene composites by means of the primary frequency content of the acoustic emission event. *Composites Science and Technology*, **64**(12), 1819–1827.

Rao, A., 1990: Acoustic emission and signal analysis. *Defence Science Journal*, **40**(1), 55–70.

Rasmussen, C. E., 1996: *Evaluation of Gaussian Processes and Other Methods for Non-Linear Regression*. Phd thesis.

Rasmussen, C. E., 2004: Gaussian processes in machine learning: Advanced lectures on machine learning. volume 3176 of *Lecture Notes in Computer Science*. Springer Berlin / Heidelberg, 63-71.

Rasmussen, C. E. and C. K. I. Williams, 2006: *Gaussian Processes for Machine Learning*. The MIT Press.

Reddy, J. N., 1984: A refined nonlinear theory of plates with transverse shear deformation. *International Journal of Solids and Structures*, **20**(9-10), 881–896.

Reddy, J. N., 2002: *Energy Principles and Variational Methods in Applied Mechanics*. John Wiley & Sons, New York.

Reddy, J. N., 2004: *Mechanics of Laminated Composite Plates and Shells: Theory and Analysis*. CRC Press, New York, 2nd edition.

Reinhardt, H. W., C. U. Grosse, and A. T. Herb, 2000: Ultrasonic monitoring of setting and hardening of cement mortar: A new device. *Materials and Structures*, **33**, 580–583.

Rios-Soberanis, C. R., 2011: Acoustic emission technique, an overview as a characterization tool in materials science. *Journal of Applied Research and Technology*, **9**(3), 367–379.

Rippengill, S., K. Worden, K. M. Holford, and R. Pullin, 2003: Automatic classification of acoustic emission patterns. *Strain*, **39**(1), 31–41.

Rose, J. L., 1999: *Ultrasonic Waves in Solid Media*. Cambridge University Press, Cambridge.

Rose, J. L., 2004: Ultrasonic guided waves in structural health monitoring. *Key Engineering Materials*, **270-273**, 14–21.

Rytter, A., 1993: *Vibrational based inspection of civil engineering structures*. Phd thesis.

Salas, K. I. and C. E. S. Cesnik, 2010: Guided wave structural health monitoring using clover transducers in composite materials. *Smart Materials and Structures*, **19**(1), 015014.

Santos, M. J., A. R. Ferreira, and J. M. Perdigao, 2004: Practical considerations on ultrasonic guided wave propagation: Immersion and contact methods. *Materials Evaluation*, **62**(4), 443–449.

Sause, M., A. Gribov, A. Unwin, and S. Horn, 2012: Pattern recognition approach to identify natural clusters of acoustic emission signals. *Pattern Recognition Letters*, **33**(1), 17–23.

Scherbaum, F., 2001: *Of Poles and Zeros: Fundamentals of Digital Seismology*. Modern Approaches in Geophysics. Springer, 2nd edition.

Scholey, J., P. Wilcox, M. Wisnom, and M. Friswell, 2010a: A practical technique for quantifying the performance of acoustic emission systems on plate-like structures. *Ultrasonics*, **49**(6-7), 538–548.

Scholey, J. J., P. D. Wilcox, M. R. Wisnom, and M. I. Friswell, 2010b: Quantitative experimental measurements of matrix cracking and delamination using acoustic emission. *Composites Part A: Applied Science and Manufacturing*, **41**(5), 612–623.

Scholz, M., 2002: *Nonlinear PCA based on neural networks*. Diploma thesis.

Scholz, M., M. Fraunholz, and J. Selbig, 2008: Nonlinear principal component analysis: Neural network models and applications. In *Principal Manifolds for Data Visualization and Dimension Reduction*, Gorban, A. N., Kegl, B., Wunsch, D. C., and Zinovyev, A. Y., editors, volume 58 of *Lecture Notes in Computational Science and Engineering*. Springer Berlin Heidelberg, 44-67.

Scholz, M. and R. Vigario, 2002: Nonlinear pca: a new hierarchical approach. In *Proceedings of European Symposium on Artificial Neural Networks (ESANN)*, D-side, Bruges, Belgium, 439-444.

Schubert, F., 2004: Basic principles of acoustic emission tomography. *DGZfP-Proceedings BB 90-CD, EWGAE 2004, 26th European Conference on Acoustic Emission Testing* 11.

Schubert, K. J. and A. S. Herrmann, 2011: On attenuation and measurement of lamb waves in viscoelastic composites. *Composite Structures*, **94**(1), 177–185.

Schulte, R. T., 2010: *Modellierung und Simulation von wellenbasierten Structural Health Monitoring - Systemen mit der Spektral-Elemente Methode*. Phd thesis.

Seydel, R. and F.-K. Chang, 2001: Impact identification of stiffened composite panels: I. system development. *Smart Materials and Structures*, **10**, 354–369.

Shadrivov, I. V., A. B. Kozyrev, D. W. Van der Weide, and Y. S. Kivshar, 2008: Tunable transmission and harmonic generation in nonlinear metamaterials. *Applied Physics Letters*, **93**, 16903–(1–3).

Shan, Q. and G. King, 2003: Fuzzy techniques for impact locating and magnitude estimating. *Insight NonDestructive Testing and Condition Monitoring*, **45**(3), 190–195.

Silk, M. G. and K. F. Baiton, 1979: The propagation in metal tubing of ultrasonic wave modes equivalent to lamb waves. *Ultrasonics*, **17**(1), 11–19.

Soerensen, B. F., K. Joergensen, T. K. Jacobsen, and R. C. Oestergaard, 2004: A general mixed mode fracture mechanics test specimen: The dcb-specimen loaded with uneven bending moments. Technical report, Riso National Laboratory.

Soerensen, B. F., K. Joergensen, T. K. Jacobsen, and R. C. Oestergaard, 2006: Dcb-specimen loaded with uneven bending moments. *International Journal of Fracture*, **141**(1-2), 163–176.

Sohn, H., 2007: Effects of environmental and operational variability on structural health monitoring. *Philosophical Transactions of the Royal Society A: Mathematical, Physical and Engineering Sciences*, **365**(1851), 539–560.

Sohn, H., C. R. Farrar, F. M. Hemez, D. D. Shunk, D. W. Stinemates, B. R. Nadler, and J. J. Czarnecki, 2004: A review of structural health monitoring literature: 1996-2001. Technical report, Los Alamos National Laboratory Report.

Sohn, H., C. R. Farrar, N. F. Hunter, and K. Worden, 2001: Structural health monitoring using statistical pattern recognition techniques. *Journal of Dynamic Systems, Measurement and Control*, **123**, 706–711.

Sohn, H., K. Worden, and C. R. Farrar, 2002: Statistical damage classification under changing environmental and operational conditions. *Journal of Intelligent Material Systems and Structures*, **13**(9), 561–574.

Srivastava, A. and F. L. d. Scalea, 2009: On the existence of antisymmetric or symmetric lamb waves at nonlinear higher harmonics. *Journal of Sound and Vibration*, **323**(3-5), 932–943.

Staszewski, W., C. Boller, and G. R. Tomlinson, 2004: *Health Monitoring of Aerospace Structures: Smart Sensor Technologies and Signal Processing*. Wiley, Munich.

Staszewski, W. J., 2000: Advanced data pre-processing for damage identification based on pattern recognition. *International Journal of Systems Science*, **31**(11), 1381–1396.

Staszewski, W. J., 2002: Intelligent signal processing for damage detection in composite materials. *Composite Science and Technology*, **62**(7-8), 941–950.

Staszewski, W. J., 2005: Ultrasonic/guided waves for structural health monitoring. *Key Engineering Materials*, **293-294**, 49–62.

Staszewski, W. J. and A. N. Robertson, 2007: Time-frequency and time-scale analyses for structural health monitoring. *Philosophical Transactions of the Royal Society A*, **365**(1851), 449–477.

Staszewski, W. J. and K. Worden, 2001: An overview of optimal sensor location methods for damage detection. In *Proceeding of the 8th SPIE Symp. on Smart Structures and Materials, Conf. on Modeling, Signal processing and Control of Smart Structures*, Rao, V. S., editor, volume 4326, Newport Beach, CA, 179-187.

Su, Z., C. Yang, N. Pan, L. Ye, and L.-M. Zhou, 2007: Assessment of delamination in composite beams using shear horizontal (sh) wave mode. *Composites Science and Technology*, **67**(2), 244–251.

Su, Z., L. Ye, and Y. Lu, 2006: Guided lamb waves for identification of damage in composite structures: A review. *Journal of Sound and Vibration*, **295**(3-5), 753–780.

Subasi, A., 2007: Application of adaptive neuro-fuzzy inference system for epileptic seizure detection using wavelet feature extraction. *Computers in Biology and Medicine*, **37**(2), 227–244.

Surgeon, M. and M. Wevers, 1999: Modal analysis of acoustic emission signals from cfrp laminates. *NDT&E International*, **32**, 311–322.

Szabo, T. L. and J. Wu, 2000: A model for longitudinal and shear wave propagation in viscoelastic media. *Journal of the Acoustical Society of America*, **107**(5), 2437–2446.

Taha, M. M. R., A. Noureldin, J. L. Lucero, and T. J. Baca, 2006: Wavelet transform for structural health monitoring: A compendium of uses and features. *Structural Health Monitoring*, **5**(3), 267–295.

Tibaduiza, D.-A., M.-A. Torres Arredondo, L. Mujica, J. Rodellar, and C.-P. Fritzen, 2013: A study of two unsupervised data driven statistical methodologies for detecting and classifying damages in structural health monitoring. *Journal of Mechanical Systems and Signal Processing*.

Tibaduiza-Burgos, D., L. Mujica, and J. Rodellar, 2011: Comparison of several methods for damage localization using indices and contributions based on pca. *Journal of Physics: Conference Series*, **305**(1).

Torres Arredondo, M. A., I. Buethe, D.-A. Tibaduiza, J. Rodellar, and C.-P. Fritzen, 2012: Damage detection and classification in pipework using acousto-ultrasonics and probabilistic non-linear modelling. In *Civil Structural Health Monitoring Workshop (CSHM-4)*, Berlin, Germany (on CD-ROM).

Torres Arredondo, M. A. and C.-P. Fritzen, 2010: On the application of digital signal processing techniques and statistical analysis for the localization of acoustic emissions. In *Proceedings of the 5th European Workshop in Structural Health Monitoring, EWSHM 2011*, Casciati, F. and Giordano, M., editors, DEStech Publications, Inc., Sorrento, Italy, 1017-1022.

Torres Arredondo, M. A. and C.-P. Fritzen, 2011: A viscoelastic plate theory for the fast modelling of lamb wave solutions in ndt/shm applications. *Ultragarsas (Ultrasound)*, **66**(2), 7–13.

Torres Arredondo, M. A. and C.-P. Fritzen, 2012a: Characterization and classification of modes in acoustic emission based on dispersion features and energy distribution analysis. *Journal of Shock and Vibration*, **19**(1-9), 825–833.

Torres Arredondo, M. A. and C.-P. Fritzen, 2012b: Impact monitoring in smart structures based on gaussian processes. In *Proceedings of the 4th International Symposium on NDT in Aerospace*, Augsburg, Germany (on CD-ROM).

Torres Arredondo, M. A. and C.-P. Fritzen, 2012c: Ultrasonic guided wave dispersive characteristics in composite structures under variable temperature and operational conditions. In *Proceedings of the 6th European Workshop in Structural Health Monitoring, EWSHM 2012*, volume 1, Dresden, Germany, 261-268.

Torres Arredondo, M. A., C.-P. Fritzen, and C. Yang, 2011: On the application of bayesian analysis and advanced signal processing techniques for the impact monitoring of smart structures. In *Proceedings of the 8th International Workshop in Structural Health Monitoring, IWSHM 2011*, Chang, F.-K., editor, volume 2, DEStech Publications, Inc., Stanford, CA, 1062-1069.

Torres Arredondo, M. A., H. Jung, and C.-P. Fritzen, 2011: A study of attenuation and acoustic energy anisotropy of lamb waves in multilayered anisotropic media for ndt and shm applications. In *Proceedings of the 6th International Workshop NDT in Progress*, Mazal, P., editor, Brno University of Technology, Prague, Czech Republic, 313-325.

Torres Arredondo, M. A., H. Jung, and C.-P. Fritzen, 2012: Towards the development of predictive models for the system design and modal analysis of acoustic emission based technologies. *Key Engineering Materials*, **518**, 396–408.

Torres Arredondo, M. A., M. M. Ramirez Lozano, and C.-P. Fritzen, 2011: *DispWare Toolbox - A scientific computer program for the calculation of dispersion relations for modal-based Acoustic Emission and Ultrasonic Testing.* Msc thesis.

Torres Arredondo, M. A., D.-A. Tibaduiza, L. Mujica, J. Rodellar, and C.-P. Fritzen, 2012: Damage assessment in a stiffened composite panel using non-linear data-driven modelling and ultrasonic guided waves. In *Proceedings of the 4th International Symposium on NDT in Aerospace*, Augsburg, Germany (on CD-ROM).

Torres Arredondo, M. A., D.-A. Tibaduiza, L. Mujica, J. Rodellar, and C.-P. Fritzen, 2013: Data-driven multivariate algorithms for damage detection and classification: Evaluation and comparison. *International Journal of Structural Health Monitoring.*

Trujillo, D. M. and H. R. Busby, 1997: *Practical Inverse Analysis in Engineering.* CRC Press, London.

Uebeyli, E. D., 2008: Adaptive neuro-fuzzy inference system employing wavelet coefficients for detection of ophthalmic arterial disorders. *Expert Systems with Applications*, **34**(3), 2201–2209.

Uhl, T., 2007: The inverse identification problem and its technical application. *Archive of Applied Mechanics*, **77**(5), 325–337.

Ultsch, A., 1993: *Self-organizing neural networks for visualization and classification.* Concepts, Methods and Applications in Information and Classification. Springer.

Ultsch, A. and F. Moerchen, 2005: Esom-maps: tools for clustering, visualization, and classification with emergent som. Technical report, Data Bionics Research Group, University of Marburg.

Van Velsor, J. K. and J. L. Rose, 2007: Guided-wave tomographic imaging of defects in pipe using a probabilistic reconstruction algorithm. *Insight NonDestructive Testing and Condition Monitoring*, **49**(9), 532–537.

Vary, A., 1990: Acousto-ultrasonics. In *Non-Destructive Testing of Fibre-Reinforced Plastics*, Summerscales, J., editor, volume 2. Elsevier Applied Science, London, 1-54.

Vary, A. and K. J. Bowles, 1979: An uitrasonic- acoustic technique for nondestructive evaluation of fiber composite quality. *Polymer Engineering and Science*, **19**(5), 373–376.

Vasiliev, V. V. and E. V. Morozov, 2007: *Advanced mechanics of composite materials.* Elsevier, Oxford, 2nd edition.

Velichko, A. and P. D. Wilcox, 2007: Modeling the excitation of guided waves in generally anisotropic multilayered media. *The Journal of the Acoustical Society of America*, **121**(1), 60–69.

Velichko, A. and P. D. Wilcox, 2009: Excitation and scattering of guided waves: Relationships between solutions for plates and pipes. *The Journal of the Acoustical Society of America*, **121**(1), 3623–3631.

Vesanto, J., J. Himberg, E. Alhoniemi, and J. Parhankangas, 2000: Som toolbox for matlab 5.

Viktorov, I., 1967: *Rayleigh and Lamb waves - Physical Theory and Applications*. Plenum Press, New York.

Vives, A. A., 2008: *Piezoelectric Transducers and Applications*. Springer, Berlin, 2nd edition.

Wang, L. and F. G. Yuan, 2007a: Active damage localization technique based on energy propagation of lamb waves. *Smart Materials and Structures*, **3**(2), 201–217.

Wang, L. and F. G. Yuan, 2007b: Lamb wave propagation in composite laminates using a higher-order plate theory. volume 6531 of *Proceedings of SPIE - The International Society for Optical Engineering*, Society of Photo-Optical Instrumentation Engineers, Bellingham.

Westerhuis, J. A., T. Kourti, and J. F. MacGregor, 1999: Comparing alternative approaches for multivariate statistical analysis of batch process data. *Journal of Chemometrics*, **13**(3-4), 397–413.

Whitney, J. and C. Sun, 1973: A higher order theory for extensional motion of laminated composites. *Journal of Sound and Vibration*, **30**(1), 85–97.

Wilcox, P. D., 1998: *Lamb Wave Inspection of Large Structures Using Permanently Attached Transducers*. Phd thesis.

Wilcox, P. D., 2004: Modeling the excitation of lamb and sh waves by point and line sources. In *Review of Progress in Quantitative Nondestructive Evaluation*, Thompson, D. and Chimenti, D., editors, volume 23, AIP, New York, 206-213.

Wilcox, P. D., C. Lee, J. J. Scholey, M. I. Friswell, M. Wisnom, and B. Drinkwater, 2006: Progress towards a forward model of the complete acoustic emission process. *Advanced Materials Research*, **13-14**, 69–76.

Williams, C. K. I. and D. Barber, 1998: Bayesian classification with gaussian processes. *IEEE Transactions on Pattern Analysis and Machine Intelligence*, **20**(12), 1342–1351.

Williams, C. K. I., C. S. Qazaz, C. M. Bishop, and H. Zhu, 1995: On the relationship between bayesian error bars and the input data density. 160-165.

Wold, S., P. Geladi, K. Esbensen, and J. Oehman, 1987: Multi-way principal components-and pls-analysis. *Journal of Chemometrics*, **1**(1), 41–56.

Wolfe, J. P., 2005: *Imaging Phonons: Acoustic Wave Propagation in Solids*. Cambridge Univ. Press, Cambridge.

Worden, K., 2003: Sensor validation and correction using auto-associative neural networks and principal component analysis. In *Proceedings of IMAC-XXI: Conference & Exposition on Structural Dynamics*, Orlando, USA, 1-10.

Worden, K. and G. Manson, 2007: The application of machine learning to structural health monitoring. *Philosophical Transactions of the Royal Society A: Mathematical, Physical and Engineering Sciences*, **365**(1851), 515–537.

Worden, K., G. Manson, and D. Allman, 2003: Experimental validation of a structural health monitoring methodology: Part i. novelty detection on a laboratory structure. *Journal of Sound and Vibration*, **259**(3), 323–343.

Worden, K., G. Manson, and N. R. J. Fieller, 2000: Damage detection using outlier analysis. *Journal of Sound and Vibration*, **229**(3), 647–667.

Worden, K. and W. J. Staszewski, 2000: Impact location and quantification on a composite panel using neural networks and a genetic algorithm. *Strain*, **36**(2), 61–68.

Worden, K., W. J. Staszewski, and J. J. Hensman, 2011: Natural computing for mechanical systems research: A tutorial overview. *Mechanical Systems and Signal Processing*, **25**(1), 4–111.

Worlton, D. C., 1957: Ultrasonic testing with lamb waves. *Non-Destructive Testing*, **15**(4), 218–222.

Wu, H., A. Yan, G. Fu, and R. Gibson, 2006: Mechanics based durability modeling of frp bridge deck. In *Proceedings of the Convention and Trade Show American Composites Manufacturers Association*, St. Louis, MO, USA, 1-6.

Xu, X., F. Xiao, and S. Wang, 2008: Enhanced chiller sensor fault detection, diagnosis and estimation using wavelet analysis and principal component analysis methods. *Applied Thermal Engineering*, **28**, 226–237.

Yan, A.-M., G. Kerschen, P. D. Boe, and J.-C. Golinval, 2005: Structural damage diagnosis under varying environmental conditions part i: A linear analysis. *Mechanical Systems and Signal Processing*, **19**(4), 847–864.

Yan, G. and L. Zhou, 2009: Impact load identification of composite structure using genetic algorithms. *Journal of Sound and Vibration*, **319**(3-5), 869–884.

Yang, B., E. Pan, and F. Yuan, 2003: Three-dimensional stress analyses in composite laminates with an elastically pinned hole. *International Journal of Solids and Structures*, **40**(8), 2017–2035.

Yang, C., M. A. Torres Arredondo, and C.-P. Fritzen, 2011: Acoustic emission simulation for online impact detection. In *Proceedings of COMSOL Conference*, Stuttgart, Germany (on CD-ROM).

Yokozeki, T., A. Kuroda, A. Yoshimura, T. Ogasawara, and T. Aoki, 2010: Damage characterization in thin-ply composite laminates under out-of-plane transverse loadings. *Composite Structures*, **93**(1), 4957.

Yu, L., V. Giurgiutiu, and P. Pollock, 2008: A multi-mode sensing system for corrosion detection using piezoelectric wafer active sensors. In *Proceedings of Sensors and Smart Structures Technologies for Civil, Mechanical, and Aerospace Systems*, San Diego, USA.

Yuan, F. G. and C. C. Hsieh, 1998: Three-dimensional wave propagation in composite cylindrical shells. *Composite Structures*, **42**(4), 153–167.

Zhang, G., S. Zhang, and Y. Wang, 2000: Application of adaptive time-frequency decomposition in ultrasonic nde of highly scattering materials. *Ultrasonics*, **38**(10), 961–964.

Zhou, C., M. Hong, Z. Su, Q. Wang, and L. Cheng, 2012: Evaluation of fatigue cracks using nonlinearities of acousto-ultrasonic waves acquired by an active sensor network. *Smart Materials and Structures*, **22**(1), 1–12.

Zhou, G., 1998: The use of experimentally-determined impact force as a damage measure in impact damage resistance and tolerance of composite structures. *Composite Structures*, **42**(4), 375–382.

Ziola, S. M. and M. R. Gorman, 1991: Source location in thin plates using cross-correlation. *The Journal of the Acoustical Society of America*, **90**(5), 2551–2556.

A. Appendix A

A.1. Christoffel Equation

The system of equations presented in Eq.(2.5) can be expressed in a matrix form where the eigenvalues and eigenvectors of the Christoffel matrix fully provide the bulk modes. This can be expressed as [Nayfeh 1995]:

$$\begin{bmatrix} \Lambda_{11}-c_{ph}^2 & \Lambda_{12} & \Lambda_{13} \\ \Lambda_{12} & \Lambda_{22}-c_{ph}^2 & \Lambda_{23} \\ \Lambda_{13} & \Lambda_{23} & \Lambda_{33}-c_{ph}^2 \end{bmatrix} \begin{bmatrix} U_1 \\ U_2 \\ U_3 \end{bmatrix} = 0, \tag{A.1}$$

where the elements of Λ_{im} are given by:

$$\begin{aligned}
\Lambda_{11} &= \tfrac{1}{\rho}\left(C_{11}n_1^2 + C_{66}n_2^2 + C_{55}n_3^2 + 2C_{16}n_1n_2 + 2C_{15}n_1n_3 + 2C_{56}n_2n_3\right), \\
\Lambda_{12} &= \tfrac{1}{\rho}\left(C_{16}n_1^2 + C_{26}n_2^2 + C_{45}n_3^2 + (C_{12}+C_{66})n_1n_2 + (C_{14}+C_{56})n_1n_3 + (C_{46}+C_{25})n_2n_3\right), \\
\Lambda_{13} &= \tfrac{1}{\rho}\left(C_{15}n_1^2 + C_{46}n_2^2 + C_{35}n_3^2 + (C_{14}+C_{56})n_1n_2 + (C_{13}+C_{55})n_1n_3 + (C_{36}+C_{45})n_2n_3\right), \\
\Lambda_{22} &= \tfrac{1}{\rho}\left(C_{66}n_1^2 + C_{22}n_2^2 + C_{44}n_3^2 + 2C_{26}n_1n_2 + 2C_{46}n_1n_3 + 2C_{24}n_2n_3\right), \\
\Lambda_{23} &= \tfrac{1}{\rho}\left(C_{56}n_1^2 + C_{24}n_2^2 + C_{34}n_3^2 + (C_{46}+C_{25})n_1n_2 + (C_{36}+C_{45})n_1n_3 + (C_{23}+C_{44})n_2n_3\right), \\
\Lambda_{33} &= \tfrac{1}{\rho}\left(C_{55}n_1^2 + C_{44}n_2^2 + C_{33}n_3^2 + 2C_{45}n_1n_2 + 2C_{35}n_1n_3 + 2C_{34}n_2n_3\right).
\end{aligned} \tag{A.2}$$

Eq.(A.1) can be solved once the material properties and the direction of propagation are selected.

A.2. Equations of Motion in Cylindrical Coordinates

The displacement equations of motion in a cylindrical coordinate system can be written as [Achenbach 1984]:

$$\nabla^2 u_r - \frac{u_r}{r} - \frac{2}{r^2}\frac{\partial u_\theta}{\partial \theta} + \frac{1}{1-2\nu}\frac{\partial \triangle}{\partial r} = \frac{1}{C_T^2}\frac{\partial^2 u_r}{dt^2}, \tag{A.3a}$$

$$\nabla^2 u_\theta - \frac{u_\theta}{r} - \frac{2}{r^2}\frac{\partial u_r}{\partial \theta} + \frac{1}{1-2\nu}\frac{\partial \triangle}{\partial \theta} = \frac{1}{C_T^2}\frac{\partial^2 u_\theta}{dt^2}, \tag{A.3b}$$

$$\nabla^2 u_z + \frac{1}{1-2\nu}\frac{\partial \triangle}{\partial z} = \frac{1}{C_T^2}\frac{\partial^2 u_z}{dt^2}, \tag{A.3c}$$

where u_r, u_θ and u_z are the displacement vectors in the directions of r, θ and z (see Figure 2.5), ν the poisson ratio and C_T is the transverse wave velocity. Additionally, ∇^2 denotes the Laplacian operator given by:

$$\nabla^2 = \frac{\partial^2}{\partial r^2} + \frac{1}{r}\frac{\partial}{\partial r} + \frac{1}{r^2}\frac{\partial^2}{\partial \theta^2} + \frac{\partial^2}{dz^2}, \tag{A.4}$$

and $\triangle$ denotes the dilatation defined as:

$$\triangle = \frac{\partial u_r}{\partial r} + \frac{1}{r}\left(\frac{\partial u_\theta}{\partial r} + u_r\right) + \frac{\partial u_z}{\partial z}. \tag{A.5}$$

The corresponding stresses in cylindrical coordinates are given in terms of the displacements as:

$$\sigma_{rr} = \lambda\left(\frac{\partial u_r}{\partial r} + \frac{u_r}{r} + \frac{1}{r}\frac{\partial u_\theta}{\partial \theta} + \frac{\partial u_z}{\partial z}\right) + 2\mu\frac{\partial u_r}{\partial r}, \tag{A.6a}$$

$$\sigma_{\theta\theta} = \lambda\left(\frac{\partial u_r}{\partial r} + \frac{u_r}{r} + \frac{1}{r}\frac{\partial u_\theta}{\partial \theta} + \frac{\partial u_z}{\partial z}\right) + 2\mu\left(\frac{u_r}{r} + \frac{1}{r}\frac{\partial u_\theta}{\partial \theta}\right), \tag{A.6b}$$

$$\sigma_{zz} = \lambda\left(\frac{\partial u_r}{\partial r} + \frac{u_r}{r} + \frac{1}{r}\frac{\partial u_\theta}{\partial \theta} + \frac{\partial u_z}{\partial z}\right) + 2\mu\frac{\partial u_z}{\partial z}, \tag{A.6c}$$

$$\sigma_{r\theta} = \mu\left(\frac{\partial u_\theta}{\partial r} - \frac{u_\theta}{r} + \frac{1}{r}\frac{\partial u_r}{\partial \theta}\right), \tag{A.6d}$$

$$\sigma_{\theta z} = \mu\left(\frac{\partial u_\theta}{\partial z} + \frac{1}{r}\frac{\partial u_z}{\partial \theta}\right), \tag{A.6e}$$

$$\sigma_{zr} = \mu\left(\frac{\partial u_z}{\partial r} + \frac{\partial u_r}{\partial z}\right), \tag{A.6f}$$

$$\mu = \frac{E}{2(1+\nu)}, \tag{A.6g}$$

$$\lambda = \frac{E}{(1+\nu)(1-2\nu)}, \tag{A.6h}$$

where λ and μ are the Lamé connecting the components of an elastic stress at some point of a linearly-elastic (or solid deformable) isotropic body with the components of the deformation at this point [Hearn 1977]. They are related to the modulus of elasticity E (Young's modulus) and Poisson's ratio ν. The Lamé constants depend on the material

and its temperature.

A.3. Components of the General Matrix for Cylindrical Waveguides

By substituting Eq.(2.8a) to Eq.(2.8d) into Eq.(2.6a) to Eq.(2.6c), making use of the stress-displacement relations, i.e. Eq.(A.6a) to Eq.(A.6f) , and finally substituting the Bessel solutions from Eq.(2.11a) to Eq.(2.11c), the system of equations can be expressed into the product of a matrix **K** and a vector of amplitudes **A**. The general system yields to:

$$\begin{bmatrix} u_z \\ u_r \\ u_\theta \\ \sigma_{rr} \\ \sigma_{rz} \\ \sigma_{r\theta} \end{bmatrix} = \mathbf{KA} = \begin{bmatrix} K_{11} & K_{12} & K_{13} & K_{14} & K_{15} & K_{16} \\ K_{21} & K_{22} & K_{23} & K_{24} & K_{25} & K_{26} \\ K_{31} & K_{32} & K_{33} & K_{34} & K_{35} & K_{36} \\ K_{41} & K_{42} & K_{43} & K_{44} & K_{45} & K_{46} \\ K_{51} & K_{52} & K_{53} & K_{54} & K_{55} & K_{56} \\ K_{61} & K_{62} & K_{63} & K_{64} & K_{65} & K_{66} \end{bmatrix} \begin{bmatrix} A_1 \\ A_2 \\ A_3 \\ A_4 \\ A_5 \\ A_6 \end{bmatrix}. \tag{A.7}$$

After long and non trivial calculations, the terms of the matrix **K** are given below. The terms for u_z are given by:

$$K_{11} = i\left(kW_n\left(\zeta_1 r\right)\right), \tag{A.8a}$$

$$K_{12} = i\left(kZ_n\left(\zeta_1 r\right)\right), \tag{A.8b}$$

$$K_{13} = i\left(\lambda_2 \beta W_n\left(\zeta_2 r\right)\right), \tag{A.8c}$$

$$K_{14} = i\left(\beta Z_n\left(\zeta_2 r\right)\right), \tag{A.8d}$$

$$K_{15} = 0, \tag{A.8e}$$

$$K_{16} = 0. \tag{A.8f}$$

The terms for u_r are given by:

$$K_{21} = \frac{n}{r} W_n\left(\zeta_1 r\right) - \lambda_1 \alpha W_{n+1}\left(\zeta_1 r\right), \tag{A.9a}$$

$$K_{22} = \frac{n}{r} Z_n\left(\zeta_1 r\right) - \alpha Z_{n+1}\left(\zeta_1 r\right), \tag{A.9b}$$

$$K_{23} = kW_{n+1}\left(\zeta_2 r\right), \tag{A.9c}$$

$$K_{24} = kZ_{n+1}\left(\zeta_2 r\right), \tag{A.9d}$$

$$K_{25} = \frac{n}{r} W_n\left(\zeta_2 r\right), \tag{A.9e}$$

$$K_{26} = \frac{n}{r} Z_n\left(\zeta_2 r\right). \tag{A.9f}$$

The terms for u_θ are given by:

$$K_{31} = i\left(\frac{n}{r}W_n(\zeta_1 r)\right), \tag{A.10a}$$

$$K_{32} = i\left(\frac{n}{r}Z_n(\zeta_1 r)\right), \tag{A.10b}$$

$$K_{33} = -i\left(kW_{n+1}(\zeta_2 r)\right), \tag{A.10c}$$

$$K_{34} = -i\left(kZ_{n+1}(\zeta_2 r)\right), \tag{A.10d}$$

$$K_{35} = i\left(\frac{n}{r}W_n(\zeta_2 r) - \beta W_{n+1}(\zeta_2 r)\right), \tag{A.10e}$$

$$K_{36} = i\left(\frac{n}{r}Z_n(\zeta_2 r) - \lambda_2\beta Z_{n+1}(\zeta_2 r)\right). \tag{A.10f}$$

The terms for σ_{rr} are given by:

$$K_{41} = \mu\left(\left(k^2-\beta^2\right) + \frac{2n}{r^2}(n-1)W_n(\zeta_1 r) + \frac{2}{r}\alpha W_{n+1}(\zeta_1 r)\right), \tag{A.11a}$$

$$K_{42} = \mu\left(\left(k^2-\beta^2\right) + \frac{2n}{r^2}(n-1)Z_n(\zeta_1 r) + \frac{2\lambda_1}{r}\alpha Z_{n+1}(\zeta_1 r)\right), \tag{A.11b}$$

$$K_{43} = \mu\left(2\lambda_2 k\beta W_n(\zeta_2 r) - \frac{2(n+1)}{r}kW_{n+1}(\zeta_2 r)\right), \tag{A.11c}$$

$$K_{44} = \mu\left(2k\beta Z_n(\zeta_2 r) - \frac{2(n+1)}{r}kZ_{n+1}(\zeta_2 r)\right), \tag{A.11d}$$

$$K_{45} = \mu\left(\frac{2n(n-1)}{r^2}W_n(\zeta_2 r) - \frac{2n}{r}\beta W_{n+1}(\zeta_2 r)\right), \tag{A.11e}$$

$$K_{46} = \mu\left(\frac{2n(n-1)}{r^2}Z_n(\zeta_2 r) - \frac{2\lambda_2}{r}n\beta Z_{n+1}(\zeta_2 r)\right). \tag{A.11f}$$

The terms for σ_{rz} are given by:

$$K_{51} = \mu i\left(\frac{2n}{r}kW_n(\zeta_1 r) - 2\alpha kW_{n+1}(\zeta_1 r)\right), \tag{A.12a}$$

$$K_{52} = \mu i\left(\frac{2n}{r}kZ_n(\zeta_1 r) - 2\lambda_1\alpha kZ_{n+1}(\zeta_1 r)\right), \tag{A.12b}$$

$$K_{53} = \mu i\left(\frac{2\lambda_2}{r}n\beta W_n(\zeta_2 r) + \left(k^2-\beta^2\right)W_{n+1}(\zeta_2 r)\right), \tag{A.12c}$$

$$K_{54} = \mu i\left(\frac{2n}{r}\beta Z_n(\zeta_2 r) + \left(k^2-\beta^2\right)Z_{n+1}(\zeta_2 r)\right), \tag{A.12d}$$

$$K_{55} = \mu i\left(\frac{n}{r}kW_n(\zeta_2 r)\right), \tag{A.12e}$$

$$K_{56} = \mu i\left(\frac{n}{r}kZ_n(\zeta_2 r)\right). \tag{A.12f}$$

Table A.1. *Required substitutions for the appropriate selection of the parameters and Bessel functions required during the root finding procedure.*

$C_{ph} > C_L$	$C_L > C_{ph} > C_T$	$C_T > C_{ph}$
$\zeta_1 = \sqrt{\zeta_1^2}$	$\zeta_1 = \sqrt{\zeta_1^2}$	$\zeta_1 = \sqrt{\zeta_1^2}$
$\zeta_2 = \sqrt{\zeta_2^2}$	$\zeta_2 = \sqrt{\zeta_2^2}$	$\zeta_2 = \sqrt{\zeta_2^2}$
$\lambda_1 = 1$	$\lambda_1 = -1$	$\lambda_1 = -1$
$\lambda_2 = 1$	$\lambda_2 = 1$	$\lambda_2 = -1$
$Z_n(\zeta_1 r) = J_n(\zeta_1 r)$	$Z_n(\zeta_1 r) = I_n(\zeta_1 r)$	$Z_n(\zeta_1 r) = I_n(\zeta_1 r)$
$W_n(\zeta_1 r) = Y_n(\zeta_1 r)$	$W_n(\zeta_1 r) = K_n(\zeta_1 r)$	$W_n(\zeta_1 r) = K_n(\zeta_1 r)$
$Z_n(\zeta_2 r) = J_n(\zeta_2 r)$	$Z_n(\zeta_2 r) = J_n(\zeta_2 r)$	$Z_n(\zeta_2 r) = I_n(\zeta_2 r)$
$W_n(\zeta_2 r) = Y_n(\zeta_2 r)$	$W_n(\zeta_2 r) = Y_n(\zeta_2 r)$	$W_n(\zeta_2 r) = K_n(\zeta_2 r)$

The terms for $\sigma_{r\theta}$ are given by:

$$K_{61} = \mu i \left(\frac{2n(n-1)}{r^2} W_n(\zeta_1 r) - \frac{2n}{r} \alpha W_{n+1}(\zeta_1 r) \right), \tag{A.13a}$$

$$K_{62} = \mu i \left(\frac{2n(n-1)}{r^2} Z_n(\zeta_1 r) - \frac{2\lambda_1}{r} n\alpha Z_{n+1}(\zeta_1 r) \right), \tag{A.13b}$$

$$K_{63} = \mu i \left(-\lambda_2 \beta k W_n(\zeta_2 r) + \frac{2(n+1)}{r} k W_{n+1}(\zeta_2 r) \right), \tag{A.13c}$$

$$K_{64} = \mu i \left(-\beta k Z_n(\zeta_2 r) + \frac{2(n+1)}{r} k Z_{n+1}(\zeta_2 r) \right), \tag{A.13d}$$

$$K_{65} = \mu i \left(\frac{2n(n-1) - \beta^2 r^2}{r^2} W_n(\zeta_2 r) + \frac{2\beta}{r} W_{n+1}(\zeta_2 r) \right), \tag{A.13e}$$

$$K_{66} = \mu i \left(\frac{2n(n-1) - \beta^2 r^2}{r^2} Z_n(\zeta_2 r) + \frac{2\lambda_2}{r} \beta Z_{n+1}(\zeta_2 r) \right), \tag{A.13f}$$

where the terms α and β are given by:

$$\alpha = \mid \zeta_1 \mid, \tag{A.14}$$

$$\beta = \mid \zeta_2 \mid, \tag{A.15}$$

additionally, $Z_n(\bullet)$ and $W_n(\bullet)$ are Bessel functions of order n. The selection of the appropriate Bessel functions and of the terms λ_1 and λ_2 are provided in Table A.1 [Pavlakovic and Lowe 2003]. The functions $J_n(\bullet)$ and $Y_n(\bullet)$ are Bessel functions of the first and second kind, respectively. The functions $I_n(\bullet)$ and $K_n(\bullet)$ correspond to modified Bessel functions of the first and second kind, respectively.

B. Appendix B

Substitution of the constitutive relations calculated in Section 3.2.2 into Eq.(3.12), and further substitution of Eq.(3.13) yields to the equations of motion. For the case of symmetric laminates the equations of motion can be decoupled into two independent matrices $\mathbf{L_S}$ and $\mathbf{L_A}$. In order to obtain solutions for the symmetric and antisymmetric modes of propagation, combinations of frequency and wavenumber where the matrices determinants go to zero must be found.

After long and non trivial calculations, the symmetric modes are governed by:

$$\mathbf{L_S G_S} = \begin{bmatrix} L_s^{11} & L_s^{12} & L_s^{13} & L_s^{14} & L_s^{15} \\ L_s^{12} & L_s^{22} & L_s^{23} & L_s^{15} & L_s^{25} \\ L_s^{13} & L_s^{23} & L_s^{33} & L_s^{34} & L_s^{35} \\ L_s^{14} & L_s^{15} & L_s^{34} & L_s^{44} & L_s^{45} \\ L_s^{15} & L_s^{25} & L_s^{35} & L_s^{45} & L_s^{55} \end{bmatrix} \begin{bmatrix} U_0 \\ V_0 \\ \Psi_z \\ \Xi_x \\ \Xi_y \end{bmatrix}, \tag{B.1}$$

where the terms of $\mathbf{L_S}$ are given by:

$$\begin{aligned} L_s^{11} &= A_{11}k_x^2 + A_{66}k_y^2 + 2A_{16}k_xk_y - \omega^2 I_0, \\ L_s^{12} &= A_{16}k_x^2 + A_{26}k_y^2 + (A_{12} + A_{66})k_xk_y, \\ L_s^{13} &= i\kappa_1 \left(A_{13}k_x + A_{36}k_y\right), \\ L_s^{14} &= D_{11}k_x^2 + D_{66}k_y^2 + 2D_{16}k_xk_y - \omega^2 I_1, \\ L_s^{15} &= D_{16}k_x^2 + D_{26}k_y^2 + (D_{12} + D_{66})k_xk_y, \\ L_s^{22} &= A_{66}k_x^2 + A_{22}k_y^2 + 2A_{26}k_xk_y - \omega^2 I_0, \\ L_s^{23} &= -i\kappa_1 \left(A_{36}k_x + A_{23}k_y\right), \\ L_s^{25} &= D_{66}k_x^2 + D_{22}k_y^2 + 2D_{26}k_xk_y - \omega^2 I_2, \end{aligned} \tag{B.2a}$$

$$
\begin{aligned}
L_{\mathrm{s}}^{33} &= -\kappa_7^2 D_{55} k_x^2 - \kappa_4^2 D_{44} k_y^2 - 2\kappa_4 \kappa_7 D_{45} k_x k_y - \kappa_1^2 A_{33} + \omega^2 I_2, \\
L_{\mathrm{s}}^{34} &= i\left(2\kappa_7^2 D_{55} - \kappa_1 D_{13}\right) k_x + i\left(2\kappa_4 \kappa_7 D_{45} - \kappa_1 D_{36}\right) k_y, \\
L_{\mathrm{s}}^{35} &= i\left(2\kappa_4 \kappa_7 D_{45} - \kappa_1 D_{36}\right) k_x + i\left(2\kappa_4^2 D_{44} - \kappa_1 D_{23}\right) k_y, \\
L_{\mathrm{s}}^{44} &= H_{11} k_x^2 + H_{66} k_y^2 + 2H_{16} k_x k_y + 4\kappa_7^2 D_{55} - \omega^2 I_4, \\
L_{\mathrm{s}}^{45} &= H_{16} k_x^2 + H_{26} k_y^2 + \left(H_{12} + H_{66}\right) k_x k_y + 4\kappa_4 \kappa_7 D_{45}, \\
L_{\mathrm{s}}^{55} &= H_{66} k_x^2 + H_{22} k_y^2 + 2H_{26} k_x k_y + 4\kappa_4^2 D_{44} - \omega^2 I_4.
\end{aligned}
\tag{B.2b}
$$

The antisymmetric modes are governed by:

$$
\mathbf{L}_{\mathrm{A}}\mathbf{G}_{\mathrm{A}} = \begin{bmatrix}
L_{\mathrm{A}}^{11} & L_{\mathrm{A}}^{12} & L_{\mathrm{A}}^{13} & L_{\mathrm{A}}^{14} & L_{\mathrm{A}}^{15} & L_{\mathrm{A}}^{16} \\
L_{\mathrm{A}}^{12} & L_{\mathrm{A}}^{22} & L_{\mathrm{A}}^{23} & L_{\mathrm{A}}^{24} & L_{\mathrm{A}}^{25} & L_{\mathrm{A}}^{26} \\
L_{\mathrm{A}}^{13} & L_{\mathrm{A}}^{23} & L_{\mathrm{A}}^{33} & L_{\mathrm{A}}^{34} & L_{\mathrm{A}}^{35} & L_{\mathrm{A}}^{36} \\
L_{\mathrm{A}}^{14} & L_{\mathrm{A}}^{24} & L_{\mathrm{A}}^{34} & L_{\mathrm{A}}^{44} & L_{\mathrm{A}}^{45} & L_{\mathrm{A}}^{46} \\
L_{\mathrm{A}}^{15} & L_{\mathrm{A}}^{25} & L_{\mathrm{A}}^{35} & L_{\mathrm{A}}^{45} & L_{\mathrm{A}}^{55} & L_{\mathrm{A}}^{56} \\
L_{\mathrm{A}}^{16} & L_{\mathrm{A}}^{26} & L_{\mathrm{A}}^{36} & L_{\mathrm{A}}^{46} & L_{\mathrm{A}}^{56} & L_{\mathrm{A}}^{66}
\end{bmatrix} \begin{bmatrix}
W_0 \\ \Psi_x \\ \Psi_y \\ \Xi_z \\ \Phi_x \\ \Phi_y
\end{bmatrix},
\tag{B.3}
$$

where the terms of $\mathbf{L}_{\mathrm{A}}$ are given by:

$$
\begin{aligned}
L_{\mathrm{A}}^{11} &= -\kappa_6^2 A_{55} k_x^2 - \kappa_3^2 A_{44} k_y^2 - 2\kappa_3 \kappa_6 A_{45} k_x k_y + \omega^2 I_0, \\
L_{\mathrm{A}}^{12} &= i\kappa_6 \left(\kappa_6 A_{55} k_x + \kappa_3 A_{45} k_y\right), \\
L_{\mathrm{A}}^{13} &= i\kappa_3 \left(\kappa_6 A_{45} k_x + \kappa_3 A_{44} k_y\right), \\
L_{\mathrm{A}}^{14} &= -\kappa_6 \kappa_8 D_{55} k_x^2 - \kappa_3 \kappa_5 D_{44} k_y^2 - \left(\kappa_3 \kappa_8 + \kappa_5 \kappa_6\right) D_{45} k_x k_y + \omega^2 I_2, \\
L_{\mathrm{A}}^{15} &= 3i\left(\kappa_6 \kappa_8 D_{55} k_x + \kappa_3 \kappa_8 D_{45} k_y\right), \\
L_{\mathrm{A}}^{16} &= 3i\left(\kappa_5 \kappa_6 D_{45} k_x + \kappa_3 \kappa_5 D_{44} k_y\right), \\
L_{\mathrm{A}}^{22} &= D_{11} k_x^2 + D_{66} k_y^2 + 2D_{16} k_x k_y + \kappa_6^2 A_{55} - \omega^2 I_2, \\
L_{\mathrm{A}}^{23} &= D_{16} k_x^2 + D_{26} k_y^2 + \left(D_{12} + D_{66}\right) k_x k_y + \kappa_3 \kappa_6 A_{45}, \\
L_{\mathrm{A}}^{24} &= i\left(\kappa_6 \kappa_8 D_{55} k_x + \kappa_5 \kappa_6 D_{45} k_y + 2\kappa_2 \left(D_{13} k_x + D_{36} k_y\right)\right),
\end{aligned}
\tag{B.4a}
$$

$$
\begin{aligned}
L_{\mathrm{A}}^{25} &= H_{11}k_x^2 + H_{66}k_y^2 + 2H_{16}k_xk_y + 3\kappa_6\kappa_8 D_{55} - \omega^2 I_4,\\
L_{\mathrm{A}}^{26} &= H_{16}k_x^2 + H_{26}k_y^2 + (H_{12}+H_{66})\,k_xk_y + 3\kappa_5\kappa_6 D_{45},\\
L_{\mathrm{A}}^{33} &= D_{66}k_x^2 + D_{22}k_y^2 + 2D_{26}k_xk_y + \kappa_3^2 A_{44} - \omega^2 I_2,\\
L_{\mathrm{A}}^{34} &= i\left(\kappa_3\kappa_8 D_{45}k_x + \kappa_3\kappa_5 D_{44}k_y + 2\kappa_2\left(D_{36}k_x + D_{23}k_y\right)\right),\\
L_{\mathrm{A}}^{35} &= H_{16}k_x^2 + H_{26}k_y^2 + (H_{12}+H_{66})\,k_xk_y + 3\kappa_3\kappa_8 D_{45},\\
L_{\mathrm{A}}^{36} &= H_{66}k_x^2 + H_{22}k_y^2 + 2H_{26}k_xk_y + 3\kappa_3\kappa_5 D_{44} - \omega^2 I_4,\\
L_{\mathrm{A}}^{44} &= -\kappa_8^2 H_{55}k_x^2 - \kappa_5^2 H_{44}k_y^2 - (\kappa_5+\kappa_8)\,H_{45}k_xk_y - 4\kappa_2^2 D_{33} + \omega^2 I_4,\\
L_{\mathrm{A}}^{45} &= 3i\left(\kappa_8^2 H_{55}k_x + \kappa_5\kappa_8 H_{45}k_y\right) - 2i\kappa_2\left(H_{13}k_x + H_{36}k_y\right),\\
L_{\mathrm{A}}^{46} &= 3i\left(\kappa_5\kappa_8 H_{45}k_x + \kappa_5^2 H_{44}k_y\right) - 2i\kappa_2\left(H_{36}k_x + H_{23}k_y\right),\\
L_{\mathrm{A}}^{55} &= K_{611}k_x^2 + K_{66}k_y^2 + 2K_{216}k_xk_y + 9\kappa_8^2 H_{55} - \omega^2 I_6,\\
L_{\mathrm{A}}^{56} &= K_{16}k_x^2 + K_{26}k_y^2 + (K_{12}+K_{66})\,k_xk_y + 9\kappa_5\kappa_8 H_{45},\\
L_{\mathrm{A}}^{66} &= K_{66}k_x^2 + K_{22}k_y^2 + 2K_{26}k_xk_y + 9\kappa_5^2 H_{44} - \omega^2 I_6,
\end{aligned}
\tag{B.4b}
$$

where $k_x = k\cos(\theta)$, $k_y = k\sin(\theta)$ are the components of the wavenumber vector and k is the wavenumber. Additionally,

$$
(A_{ij}, D_{ij}, H_{ij}, K_{ij}) = \int_{-h/2}^{h/2} \tilde{C}_{ij}(1, z^2, z^4, z^6)dz, \tag{B.5}
$$

where $i, j = 1,,2...,6$, $\tilde{C}_{ij}$ are the elements of the complex stiffness matrix, ρ is the density of the material and h the thickness of the plate. The resulting complex wavenumber $k = k_{Re} + ik_{Im}$ is used to describe the phase velocity of waves travelling through their real part k_{Re}, and the amplitude decay through their imaginary part k_{Im}.

ISSN 2191-5601